Structural complexity in strongly correlated Pr2-xSrxNiO4+δ, explored by in situ single crystal X-ray and neutron diffraction

Rajesh Dutta

université de BORDEAUX

THÈSE PRÉSENTÉE

POUR OBTENIR LE GRADE DE

DOCTEUR DE

L'UNIVERSITÉ DE BORDEAUX

ÉCOLE DOCTORALE DES SCIENCES CHIMIQUES (SC)

SPÉCIALITÉ

PHYSICO - CHIMIE DE LA MATIÈRE CONDENSÉE

Par Rajesh DUTTA

Structural Complexity in Strongly Correlated $Pr_{2-x}Sr_xNiO_{4+\delta}$, Explored by *in situ* Single Crystal X-ray and Neutron Diffraction

Sous la direction de : Dr. Antoine VILLESUZANNE
(co-directeur : Prof. Werner PAULUS)

Soutenue le 27.11.2017

Membres du jury :

M. GUIONNEAU Philippe, Professeur des Universités, Université de Bordeaux,	Président
M. ROTH Georg, Professeur des Universités, RWTH Aachen,	Rapporteur
Mme. MARTIN Christine, DR CNRS, Laboratoire CRISMAT	Rapporteur
M. RAMACHANDRA RAO M.S, Professeur des Universités, IIT MADRAS	Examinateur
M. PAPET Philippe, Professeur des Universités, Université de Montpellier	Examinateur
M. VILLESUZANNE Antoine, CR CNRS, ICMCB Bordeaux	Examinateur
M. PAULUS Werner, Professeur des Universités, Université de Montpellier	Examinateur

Abstract

There is increasing interest in recent years in the structural aspects and physical properties of layered rare earth (*Ln*) transition metal oxides especially those with K_2NiF_4-type or related structure. Due to their relatively high and faster ionic and electronic transportation already at moderate temperature than that of perovskite oxides, these K_2NiF_4-type oxides have attracted much more attention as promising materials for cathode of next generation IT-SOFCs and oxygen separation membranes, oxygen sensors, etc. At the same time, these mixed ionic and electronic conducting oxides (MIEC) shows a rather wide range of oxygen non-stoichiometry and high oxygen mobility accommodating extra oxygen in the interstitial lattice sites, which is another aspect of interest, discussed through the understanding of oxygen diffusion at low temperature. A high oxygen doping level has been shown to induce a special lattice dynamic, allowing the apical oxygen atoms to easily move to vacant interstitial sites on a shallow energy diffusion pathway. It is fundamental to understand the mechanism of oxygen diffusion and more importantly, the crystal structure of this K_2NiF_4-type in terms of complex superstructures due to excess oxygen ordering.

Hole doping in Pr_2NiO_4, either by substituting Pr with Sr cations or by O^{2-} ion intercalation on interstitial lattice sites modifies the structural (long range ordering of O^{2-} ions) and electronic/charge ordering in $Pr_{2-x}Sr_xNiO_{4+\delta}$. The average structure of $Pr_{2-x}Sr_xNiO_{4+\delta}$ changes from orthorhombic to tetragonal depending on the Sr-dope concentration. Due to oxygen intercalation δ up to 0.25 and long-range ordering of those excess O^{2-} ions, $Pr_2NiO_{4+\delta}$ forms *(3+n)-D* incommensurately modulated complex superstructures present in maximum eight incommensurate twin individuals along with diffuse scattering gives a clear idea on oxygen ordering and lattice order/disorder state in local scale at different experimental condition. The evolution of the modulation vectors in the *(HKn, n-integer)* plane, as function of temperature is not linear rather goes to more incommensurate from nearly commensurate as starting phase and disappears completely at the temperature where LTO to HTT phase transition take place. The modulation vector follows the same path during increasing temperature under pressure but it is not reversible during cooling, it remains almost at same position

where pressure forces the system to lock with that modulation vector even the pressure is released at ambient. The transition *(LTO to HTT)* temperature also shifted to higher temperature region with increasing oxygen pressure along with increasing *c*-axis parameter. We were able to follow up the detailed structural changes along with complex phase diagram and thermo dynamical stability of the modulation of that titled compounds by using *in-situ* single crystal x-ray diffraction method.

Depending on the hole-doping concentration, the charges on the TM-sites tend to segregate into stripes for low hole doping, whereas 2D-cherckerboard ordering is observed for higher doping concentrations. Hole doping achieved by oxygen insertion has been shown to be electronically equivalent to cation substitution, but long-range oxygen order is observed in addition to charge and spin ordering, an additional degree of freedom. Single crystal X-ray diffraction on oxygen doped $Pr_2NiO_{4.25}$ with hole concentration $n_h = 0.5$ reveals the checkerboard-type charge ordering (ε =1/2) at RT and still exist at low temperature T = 80K along with stripe charge ordering ($\varepsilon = 1/3$) where the average structure and modulation vector of oxygen order remains unchanged. Neutron diffraction on Sr-doped $Pr_{1.5}Sr_{0.5}NiO_4$ sample with same hole concentration n_h =0.5 shows similar checkerboard charge ordering without stripe charge ordering as well no oxygen ordering at 2K. Simultaneous CB and stripe charge order in $Pr_2NiO_{4.25}$ might emerge from nano phase separation where system exhibits oxygen ordering that might also play the similar role to segregate the charges in nano phase regime. Another features stripeless incommensurate magnetic ordering in $Pr_{1.5}Sr_{0.5}NiO_4$ could be understood in the frame of stacking fault in CB matrix while induce the stripe magnetic order via complex superexchange between Ni^{2+} crossing the stacking domain wall. However, strong magnetic correlation and long range ordering along c^* has been found in oxygen doped $Pr_2NiO_{4.25}$ sample having stripe magnetic unit cell where c axis is doubled. In this context, the main interest of this thesis is to understand all the above-mentioned structural and magnetic ordering besides low temperature oxygen mobility and lattice dynamics in pure oxygen doped $Pr_2NiO_{4.25}$ showing complex oxygen ordering, together with the corresponding $Pr_{1.5}Sr_{0.5}NiO_4$ phase, as well as the oxygen co-doped $Pr_{2-x}Sr_xNiO_{4+\delta}$ (x=0.125, δ=0.12) in order to conclude on similarities and differences of their respective complex structural and magnetic ordering phenomena.

Table of Contents

Introduction 1

1. Oxygen Mobility in solids 11

1.1. Why is the oxygen migration important? 11

1.1.1. Crystal structure and potential application of RP-type oxides 11

1.2. Principle of oxygen diffusion at high temperature 14

1.2.1. vacancy and interstitial diffusion 16

1.2.2. Diffusion path of oxygen ions 16

1.2.2.1. Fluorite-type oxides 17

1.2.2.2. Perovskite and Layered Perovskite type oxides 19

1.3. Low-T oxygen diffusion and Brownmillerite-type oxides via lattice dynamics and structural instability 14

1.3.1. Oxygen mobility in Brownmillerite-type oxides 25

1.3.2. Phonon assisted diffusion in RP oxides 28

1.4. Summary 34

References 35

2. Fascinating world of oxygen, charge and spin ordering phenomena in strongly correlated layered transition metal oxides 41

2.1. Physical interaction in strongly correlated electron system 43

2.1.1. Hubbard model 43

2.1.2. Jahn-Teller effect 45

2.1.3. Superexchange in Hubbard model 45

2.2. Complex ordering and electronic phase separation 46

2.2.1. Combined picture of ordering pheneomena 47

2.2.2. Electronic inhomogeneity and phase separation in correlated oxides 50

2.3. Stripe to checkerboard and other competing states in TMOs 54

2.3.1. Charge and spin order in $Ln_{2-x}Sr_xNiO_{4+\delta}$ (Ln = La, Pr and Nd) 56

References 66

3. Instrumentation and experimental methods **73**

3.1. Crystal growth by TSFZ method using image furnace 75

3.2. X-ray Laue back scattering technique 78

3.3. Thermogravimetry analysis (TGA) set up 80

3.4. DC magnetometry 81

3.5. Unconventional capillary-gas-pressure cell 82

3.6. Electrochemical cell 85

3.7. Single crystal diffraction 86

References 90

4. Twinning Scheme and structural studies of as grown $Pr_{2-x}Sr_xNiO_{4+\delta}$ (x = 0, 0.125, 0.25 and 0.5) by SC X-ray diffraction **91**

4.1. Phase study by X-ray powder diffraction 93

4.2. Investigation of microstructure by single crystal diffraction: The beauty of complexity ... 96

4.2.1. As grown oxygen doped $Pr_2NiO_{4+\delta}$ oxides 96

4.2.1.1. 1st impression on obtained diffraction pattern 96

4.2.1.2. Twinning of $Pr_2NiO_{4+\delta}$ oxides 100

4.2.1.3. *(3+1)*-dimensional incommensurate modulated structure in *(hkn)* plane where n = integer 104

4.2.1.4. *(3+2)*-dimensional incommensurate modulated structure in *(hkn/2)* plane where n = odd integer 112

4.2.1.5. *3D* oxygen ordering and diffuse scattering in $Pr_2NiO_{4.25}$ 115

4.2.1.6. *3D* volumetric representation of the oxygen ordering in $Pr_2NiO_{4.25}$ single crystal 117

4.3. *(3+1)*-dimensional modulated structure of $Pr_{1.875}Sr_{0.125}NiO_{4+\delta}$ at RT 119

4.4. Structure of $Pr_{2-x}Sr_xNiO_{4+\delta}$ (x = 0.25 and 0.5) explored by single crystal X-ray diffraction at RT 122

4.5. Summary 122

4.6. Difficulties 126

References 127

5. Investigation of T-dependent modulated structure of Pr2NiO4.25 by in situ single crystal synchrotron X-ray radiation diffraction 129

5.1. Measurements strategy 131

5.2. Results and discussion 131

5.2.1. Structural modulation associated to RT phase 131

5.2.2. Evolution of structure and modulation as function of temperature 133

5.2.3. Temperature dependent study of oxygen ordering in 3-dimension 141

5.3. Thermogravimetric analysis (TGA) 145

5.4. High-T vs low-T reaction 147

5.5. Summary 151

References 153

6. In situ investigation of T-dependent modulated structure of $Pr_2NiO_{4+\delta}$ under different oxygen pressure *P(O_2)* by single crystal laboratory μ-focused X-ray diffraction 155

6.1. Experimental strategy 157

6.2. Exploring structure of $Pr_2NiO_{4+\delta}$ as function of temperature under different oxygen pressure *P(O_2)* 159

6.2.1. Phase diagram of $Pr_2NiO_{4+\delta}$ during heating and cooling at ambient pressure 159

6.2.2. Phase diagram of $Pr_2NiO_{4+\delta}$ during heating and cooling under oxygen pressure of 50 and 75 bar 162

6.2.3. Ex situ studies at oxygen pressure of 75 bar 168

6.2.4. Structure of $Pr_2NiO_{4+\delta}$ under vacuum (in situ and ex situ) 170

6.3. Study of thermogravimetric analysis at different atmosphere 177

6.4. Summary 179

References 183

7. Incommensurate charge and spin stripe order in oxygen and Sr-doped $Pr_{2-x}Sr_xNiO_{4+\delta}$ explored by neutron and X-ray diffraction 185

7.1. Experimental strategy 187

7.2. SQUID magnetometry 187

7.3. Charge and spin stripes in oxygen doped $Pr_2NiO_{4+\delta}$ single crystal 194

7.3.1. Single crystal neutron 2D diffraction 196

7.3.2. Single crystal X-ray diffraction 197
7.4. $Pr_{1.875}Sr_{0.125}NiO_{4+\delta}$ single crystal 203
7.4.1. Charge stripe studied by X-ray diffraction 203
7.4.2. Charge and spin stripe studied by neutron elastic scattering 207
7.5. Correlation between charge and spin stripes in $Pr_{1.5}Sr_{0.5}NiO_{4+\delta}$ single crystal 209
7.5.1. Single crystal neutron 2D diffraction 209
7.5.2. Single crystal X-ray diffraction 214
7.6. Charge modulation in the picture of Polaron ordering 216
7.7. Possible incommensurate stripe models and stripeless spin order 221
7.8. Summary 227
References 229

8. General conclusions and future perspectives **231**

o

Introduction

Even before the discovery of superconductivity in the $La_{2-x}Ba_xCuO_4$ system, non-stoichiometric transition metal oxides crystallizing with K_2NiF_4 structure were of interest, because of their anisotropic transport properties. A wide range of oxygen non-stoichiometry and the temperature influences not only on physical properties e.g, long range magnetic ordering and electronic-ionic conductivity but also on the crystal structure. Different kind of superstructure are formed due to the ordering of excess oxygen content and it makes the system very complex from structural point of view which pay lot of attention now days. The better understanding of these transition metal oxides has challenged our view of solids in which electrons are strongly correlated and that cause several interesting physical phenomena like high temperature superconductivity (HTSC), colossal magneto resistance (CMR), glass, stripe, checkerboard (CB) type charge ordering, magnetic spin ordering as well as orbital ordering and so many. This phenomena occurs when various physical interactions are activated simultaneously which includes low temperature lattice dynamics besides spin-charge and orbital coupling.

Till now, perovskite related materials such as Ruddlesden-Popper (RP) series [1,2] of layered oxides (general formula $(A_{n+1}B_nO_{3n+1})$ and Brownmillerite [3] $ABO_{2.5+\delta}$ type oxides are known to have high electronic, ionic conductivity and oxygen mobility even at low temperature or at ambient. These phases are of particular interest as they are able to uptake or release oxygen on their interstitial or regular sites in very controlled way by electrochemical reaction at ambient temperature and this feature helps to understand the low temperature oxygen diffusion mechanism in oxides in the field of device applications e.g., SOFCs, oxygen membrane, oxygen sensors and so on.

It has been proven combining structural studies with lattice dynamical calculation that oxygen are mobile in Brownmillerite –type $Sr(Fe/Co)O_{2.5}$ and K_2NiF_4-type Ln_2MO_{4+d} (Ln = La, Pr and M = Ni, Cu, Co) via electrochemical reaction even at room temperature where in former case oxygen are filled along empty 1D oxygen vacancy channels, whereas in later case oxygen are intercalated

not in regular vacancy sites but in interstitials vacancy sites via phonon assisted diffusion mechanism [4,5]. Oxygen ions are doubly charged with ionic radius of about 1.4 Å and to conduct such large ions in solids needs a thermally activated hopping process jumping via vacant lattice sites where the energy barrier is very high. But surprisingly there are several oxides mentioned above shows oxygen diffusion at ambient. A phonon assisted diffusion mechanism based on the presence of a low lying phonon modes combined with structural instabilities has been recently proposed by Paulus *et al.*[4] which explain why the oxygen is highly mobile in the Brownmillerite frameworks already at room temperature. In Brown framework the lattice instability and dynamically triggered internal interfaces i.e., order-disorder phenomena concerning MO_4 tetrahedral chains are crucial point toward a possible understanding of oxygen diffusion along 1D-vacancy channels. On the other hand, in RP phases a similar mechanism where O_{ap}/O_{int} interaction, and low-energy phonon modes, are considered as general consequences of oxygen diffusion mechanism. Recently from Ceretti et al. [6] it has been shown via nuclear density reconstruction of $Ln_2NiO_{4+\delta}$ (Ln = Pr, Nd) a double-well potential pointing towards the interstitial vacancy sites, creating a quasi-continuous shallow energy diffusion pathway between O_{ap} of the MO_6 octahedra and interstitial sites and displacement is dynamical origin which is consistent with a phonon assisted diffusion mechanism. This large delocalization of apical oxygen atoms are driven by excess interstitial oxygen and thus activate low temperature oxygen mobility via phonon assisted diffusion mechanism [7], which is different from classical Arrhenius-type thermally activated hopping process.

The physical properties of these K_2NiF_4-type oxides changes dramatically depending on hole doping and the concentration of the dopant species as mentioned above. Hole doping in the RE_2MO_4 (RE = La, Nd, Pr and M = Ni, Cu, Co) can be achieved either by substituting three valent rare earth metal by two valent Sr or oxygen intercalation in to the vacant interstitial sites. The commensurate antiferromagnetic order $(T_N = 275\ K)$ of La_2CoO_4 persists in a very short range up to a Sr content of x = 0.3, whereas small amounts of Sr suppress commensurate antiferromagnetism in cuprates and in nickelates. $La_{2-x}Sr_xCoO_4$ with $x > 0.3$ exhibits incommensurate spin ordering with the modulation closely following the amount of doping [8]. These incommensurate phases strongly

resemble the stripe phases observed in cuprates and nickelates, but incommensurate magnetic ordering appears only at larger Sr content in the cobaltates due to a reduced charge mobility. In $La_{2-x}Sr_xNiO_4$ only 12% of Sr drive the system into a stripe phase [9,10], even less charges are necessary to suppress the commensurate AFM in the cuprates already for $x \geq 0.02$ and for larger Sr concentration, $x > 0.055$ this ordering is lost and samples become metallic and superconducting. Furthermore, at half-doping, $La_{1.5}Sr_{0.5}CoO_4$, checkerboard (CB) charge ordering occurs at high temperature, coexisting with magnetic ordering below $T_{mag} \sim 40$ K [11, 12]. Thus the magnetic correlations as a function of doping in the $La_{2-x}Sr_xCoO_4$ series reflects the commensurate AFM ordering is much more stable than in the isostructural cuprates and nickelates persisting up to $x = 0.03$ because of an efficient trapping of the charge carriers Co^{3+} site.

Several studies show charge and spin stripe-type and checkerboard-type phases exist in these Sr-doped oxides because of spatial inhomogeneity [13, 14] that might come from conventional high temperature synthesis. It has been stated in Anissimova et al. [15] in layered compounds such as $La_{2-x}Sr_xNiO_4$ and $La_{2-x}Ba_xCuO_4$, the doped charge carriers can segregate into periodically spaced charge stripes separating narrow domains of antiferromagnetic order. The manganite is an important oxide family in which the presence of inhomogeneous states, which is actually a nanoscale mixture of phases, particularly in the presence of quenched disorder [16-18], that leads to understand the CMR effects. However, once the inevitable quenched disorder is considered which might arise from the lattice distorting chemical doping procedure, fluctuations of dopant density or strain fields, the region in which the two states are nearly degenerate (that is, they can coexist) is dramatically modified. This is valid for the antiferromagnetic insulating (AFI) versus superconducting (SC) state competition in cuprates. [19]. Very weak disorder incorporating coulomb forces or cooperative oxygen octahedra distortions are strong enough to induce such inhomogeneous phase. Existence of inhomogeneous states in HTSC cuprates has been shown to be responsible for the stripe phases in this oxide, Tranquada *et al.* [20]. Other recently synthesized cuprate based compounds also have inhomogeneous states [21], and additionally, a new charge ordered "checkerboard" state has been observed [22]. This state also exists in Bi-S-Ca-Cu-O system [23] and appears to compete with

superconductivity. With the help of powerful microscopic techniques, doped HTSC systems revealed inhomogeneous states. The intermediate states between the AFI and SC states do not seem universal they could have stripes, a charge checkerboard, or glassy patterns that is a hallmark of such strongly correlated complex oxides.

Compare to Sr-doping, another important aspect electronically equivalent that is oxygen intercalation into the interstitial vacancy sites via topo tactic electrochemical redox reaction already at ambient. Cation doping needs high temperature synthesis that produces disorder, inhomogeneity in the system where as for oxygen doping at ambient would be an alternative way to control the degree of disorder being far from thermodynamically equilibrium. Recently, Maity *et al.* [24] it has been shown electrochemical oxidation of $SrFeO_{2.5}$ to $SrFeO_3$ on a single crystal, the reaction proceeds following the phase sequence $SrFeO_{2.5}/SrFeO_{2.75}/SrFeO_{2.875}/SrFeO_3$, structurally accompanied by establishing a complex series of long-range oxygen vacancy ordering, which gets instantly organized at ambient temperature. BP-type $SrFeO_{2.5}$ is an antiferromagnet with T_N = 670 K [25] whereas cubic $SrFeO_3$ shows screw type antiferromagnetic ordering below T_N = 134 K [26]. Oxygen intercalation reactions proceeding at ambient temperature thus not only allow us to show the complex structural changes involved in developing long range superstructures, but equally allow us to adjust the doping concentrations and the respective changes in the physical properties, which are interesting e.g. for the development of oxygen membranes and the related applications for energy materials. It might be equally interesting to modify the electronic properties, presently achieved by Sr-doping in perovskite-type oxides for spintronics. The fact that both Sr-doping of trivalent rare earth metals and oxygen intercalation result in hole doping means those similar changes in the magnetic electronic properties can be expected. Together with microstructural modifications of the twin structure, this might also allow us to yield new physical properties. Another most promising compound in this K_2NiF_4-type family is $Pr_2NiO_{4+\delta}$ oxides that can also reversibly intercalate oxygen ($0 \leq \delta \leq 0.25$) via electrochemical reaction in "operando condition" at ambient. The structure pass through clearly three distinct line phases from starting average *Fmmm* to the tetragonal $P4_2/ncm$ to the final orthorhombic phase *Bmab* at the stoichiometric limit. It is clear indication that complex

super structure in the *Fmmm* phase related to the oxygen ordering as well as charge ordering which found to be commensurately modulated with four twin individuals in case of oxygen ordering. In the course of electrochemical reduction the commensurate modulation vector $\boldsymbol{q}$ did not change but the intensity drops down quickly as the intermediate tetragonal phase $P4_2/ncm$ starts to grow. This is how low temperature oxygen doping opens a new gate to investigate the structural and electronic ordering in those above-mentioned TMOs.

In addition to effect of excess oxygen on physical properties, the modulation of the superstructure related to mostly oxygen ordering that is found in these K_2NiF_4-type oxides, became exciting field of study now days as it is very complex. In perovskite and related TMOs oxide compounds showing oxygen nonstoichiometric, ordering of oxygen vacancies (order/disorder) has long been interesting topic of solid-state chemistry [27]. Not so many work has been done so far to study the modulated structure of non-stoichiometric oxides as function of temperature, as it is also difficult to control the stoichiometry of oxygen during crystal growth. Very earlier, the modulated structure found in superconducting oxides of Bi-Sr-Ca-Cu-O system has been attributed to ordering of excess oxygen in $BiO_{1+\delta}$ layers [28,29]. This extra oxygen also explains why there is a mixture of Cu^{2+} and Cu^{3+} in the superconductor, and thus is the connection between the modulation and superconductivity in the Bi-Sr-Ca-Cu-O system. Compare to this superconducting oxides, ordering of interstitial oxygen atoms in $Ln_2MO_{4+\delta}$ (M = Cu, Ni, Co), (Ln = Nd, La) [30--34] was observes mostly by using transmission electron microscopy (TEM) as BiO and LaO double layer of NaCl type are sandwiched by perovskite-like layer in similar fashion. The lattice mismatch between these two different types of layers must be the reason of excess oxygen incorporation [35,36]. However, the excess oxygen atoms in $La_2MO_{4+\delta}$ becomes ordered to minimize the increase in elastic energy caused by the incorporation. Ordering of these interstitial oxygen atoms and subsequent structural relaxation leads to rather weak extra satellite reflections in addition to strong Bragg reflections. The first TEM study of oxygen interstitial ordering in this family of oxides was reported for $La_2NiO_{4+\delta}$ by Hiroi *et al.* [30] even though the proposed superstructure model was not in agreement with that proposed by Brown et al. [37]. There are many contradiction to propose model e.g., triclinic, monoclinic reported by

various author somewhere else. It is important to note that interstitial oxygen are mobile and superstructure reflections could be changed by extra electron beam radiation, but in the case of $Nd_2NiO_{4+\delta}$ the observed superstructure were found to be rather stable to electron beam irradiation [31]. In Tranquada *et al.* [34] it is reported after finding large super cell associated with oxygen ordering in the TEM study by Hiroi *et al.* that the superlattice reflections were not caused by excess interstitial oxygen, but rather by a charge- density wave ordering [38]. This could be a question of the stoichiometry of oxygen in the single crystal. Moreover, it has been suggested that a miscibility gap exists in the temperature versus oxygen content (4+δ) phase diagram, which is $0 < \delta < 0.08$ for $La_2CuO_{4+\delta}$, $0.02 < \delta < 0.012$ for $La_2NiO_{4+\delta}$ and $0 < \delta < 0.15$ for $La_2CoO_{4+\delta}$ at room temperature [39-42]. Initially it was finding for the superconductivity in $La_2NiO_{4+\delta}$ isostructural compound as in La_2CuO_4 which becomes superconducting below 38 K when excess oxygen are introduced to form the holes into the CuO_2 layers. However, no evidence of superconductivity was found in $La_2NiO_{4+\delta}$, nevertheless the crystal chemistry underlying the existence of oxygen interstitials in this family of oxides and the ordering thereof remain a fascinating subject for study.

In this present thesis Sr-doped with different Sr concentration as well as oxygen doped Pr_2NiO_4 single crystal has been investigated mostly the complex oxygen ordering as function of temperature and oxygen pressure which has not been reported so far in the literature. As mentioned before the structure changes from starting average *Fmmm* to the tetragonal $P4_2/ncm$ to the final orthorhombic phase *Bmab* at the stochiometric limit during electrochemical reduction process at ambient temperature. From neutron powder diffraction studies on $Pr_2NiO_{4+\delta}$ shows a tructural phase transition low temperature orthorhombic LTO *(Fmmm)* to high-temperature tetragonal HTT *(I4/mmm)* occurs nearly at 673K [43]. The aim of the thesis was to investigate how the oxygen ordering change/evolve with temperature following the structural modification in single crystal by in-situ x-ray diffraction method using synchrotron radiation. Also to follow up the effect of oxygen pressure in addition to temperature on the observed oxygen ordering as well as to develop a new structural phase diagram as function of T, $P(O_2)$, a sophisticated capillary gas pressure cell was designed which was nicely adopted for the single crystal diffractometer (STOE, STADIVARY)

installed at University Montpellier and at the Swiss Norwegian beamline BM01 at ESRF, Grenoble. The crystal story in terms of oxygen content is completely time dependent as it changes over long period. However, as grown oxygen doped $Pr_2NiO_{4+\delta}$ single crystal shows twin features with maximum four individuals and surprisingly the modulation vector related to superstructure reflection appears as commensurate once $\delta = 0.25$, a slight deviation from $\delta = 0.25$ give rise incommensurate modulation, this information is absolutely impossible to obtain by using conventional powder diffraction technique. On the other hand, from x-ray single crystal diffraction Sr-doped $Pr_{2-x}Sr_xNiO_{4+\delta}$ with $x = 0.125$, 0.25 and 0.5 does not show any oxygen ordering as there is no excess interstitial oxygen which is not incorporated with increasing Sr concentration. Since, these Sr-doped phases are electronically homologous as oxygen doped phase, it might be interesting to investigate and compare charge and spin ordering using single crystal neutron diffraction/scattering technique with different oxygen dope sample.

Use of electron diffraction and transmission microscopy should be more advantageous in comparison with X-ray and neutron diffraction methods, as it gives deep information on ordered structure if the order is short ranged or multiple in mode. This is how now days Synchrotron radiation large scale facilities and also micro focused X-ray laboratory single crystal diffractometer enables one to follow up the detailed structural changes along with complexity that arise from mostly oxygen ordering in this titled compound. That also confirms indirectly that the order is not short ranged, it is long-range order with higher harmonics. In this context, the main interest of this thesis is to understand the structural complexity besides low temperature oxygen mobility and lattice dynamics in the strongly correlated K_2NiF_4-type TMOs.

References:

1. Ruddlesden, S. N.; Popper, P. Acta Cryst 1957, 10, 538-539.
2. Ruddlesden, S. N.; Popper, P. Acta Cryst 1958, 11, 54-55.
3. Colville, A. A.; Geller, S. Acta Crystallogr B Struct Crystallogr Cryst Chem 1971, 27, 2311-2315.
4. Werner Paulus, Helmut Schober, Stefan Eibl, Mark Johnson, Tanguy Berthier, Olivier Hernandez, Monica Ceretti, Marie Plazanet, Kazimierz Conder and Carlo Lamberti, Lattice Dynamics To Trigger Low Temperature Oxygen Mobility in Solid Oxide Ion Conductors, *J.* Am. Chem. Soc., 2008, 130 (47), pp 16080–16085.
5. Antoine Villesuzanne, Werner Paulus, Alain Cousson, Shoichi Hosoya, Loïc Le Dréau, Olivier Hernandez, Carmelo Prestipino, Mohamed Ikbel Houchati, Juerg Schefer, On the role of lattice dynamics on low-temperature oxygen mobility in solid oxides: a neutron diffraction and first-principles investigation of $La_2CuO_{4+\delta}$, J Solid State Electrochem (2011) 15:357–366.
6. M. Ceretti, O. Wahyudi, A. Cousson, A. Villesuzanne, M. Meven, B. Pedersen, J. M. Bassat and W. Paulus, Low temperature oxygen diffusion mechanisms in $Nd_2NiO_{4+\delta}$ and $Pr_2NiO_{4+\delta}$ via large anharmonic displacements, explored by single crystal neutron Diffraction, J. Mater. Chem. A, **2015**,3, **21140-21148.**
7. A. Perrichon, A. Piovano, M. Boehm, M. Zbiri, M. Johnson, H. Schober, M. Ceretti, W. Paulus, Lattice Dynamics Modified by Excess Oxygen in $Nd_2NiO_{4+\delta}$:Triggering Low-Temperature Oxygen Diffusion, J. Phys. Chem. C, **2015**, 119 (3), pp 1557–1564.
8. M. Cwik, M. Benomar, T. Finger, Y. Sidis, D. Senff, M. Reuther, T. Lorenz and M. Braden, Magnetic Correlations in $La_{2-x}Sr_xCoO_4$ Studied by Neutron Scattering: Possible Evidence for Stripe Phases, phys Rev Let, 102, 057201 (2009).
9. J. M. Tranquada, D. J. Buttrey, V. Sachan, Incommensurate stripe order in $La_{2-x}Sr_xNiO_4$ with x = 0.225, Phys. Rev. B 54, 12318 (1996).
10. H. Yoshizawa, T. Kakeshita, R. Kajimoto, T. Tanabe, T. Katsufuji, and Y. Tokura, Stripe order at low temperatures in $La_{2-x}Sr_xNiO_4$ with $0.289 \lesssim x \lesssim 0.5$, Phys. Rev. B 61, R854(R) 2000.
11. I. A. Zaliznyak, J. P. Hill, J. M. Tranquada, R. Erwin, and Y. Moritomo, Independent Freezing of Charge and Spin Dynamics in $La_{1.5}Sr_{0.5}CoO_4$, Phys. Rev. Lett. 85, 4353 2000.
12. I. A. Zaliznyak, J. M. Tranquada, R. Erwin, and Y. Moritomo, Spin-entropy-driven melting of the charge order in $La_{1.5}Sr_{0.5}CoO_4$, Phys. Rev. B 64, 195117 2001.
13. V. J. Emery, S. A. Kivelson, and J. M. Tranquada, Stripe phases in hightemperature superconductors, Proc. Natl. Acad. Sci. USA, vol. 96, no. 26, pp. 8814–8817, 1999.
14. J. Zaanen, Stripes defeat the Fermi liquid, *Nature*, vol. 404, pp. 714–715, 2000.
15. S. Anissimova , D. Parshall , G.D. Gu, K. Marty, M.D. Lumsden, Songxue Chi, J.A. Fernandez-Baca, D.L. Abernathy, D. Lamago, J.M. Tranquada & D. Reznik, Direct

observation of dynamic charge stripes in La2–xSrxNiO4, Nature Communications, 3467 (2014).

16. J. Burgy, M. Mayr, V. Martin-Mayor, A. Moreo, and E. Dagotto, Colossal Effects in Transition Metal Oxides Caused by Intrinsic Inhomogeneities, Phys. Rev. Lett. 87, 277202, 2001.
17. Jan Burgy, Adriana Moreo, and Elbio Dagotto, Relevance of Cooperative Lattice Effects and Stress Fields in Phase-Separation Theories for CMR Manganites, Phys. Rev. Lett. 92, 097202, 2004.
18. S. Yunoki, J. Hu, A. L. Malvezzi, A. Moreo, N. Furukawa, and E. Dagotto, Phase Separation in Electronic Models for Manganites, Phys. Rev. Lett. 80, 845, 1998.
19. Gonzalo Alvarez, Matthias Mayr, Adriana Moreo, and Elbio Dagotto, Areas of superconductivity and giant proximity effects in underdoped cuprates, Phys. Rev. B 71, 014514, 2005.
20. J. M.tranquada, B. J. sternlieb, J. D. Axe, Y. Nakamura, S. Uchida, Evidence for stripe correlations of spins and holes in copper oxide superconductors, Nature 375, 561 - 563, 1995.
21. Y. Kohsaka, K. Iwaya, S. Satow, T. Hanaguri, M. Azuma, M. Takano, and H. Takagi, Imaging Nanoscale Electronic Inhomogeneity in the Lightly Doped Mott Insulator $Ca_{2-x}Na_xCuO_2Cl_2$, Phys. Rev. Lett. 93, 097004, 2004.
22. T. Hanaguri, C. Lupien, Y. Kohsaka, D.-H. Lee, M. Azuma, M. Takano, H. Takagi & J. C. Davis, A 'checkerboard' electronic crystal state in lightly hole-doped $Ca_{2-x}Na_xCuO_2Cl_2$, Nature 430, 1001-1005, 2004.
23. Michael Vershinin, Shashank Misra, S. Ono, Y. Abe, Yoichi Ando, Ali Yazdani, Local Ordering in the Pseudogap State of the High-Tc Superconductor $Bi_2Sr_2CaCu_2O_{8+\delta}$, Science, 303, 5666, 2004.
24. A Maity, R Dutta, B Penkala, M Ceretti, A Letrouit-Lebranchu, D Chernyshov, A Perichon, A Piovano, A Bossak, M Meven and W Paulus, Solid-state reactivity explored *in situ* by synchrotron radiation on single crystals: from $SrFeO_{2.5}$ to $SrFeO_3$ via electrochemical oxygen intercalation, J. Phys. D: Appl. Phys. 48 (2015).
25. M. Schmidt and S. J. Campbell, Crystal and Magnetic Structures of $Sr_2Fe_2O_5$ at Elevated Temperature, Journal of Solid State Chemistry, vol. 156, pp. 292–304,2001.
26. M. Reehuis, C. Ulrich, A. Maljuk, C. Niedermayer, B. Ouladdiaf, A. Hoser,T. Hofmann, and B.Keimer, Neutron diffraction study of spin and charge orderingin $SrFeO_{3-\delta}$, Phys. Rev. B, vol. 85, pp. 184109–184123, 2012.
27. M. Takano, T. Okita, N. Nakayama, Y. Y. Takeda, O. Yamamoto, and J. B. Goodenough, Dependence of the structure and electronic state of $SrFeO_x$ ($2.5 \leq x \leq 3$) on composition and temperature, J. Solid State Chem. 73, 140 (1988).
28. E. A. Hewat, J. J. Capponi and M. MAREZIO, A model for the superstructure of $Bi_2Sr_2CaCn2O_{8.2}$, Physica C 157, 502 (1989).

29. Y. Le Page, W. R. McKinnon, J.-M. Tarascon, and P. Barboux, Origin of the incommensurate modulation of the 80-K superconductor $Bi_2Sr_2CaCu_2O_{8.21}$ derived from isostructural commensurate $Bi_{10}Sr_{15}Fe_{10}O_{46}$, Phys. Rev. B 40, 6810, 1989.
30. Zenji Hiroi, Takeshi Obata, Mikio Takano, and Yoshichika Bando, Ordering of interstitial oxygen atoms in $La_2NiO_{4+\delta}$ observed by transmission electron microscopy, Phys. Rev. B, 41, 1990.
31. L. C. Otero-Diaz, A. R. Landa, F. Fernandez, R. Saez-Puche, R. Withers, AND B. G. Hyde, A TEM Study of the Ordering of Excess Interstitial Oxygen Atoms in $Ln_2NiO_{4+\delta}$ (Ln = La, Nd), J. Solid State Chem, 97, 443-451 (1992).
32. A. Demourgues, F. Weill, B. Darriet, A. Wattiaux, J. C. Grenier, P. gravereau, M. Pouchard, Additional oxygen ordering in $La_2NiO_{4.25}$ Electron and neutron diffraction study, J. Solid state chem, 106, 317-329 (1993).
33. A. demourgues, F. weill, J. C. grenier, A. Wattiaux, M. Pouchard, Electron microscopy study of electrchemically prepared $La_2NiO_{4+\delta}$ ($0.17 \leq \delta \leq 0.26$), Physica C 192, 425-434 (1992).
34. J. M. Tranquada, Y. Kong, and J. E. Lorenzo, Oxygen intercalation, stage ordering, and phase separation in $La_2NiO_{4+\delta}$ with $0.05 \leq \delta \leq 0.11$, Phys. Rev. B, 50 1990.
35. H. W. Zandbergen, W. A. Groen, F. C. Mijlhoff, G. van Tendeloo, and S. Amelinckx, Models for the modulation in $A_2B_2Ca_nCu_{1+n}O_{6+2n}$, A, B=Bi, Sr OR Tl, Ba and n=0, 1, 2, Physica C 156, 325 (1988).
36. Y. Ikeda, Z. Hiroi, H. Ito, S. Shimomura, M. Takano, and Y. Bando, Bi, Pb-Sr-Cu-O system including a modulation-free superconductor, Physica C 165, 189 (1990).
37. D. Brown, The Bond-Valence Method: An Empirical Approach to Chemical Structure and Bonding (1981), Modelling the structures of La_2NiO_4, Zeitschrift für Kristallographie 199, 255-272 (1992).
38. J. M. Tranquada, D. J. Buttrey and D. E. Rice, Phase Separation, Charge-Density Waves, and Magnetism, in $La_2NiO_{4+\delta}$ with $\delta = 0.105$, Phys. Rev. Lett. 70, 1993.
39. J. D. Jorgensen, B. Dabrowski, Shiyou Pei, D. G. Hinks, L. Soderholm, B. Morosin, J. E. Schirber, E. L. Venturini, and D. S. Ginley, Superconducting phase of $La_2CuO_{4+\delta}$: A superconducting composition resulting from phase separation, Phys. Rev. B 38, 11337, 1998.
40. J. D. Jorgensen, B. Dabrowski, Shiyou Pei, D. R. Richards, and D. G. Hinks, Structure of the interstitial oxygen defect in $La_2NiO_{4+\delta}$, Phys. Rev. B 40, 2187, 1989.
41. C. Chaillout, S. W. Cheong, Z. Fisk, M. S. Lehmann, M. Marezio, B. Morosin and J. E. Schirber, The Crystal Structure of Superconducting $La_2CuO_{4.032}$ by Neutron Diffraction, Physica Scripta. Vol. T29, 97-99, 1989.
42. B. Dabrowski, J. D. Jorgensen, D. G. Hinks, S. Pei, D. R. Richards, H. B. Vanfleet, and D. L. Decker, $La_2CuO_{4+\delta}$ and $La_2NiO_{4+\delta}$: Phase separation resulting from excess oxygen defects, Physica C 162-164, 99 (1989).
43. PhD thesis, Exploring oxygen mobility in $(Pr/Nd)_2NiO_{4+\delta}$: Single crystal growth, isotropic exchange depth profiling and structural characterization by X-ray, neutron and electron diffraction, Olivia Wahyudi, 2011.

Chapter 1.

Oxygen Mobility in Solid Oxides

1.1 Why is the Oxygen Migration Important?

Ruddlesden-popper phases especially those with K_2NiF_4-type structure, are of particular interest, as they exhibit high ionic and electronic conductivity already at moderate temperatures. Among all these mixed ionic electronic conductors (MIEC), $Pr_2NiO_{4+\delta}$ phases have attracted much attention as best promising materials now days, showing a rather wide range of oxygen non-stoichiometric and high anisotropic oxygen diffusion profile in single crystal accommodating extra oxygen on interstitial lattice sites, suitable for next generation SOFCs cathode material through the understanding of oxygen diffusion at low temperature dynamically activated by low energy phonon mode. A high oxygen doping level has been shown to induce a special lattice dynamic, allowing the apical oxygen atoms to easily move to vacant interstitial sites on a shallow energy diffusion pathway [63, 75]. Recently, in Bassat et al.[22] it has been shown that in the range of temperature from 450 - 700 ^{0}C the measured oxygen diffusivity is highly anisotropic as the value of the diffusion coefficient in NiO2 plane is 3-order higher than that along *c*-axis and besides this the diffusion profile in $Pr_2NiO_{4+\delta}$ single crystal is much higher than that in $Nd_2NiO_{4+\delta}$ (Fig 1.1) explained by classical push-pull mechanism for H-Temperature and presence of less low-energy phonon modes in $Nd_2NiO_{4+\delta}$ compared to $Pr_2NiO_{4+\delta}$. In this scenario the lattice instability and dynamics play a versatile role and explain how it amplifies the diffusion of O^{2-} ions at low (-moderate) temperature not only in RP-type oxides [52] but also in brownmillerite-type $SrCoO_{2.5}$ and $SrFeO_{2.5}$ oxide framework, proven by Paulus et al. [58]. This is the reason why $Pr_2NiO_{4+\delta}$ became highly interested compound because of its high anisotropic oxygen mobility compared to other MIEC oxides even at room temperature via phonon assisted diffusion mechanism which make this compound as a good candidate for cathode material in the SOFCs devices working at ambient. Now it is fundamental to understand the

mechanism of oxygen diffusion as the energy barrier is quite high for big size of oxygen ions (r = 1.4 Å) and it requires very high temperature to start the migration in the solids compared to mechanism that allows one to examine such diffusion at low temperature.

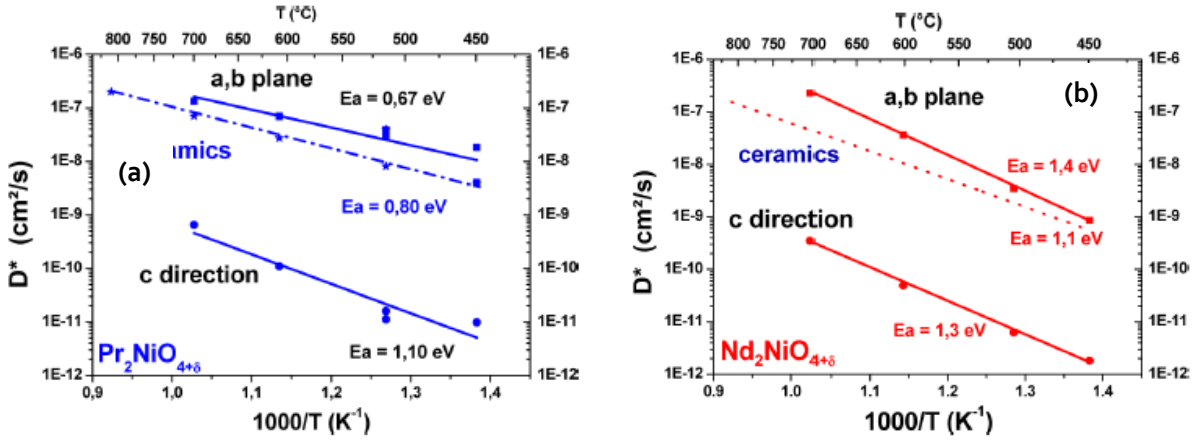

Figure 1.1: D* vs 1000/T for (a) $Pr_2NiO_{4+\delta}$ and (b) $Nd_2NiO_{4+\delta}$ single crystal, reproduced from Fig. 5 and 4 of ref. [22].

1.1.1 Crystal Structure and Potential Application of Ruddlesden-Popper-type Oxides

Among the various types of oxides, Ruddlesden–Popper (RP) oxides with general formula $A'_{n-1}A_2B_nO_{3n+1}$ ($n \geq 1$) are promising candidates for such electrochemical energy devices, owing to their attractive physicochemical properties, including the anisotropic nature of oxygen migration[22] and controllable stoichiometry [74]. The RP phases are made with n consecutive perovskite layers (ABO_3) alternating with rock-salt layers (AO) along the crystallographic c-axis. Figure 1.2 represents the stoichiometric ideal tetragonal *I4/mmm* unit-cells of RP-type oxides for n = 1, 2, and 3. For $n \geq 1$, the additional ABO_3 blocks are introduced between two AO rock-salt layers. A-site cations are normally rare (or alkaline) earth ions with coordination number of 9 whereas B site cations are transition metal ions, forming an extensive series of compositions. The A-site cations have a coordination number of 9 (see Fig.1.2 red polyhedral), locating at the boundary between AO and ABO_3 layers, while the B-site cations are positioned at the center of each BO_6 octahedron. Here

the structure has been drawn with respect to stoichiometric RP phases which also exhibits a rather wide range of oxygen non-stoichiometry.

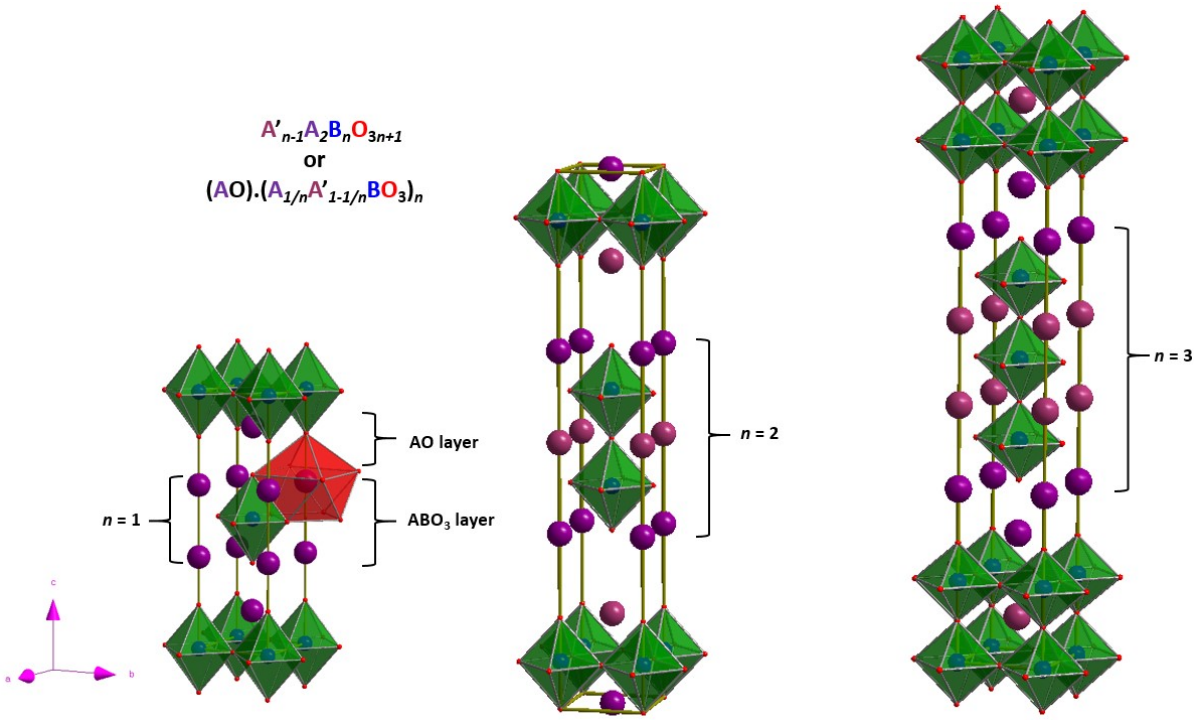

Figure 1.2: Schematic of Ruddlesden-Popper -type $A_{n+1}B_nO3_{n+1}$ structure with n= 1, 2 and 3, where n represents the number of sandwiched perovskite layers between rock salt AO layer.

In past decades, several investigation on high oxygen deficiency $La_{1-x}Sr_xCoO_{3-\delta}$ [4–6] and $La_{1-x}Sr_xCo_{1-y}Fe_yO_{3-\delta}$ [7–10] perovskites are mainly used to for oxygen diffusion and surface exchange at intermediate temperatures and Teraoka and his coworkers they found high oxygen permeation flux in $La_{1-x}Sr_xCo_{1-y}Fe_yO_{3-\delta}$ ($0 \le x \le 1$, $0 \le y \le 1$) and immediately they proposed to use as membrane for separating oxygen from air [30]. Besides air separation for pure oxygen production, another important application of MIEC is as cathode material for solid-oxides fuel cells (SOFCs) in which electrochemical oxidation of oxygen ions take place. Compare to perovskite oxides, several A_2BO_4-type oxides are becoming prominent candidate in application of SOFCs devices because of their high oxygen surface exchange kinetics and mobility which is anisotropic in nature that can be found mostly in single crystal [21, 22–26, 22]. It is well known that A_2BO_4 oxides can accommodate excess amount of oxygen in to their interstitial sites which are located in the AO layer, in the other way

around appropriate doping in the structure can also gives oxygen vacancies. In this way A_2BO_4 oxides conducts oxygen migration via either oxygen interstitials or oxygen vacancies channels in a particular direction depending on the tilting of BO_6 octahedra. A fundamental understanding of oxygen migration in A_2BO_4 ($n = 1$) and related other perovskite derivatives is therefore necessary to optimize superior oxygen ion transport for the development of applications in electrochemical energy devices, chemical sensors, and oxygen permeation membranes. In this chapter we will try to give a general overview of oxygen migration mechanisms depending on oxygen non-stoichiometry and wide range of temperature for example, classical high temperature diffusion process to dynamically activated phonon assisted diffusion mechanism already at low temperature which makes our titled compound interesting to investigate several physical phenomena in this complex scenario.

1.2 Principle of Oxygen Diffusion at High Temperature Range

Very common and routine way to migrate oxygen ions through MIEC membranes is three steps process, 1st oxygen exchange occurs at the gas–solid interface of retention side, 2nd oxygen–electron (or hole) recombined diffusion through the membrane bulk, and 3rd oxygen exchange at the solid-gas interface of permeation side, as shown in Fig. 1.3. The reactions related to oxygen exchange at the gas–solid interfaces are so called "surface exchange reactions".

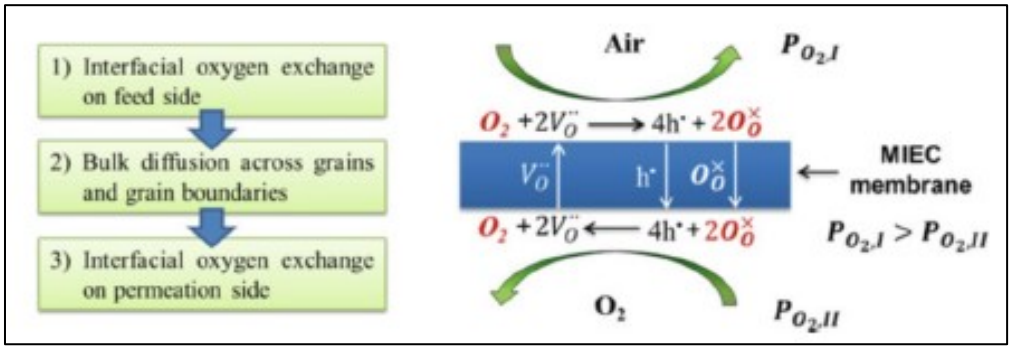

Figure 1.3: Mechanism of oxygen permeation through an MIEC membrane. **Reproduce from Fig. 1.1 of ref. [71].**

Here the oxygen interstitial or vacancies comes in to the play as the diffusion paths for oxygen ions through the bulk can be made by either the oxygen vacancies or the oxygen interstitial sites. Most of the ABO_3 perovskite and fluorite oxides, the migration of oxygen ions follows the vacancy diffusion

mechanism, whilst for the RP-type oxides, the transport of oxygen ions follows the interstitial diffusion mechanism or combination of interstitial and vacancy diffusion mechanism.

Diffusion of any motifs in the structure can be described in terms of atoms', ions', or molecules' movements driven by any physical potential gradient. Diffusion coefficient is an important physical parameter which tells us the quality, how fast is the oxygen transport in solid oxides, and this coefficient is strongly related to the crystalline microstructure of materials. For MIEC membranes, they usually have a fluorite- or perovskite-type crystalline structure with high oxygen ionic or vacancy diffusion coefficients ranging from 10^{-9} to 10^{-5} cm^2 s^{-1} at elevated temperatures. In a polycrystalline material, besides the diffusion of species in grain bulk (bulk diffusion), they also can transport along dislocations, grain boundaries, and inner surfaces. Therefore, the microstructure has significant effect on the diffusion coefficient of a material.

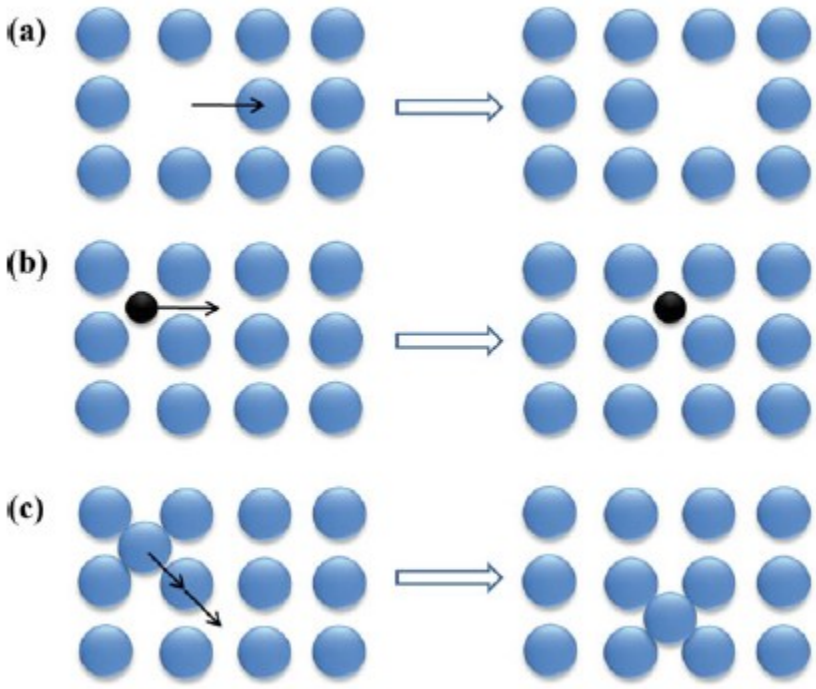

Figure 1.4: Diffusion in solid, (a) vacancy diffusion, (b) interstitial diffusion (hopping), (c) interstitial diffusion (squeezing) **Reproduce from Fig. 2.17 of ref. [71].**

1.2.1 Vacancy and Interstitial Diffusion

With vacancy diffusion, atoms jump from one lattice site to an adjacent vacancy and needs so called activation energy to break bonds with nearest atoms and causes lattice distortion during jump. This energy comes from the thermal energy of atomic vibration from the system. Thus, the direction of the vacancy flow is opposite to the diffusion direction of the atom, as shown in Fig. 1.4a. In the mechanism of vacancy diffusion occurs in most fluorite- or perovskite-type MIEC materials, mostly the oxygen ions are the concerned motion species in the material lattice. Besides, vacancy diffusion, interstitial diffusion of oxygen ions occurs in some layer-typed MIEC materials. In the case of interstitial diffusion, the interstitial atoms can jump to an adjacent interstitial site, as shown in Fig. 1.4b. Interstitial diffusion is much faster than vacancy diffusion because of weaker bonding of interstitial atoms and normally the number of interstitial sites are many more than vacancy sites are present. Another mechanism for interstitial diffusion is that the interstitial atom transports to the normal lattice site by squeezing the occupant into an adjacent interstitial site, as shown in Fig. 1.4c. In this aspect the point defects in solids are very important, especially related to oxygen diffusion via point defects like vacancy or interstitial.

1.2.2 Diffusion Path of Oxygen Ions

It is important to know the diffusion path of oxygen ions in oxides as they are fabricated into devices, such as SOFCs and MIEC membranes and other energy devices. In order to migrate the oxygen ions in solid oxides there should exist an optimal path which could be grain boundaries in case polycrystalline material, some defined energetically favorable crystallographic direction in single crystal, all of this needs a minimal diffusion activation energy with maximal diffusion probability. Obviously, materials with different crystalline microstructures have various diffusion paths for oxygen ions which varies from system to system. Fluorite-, perovskite-, and RP-type oxides are the most commonly used materials in the field of MIEC membranes and SOFCs, and this is why, their oxygen ionic diffusion paths will be introduced in the following sections to understand the influence of microstructure and crystal structure on diffusion process.

1.2.2.1 Fluorite-Type Oxides

CeO_2 is commonly described cubic fluorite oxides which shows quite high ionic conductivity and mobility at elevated temperatures, in which oxygen anions form the eight coordinated cubic interstices, and half of them are alternately occupied by the cations. Yashima *et al.* investigated the oxygen ionic diffusion path in fluorite-type oxides by studying maximum entropy method (MEM), and MEM-based pattern fitting technique together with the data of neutron powder diffraction on δ-$Bi_{1.4}Yb_{0.6}O_3$ and $Ce_{0.93}Y_{0.07}O_{1.96}$ at elevated temperatures [31]. Fig. 1.5a shows *(110)* plane of reconstructed nuclear density map where one can see the oxygen ionic diffusion paths and the structural disorders. The oxygen ionic diffusion paths lie along the [001] direction in the *(110)* plane (white arrows in Fig. 1.5a). As we know that cubic symmetry of any kind of material possess three equivalent directions, i.e., [100], [010], and [001] and thus, the diffusion paths becomes a three-dimensional network where it was found that the oxygen ions are distributed over a broad region showing a complicated disorder picture compared with the cations.

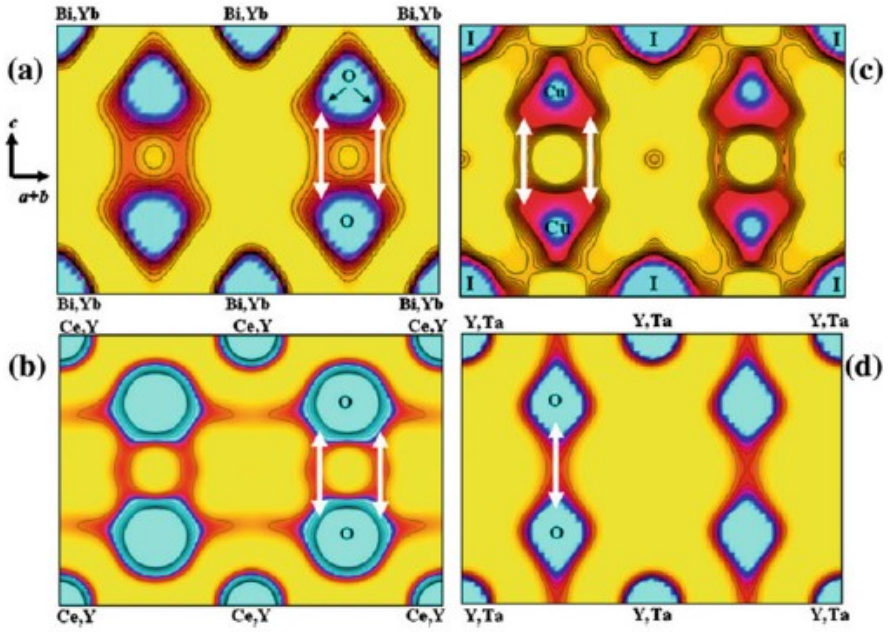

Figure 1.5: Nuclear density distribution on the (110) plane of the fluorite-type (a) δ-$Bi_{1.4}Yb_{0.6}O_3$ at 738 ^{0}C, (b) $Ce_{0.93}Y_{0.07}O_{1.96}$ at 1434 ^{0}C, (c) electron density distribution on the (110) plane of the fluorite-type α-CuI at 487 ^{0}C, and (d) $Y_{0.785}Ta_{0.215}O_{1.715}$ at 535 ^{0}C. Reproduced from Ref. [72]

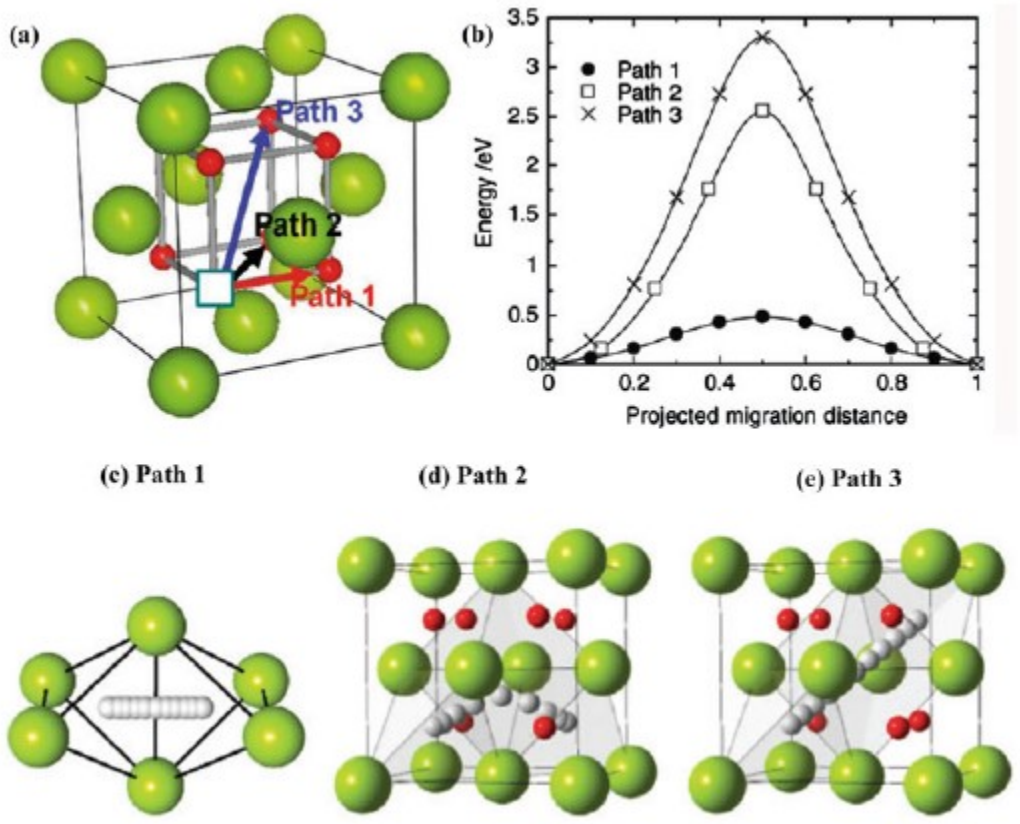

Figure 1.6: (a) Three possible migration pathways of oxygen ions in ceria; (b) energy profiles during oxide ion hopping for Paths 1–3, and (c)–(e) corresponding trajectories of hopping oxygen ions. Large light-green spheres indicate cerium, and small white and red (brighter and darker small) spheres correspond to hopping and non-hopping oxygen ions, respectively. **Reproduced from Ref. [73].**

This kind of disorder is strengthened with the increase in temperature could be the reason of the high oxygen ionic conductivity and the high atomic displacement at higher temperatures. Therefore, the diffusion path along the <100> direction and the disorder of oxygen ions in δ-$Bi_{1.4}Yb_{0.6}O_3$ are the key to understand its high ionic conductivity as well.

Another example of this kind material is cubic Yttria-doped ceria which also shows a good ionic conductivity with high oxygen diffusion. Two different types of anisotropic diffusion paths were observed in the reconstructed nuclear density map via MEM (Fig. 1.5b). One of them goes along the [100] direction and another along the [110] direction where the nuclear density is lower along

compared to other direction. Also in the nuclear density map it is clearly visible that the diffusion path along the [100] directions (shown by the white arrows in Fig. 1.5b) is not a straight line rather a curved line. This feature was attributed to the coulomb interaction between the cations and anions [32]. In the folloing study Yashima *et al.* found the diffusion paths along the [100] directions in other fluorite-type materials, such as α-copper iodide (α-CuI) (Fig. 1.5c) and $Y_{0.785}Ta_{0.215}O_{1.715}$ (Fig. 1.5d) where the electron density map shows more complicated situation for the diffusion path. Thus, from these example it is clear to see the diffusion path along the [100] directions is a favorable one in this the fluorite-type ionic conductors. Interestingly there are other series of investigation carried out by Nakayama and Martin where they studied the diffusion paths of oxygen vacancies in the ceria single crystal [33] which might supports the finding in Yttria doped ceria oxides. They showed three possible paths can exist for such oxygen migration to the adjacent vacant sites, i.e., along the [100], [110], and [111] directions, as shown schematically in Fig. 1.6a and corresponding simulated energy profiles for those three possible paths are shown in Fig. 1.6b. For all the three possible path the calculated activation energy reaches a maximum for oxygen diffusion only path 1 contribute to the process in the ceria single crystal as one can see the activation energies of paths 2 and 3 are much larger than that of path 1 (~0.5 eV). Another supporting work on yttria-doped ZrO_2 in Shimojo *et al.* where they investigate the oxygen ionic migration by performing a molecular dynamics (MD) simulation method and what they found is oxygen ions hop dominantly along the [100] direction between adjacent tetrahedral following the above shown path 1 [34]. From such observation and investigation, one can conclude the main path for oxygen ionic diffusion take place along the [100] direction with a curved line.

1.2.2.2 Perovskite- and Layered-Perovskite- Type Oxides

Perovskite or (layered-Perovskite) oxides with chemical formula ABO_3 or (A_2BO_4) are important class of functional materials showing wide range of stoichiometry and crystalline structures and serves as a good oxygen ion conductors mostly used in SOFCs, MIEC membranes, and several energy applications. The ideal cubic-perovskite structure consist of BO_6 octahedra and the A cation coordination number of 12. Oxygen vacancy diffusion is the dominant mechanism for oxygen ions

in the material. $LaGaO_3$-based perovskite oxides have been intensively studied because of their huge applications in IT- SOFCs and MIEC membranes. Among the series, (Sr, Mg)-doped $LaGaO_3$ has been well addressed because of its higher ionic conductivity than YSZ at intermediate temperatures. Islam *et al.* showed the possible migration path of oxygen ions in $LaGaO_3$, $LaCoO_3$, and $CaZrO_3$ single crystals based upon the energy minimization and interatomic potentials and quantum mechanical (QM) methods [35–37] and what they found is that the hopping migration occurs between two oxygen sites along the BO_6 octahedron edge through a slightly curved trajectory because of outward relaxation of adjacent cations.

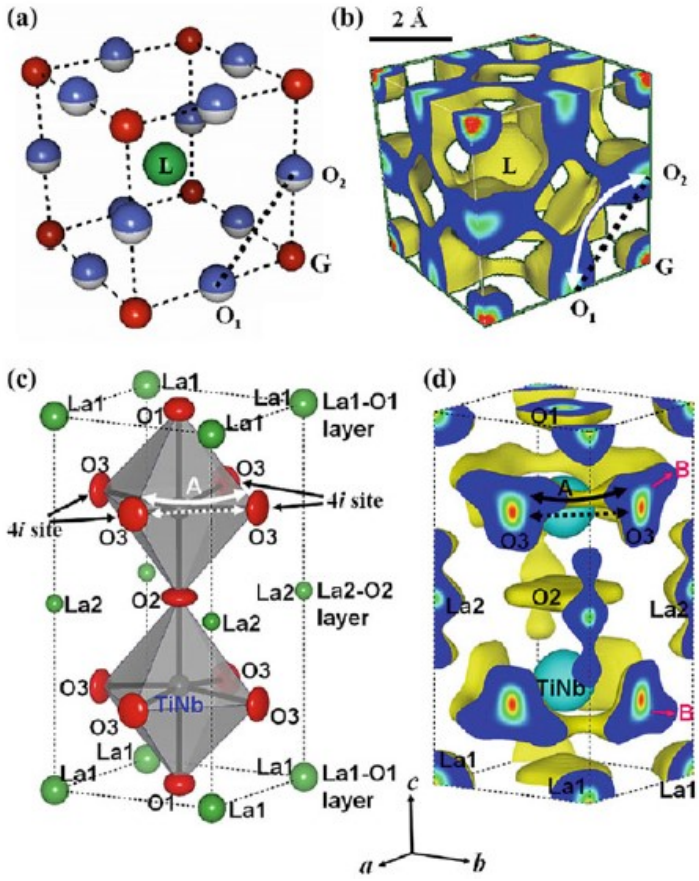

Figure 1.7: (a) Crystal structure and (b) isosurface of nuclear density (0.05 fm $Å^{-3}$) in cubic $(La_{0.8}Sr_{0.2})(Ga_{0.8}Mg_{0.15}Co_{0.05})O_{2.8}$ at 1392 ^{0}C. (c) Crystal structure and (d) isosurface of nuclear density (0.08 fm $Å^{-3}$) in the tetragonal $La_{0.64}(Ti_{0.92}Nb_{0.08})O_{2.99}$ with a double perovskite-type structure at 1358 ^{0}C. Reproduced from Ref. [72].

Following, Yashima *et al.* confirmed again the above mentioned migration path by using MEM based on neutron diffraction data for the composition of $La_{0.8}Sr_{0.2}Ga_{0.8}Mg_{0.15}Co_{0.05}O_{2.8}$, as shown in Fig. 1.7a and b, which is crystallized in cubic perovskite structure at very high temperatures (1198–1392 ^{0}C) [31]. They also confirmed that the nuclear density in the diffusion path is higher at higher temperatures, which is consistent with the oxygen ionic motion that increases with temperature. Also they have investigated another research on a double perovskite $La_{0.64}(Ti_{0.92}Nb_{0.08})O_{2.99}$, which has lower symmetry of tetragonal *P4/mmm* in the temperature range of 496–1358 ^{0}C, as an example to illustrate the oxygen ionic migration path. They disclosed that the nuclear probability density of an O3 atom is connected with that of nearest neighbor O3 atoms, and thus, this finding indicates that the diffusion of oxygen ions is going along a pathway following the [110] and [1-10] directions (path A in Fig. 1.7c). In other words, the diffusion paths of O3 atoms exist along the [110] directions around the center of the path. Similarly, the O3 atom migrates along a curved route as that occurring in cubic perovskite oxides. However, in the present double perovskite, a two-dimensional diffusion pathway is present, i.e., the O3 atoms migrate along the [110] and [1-10] directions (Fig. 1.7c and d). This result indicates that the mobility of the oxygen ions in the *a*-*b* plane would be much higher rather than that along the c-axis.

Riddlesden-Popper phases also known as K_2NiF_4-type oxides are belongs to layered perovskite family, $Ln_2NiO_{4+\delta}$ (Ln = La, Pr and Nd) is one of them most promising material which has been widely studied as it shows very good ion conductivity and mobility with broad range of oxygen non-stoichiometry. Figure 1.8 shows oxygen migration in mixed oxide-ionic conductor $Pr_{1.8}La_{0.2}Ni_{0.74}Cu_{0.21}Ga_{0.05}O_{4+\delta}$ via nuclear density map from MEM analysis carried out in tetragonal cell unit cell consisting a (Pr, La)(Ni, Cu, Ga)O_3 perovskite layer and a (Pr, La)O rock salt-type layer [38]. The excess interstitial oxygen accommodated in the rock salt layer (O3 in Fig. 1.8a). In this investigation it has been shown that at temperature region ~606.6 ^{0}C there is no oxygen migration or almost about to start moving whereas at elevated temperature ~ 1016.6 ^{0}C the oxygen atom at the O2 site has high anisotropic thermal motion along the [100] directions and the hopping reaction occurs through the O2 and interstitial O3 sites (see Fig.1.8b, d) which is the completely

different migration paths of oxygen ions from that observed in perovskite-type materials in case of Yttria based ceria oxides.

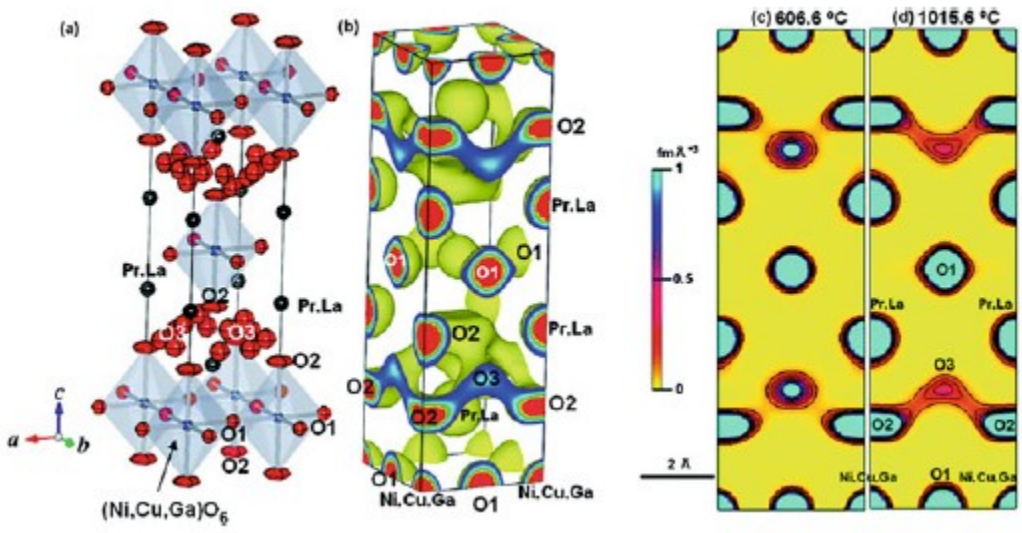

Figure 1.8: Refined crystal structure (a) and isosurface of nuclear density (b) at 0.05 fm Å^{-3} of the mixed oxide-ionic and electronic conductor $(Pr_{0.9}\text{-}La_{0.1})_2(Ni_{0.74}Cu_{0.21}Ga_{0.05})O_{4+\delta}$ determined in situ at 1015.6 ^{0}C. Unit cell: tetragonal *I4/mmm*, *a*=3.875(3) Å and *c*=12.738(9) Å. Nuclear density distribution on the (100) plane of the mixed conductor $(Pr_{0.9}\text{-}La_{0.1})_2(Ni_{0.74}Cu_{0.21}Ga_{0.05})O_{4+\delta}$ at 606.6 ^{0}C (c) and 1015.6 ^{0}C (d). Contour lines from 0.1 to 1.0 by the step of 0.1 fm Å^{-3}. Reproduced from Ref. [38].

Several theoretical studies of oxygen diffusion in $Ln_2NiO_{4+\delta}$ (*Ln* = La, Pr) [39-41] oxides has been investigated using molecular dynamics simulations. Oxygen diffusion in our titled compound $Pr_2NiO_{4+\delta}$ is highly anisotropic, and the diffusion take place via an interstitialcy mechanism in the *a*–*b* plane even though a small contribution from limited vacancy migration along crystallographic *c*-axis has been reported [41]. The theoretical calculations on oxygen diffusivity shows a very weak dependence upon the oxygen non-stoichiometry which causes the variation in activation energy for oxygen migration mostly interstitial oxygen and results are consisted with experimentally observed one. Parfitt et al. [41] concluded that the interstitial oxygen intercalation ($\delta = 0.09875$) into the Pr_2O_2 rock salt layers causes a local distortion of the NiO_6 octahedra, shown schematically in Fig. 1.9d and the driving force for this is the Coulombic repulsion between apical and the interstitial oxygen ion itself. The mechanism of oxygen ion in this K_2NiF_4 family, mostly in nickelates, cuprates and

cobalties is conducted by transporting apical oxygen sites to nearest interstitial oxygen sites making a continuous thermodynamically favorable easy path for bulk oxygen ionic diffusion.

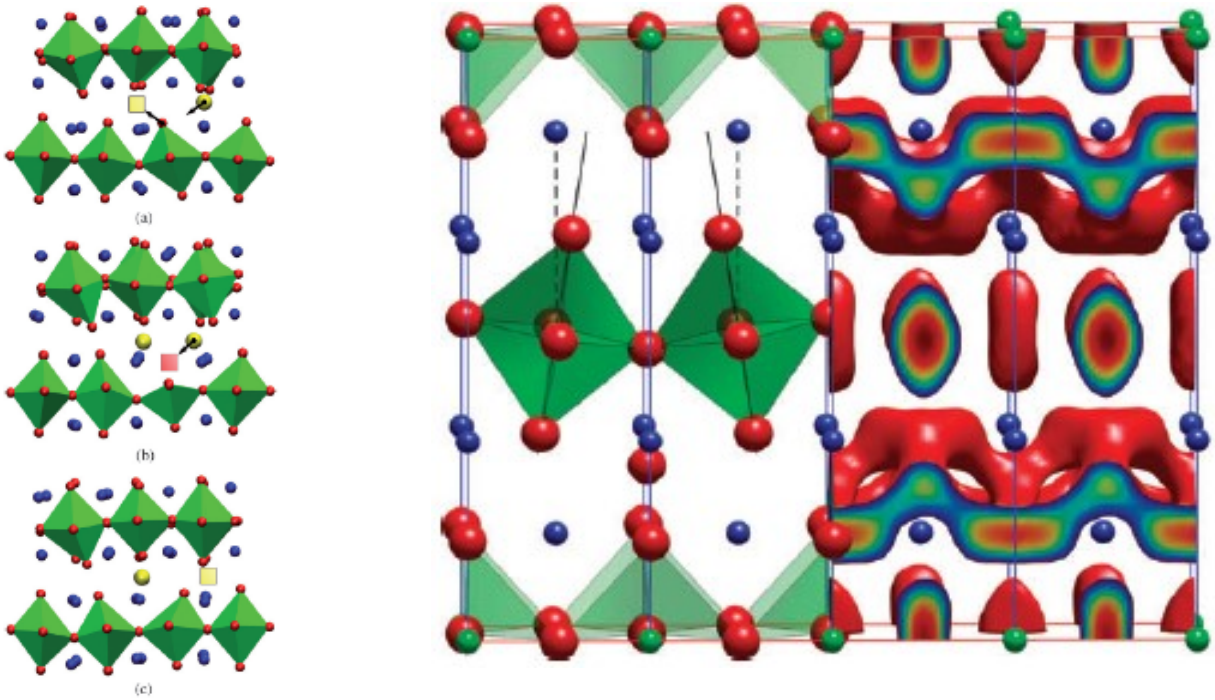

Figure 1.9: left (a–c): Snapshots of a typical diffusion process occurring during a molecular dynamics simulation of $La_2NiO_{4+\delta}$ at 900 K and $\delta = 0.09$. Only a small subset of ions is plotted to aid visualization. Lanthanum ions are represented by blue spheres, nickel–oxygen polyhedra are plotted in green and individual oxygen ions represented by red spheres, or yellow in the case of interstitial ions. Vacant sites relevant to the diffusion process are indicated by red and yellow squares, see text for details. Reproduced from Fig. 3 of ref. [39]. Right (d) the crystal structure of $Pr_2NiO_{4+\delta}$ (O ions in red, NiO_6 octahedra in green and Ni ions in blue, the c-axis is the vertical axis) and the isosurface connecting the O diffusion sites in the *a*–*b* plane from MD at 1100 K and $\delta = 0.09875$ comparison with maximum entropy method results, reprinted form ref. [41].

Savvin et al. confirmed the diffusion of O^{2-} ions in the *a*–*b* plane is also consistent with the MD studies carried out in tetragonal $La_{2-x}Sr_xCuO_{4-\delta}$. Also, the diffusion process is similar to the interstitialcy mechanism predicted for $La_2NiO_{4+\delta}$ in several studies. Chroneos et al.[39] it has been reported and showed nicely that diffusion proceeds via the promotion of an apical oxygen ion into an adjacent accessible interstitial site leaving a vacant site on one of the NiO_6 octahedra. This vacant site is then filled by a second neighboring interstitial site shown in Fig 1.9a-c. As a very rare event the vacant apical site was filled by a equatorial oxygen ion which was able to move between adjacent layers, however this occurred only a few times during the entire 250 ps of the simulations.

1.3 Low-*T* Oxygen Diffusion in *RP*- and Brownmillerite-type Oxides via Lattice Dynamics and Structural Instability

All the above-mentioned diffusion mechanism in several oxides framework needs quite high operating temperature around 800 – 900 ^{0}C in application of SOFCs and oxygen membrane devices. In the beginning strong interest arose in utilization of metal interconnects instead of $LaCrO_3$-based oxide interconnects [43]. Because of the severe corrosion of metals at high temperatures, operation temperature needs to be lowered. Thermodynamic conversion efficiency increases with decreasing temperature for reformed gas (a mixture of CO and hydrogen). Sealing technique becomes less difficult with lowered temperature. For a small system, radiation heat loss becomes less severe by decreasing temperature. Hence, heat management becomes easier at lower temperatures [44]. But decreasing operation temperature gives rise to additional materials issues like oxide ionic conductivity decreases rapidly with decreasing temperature, the electrode activity also decreases drastically with decreasing temperature, even though nickel is still the best choice for operation in the intermediate temperature region the most frequently observed effects on nickel anodes are sulfur poisoning. Materials like $Pr_2NiO_{4+\delta}$, $Nd_2NiO_{4+\delta}$ and $La_2CoO_{4+\delta}$ oxides with high ionic-electronic conductivity and high oxygen diffusion at low temperature is highly demanding in such technological aspect as it intercalated oxygen reversibly by electrochemical oxidation even at RT. However, one of the most distinctive and technologically important features of ABO_3 perovskites is the strong coupling between their functional properties and particular structural distortions. The Goldschmidt's tolerance factor, t, is a commonly used empirical measure that relates the chemical composition of a particular perovskite to its tendency to undergo a structural distortion and is defined as $t = (R_A + R_O)/\sqrt{2}(R_B + R_O)$, where R_A, R_B and R_O are the ionic radii of A, B and oxide ions respectively. Materials with $t < 1$ generally undergo different octahedral tilting, which are associated with unstable zone-boundary phonons of the cubic structure and generally have a significant effect on the properties of perovskites. Most of the rare earth nickelates [45,46] and manganites [47,48] exhibits octahedral tilt distortions that affects both metal–insulator and magnetic ordering transitions, and corresponding transition temperature increases as t decreases.

Also on the other hand this octahedral tilting is responsible for showing fast ionic transport properties in the perovskite-related phases like $La_2NiO_{4+\delta}$ [49, 50], $Pr_2NiO_{4+\delta}$[41], $La_2CoO_{4+\delta}$ [51] and $La_2CuO_{4+\delta}$ [52]. However, there exists few materials like $SrFeO_{2.5}$ [58], $Pr_2NiO_{4+\delta}$ [63] and $Nd_2NiO_{4+\delta}$ [63, 53] which shows very high oxygen diffusion already at low temperature associated with soft, low energy phonon modes which amplify the diffusion rate in presence of interstitial oxygen and the process is so called "phonon-assisted" diffusion mechanism different from classical hopping (or push-pull) mechanism. Lattice relaxation is also assumed to be responsible for enabling fast oxygen diffusion in other families of oxides [54] such as the melilites [55]. There exist several possible transport paths for oxygen diffusion to take place via intercalation at lower temperatures and one of them is topo tactic electrochemical oxidation-reduction reaction. First principles-based lattice dynamical calculation and atomistic simulations together have been investigated in finding such new diffusion mechanisms. Three primary structure types that intercalate oxygen faster belong to the oxygen deficient Brownmillerite structure, Ruddlesden-Popper type structures and structure containing active tetrahedral moieties as the oxygen excess apatite. Most importantly, lattice dynamics characterized by the significant structural relaxation and cooperative motion of local polyhedral activate the conduction of oxygen ions, without necessitating an interstitial oxygen ion/vacancy hopping pathway as discussed earlier for high temperature case.

1.3.1 Oxygen Mobility in Brownmillerites-type Oxides

$CaFeO_{2.5}$, $SrCoO_{2.5}$ and $SrFeO_{2.5}$ are example compound of Brownmillerite family for oxygen ion conduction [56-58]. The key characteristic of the Brownmillerite structures is the alternating octahedral and tetrahedral layers, and the 1D ordered vacancy channels in the tetrahedral layers which have themselves an average diameter of about 3.5 Å (Fig.1.10) at low temperature. It has been shown recently that in the case of the isostructural $SrCoO_{2.5}$ and $SrFeO_{2.5}$ these channels can be filled up completely already at room temperature (RT) to form the cubic perovskite $Sr(Co,Fe)O_3$ in [57,59,61]a reversible topotactic redox reaction [60] *i.e.* by electrochemical oxidation. The underlying atomistic mechanism for this unusually fast oxygen transport kinetics at low temperatures in Brownmillerites $(Sr,Ca)FeO_{2.5}$was revealed recently using inelastic neutron

scattering and ab initio molecular dynamics [58]. Structural differences also arise from the order-disorder phenomena concerning the FeO_4 tetrahedral chains. $CaFeO_{2.5}$, crystallizing in the *Pnma* space group, shows an ordered tetrahedral layer, while it is disordered for $SrFeO_{2.5}$. The disorder is best described in the *Imma* space group, implying split positions of iron and oxygen atoms along the tetrahedral chain (see Figure 1.10). This disorder is equivalent to a superposition of the two FeO_4 chain formations given in Figure 1.10b and, as will be shown later, is of dynamical origin already at and above RT. This type of structural disorder is unique and only present in Brownmillerite-type frameworks (Figure 1.10). The disorder scheme is a crucial point toward a possible understanding of oxygen diffusion along the 1D vacancy channels, as we may postulate that the dynamically disordered MO_4 chains may behave as internal interfaces, allowing a permanent variation of the apical to in plane oxygen distances of adjacent MO_4 chains between 3.5 and 5.3 Å (Figure 1.10b). For an oxygen atom, moving along the vacancy channel, the permanent switching mode would behave like a gate, which opens and closes with the switching frequency, thus pushing the oxygen atoms through. Consequently, the different oxygen intercalation behavior found for $CaFeO_{2.5}$ and $SrFeO_{2.5}$ at RT should be a direct response of their different lattice dynamics and ordering state. In summary, the apical oxygen atoms can exhibit large displacements, and if they get sufficiently far from their equilibrium positions, they are able to escape into the vacancy channels of the tetrahedral layer. The structure left behind is then a square pyramid, and a reoriented tetrahedron (see Fig. 1.11(a) and (b) for $SrFeO_{2.5}$), signifying the ability of the lattice to dynamically accommodate multiple polyhedral configurations. A pronounced lattice dynamics exists for the tetrahedral chains, showing a marked zig-zag switching behavior. The potential of the apical oxygens to do this is mainly determined by the Fe–O bond strength and length along the c-axis; the longer the bond, the easier to displace the oxygen atom. Therefore, the possibility of this fast kinetics strongly depends on the lattice parameter along the c-axis. The local instability of the apical oxygen atoms suggests that its structure is better described as a sequence of infinite $(FeO_2)_\infty$ layers containing square planar FeO_4 units, alternating with FeO_4 tetrahedra layers, rather than the classical description of alternating octahedral and tetrahedral layers (see Figure 1.12).

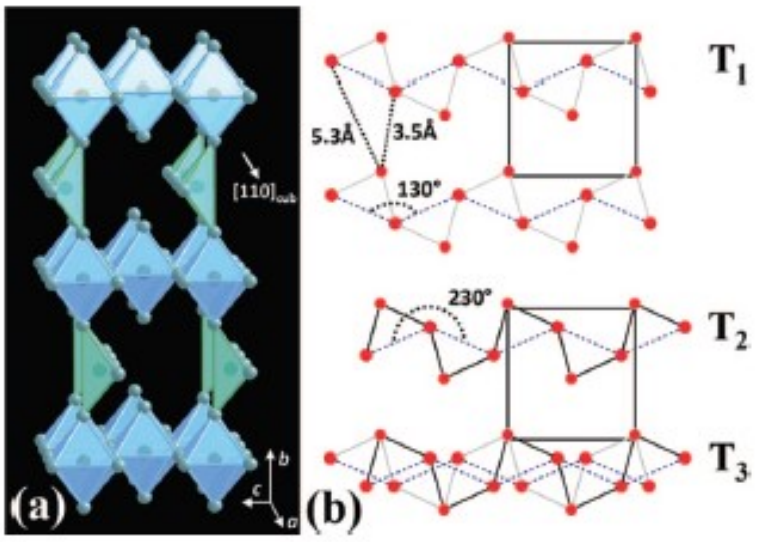

Figure 1.10: (a) Idealized scheme of the Brownmillerite structure with 1D oxygen vacancy channels along [110] with respect to the cubic perovskite phase. FeO_6 octahedra and FeO_4 tetrahedra are reported in blue and green, respectively; Sr or Ca are omitted for clarity. In reality the tetrahedral chains show a zigzag arrangement as shown in part b (T1 and T2). Dynamical switching between T1 and T2 can trigger phonon assisted oxygen diffusion along the oxygen vacancy channel while the distances from the apical O to in plane O atoms vary between 3.5 and 5.3 Å. This disorder scenario is schematically represented as T3. The coordinate system (*a*, *b*, *c*) refers to the Brownmillerite structure in *Pnma*. Reproduced from Fig. 1 of ref. [58].

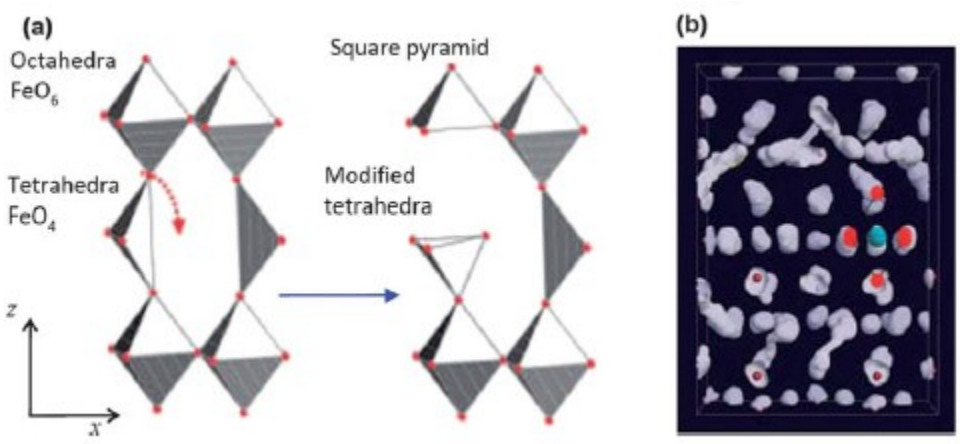

Figure 1.11: (a) $SrFeO_{2.5}$, Brownmillerite framework, before and after the diffusion of an apical oxygen atom (shown by red dashed arrow) yielding a FeO_5 square pyramid, and a modified FeO_4 tetrahedron. (b) Atomic trajectories along a 10 ps ab initio molecular dynamics run at 350 K (oxygen positions are red spheres), where the apical oxygen follow a zig-zag pattern dynamics. Reprinted from ref. [58].

The same path was found experimentally to be much slower and active only at higher temperatures in $CaFeO_{2.5}$ (above 700 K, vs. 600 K for $SrFeO_{2.5}$) [58], whose c-axis lattice parameter is shorter than that of $SrFeO_{2.5}$ (c_{CFO} = 14.77 Å and c_{SFO} = 15.85 Å) [58, 56]. While these Fe-containing

Brownmillerites would also be electronically conducting, rendering them more suitable as a cathode, the oxygen conduction path in these structures could be representative of also the purely ionic conducting BaInO2.5 at low temperatures as a candidate electrolyte material.

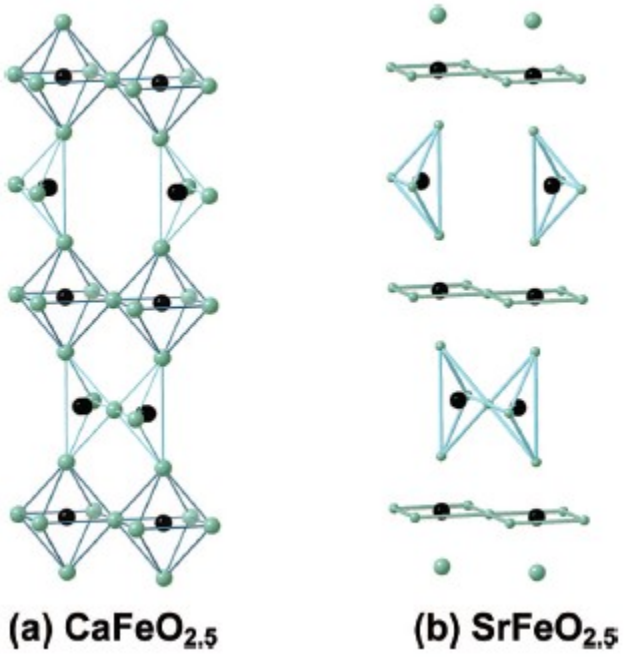

Figure 1.12: Schematic structures of $CaFeO_{2.5}$ and $SrFeO_{2.5}$. Black and gray spheres represent Fe and O atoms, respectively; Sr and Ca are omitted for clarity. (a) For $CaFeO_{2.5}$ the classical description of the Brownmillerite framework, *i.e.* the sequence of alternating octahedra and tetrahedra layers, is outlined. (b) For $SrFeO_{2.5}$, this picture has to be reconsidered, as the apical oxygen atoms are no longer associated with the FeO6 octahedra layers (see text) and have to be mainly accounted to the FeO_4 tetrahedra chains. In this way, $SrFeO_{2.5}$ yields in a sequence of square planar FeO_4 layers, alternating with layers of FeO_4 tetrahedra chains. Note that $SrFeO_2$ with infinite $(FeO_2)_\infty$ layer structure and $Sr_3Fe_2O_5$ showing a square planar FeO_4 coordination have recently been reported to be stable compounds. Reproduced from Fig. 7 of ref. [58].

1.3.2 Phonon Assisted Diffusion in Ruddlesden-Popper Oxides

In contrast to $ABO_{3-\delta}$ oxides, which are generally known as oxygen-deficient perovskites because oxygen vacancies are their dominant anion point defect, RP oxides can be both oxygen-deficient and oxygen-excess, depending upon their majority oxygen defects. In the case of oxygen-deficient RP oxides, oxygen nonstoichiometry (δ) arises from oxygen vacancies, whereas oxygen interstitials result in oxygen hyperstoichiometric RP oxides. Therefore, oxygen ion migration in RP oxides can occur via classical hopping mechanisms associated with either oxygen vacancies or oxygen

interstitialsls at higher temperature as discussed above. However, the diffusion mechanism at ambient temperature in series of oxygen excess compounds $La_2CuO_{4+\delta}$ [52], $La_2CoO_{4+\delta}$ [62], $Pr_2NiO_{4+\delta}$ [63,22] and $Nd_2NiO_{4+\delta}$ [53,64] has been investigated recently using neutron and x-ray diffraction methods along with theoretical study by DFT based ab-initio MD simulations. Many studies have shown oxygen ion transport properties in oxygen-excess RP oxides, mostly nickelates and cobalties, which can intercalate excess oxygen via topo tactic electrochemical oxidation-reduction process already at ambient. Villesuzanne et al. [52] it has been shown combining neutron diffraction studies with 1st-principles lattice dynamical calculations, the displacements of apical oxygen atoms in $La_2CuO_{4+\delta}$ and associated lattice instability i.e. low-energy phonon modes, are consider as low-temperature oxygen diffusion mechanism. The oxygen ions are diffusing are not interstitials rather apical oxygen atoms, presence of O_{int} amplify the dynamical diffusion mechanism between O_{ap} and O_{int} via shallow potential diffusion pathway. From MEM reconstruction one can see detail view of the oxygen disorder, specifically concerning the apical oxygen atoms. Whilst it confirms the strong disorder scenario in the *a*–*b* plane (see top part of Fig. 1.13). At 20 K, this density is limited to maxima pointing towards the [100] directions with respect to the F-centred unit cell, whilst at ambient temperature, densities along [100] and [110] are simultaneously present. At 20 K, the interstitial oxygen atoms are on the defined (¼ ¼ ¼) position, related to the frozen arrangement of the symmetrically enlarged $O_{int}(O_{ap})_4$ tetrahedra. This scenario changes when switching to ambient temperature. Here, the tilting of the apical oxygen atoms in the [100] and [110] directions indicates an increase of the apical oxygendisorder, probably related to dynamic fluctuations and which directly influences the displacements of the interstitial oxygen atoms. DFT calculation shows that in the presence of interstitial oxygen the displacement of apical oxygen along [110]-direction is energetically favored for -4.1 meV compared to the case of stoichiometric La2CuO4 at 20 meV.

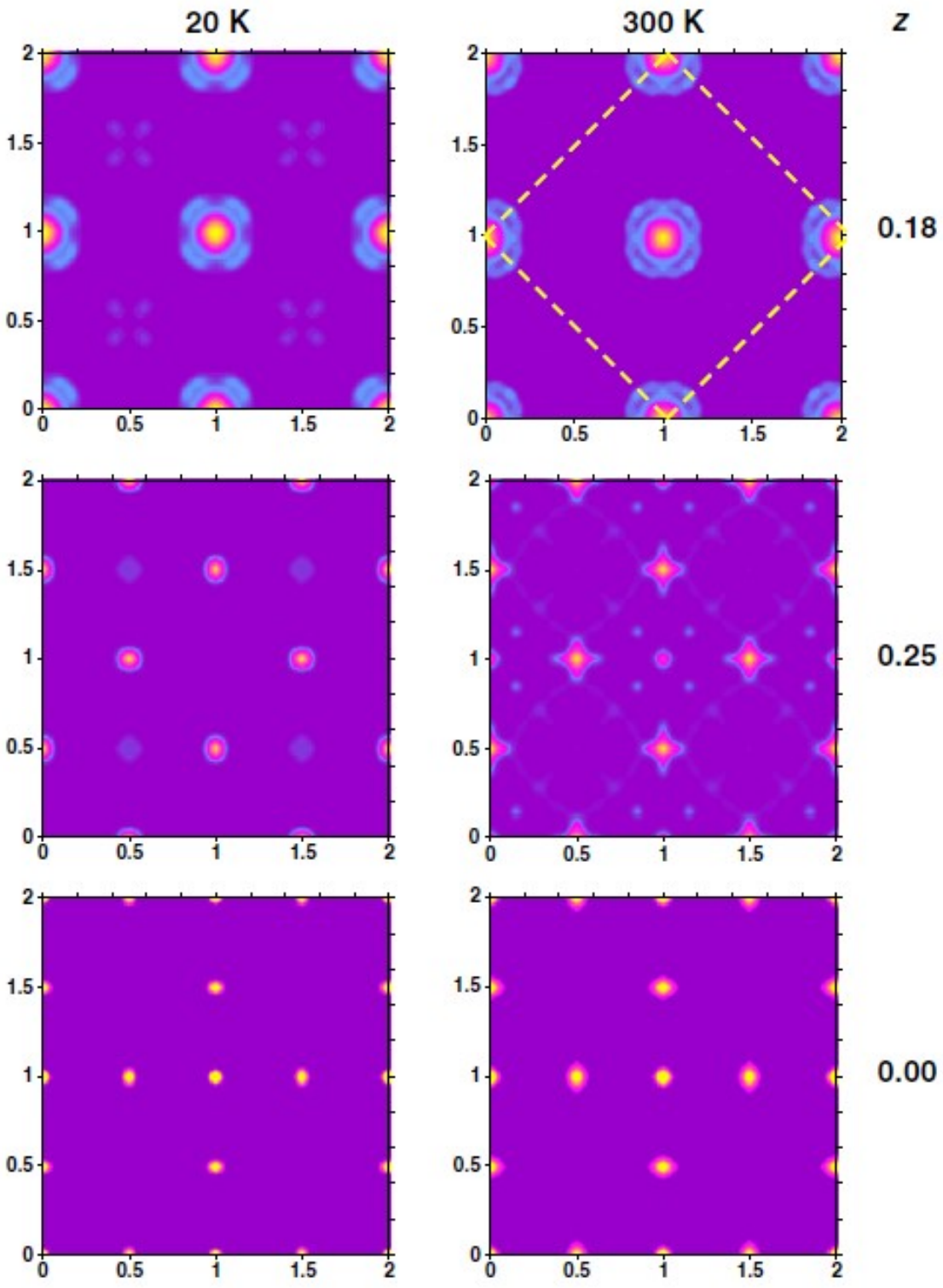

Figure 1.13: Nuclear scattering densities obtained from a $La_2CuO_{4.07}$ twinned single crystal by neutron diffraction studies and subsequent reconstruction using the maximum entropy method at 20 K and ambient temperature. Sections of the CuO_2 plane (z=0), the apical oxygen layer in z=0.18 and the interstitial oxygen section in z=0.25 are given. The F-centred unit cell is outlined for the figure at z=0.18 and 300 K. Reproduced from Fig. 2 of ref. [52].

These results strongly evidence the concept of lattice dynamics to be at the origin of low temperature oxygen mobility, with specific requirements depending on the underlying structural framework.

Another example of such oxygen excess RP oxides where in low temperature oxygen diffusion mechanism take place via large anharmonic displacements is $Pr_2NiO_{4+\delta}$ and $Nd_2NiO_{4+\delta}$ [63]. Ceretti *et al.*[63] recently have shown by single crystal neutron diffraction and subsequently by MEM analysis of $Pr_2NiO_{4.25}$ at ambient and 400 ^{0}C, a much more pronounced displacement of the apical oxygen atoms towards the interstitial lattice sites in the [110]-direction of the *F*-cell compared to the case of $La_2CuO_{4.07}$. The interstitial oxygen atoms play a predominant role in the oxygen diffusion mechanism, since they induce a strong delocalization of the apical oxygen atoms and deeply affect lattice dynamics. The large displacements of O_{ap} atoms are considered to be – at least partially – of dynamical origin, which is consistent with a phonon assisted diffusion mechanism, already activated at very moderate temperatures. Slightly above the orthorhombic–tetragonal phase transition ~ 400 ^{0}C, the anharmonic apical oxygen displacements occur towards [110]-direction of in the *F*-cell ([100]-direction in original *I4/mmm* cell) of tetragonal parent structure (Fig. 1.14) under a double-well potential creating a quasi-continuous shallow energy diffusion pathway between apical and interstitial oxygen sites.

The last example of this homologous series is $Nd_2NiO_{4+\delta}$ [53, 64] where it has been lattice dynamics modified by excess oxygen in low-temperature oxygen diffusion mechanism using positional recurrence maps where displacements of specific lattice are considered not position. Piovano et al. [64] shows in Fig. 1.15 different PRM sections of apical oxygen atoms from 40ps MD simulations for $Nd_2NiO_{4.0}$, $Nd_2NiO_{4.125}$ and $Nd_2NiO_{4.25}$ at five different temperatures: 150, 230K (LT), 310K (RT), 670, 1070K (HT). In the stoichiometric $Nd_2NiO_{4.0}$ case, the PRM at room temperature (310K or RT) shows a cross shape with preferred displacements in the [010] direction, which is expected since the low temperature orthorhombic phase (LTO) has its tilt pattern along [010]. Compare to most-oxidized $Nd_2NiO_{4.25}$ case, apical oxygen are delocalized along [110] at LT. This comes from the first neighbor interaction of NiO_6 and interstitial oxygen atoms. In this rigid case, much of the freedom of the NiO6 octahedron is pinned by the interstitial oxygen. At RT the second neighbor interaction disappears and the [110] pathway is enabled. In the intermediate $Nd_2NiO_{4.125}$

case, the apical oxygen atom at RT shows both [010] and [110] delocalization. This is consistent with the quarter filling of interstitial sites by excess oxygen atoms for δ=0.125. In LT rigid regime, every NiO_6 octahedron is strongly dependent on its neighbours, which means that the [110] strained apical oxygen drives the free apical oxygen from [010] to [110]. The diffusion pathway of mobile oxygen extracted from MD calculations show that in non-stoichiometric $Nd_2NiO_{4.10}$ the envelop of the oxygen diffusion passes through the interstitial sites (see Fig. 1.16), similar to the one reported for isostructural $La_2CoO_{4+\delta}$ and $Pr_2NiO_{4+\delta}$ where the mechanism of diffusion involves both apical and interstitial oxygen atoms with a defined scheme. Considering the effect of δ, excess oxygen in interstitial sites activates the [110] dynamics of apical oxygen atoms.

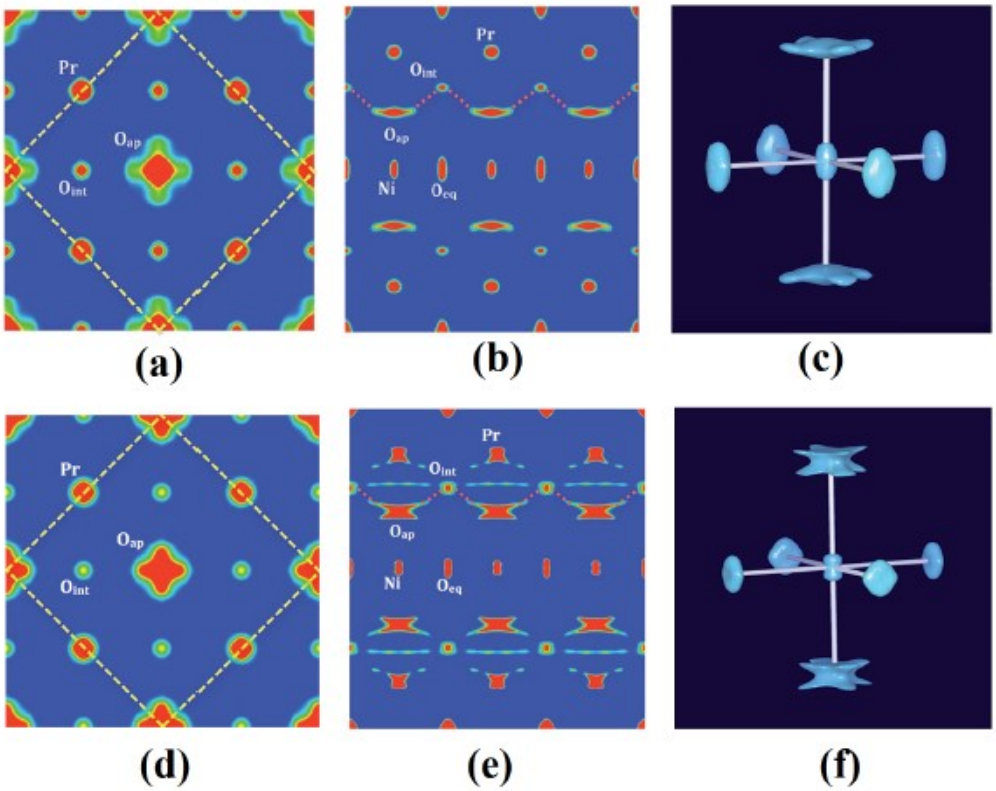

Figure 1.14: (a, b, d, e) Neuclear density maps of $Pr_2NiO_{4.25}$ obtained from neutron single crystal diffraction data by MEM analysis; (a) and (d) represents respectively the scattering densities of Pr (z = 0.14), O_{ap} (z = 0.17) and O_{int} (z = 0.25) integrated in the range $0.12 \leq z \leq 0.25$ in the 2a × 2a projection of the *I4/mmm* unit cell at RT and 400 ^{0}C. Note that the *F*-centred cell is outlined by yellow dashed bars. Similarly (b) and (e) represents respectively the scattering densities of Pr, O_{ap} and O_{int} integrated in the range $0.452 \leq y \leq 0.55$ in the 3a × c projection of the *I4/mmm* unit cell at RT and 400 ^{0}C. The red dashed lines indicates the oxygen diffusion pathways along the *a*-axis in the *I* cell, equivalent to [110]-direction in the *F*-cell, between apical and interstitial sites. (c) and (f) represents the isosurface of the NiO_6 octahedra at RT and 400 ^{0}C respectively. Figures are taken from ref. [63].

At RT the interstitial oxygen can diffuse only to the apical oxygen that the [110] octahedron tilt scheme brings closer and therefore that diffusion is linked to the specific lattice dynamics.

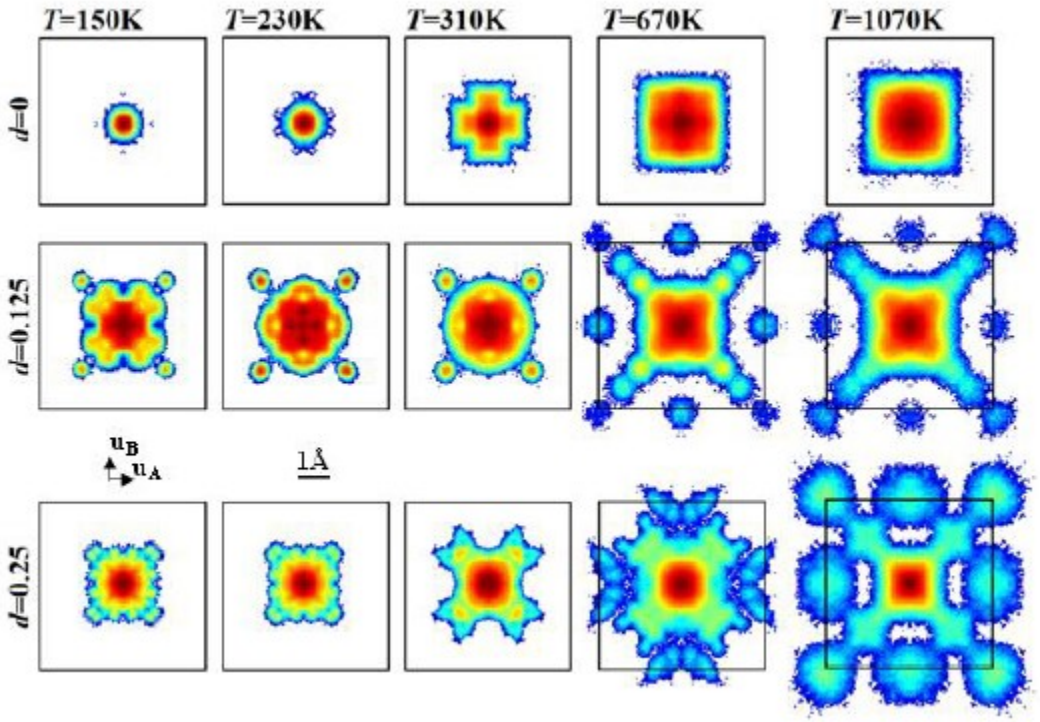

Figure 1.15: PRM of apical oxygen atoms from molecular dynamics at T=150, 230, 310, 670 and 1070K, of $Nd_2NiO_{4.0}$, $Nd_2NiO_{4.125}$ and $Nd_2NiO_{4.25}$. Each PRM is cut in space to the conventional F-cell (black border). The colour scale is logarithmic and white corresponds to zero background. Reproduced from Fig. 4 of ref. [64].

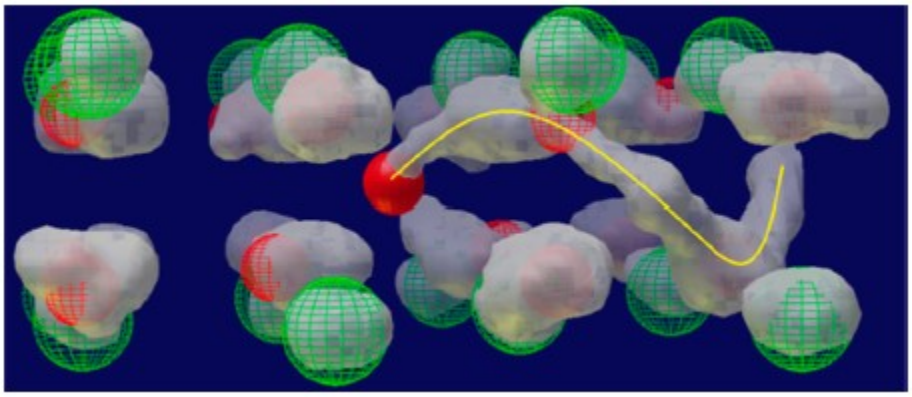

Figure 1.16: Detail of the rock-salt layer of the $Nd_2NiO_{4.10}$ supercell in the T = 310 K molecular dynamics. Wired green spheres represent Nd^{3+} ions, wired red spheres O^{2-} ions in apical sites, and plain red spheres O^{2-} ions in the interstitial site. Atoms are drawn at their initial positions. Gray clouds represent the ensemble of positions occupied by the atoms over 40 ps of the molecular dynamics. Connected clouds from apical to interstitial sites are marked with a yellow line and evidence oxygen mobility. Reproduced from Fig. 6 of ref. [53].

1.4 Summary

Developing high-performance energy and environmental devices, such as SOFCs, oxygen permeation membranes, and chemical sensors, requires discovering new oxide materials with high oxygen mobility and stability. In this regard, RP oxide materials have been considered as alternative materials to ABO_3 perovskite oxides. In this chapter, we have briefly overviewed the fundamental mechanisms of oxygen ion diffusion in RP oxides, focusing on the A_2BO_4 system. A clear distinction between RP oxides and ABO_3 oxides is that RP oxides can be both oxygen-deficient and oxygen-excess depending on the δ, which can determine whether the oxygen migration mechanism is driven by classical high temperature interstitialcy or vacancy hopping. In addition, RP oxides have an anisotropic structure, which leads to highly anisotropic diffusion properties and the oxygen migration via lattice instability mainly low-energy phonon modes already at room temperature. The standard Arrhenius equation is no longer valid for oxygen diffusion at low temperature where lattice dynamics and structural instability due to the excess oxygen, are required to explain oxygen diffusion via phonon assisted diffusion mechanism [58]. The excess oxygen intercalation in such K2NiF4-type oxides can be obtained via electrochemical oxidation reaction at low temperature, being far away from thermodynamical equilibrium in other words it's electronically equivalent to hole doping by substituting lower cation requires high temperature synthesis. This kind of high temperature synthesis can give rise to spatial inhomogeneity and order-disorder state including electronic phase separation in a microscopic to nanoscale region. Such spatial inhomogeneity and quenched order-disorder are believed to give rise electronic correlations as a results of spin-charge, oxygen and orbital ordering that take place in most complex transition metal oxides (CTMOs) and $Pr_{2-x}Sr_xNiO_{4+\delta}$ belongs to that kind of complex correlated oxides. In the next chapter we will introduce such novel physical ordering phenomena in a consequence with electronic correlation and phase separation.

Reference:

1. Adler, S.B. Factors governing oxygen reduction in solid oxide fuel cell cathodes. Chem. Rev. 2004, 104, 4791–4843.
2. Bhalla, A.S.; Guo, R.Y.; Roy, R. The perovskite structure—A review of its role in ceramic science and technology. Mater. Res. Innov. 2000, 4, 3–26.
3. Voorhoeve, R.J.H.; Johnson, D.W.; Remeika, J.P.; Gallagher, P.K. Perovskite oxides: Materials science in catalysis. Science 1977, 195, 827–833.
4. Berenov, A.V.; Atkinson, A.; Kilner, J.A.; Bucher, E.; Sitte,W. Oxygen tracer diffusion and surface exchange kinetics in $La_{0.6}Sr_{0.4}CoO_{3-\delta}$. Solid State Ion. 2010, 181, 819–826.
5. D. Lee, Y.L. Lee, A. Grimaud, W.T. Hong, M.D. Biegalski, D. organ, Y. Shao-Horn, Enhanced oxygen surface exchange kinetics and stability on epitaxial $La_{0.8}Sr_{0.2}CoO_{3-\delta}$ thin films by $La_{0.8}Sr_{0.2}MnO_{3-\delta}$ decoration. J. Phys. Chem. C 2014, 118, 14326–14334.
6. R. H. E. Van Doorn, A. J. Burggraaf, Structural aspects of the ionic conductivity of $La_{1-x}Sr_xCoO_{3-\delta}$, Solid State Ion. 2000, 128, 65–78.
7. B. J. Ingram, J.A. Eastman, K.C. Chang, S.K. Kim, T.T. Fister, E. Perret, H. You, P.M. Baldo, P.H. Fuoss, In situ X-ray studies of oxygen surface exchange behavior in thin film $La_{0.6}Sr_{0.4}Co_{0.2}Fe_{0.8}O_{3-\delta}$, Appl. Phys. Lett. 2012, 101, 051603.
8. B.C.H. Steele, J.M. Bae, Properties of $La_{0.6}Sr_{0.4}Co_{0.2}Fe_{0.8}O_{3-\delta}$ (LSCF) double layer cathodes on gadolinium-doped cerium oxide (CGO) electrolytesII. Role of oxygen exchange and diffusion. Solid State Ion. 1998, 106, 255–261.
9. L.W. Tai, M.M. Nasrallah, H.U. Anderson, D.M. Sparlin, S.R. Sehlin, Structure and electrical properties of $La_{1-x}Sr_xCo_{1-y}Fe_yO_3$. Part 1. The system $La_{0.8}Sr_{0.8}Co_{1-y}Fe_yO_3$. Solid State Ion. 1995, 76, 259–271.
10. H.J.M. Bouwmeester, H. Kruidhof, A.J. Burggraaf, Importance of the surface exchange kinetics as rate-limiting step in oxygen permeation through mixed-conducting oxides. Solid State Ion. 1994, 72, 185–194.
11. M. Al Daroukh, V.V. Vashook, H. Ullmann, F. Tietz, I.A. Raj, Oxides of the AMO_3 and A_2MO_4-type: Structural stability, electrical conductivity and thermal expansion. Solid State Ion. 2003, 158, 141–150.
12. X.Y. Chen, J.S. Yu, S.B. Adler, Thermal and chemical expansion of Sr-doped lanthanum cobalt oxide ($La_{1-x}Sr_xCoO_{3-\delta}$). Chem. Mater. 2005, 17, 4537–4546.
13. S. Hashimoto, Y. Fukuda, M. Kuhn, K. Sato, K. Yashiro, J. M Izusaki, Thermal and chemical lattice expansibility of $La_{0.6}Sr_{0.4}Co_{1-y}Fe_yO_{3-\delta}$ (y = 0.2, 0.4, 0.6 and 0.8). Solid State Ion. 2011, 186, 37–43.

14. Mastin. J, Einarsrud. M.A., Grande. T, Structural and thermal properties of $La_{1-x}Sr_xCoO_{3-\delta}$. Chem. Mater. 2006, 18, 6047–6053.
15. Lee. D, Lee. Y.L, Hong. W.T, Biegalski. M.D, Morgan. D, Shao-Horn. Y, Oxygen surface exchange kinetics and stability of $(La,Sr)_2CoO_{4\pm\delta}/La_{1-x}Sr_xMO_{3-\delta}$ (M = Co and Fe) hetero-interfaces at intermediate temperatures. J. Mater. Chem. A 2015, 3, 2144–2157.
16. Benson. S.J, Waller. D, Kilner. J.A, Degradation of $La_{0.6}Sr_{0.4}Co_{0.8}Fe_{0.2}O_{3-\delta}$ in carbon dioxide and water atmospheres. J. Electrochem. Soc. 1999, 146, 1305–1309.
17. Ding. H.P, Virkar. A.V, Liu. M.L, Liu. F, Suppression of Sr surface segregation in $La_{1-x}Sr_xCo_{1-y}Fe_yO_{3-\delta}$: A first principles study. Phys. Chem. Chem. Phys. 2013, 15, 489–496.
18. Oh. D, Gostovic. D, Wachsman. E.D, Mechanism of La0.6Sr0.4Co0.2Fe0.8O3 cathode degradation. J. Mater. Res. 2012, 27, 1992–1999.
19. Simner. S.P, Anderson. M.D, Engelhard. M.H, Stevenson. J.W, Degradation mechanisms of La-Sr-Co-Fe-O_3 SOFC cathodes. Electrochem. Solid State Lett. 2006, 9, A478–A481.
20. Brown, I.D, Modeling the structures of La_2NiO_4, Z. Kristallogr. 1992, 199, 255–272.
21. Aguadero. A, Escudero. M.J, Perez. M, Alonso. J.A, Daza. L, Hyperstoichiometric $La_{1.9}Sr_{0.1}NiO_{4+\delta}$ mixed conductor as novel cathode for intermediate temperature solid oxide fuel cells, J. Fuel Cell Sci. Technol. 2007, 4, 294–298.
22. Bassat. J.M, Burriel. M, Wahyudi. O, Castaing. R, Ceretti. M, Veber. P, Weill. I, Villesuzanne. A, Grenier. J.C, Paulus. W, Anisotropic oxygen diffusion properties in $Pr_2NiO_{4+\delta}$ and $Nd_2NiO_{4+\delta}$ single crystals, J. Phys. Chem. C 2013, 117, 26466–26472.
23. Bassat. J.M, Odier. P, Villesuzanne. A, Marin. C, Pouchard. M, Anisotropic ionic transport properties in $La_2NiO_{4+\delta}$ single crystals. Solid State Ion. 2004, 167, 341–347.
24. Boehm. E, Bassat. J.M, Dordor. P, Mauvy. F, Grenier. J.C, Stevens. P, Oxygen diffusion and transport properties in non-stoichiometric $Ln_{2-x}NiO_{4+\delta}$ oxides. Solid State Ion. 2005, 176, 2717–2725.
25. Lee. D, Grimaud. A, Crumlin. E.J, Mezghani. K, Habib. M.A, Feng. Z.X, Hong. W.T, Biegalski. M.D, Christen. H.M, Shao-Horn. Y, Strain influence on the oxygen electrocatalysis of the (100)-oriented epitaxial $La_2NiO_{4+\delta}$ thin films at elevated temperatures. J. Phys. Chem. C 2013, 117, 18789–18795.
26. Skinner. S.J, Kilner. J.A, Oxygen diffusion and surface exchange in $La_{2-x}Sr_xNiO_{4+\delta}$, Solid State Ion. 2000, 135, 709–712.
27. Gopalakrishnan. J, Colsmann. G, Reuter. B, Studies on La2−xSrxNiO4 (0 x 1) system. J. Solid State Chem.1977, 22, 145–149.
28. Nernst W, on the electrolytic conduction of solid bodies at high temperatures. Z Electrochem 6:41–43.

29. Cales B, Baumard JF, Oxygen semipermeability and electronic conductivity in calciastabilized zirconia. J Mater Sci 17:3243–3248, 1982.
30. Teraoka Y, Zhang HM, Furukawa S, Yamazoe N, Oxygen permeation through perovskite-type oxides. Chem Lett 11:1743–1746, 1985.
31. Yashima M, Crystal structures, structural disorders and diffusion paths of ionic conductors from diffraction experiments. Solid State Ionics 179:797–803, 2008.
32. Yashima M, Kobayashi S, Yasui T, Positional disorder and diffusion path of oxide ions in the yttria-doped ceria $Ce_{0.93}Y_{0.07}O_{1.96}$. Faraday Discuss 134:369–376, 2007.
33. Nakayama M, Martin M, First-principles study on defect chemistry and migration of oxide ions in ceria doped with rare-earth cations. Phys Chem Chem Phys 11:3241–3249, 2009.
34. Shimojo F, Okazaki H, Molecular dynamics studies of yttria stabilized zirconia. II Mechanism of oxygen diffusion. J Phys Soc Jpn 61:4106–4118, 1992.
35. Khan MS, Islam MS, Bates DR, Dopant substitution and ion migration in the $LaGaO_{3-\delta}$ based oxygen ion conductor. J Phys Chem B 102:3099–3104, 1998.
36. Islam MS, Davies RA, Atomistic study of dopant site-selectivity and defect association in the lanthanum gallate perovskite. J Mater Chem 14:86–93, 2004.
37. Kuwabara A, Tanaka I, First principles calculation of defect formation energies in Sr- and Mg-doped $LaGaO_3$. J Phys Chem B 108:9168–9172, 2204.
38. Yashima M, Enoki M, Wakita T, Ali R, Matsushita Y, Izumi F, Ishihara T, Structural disorder and diffusional pathway of oxide ions in a doped Pr_2NiO_4-based mixed conductor. J Am Chem Soc 130:2762–2763, 2008.
39. A. Chroneos, D. Parfitt, John A. Kilner and Robin W. Grimes, Anisotropic oxygen diffusion in tetragonal $La_2NiO_{4+\delta}$: molecular dynamics Calculations, J. Mater. Chem., 2010, 20, 266–270.
40. A. Chroneos, R. V. Vovk, I. L. Goulatis and L. I. Goulatis,J. Oxygen transport in perovskite and related oxides: A brief review Alloys Compd., 2010, 494, 190.
41. D. Parfitt, A. Chroneos, John A. Kilner and Robin W. Grimes, Molecular dynamics study of oxygen diffusion in $Pr_2NiO_{4+\delta}$, Phys. Chem. Chem. Phys., 2010, 12, 6834–6836.
42. S. N. Savin, G. N. Mazo and A. K. Ivanov-Schitz, Simulation of ion transport in layered cuprates $La_{2-x}Sr_xCuO_{4-\delta}$ Crystallogr. Rep., 2008, 53, 291.
43. K. Hilpert, W.J. Quadakkers, L. Singheiser, Chapter 74. Interconnects, Fuel Cell Handbook Vol. 4, pp. 1037–1054 (2003).
44. M. Suzuki, T. Sogi, K. Higaki, T. Ono, N. Takahashi, K. Shimazu, T. Shigehisa, Development of SOFC Residential Cogeneration System at Osaka Gas and Kyocera, SOFC X, ECS Trans. 7(1) 27–30 (2007).

45. M. L. Medarde, Structural, magnetic and electronic properties of $RNiO_3$ perovskites (R = rare earth) J. Phys.: Condens. Matter 1997, 9, 1679–1707.

46. G. Catalan, Progress in perovskite nickelate research Phase Trans. 2008, 81, 729–749.

47. H. Y. Hwang, S. Cheong, P. G. Radaelli, M. Marezio, B. Batlogg, Lattice Effects on the Magnetoresistance in Doped $LaMnO_3$ Phys. Rev. Lett. 1995, 75, 914–917.

48. T. Kimura, S. Ishihara, H. Shintani, T. Arima, K. Ishikaza, Y. Tokura, Distorted perovskite with e1g configuration as a frustrated spin system Phys. Rev. B 2003, 68, 060403(R).

49. C. Frayret, A. Villesuzanne, Pouchard, Application of Density Functional Theory to the Modeling of the Mixed Ionic and Electronic Conductor $La_2NiO_{4+\delta}$: Lattice Relaxation, Oxygen Mobility, and Energetics of Frenkel Defects M. Chem. Mater. 2005, 17, 6538–6544.

50. A. Chroneos, D. Parfitt, J. A. Kilner, R. W. Grimes, Anisotropic oxygen diffusion in tetragonal $La_2NiO_{4+\delta}$: molecular dynamics calculationsJ. Mater. Chem. 2009, 20, 266–270.

51. A. Kushima, D. Parfitt, A. Chroneos, B. Yildiz, J. A. Kilner, R. W. Grimes, Interstitialcy diffusion of oxygen in tetragonal $La_2CoO_{4+\delta}$, Phys. Chem. Chem. Phys. 2011, 13, 2242–2249.

52. A. Villesuzanne, W. Paulus, A. Cousson, S. Hosoya, L. Le Dréau, O. Hernandez, C. Prestipino, M. I. Houchati, J. Schefer, On the role of lattice dynamics on low-temperature oxygen mobility in solid oxides: a neutron diffraction and first-principles investigation of $La_2CuO_{4+\delta}$, J. Solid State Electrochem. 2011, 15, 357–366.

53. Perrichon, A. Piovano, A.; Boehm, M. Zbiri, M. Johnson, M. Schober, H. Ceretti, M. Paulus, W. Lattice Dynamics Modified by Excess Oxygen in $Nd_2NiO_{4+\delta}$: Triggering Low-Temperature Oxygen DiffusionJ. Phys. Chem. C 2014, 119, 1557–1564.

54. E. Kendrick, J. Kendrick, K. S. Knight, M. S. Islam, P. R. Slater, Cooperative mechanisms of fast-ion conduction in gallium-based oxides with tetrahedral moieties Nat. Mater. 2007, 6, 871–875.

55. X. Kuang, M. A. Green, H. Niu, P. Zajdel, C. Dickinson, J. B. Claridge, L. Jantsky, M. J. Rosseinsky, Interstitial oxide ion conductivity in the layered tetrahedral network melilite structure Nat. Mater. 2008, 7, 498– 504.

56. S. Inoue1, M. Kawai1, N. Ichikawa, H. Kageyama, W. Paulus and Y. Shimakawa, Anisotropic oxygen diffusion at low temperature in perovskite-structure iron oxides, Nature Chemistry 2, 213 217(2010).

57. Ronan Le Toquin, W. Paulus, A. Cousson, C. Prestipino and C. Lamberti, Time-Resolved in Situ Studies of Oxygen Intercalation into $SrCoO_{2.5}$, Performed by Neutron Diffraction and X-ray Absorption SpectroscopyJ. AM. CHEM. SOC. 2006, 128, 13161-13174.

58. W. Paulus, H. Schober,S. Eibl, M. Johnson, T. Berthier,O. Hernandez, M. Ceretti, M. Plazanet, K. Conder and C. Lamberti, Lattice Dynamics To Trigger Low Temperature Oxygen Mobility in Solid Oxide Ion Conductors, J. Am. Chem. Soc., 2008, 130 (47).
59. O. Haas, F. Holzer, S. Muller, J. M. McBreen, X. Q. Yang, X. Sun, M. Balasubramanian, X-ray absorption and diffraction studies of $La_{0.6}Ca_{0.4}CoO_3$ perovskite, a catalyst for bifunctional oxygen electrodes Electrochim. Acta 2002, 47, 3211-3217.
60. C. Lamberti, S. Bordiga, F. Bonino, C. Prestipino, G. Berlier, L. Capello, F. D'Acapito, F. X. Llabres Xamena, A. Zecchina, Determination of the oxidation and coordination state of copper on different Cu-based catalysts by XANES spectroscopy *in situ* or in *operando* conditions Phys. Chem.Chem. Phys. 2003, 5, 4502-4509.
61. A. Nemudry, P. Weiss, I. Gainutdinov, V. Boldyrev and R. Schollhorn, Room Temperature Electrochemical Redox Reactions of the Defect Perovskite $SrFeO_{2.5+x}$ Chem. Mater., 1998, 10, 2403
62. L. Dréau, C. Prestipino, O. Hernandez, J. Schefer, G. Vaughan, S. Paofai, J. Perez- Mato, S. Hosoya, and W. Paulus, Structural Modulation and Phase Transitions in $La_2CoO_{4.14}$ Investigated by Synchrotron X-ray and Neutron Single-Crystal Diffraction, Inorg. Chem., vol. 51, pp. 9789–9798, 2012.
63. M. Ceretti, O. Wahyudi, A. Cousson, A. Villesuzanne, M. Meven, B. Pedersen, J. M. Bassat, and W. Paulus, "Low temperature oxygen diffusion mechanisms in $Nd_2NiO_{4+\delta}$ and $Pr_2NiO_{4+\delta}$ via large anharmonic displacements, explored by single crystal neutron diffraction," J. Mater. Chem. A, vol. 3, no. 42, pp. 21140– 21148, 2015.
64. A. Piovano, A. Perrichon, M. Bohem, M. Johnson, W. Paulus, Positional Recurrence Maps: a powerful tool to decorrelate static and dynamical disorder in distribution maps from molecular dynamics simulations, PCCP, The Royal Society of Chemistry, 2013.
65. V.V. Vashook, H. Ullmann, O.P. Olshevskaya, V.P. Kulik, V.E. Lukashevich, L.V. Kokhanovskij, Composition and electrical conductivity of some cobaltates of the type $La_{2-x}Sr_xCoO_{4-\delta}$, T. Nakamura, K. Yashiro, K. Sato, J. Mizusaki, Oxygen nonstoichiometry and defect equilibrium in $La_{2-x}Sr_xNiO_{4+\delta}$. Solid State Ion. 2009, 180, 368–376.
66. Vashook, V.V.; Trofimenko, N.E.; Ullmann, H.; Makhnach, L.V. Oxygen nonstoichiometry and some transport properties of $LaSrNiO_{4-\delta}$ nickelate. Solid State Ion. 2000, 131, 329–336.
67. Opila, E.J.; Tuller, H.L.; Wuensch, B.J.; Maier, J. Oxygen tracer diffusion in $La_{2-x}Sr_xCuO_{4-\delta}$ single-crystals. J. Am. Ceram. Soc. 1993, 76, 2363–2369.
68. Mazo, G.N.; Savvin, S.N. The molecular dynamics study of oxygen mobility in $La_{2-x}Sr_xCuO_{4-\delta}$. Solid State Ion. 2004, 175, 371–374.

69. Tealdi. C, Ferrara. C, Mustarelli. P, Islam. M.S, Vacancy and interstitial oxide ion migration in heavily doped $La_{2-x}Sr_xCoO_{4\pm\delta}$. J. Mater. Chem. 2012, 22, 8969–8975
70. Xuefeng Zhu, Weishen Yang, Mixed Conducting Ceramic Membranes Fundamentals, Materials and Applications, Springer, ISSN 2196-6990.
71. Yashima M, Crystal structures, structural disorders and diffusion paths of ionic conductors from diffraction experiments. Solid State Ionics 179:797–803, 2008.
72. Nakayama M, Martin M, First-principles study on defect chemistry and migration of oxide ions in ceria doped with rare-earth cations. Phys Chem Chem Phys 11:3241–3249, 2009.
73. W. Paulus, A. Cousson, G. Dhalenne, J. Berthonc, A. Revcolevschi, S. Hosoyad, W. Treutmann, G. Heger, R. Le Toquin, Neutron diffraction studies of stoichiometric and oxygen intercalated La_2NiO_4 single crystals, Solid State Sciences 4 (2002) 565–573.
74. O. Wahyudi, M. Ceretti, I. Weill, A. Cousson, F. Weill, M. Meven, M. Guerre, A. Villesuzanne, J.-M. Bassat and W. Paulus, CrystEngComm, 17, 6278-6285 (2015).

Chapter 2.

Fascinating world of Oxygen, Charge and Spin Ordering Phenomena in Strongly Correlated Layered TMOs

The most complicated physical phenomena so far has been studied widely in complex transition metal oxides (CTMO) is high-Tc superconductivity, colossal magnetoresistance (CMR), multiferroics, metal-insulator transition and so many which have attracted much more attention over last quarter century in condensed matter science as they exhibits strong electronic correlations. Besides, charge-spin and orbital ordering from such electronic correlations became a fascinating subject to study now days. The electron correlation in the system cannot be explained with help of one-electron model based on atomic theories in solid state physics where two basic things are important to know, 1st, what are the building blocks and how are they arranged in the material i.e. the crystal structure and related symmetry? 2nd, how do these building blocks move inside the structure and what are their internal degrees of freedom? The most important species in solids is electron which is characterized by its negative charge (e-), spin moment ($S = \pm½$) and orbital symmetry and many investigation on CTMO shows the strong electron-electron and electron-lattice interactions usually lead to a novel quantum collective behaviours in multiple length and time scales, such as the periodical modulation of antiferromagnetic spins, charges modulation, e.g. stripe-like order in cuprates and nickelates , the CE-ordered phase in manganites, and the checkerboard-like charge order in the half-doped compounds and so on. It is fundamental to understand the interplay between lattice, spin, and charge degrees of freedom which gives a deeper vision to such novel functionality and physical properties that makes the correlated oxides a good candidate for devices applications. Ideal single-layered perovskite with K_2NiF_4-type structure mostly $La_2MO_{4+\delta}$ (M = Co, Ni, Cu) oxides goes through several phase transition from HTT→LTO→LTLO→LTT depending on the MO_6 octahedral tilting [1] related to bond-length mismatch arise from deferent radii of the cations. Antiferromagnetically ordered spin on a square type lattice of La_2NiO_4 and La_2CoO_4 can

be explained by Ising type anisotropy model through finite temperature while that order in the 2D-Heisenberg model system e.g. La_2CuO_4 is stabilized through a finite interlayer coupling. The suppression of such long range antiferromagnetic order has been studied extensively in Nickelates by substituting an earth-alkaline ions on *A* sites so called hole doping in the A_2BX_4 structure or equivalently introducing excess interstitial oxygen removes that removes electrons from valence band and reduce the bond-length mismatch. In this fashion charge carriers (*e*-/holes) are induced with different proportion as a modulated charge density wave that give rise to so-called stripes like pattern in the diffraction, meanwhile spin moments are ordered antiferromagnetically across a stripe border. There are lot of theoretical as well experimental works have been carried out in order to understand this enduring physical phenomena and it was found that depending on the hole concentrations, system exhibits different kind of charge order pattern from glassy phase to stripe to checkerboard associated with spin and orbital ordering. Besides, excess oxygen in the single-layered perovskite structure has a great influence on the structural, magnetic, and transport properties of the system, since the mobile hole concentration is varied and oxygen ions perturb the local crystal structure. Mobile oxygen can get ordered in layers for a critical value of δ and gives complex ordering of oxygen superstructure reflections even at room temperature.

In this chapter we will draw an overview from several works already has been reported on the novel complex phenomena (charge, spin, orbital and oxygen ordering) along with electronic phase separation in layered complex transition metal oxides (CTMOs). This won't be a balanced review as there would be much many to cover, we will focus on specially hole doped nickelates and cuprates relying on experiments as those two question mentioned in the begin can be readily answered by doing modern scattering experiments like neutron and synchrotron x-ray scattering also using transmission electron microscopy.

2.1 Physical Interactions in Strongly Correlated Electron Systems

2.1.1 Hubbard Model

Fundamental to the major problem of high-Tc superconductivity in hole doped cuprates is correlation between antiferromagnetic spin that involves strong coulomb interaction and the kinetic energy of the charge carrier. Story began in 1986 with the discovery of high-Tc superconductivity in La-Ba-Cu-O system by Bendorz and Muller [2] after the theoretical proposal of bipolarons in conducting polymers [3], hoping that polaronic centers (Jahn-Teller-active sites) might pair between themselves and give rise to superconductivity. Any investigations of correlated electron physics in a microscopic level needs model of many-body problem with extreme complexity. Various theoretical models were formed to solve this kind of physical problem and among them Hubbard model has been widely used to describe strong electronic interactions within a simple picture.

In the review of Strongly correlated electronic materials by Dagotto [4] it has been explained that two fundamental parameters that control the correlations between electrons are, the tunneling electron hopping amplitude t (or the one-electron bandwidth W) and the density of charge carriers (the band filling, n). Competition between the hopping amplitude t and the on-site electron–electron Coulomb repulsion energy U as a result of Mott transition (insulator–metal transition) that occurs in mostly correlated-electron systems. The electron hopping can be controlled either by the bandwidth or by the band filling where electron mobility becomes an important factor that depends on the distance and angles between neighboring atoms and the hole or electron doping levels. The Hubbard model can therefore qualitatively explain and predict theoretically the metal-to-insulator transition in some perovskites. The system exhibits several changes from static order to dynamical order in spin and charge depending on the parameter U and t. As it is schematically shown in Fig. 2.1(left) that at higher limit of U/t where every electron localizes on an atomic site when the number of electrons precisely equals the number of atomic sites and the ground state is insulator and the transition from insulator to the metallic state take place at a critical value of $(U/t)_c$ upon decreasing U/t. The tolerance factor (t) measure of $GdFeO_3$-type distortion in perovskite give rises to bond-angle distortion and that decreases the one-electron bandwidth (W) as function of radii of RE atoms

in Perovskite. For example, in the insulator-metal transition in (Pr,Nd)NiO_3 [5], with a maximum tolerance factor ($f \approx 0.96$) close to unity limit of charge transfer gap, is a paramagnetic metal with one conduction d electron per Ni atom, whereas other $RENiO_3$ materials with smaller f values shows antiferromagnetic insulating ground states and undergo a thermally induced insulator–metal transition (IMT).

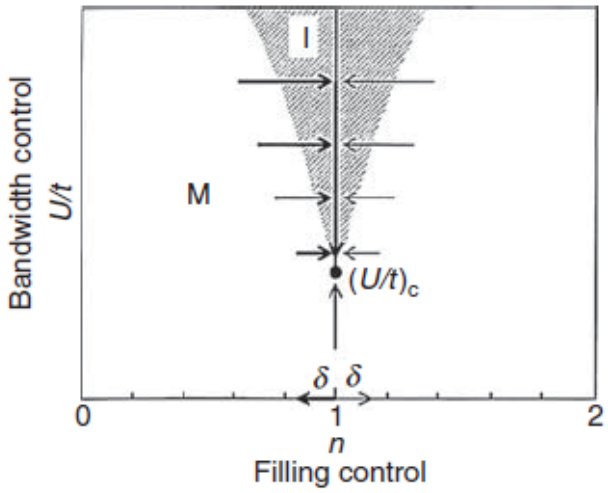

Figure 2.1: Insulator –metal transitions in correlated-electron system controlled by the bandwidth W (or equivalently by the hopping amplitude t) or the band filling n (doping x). U is the on-site Coulomb repulsion interaction, and (U/t)c represents the critical value at which the transition occurs. Note: $\delta = 1-n$ for $n<1$; $\delta = n-1$ for $n>1$. Reproduced from Fig. 1 of Dagotto et al [4].

Similarly, other way to control the electron correlation is band filling (n) or doping charge carrier (density $x = 1\text{-}n$) observed in Ruddlesden-Popper phase e.g., $La_{2-x}(Ba,Sr)_xCuO_4$ oxides where valance state of Cu^{2+} becomes $Cu^{(2+x)+}$ after Sr-dope and a small amount of hole doping give rise to superconducting state. The later on investigation of superconductivity in layered $La_{2-x}Ba_xCuO_4$ [6] compound by the same group of Bendorz and Muller confirms the actual superconducting phase dominated by built in broken symmetry in CuO_2 layers separated by La_2O_2 spacer layer, exactly like perovskite $LaCuO_3$ where Cu^{2+} with one hole in any of the two e_g orbitals lowering the energy by structural distortion so called jahn-Teller effect which breaks the degeneracy of the ϵ_g orbitals. Anderson [7] et al. pictured out that the parent compound La_2CuO_4 is an antiferromagnetic Mott insulator explained by superexchange interaction between Cu magnetic moments, which can be understood in the frame of Hubbard model.

2.1.2. Jahn-Teller (JT) Effect

The JT effect can be observed through Kramer's ions with an even number of electrons in the unfilled outermost *3d-, 4d- or 5d-* shell following the Kramer's degeneracy theorem. Along with cubic crystal filed splitting, Jahn-Teller effect causes another kind of splitting of e_g orbitals because of the lattice distortion, orthorhombic distortions due to the different ion sizes e.g. in manganites, if the crystal field symmetry is so high in the ground state of Mn^{3+} ions then it will be energetically favorable to lift the orbital degeneracy by distorting the structure. The electronic instability of Mn^{3+} ions in asymmetric MnO_6 octahedra which share same oxygen ion with neighbor octahedra, the JT distortion could be cooperative and as result of MnO_6 octahedra rotation leads to a change in lattice symmetry. On the other hand $Mn4^+$ does not show any JT distortion because the e_g states are not occupied by electrons but when Mn^{4+} is replaced by Mn^{3+} there is a possibility for that e_g electron to hop from one site to neighbor site and it takes the JT distortion with itself, this kind of combination of electron hopping and distortion is called polaron.

2.1.3 Super Exchange in Hubbard frame

Coming back to the previous example of La_2CuO_4 where Anderson et al. suggest it is a antiferromagnetic and Mott insulator, considering Cu^{2+} with one electron in eg shell. After Tranquada et el. the crystal structure of La_2CuO_4 [8] in Fig. 2.2 (left) shows CuO_2 layers are stacked in a sequence and the antiferromagnetic spins are pointing along b-axis in orthorhombic cell. As mentioned before two parameters bandwidth correspond to electron hopping amplitudes t that reduce its kinetic energy and other is Coulomb Interaction energy U between two electrons. Now In Hubbard model says if the energy U is higher than one electron band width W then every electron localizes on an atomic site even though it is localized it tries to reduce its energy further by hopping to the nearest neighbor sites with antiparallel spin obeying Pauli's exclusion principle. In that way the calculated superexchange energy between two electrons with antiparallel spin is $J = 4t^2/U$ shown in Fig. 2.2 (right).

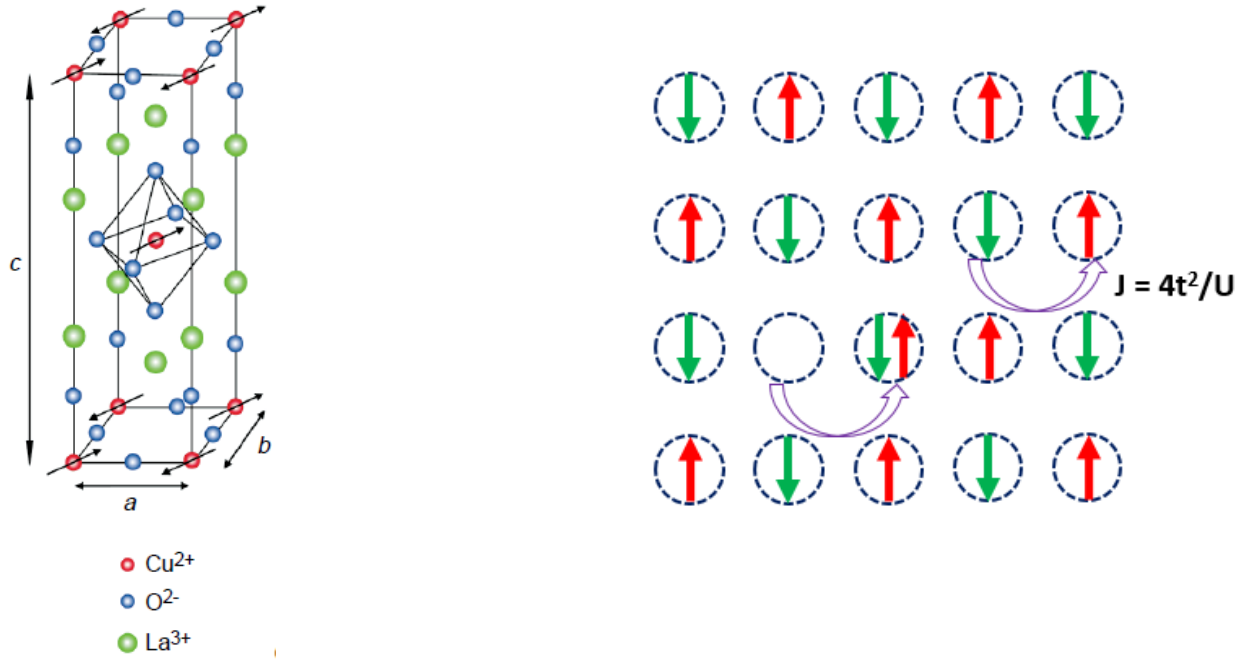

Figure 2.2: (Left) The tetragonal unit cell of $La_2CuO_{4+\delta}$. Arrows indicate the orientation of magnetic moments in the antiferromagnetic phase. The lattice parameters shown correspond to the low-temperature orthorhombic (LTO) crystal structure, reprinted from Fig. 2. of Wells et al [91]. (Right) Animation of Superexchange and Hubbard Model.

2.2 Complex Ordering and Electronic Phase Separation

So far it is found that in Mott insulator, all the d-electrons are localized on their atomic sites that activates the spin and orbital degrees of freedom simultaneously and the combination of these D.O.F give rises versatile spin-orbital ordering pattern e.g. in $LaMnO_3$, such linear combination of e_g orbitals generates other orbital state which gives a lattice strain compressing the *c*-axis as results the magnetic spins are coupled in FM fashion on *ab* plane, whereas they are coupled AFM way along *c*-axis [10]. In other word the JT effect couples the magnetic, electron orbital and lattice degrees of freedom playing a significant roles in the electronic properties of manganites, e.g. spin and orbital ordering, magnetism, electronic phase separation and CMR effect. The spatial correlations of charge and spin in single-layered perovskites will be of particular importance for the discussion of static spin correlations in electron, hole-doped as well as pure oxygen doped $RE_{2-x}AE_xMO_{4+\delta}$ oxides. With the strong electronic correlation effect, electrons that localize on specific atomic sites in CTMOs frequently shows cooperative electronic ordering phenomena, i.e. charge

order, orbital order and spin order. These novel quantum collective behaviors are believed to play an important role in controlling these fascinating physical properties.

2.2.1 Combined Picture of Ordering Phenomena

Doping holes or electrons or inserting excess oxygen in compounds induces mixed valance state from integer valance-state of most transition metal ions like Cu, Ni, Mn and Fe and these mixed valance-state appears as a periodic array under certain condition even though the compound remains electrically insulating or marginally metallic over a broad range of band fillings. This periodic arrangements of charge carriers is called charge ordering that gives different kind of patterns such as stripes and checker board for half-doped compounds. Another example of ordering phenomena is orbital ordering where due to the 3d-orbital degeneracy the population of such occupied orbitals in transition metal ions gives a long range order pattern known as orbital order which has an indirect consequences of JT effects. In addition CE-type ordering also has been reported in half-doped manganites [9,10] where orbital and charge order are simultaneously present, e.g. in $Pr_{0.5}Ca_{0.5}MnO_3$ magnetic spin are coupled antiferromagnetically in *a*-*b* plane together with charge/orbital pattern in same plane. Beside these charge/orbital ordering the long range spin order appears as a result of coupling between spin, charge, lattice and orbital D.O.F. Complete different but another related ordering co-exist along with those electronic or magnetic ordering that is oxygen ordering when the excess oxygen are interacted in the structure, and get ordered under certain conditions. In a 1st step, oxygen doping destroy the crystal structure locally keeping the average structure same.

A complex phase diagram of Sr- and oxygen co-doped La_2NiO_4 oxides has been shown in Hucker et. al. [11] where in the range of $0.02 \leq x \leq 0.06$ Sr-doped phases are similar to the pure phase with miscibility gap for pure $La_2NiO_{4+\delta}$ (see Fig. 2.3). It has been obserbed in many Nickelates and cobaltates that oxygen doping suppress the long-range antiferromagntic spin order and induce a new stripe charge order [12, 13]. Such charge, spin and orbital ordering in some transition-metal (M) oxides $(RE,AE)_2MO_4$, with the K_2NiF_4-type structure has been illustrated in Fig.2.4 reprinted from Ulbrich et. al. [14]. Hole doping in the nickelates [15-17] e.g. in parent Mott

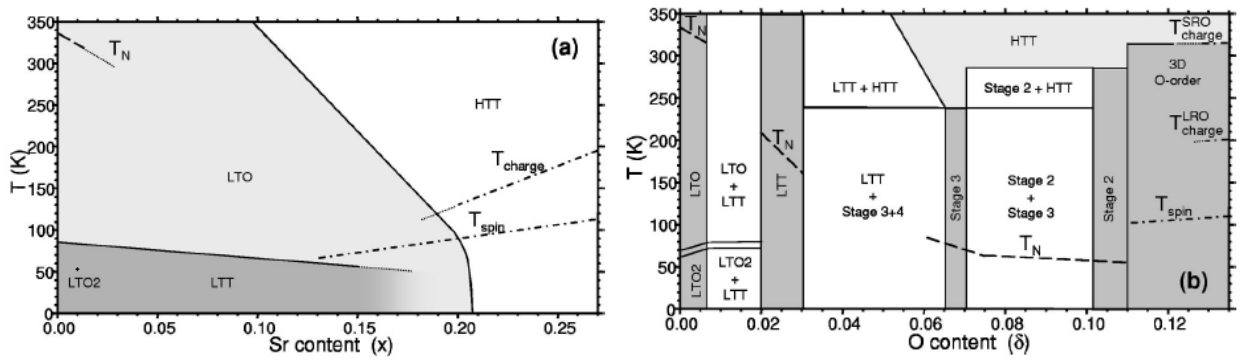

Figure 2.3: Schematic phase diagram of (a) $La_{2-x}Sr_xNiO_4$ and (b) $La_2NiO_{4+\delta}$. The dotted lines in both diagrams indicate unknown phase boundaries. SRO and LRO are standing for short- and long-range order, respectively. Reproduced from Fig. 1. of Hücker et al [11] where original references can be found.

insulator La_2NiO_4 forms a charge (hole) and spin stripe pattern running parallel to the diagonal direction of the NiO4 squares "*diagonal stripe*" (see Fig 2.4c). These stripes could be commensurate or incommensurate depending on the hole concentration and the in plane length of that stripe given by d-spacing of the corresponding plane. Whereas, a similar hole stripe but not diagonal also exists in highly doped cuprates e.g. $La_{2-x}Sr_xCuO_4$ [18-20] running along the [1 0 0] or [0 1 0] direction "*vertical or horizontal stripe*" (see Fig 2.4 b). even for low doped cuprates shows diagonal stripes [21-23]. In the lower panels of Fig. 2.4 illustrate the predicted position of that charge and spin order superstructure reflections in tetragonal unit cell where for nickelates the charge order peaks appears at *(ϵ, ϵ, l)* whereas for spin order it is *(1/2.ϵ, 0, l)*, (where, incommensurability are related with hole concentration as $\epsilon = x + 2\delta$, will be discussed in more details in the following section about its importance) these theoretical schemes are well explained in several literatures. It has been reported in case of stripe ordering seen in nickelates that stripes acts as a separator or a domain wall in the antiferromagnetic region where antiferromagnetic spins are ordered between such two charge stripes and that is the reason why the magnetic modulation length is always double of that charge one and we get $\epsilon_s = ½\ \epsilon_{ch}$ like the situation of spin - charge - density wave found in Cr where structural modulations are coupled half periods of magnetic spins that arising from magnetostriction. In the similar fashion using the model of charge and spin-density wave, interplay between charge

and spin order in transition metal oxides can be understood. Another complex ordering takes place in the half doped (x=1/2) manganites e.g. $La_{0.5}Ca_{0.5}MnO_3$ as a consequence of the close interplay among the spin of both Mn^{4+} and Mn^{3+}, charge, orbital, and lattice degrees of freedom, as shown in Figure 2.4d. According to Goodenough model [24], Mn^{4+} (with three t_{2g} electrons) and Mn^{3+} (with one e_g electron) should coexist and give rise the checkerboard type pattern accompanied with orbital ordering of Mn^{3+}. This is the case where all the above electronic interaction are present simultaneously like the spin ordering pattern is the compromise between the antiferromagnetic superexchange interaction among the t2g local spins and the ferromagnetic doubleexchange interaction mediated by the eg electron which is strongly JT active hopping between the Mn^{3+} and Mn^{4+} sites. The orbital ordering regulates the anisotropic e_g electron hopping, and hence, the Mn^{4+} sites adjacent to the lobe of the e_g orbital on the nearest Mn^{3+} site is linked through a ferromagnetic interaction and a ferromagnetic zigzag chains that are antiferromagnetically stacked, appear along the diagonal direction. The insulating behavior of non-cuprates compound makes itself different from other cuprates in stripe phases as consequence of electron-lattice interactions whereas all the observed ordering phenomena must be considered as real interaction or electronic correlation not just a hazards or exception in CTMOs.

Several studies mostly on nickelates [25-28] have confirmed that intercalation of excess oxygen induces the cooperative MO_6 octahedral tilting and also compare to AE ion substitution oxygen are mobile and get ordered under certain conditions and that ordering appears as superstructure reflections on the diffraction pattern in addition to Bragg reflections that can be seen by electron microscopy, neutron or x-ray scattering experiments.. This oxygen doping also limited to the RE doping e.g. in $La_2NiO_{4+\delta}$ [29] the maximum of the excess oxygen content decreases with increasing Sr-dpoing up to x=1/3. Also oxygen doping in parent La_2CuO_4 induces superconductivity through lattice instability and phase separation as it was found in $La_{2-x}Ba_xCuO_4$ (with $x = 0.15$) [2]. Undoped La_2CuO_4 is semiconductor but upon doping oxygen (δ=0.06) or Ba (x=0.15) up to certain concentration superconductivity appears and the volume fraction of the superconducting phase start to decrease with increasing doping concentration by competing with antiferromagnetic ordering on Cu sites [30]. Tranquada et. al. [26] confirmed different one-dimensional staging ordering of excess

oxygen layers through temperature dependent phase separation in oxygen excess $La_2NiO_{4+\delta}$ ($0.05 \leq \delta \leq 0.11$) compounds just like staging of intercalates in graphite.

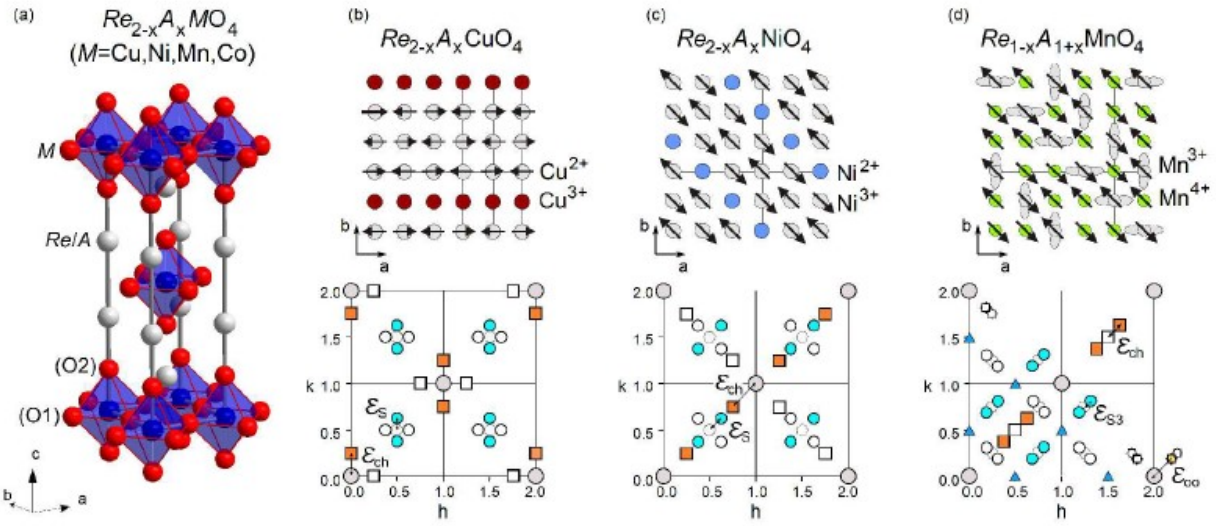

Figure 2.4: (a) Crystal structure of $Re_{2-x}A_xMO_4$ with Re= La or a rare earth, A = Sr or Ca. (Upper panels) Schematic ordering of charges, magnetic moments and orbitals proposed for cuprates (b), nickelates (c) and manganites (d). In cuprates and nickelates regions of nn antiferromagnetism are separated by the charged stripes which act as domain walls. (Lower panels) Predicted charge and spin order position in reciprocal space for the purely two-dimensional ordering as upper panels. For cuprates and nickelates charge and magnetic modulation yield corresponding scattering at satellites displaced from the original Bragg positions by ϵ_{ch} and ϵ_{sc}, respectively. In the stripe ordering in layered manganites (c) charges, orbital and magnetic moments give rise to four different types of super-structure scattering associated with charge, orbital, Mn^{3+}- and Mn^{4+} spin moment ordering. Reproduced from Fig. 1. of ref. Ulbrich et al. [14].

2.2.2 Electronic inhomogeneity and Phase Separation in Correlated Oxides

By the introduction of long range coulomb interactions make the phase separation frustrated and as a results a modulated CDW or superconducting phase appears. Phase separation with the model of holes in AFM domain is reflections of the e- attempt to minimize their zero-point kinetic energy. Phase separation is the simplest solution of frustrated situation where AFM ordering and allowing itineracy for holes away from ½-filling band they try to maintain simultaneously and these two requirements contradict each other. In the case of mobile dopant on laboratory timescale we know that there exist a miscibility gap at small doping concentration where long range coulomb

interaction does not forbid it. Another case in which the distribution of dopant atoms are quenched where the long range coulomb interactions forbid the holes to get phase separated and as a result charge-spin density inhomogeneity occurs. We will go through several reviews on such phase separation in the following.

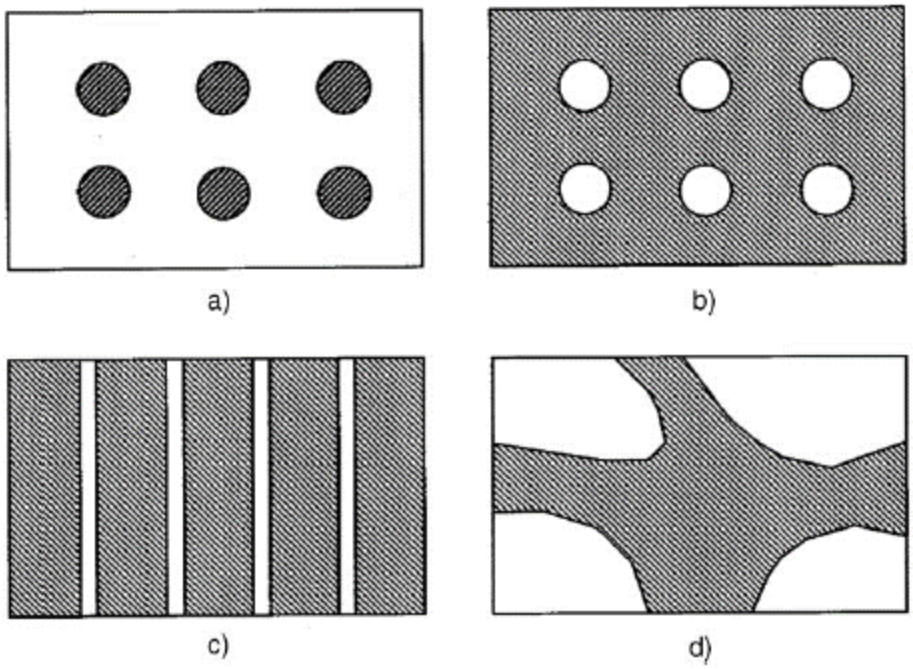

Figure 2.5: Schematic of electronic phase separation. Shaded portions indicate FM metallic regions; the unshaded portions correspond to AFM insulating regions. a) FM metallic puddles in an insulating AFM background. b) Metallic regions with insulating droplets. c) Charged stripes. d) Phase separation on the mesoscopic scale. Taken from Fig 1. of ref. [32].

There are lot of works have been carried out which show that many pure single crystal of TMOs with general formula $Ln_{2-x}Sr_xMO_{4+\delta}$ exhibit inhomogeneous electronic phase separation with length scale varying from nanometer to micrometer where different electronic and magnetic phase coexist [4,31,32]. This finding of inhomogeneity and electronic phase separation was started to answer the questions regarding colossal magnetoresistance effect in manganites and colossal effects in high-Tc superconducting cuprates. Fig. 2.5 shows a schematic of different kind of electronic phase separation could take place in TMOs [32]. This phase separation has been widely discussed in manganites just after Koehler et al. [33] which reports that FM metallic regions are embedded in insulating AFM background. Another work established the phase diagram of $Nd_{0.5}Sr_{0.5}MnO_3$ where three phases

FM, AFM (A-type) and AFM (CE-type) are coexist [34]. The volume fraction of such electronic inhomogeneity depends on external responses like applied magnetic or electric field and can be probed by X-ray and neutron diffraction as well as by studying magnetization and transport measurements. Detecting length scale of inhomogeneity is a crucial point as it is depends on the probing method. Renner et al. [35] they found the nanoscopic electronic inhomogeneity in $Bi_{1-x}Ca_xMnO_3$ by STM where the charge ordered phase are correlated with structural one along with metallic domain. The nanoscopic inhomogeneity was also found in 2D thin film of $La_{1-x}Ca_xMnO_3$ by Mori group [36] where the $Mn^{3+}O_6$ octahedra separated by stripe of $Mn^{4+}O_6$ octahedra. Other mesoscopic electronic phase separation was detected via TEM by Uehara group [37] in $(La,Pr,Ca)MnO_3$ system where the phase separation is between x=1/2-type CO insulating and FM metallic domains with typical size 0.5 micron relevant to CMR. This was kind of new phase separation which is not due to charge segregation. All these example point towards the CMR in manganites because of such electronic nano-mesoscopic inhomogeneity.

A complete and complex structural, electronic and magnetic phase diagram of strongly correlated bilayer manganites has been shown in Fig. 2.6D after Dagotto et al. [4]. There are other TMOs e.g. high-T_c cuprate where it has been found that the competition between two ordered phases in presence of quenched disorder can be applied where the electronic phase separation is due to variation of superconducting cluster and AFM cluster with presence of charge stripes and spatially inhomogeneous superconducting gap [38-40]. Fig. 2.6 A-C shows several inhomogeneous phases in HTSC from perfect stripe to randomly distributed nanoscale region of d-wave SC gap and checkerboard-type charge order phase in Na-doped cuprates. Also in most of cobaltates memberes were known to be FM metallic but later it was proven later that FM order was not so long indeed it shows magnetic spin glassy feature and they are electronically and magnetically phase separated [41-43]. The modulated structure in oxygen doped nickelates e.g. La_2NiO_{4+d} is an example of showing frustrated and fluctuating phase separation is driven by the dynamics of the doped holes. It has similar structure as La_2CuO_{4+d} where pure undoped La_2NiO_4 is an AFM insulator, does not show any superconductivity with hole doping. The phase diagram of La_2NiO_{4+d} is wonderfully complex as

it shows oxygen staging, stripe phases and modulated magnetic ordering, reported elsewhere, the phase separation is limited by the oxygen diffusion and competition between strain energy and ordered CDW state [45,17]. Basic difference between nickelates and cuprates is Ni is spin one and Cu is spin half, in nickelates the order is more static than superconductivity because of kinetic effect of spin fluctuations for the spin one system. For this reason $La_2NiO_{4+\delta}$ gives a direct and independent evidence of phase separation of holes in an AFM. Other strong evidence of such electronic phase separation in Sr-doped La_2NiO_4 is large colossal dielectric constant where it has direct consequences of electronic phase separation, namely a stripe ordering of holes [46].

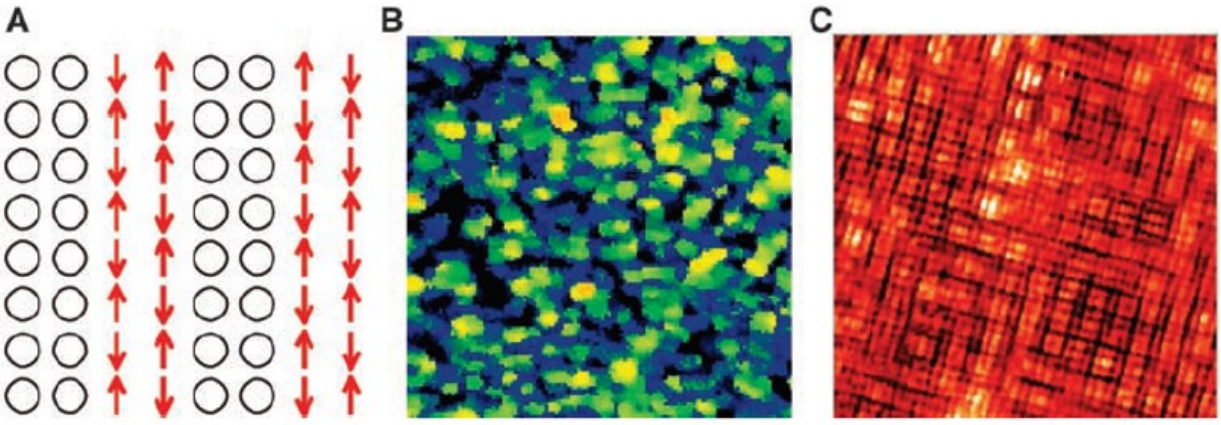

Figure 2.6: Various inhomogeneous states in HTSC materials. (A) Schematic representation of perfect stripes (circles are holes; arrows, spins). (B) d-wave SC gap real space distribution obtained by using STM techniques. Inhomogeneities at the nanoscale are observed (patches). The entire frame is 560 A° by 560 A° . (C) Recently unveiled charge-order state (checkerboard) in Na-doped cuprates. Reproduced from Fig. 3 of Dagotto et al. [32] Original ref can be found there.

(D). Structural and magnetic phase diagram of the bilayer manganite $La_{2-2x}Sr_{1+2x}Mn_2O_7$ in the range $0.3 \leq x \leq 1.0$ determined by neutron powder diffraction. Solid markers represent the magnetic transition temperature (T_C or T_N); open squares delineate the tetragonal to orthorhombic transition. Several magnetic phases are identified: ferromagnetic metal (FM), canted antiferromagnet (CAF), and A-, C-, and G-type antiferromagnetic insulators (AFI). The region marked "No LRO" has no magnetic diffraction peaks at T > 5 K. Samples in the region marked "CO" exhibit long-range charge ordering reflections in X-ray and/or electron diffraction. A temperature range schematically indicated by the yellow square shows how this long-range charge-ordered state grows then disappears at low temperature [46]. Reprinted from Fig. 1A of ref. [32].

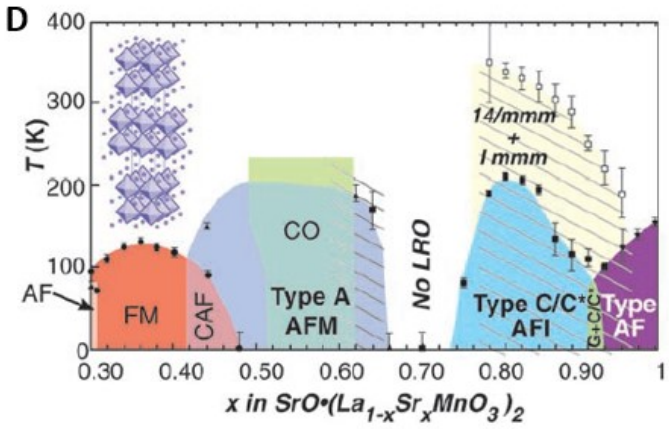

The nonlinear interaction between charge, spin orbital degrees of freedom in strongly correlated TMOs leads to a complex phase diagram where some might have stripes, checkerboard, CDW-SDW state, other might have nano to mesoscopic phase separation all are simultaneously activated and important in condensed matter physics.

2.3 Stripe to Checkerboard and other competing states in TMOs

The long range antiferromagnetic order in high-T_c superconductor completely brakes down with even small amount of hole doping into the system, has been studied considering *3d* charge fluctuations [47]. Introducing holes in CuO_2 planes of La_2CuO_4 reduce the Cu spins and decrease the frustrated long-range AFM order an order of magnitude compare to magnetic lattice dilution [48]. As a results charged magnetic domain wall formed explaining the incommensurate spin phase. This kind of interesting complex ordering pattern along with other crystalline order in TMOs system comes from long-range interaction between kinetic energy of holes with antiferromagnetic order as a results stripes form. Recently, using lattice gas model and numerical simulation Rademaker et al. [49] has identified several interesting phases from generalized Wigner crystal (at very low particle density ρ) to stripe order (ρ = 1/3 and ½) depending on the influence of long-range interactions on a square lattice. Fig 2.7(left) shows the zero temperature phase diagram obtained using Monte Carlo simulation with model considering classical particles interaction on a lattice and extended version of that phase diagram at finite temperature using mean field approximations in Fig 2.7(right) reprinted from Rademaker et al. [49]. They considered 2D-lattice gas model in their calculation where long-range interaction was isotropic for a fixed particle density, however this restrict to half filled, empty and full lattices. At ρ =1/9 the ordering state is generalized Wigner crystal phase followed by at ρ = 1/6 is characterized as a glassy phase. The phase with particle density higher than ρ =1/4 is called "*checkerboard-in-a-checkerboard*"phase. At half filling the ground state is perfect checkerboard type and in limit less than half filling one can obtain stripe pattern by introducing domain wall and according to Hubbard et al. [50] then the system would exhibit specific stripe patterns like Hubbard patterns for fixed ρ=1/3, ρ=2/5 and doped stripe pattern for ρ = 3/7.

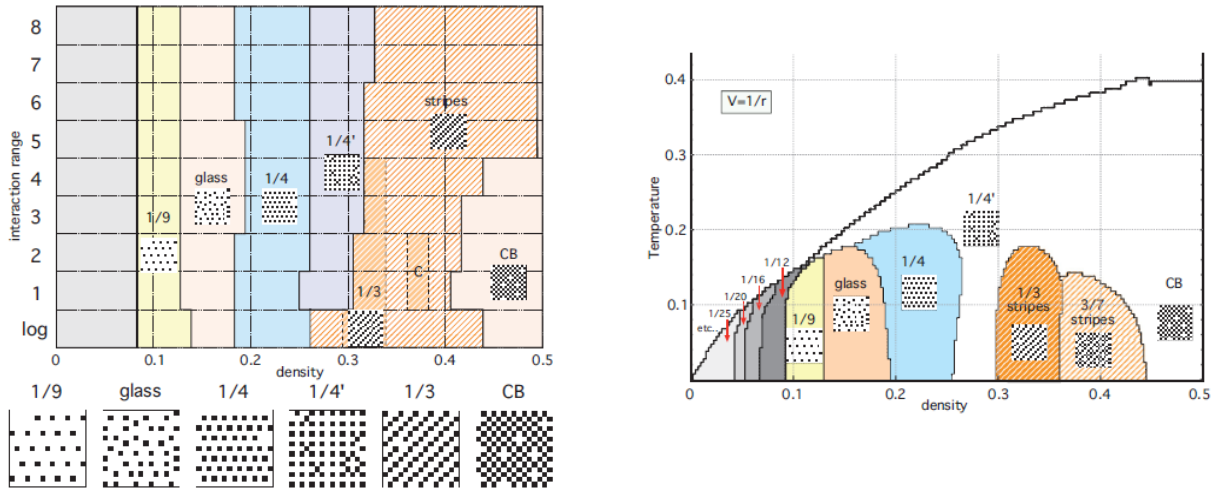

Figure 2.7: (Left) the approximate ground state phase diagram of the long-range lattice gas model on a square lattice, based on variational methods. On the vertical axis the type p of the long-range interaction V (r) is given, together with a logarithmic decaying interaction. The horizontal axis represents the particle density. From low to high densities it has been identified the following phases: The area without name depicts the dilute generalized Wigner crystal, followed by the 1/9 Wigner crystal, the 1/6 glassy phase. The 1/4 Wigner crystal, the "checkerboard-in-a-checkerboard" 1/4′ phase, stripe phases (with a plateau for the 1/3 stripe phase and "C" denotes the channeled stripes as described and finally the checkerboard phase. (Right) Mean field finite temperature phase diagram of the lattice gas model on a square lattice with V ~ 1/r interactions. Temperature is in units of the nearest-neighbor interaction. The phases are the same as in the zero temperature phase diagram of left figure. At low densities various Wigner crystalline phases has been found with densities of the form $1/pq$ with p,q integers. Close to half-filling it is checkerboard order which has a smooth crossover to the "checkerboard-in-acheckerboard" 1/4′ phase. Around n = 1/3 and 3/7 there are stripe ordered phases. The transitions towards the 1/4′ and checkerboard phase are second order, the other transitions are first order. Picture taken from Fig.1. of Rademaker et al. [49] where original refs. can be found related to the calculations.

However, this theoretical work carried out without considering any anisotropy and other complex interactions but it describes well and shows similar picture obtained from several experimental work stating that introducing domain wall causes the formation of stripes and others ordered states. All the calculation including 1-band, 2-band and 3-band Hubbard model [51-53] leads to analysis of motion of hole in AFM background with nearest neighbor hoping creates FM correlation but there is possibility that outcomes might differ in real system with more of degrees of freedom. Zaanen [47] first showed inhomogeneity in hole doped cuprate by using 3-band Hubbard calculation where they found that AFM phase was shifted by 180^0 crossing the charge stripe border

destroying the AFM long range order, however, the periodic modulation of that charge stripe leads to incommensurate spin order even though the incommensurability was smaller than experimental one [54]. The difference came from the hole density per Cu atoms along stripe, in the former it was one per Cu-site whereas in later case it was one half per Cu-site. What the important point here is doping hole leads to phase separate give rise to spin and charge inhomogeneity and also considering strong coulomb interactions frustrate the phase separation tends to form stripe and checkerboard type order.

2.3.1 Charge and Spin Order in $Ln_{2-x}Sr_xNiO_{4+\delta}$ (*Ln = La, Pr, Nd*)

The undoped parent stoichiometric compound of this family La_2MO_4 (M=Ni, Co, Cu) are insulator where the magnetic spins are antifeeromagnetically coupled in MO_2 plane via nearest neighbor exchange coupling $J_{nn.}$ Even though the single layer magnetic structure are identical but there exist a difference in the direction of the magnetic spin moment, while the spins in La_2NiO_4, La_2CoO_4 point towards [1 -1 0] direction (tilt axis of the MO_6 octahedra in orthorhombic unit cell), they align along [1 1 0] direction in La_2CuO_4 and this allow for small out of plane canting due to Dzyaloshinski-Moria interaction [55-58]. This antiferromagnetic coupling is therefore reduced by hole doping through a decrease of the average exchange parameter via the introduction of M^{3+} ions into the ideal AF M^{2+} order into the parent Ln_2MO_4 system. Depending on the electronic configuration of different transition metal ions in octahedral crystal field (HS or LS) the observed electronic phenomena may vary system to system. Simultaneous oxygen, hole and spin ordering was first observed using neutron diffraction in $La_2NiO_{4.125}$ single crystal by Tranquada group [17]. Even though nickelates are not superconductor but it is interesting to study why the insulating characteristic is contradictory with band theory. Pure undoped La_2NiO_4 is antiferromagnetic $T_N \sim$ 650K with ordered moment 1.6 μ_B [59], doping with Sr (at the cost of disordered dopant potential) or excess oxygen (certain concentration leads to long range stripe ordered state) in NiO_2 plane gradually reduce the Neél temperature T_N. and it can be induced the metallic behavior with higher doping concentration. Controlling oxygen stoichiometry during crystal growth is very difficult since it accommodates extra oxygen easily affecting the reliability of the absolute value of the total charge

concentration, $n_h = x + 2\delta$ in $La_{2-x}Sr_xNiO_{4+\delta}$ [46]. Before understand in better way we need to know about the phase diagram of $Ln_{2-x}Sr_xNiO_{4+\delta}$ as function of doping concentration. Fig. 2.8 Shows the phase diagram of $Ln_{2-x}Sr_xNiO_{4+\delta}$ (Ln = Pr, Nd, La) which is well established by several work [29, 60] where pure La_2NiO_4 ($x = 0$) exhibits a structural phase transition from the high-temperature tetragonal (HTT) phase to a low-temperature orthorhombic (LTO) phase [61] at T_{LTO} ~781 K due to higher bond-length mismatch the transition [62]. A second structural phase transition occurs into a low-temperature tetragonal (LTT) phase take place at 70K [63]. The LTO and LTT phases are both characterized by tilting of the NiO6 octahedra but the tilt axes differ right side of the Fig. 6 HTT phase is only undistorted one whereas in the LTO phase the tilt axis is along the diagonals of the NiO_2 square plane and the octahedra tilt around an axis parallel to the Ni-O bond in the LTT phase. Structural distortion is suppressed by the Sr doping [62, 11] due to the bond-length mismatch coming from large ionic radius of Sr and the oxidation of Ni similar and the reason why HTT/LTO phase boundary shifted to higher x and T for Pr and Nd compare to La.

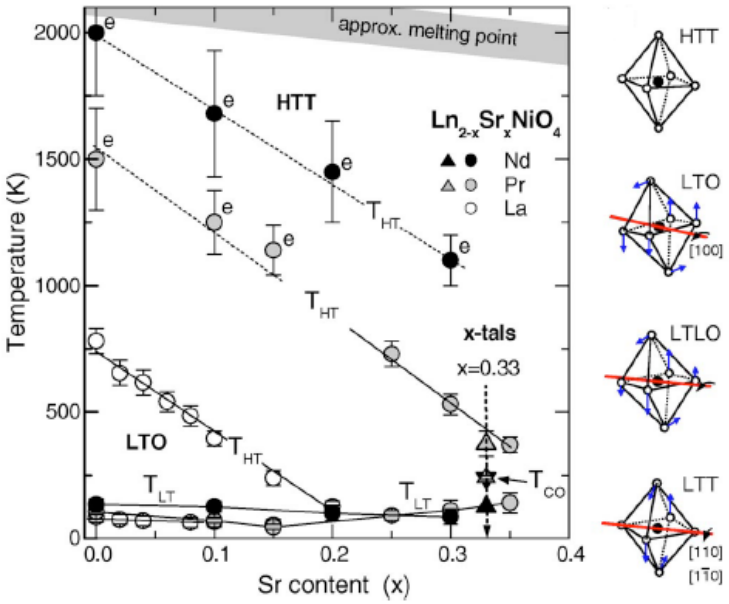

Figure 2.8: Phase diagram of $Ln_{2-x}Sr_xNiO_4$ with *Ln*=La, Pr, and Nd as obtained from x-ray powder diffraction on polycrystalline specimens. For Pr and Nd the HTT/LTO phase boundary is shifted to higher x and T with respect to La. Data points marked with an "*e*" are linear extrapolations of measurements up to 800 K. (right) Tilt directions of the NiO_6 octahedra in the different structural phases. Reproduced from Fig. 1. of ref. [1].

Sr-doped (with x = 0.2) La_2NiO_4 is the compound where an incommensurate magnetic correlation was detected 1st time by elastic neutron-scattering study by Hyden group [64]. For large amount of an oxygen-doped $La_2NiO_{4.125}$ sample, Yamada et al. [65] also find incommensurate magnetic phase where extra oxygen are responsible for higher observed T_N values that means oxygen doping amplify the interlayer magnetic coupling which might be related to superexchange path along [0 0 1] direction which is not present in case of Sr-doped case for 3D magnetic ordering. Normally the excess oxygen at certain concentration in $La_2NiO_{4+\delta}$ gets ordered and superimpose a variety of complex superstructure reflections on the reflections coming from the charge and spin stripe ordering [26, 66, 67]. Sachen et al. [61] find incommensurate peaks from short range magnetic and charge ordering at low temperature in an oxygen-stoichiometric sample with $x = 0.135$ and 0.2 where the incommensurability is quite different from the expected one $\epsilon = 0.12$ and 0.25 for both Sr concentration respectively while the magnetic correlation length increases with Sr-doping. Another interesting feature was found by Hayden et al. [64] that spin incommensurability $\epsilon_s \sim 0.08$ whereas for charge $\epsilon_{ch} \sim 0.16$ slightly below the expected value for a crystal with the same Sr content (x=0.2) but less oxygen. It is clear from these two measurements that the fluctuation in incommensurability arising from the oxygen concentration in these $La_{2-x}Sr_xNiO_{4+\delta}$ materials with the stripe order of charges and spins associated with structural distortion [61]. Turning to oxygen-doped samples, Fig. 2.3 shows the phase diagram worked out experimentally for $La_2NiO_{4+\delta}$ [26]. The intermediate phases involve stage-ordering of oxygen, as indicated in Fig. 2.9. Within this region, commensurate AF order is observed, but with a depressed T_N. Doping beyond stage-2 leads to a phase with 3D interstitial order as well as 3D ordering of charge and spin stripes. Another analysis of the structure indicates that it corresponds to an ideal oxygen excess of $\delta = 1.33$ [68].

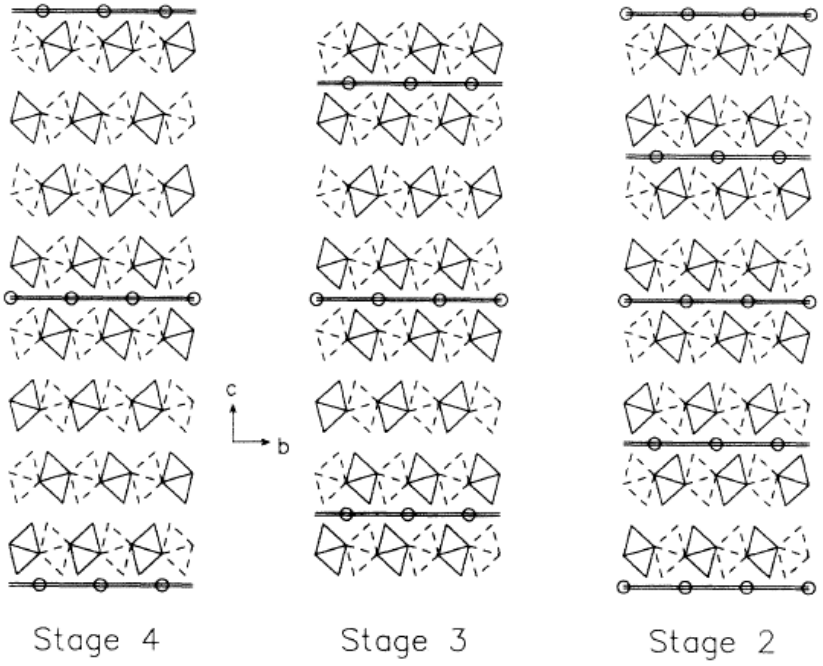

Figure 2.9: Schematic representation of stage ordering of excess oxygen in $La_2NiO_{4+\delta}$ intercalated between tilted NiO_6 octahedral layers. Reproduced from Fig. 2 of ref. [26].

Incommensurability ϵ in the oxygen doped sample of $La_2NiO_{4.133}$ [68] shows temperature dependency and exhibits different values such as 5/17, 2/7, and 5/18. To describe these various periodicities, one can consider a mixture of both Ni-centered and O-centered stripes. We denote the order along the in-plane direction, perpendicular to the stripes, with $\downarrow$ ($\uparrow$) indicating a Ni spin, $\bullet$ indicating an O site, and $\circ$ indicating a hole (i.e., the center of a charge stripe). For $\epsilon = 1/4$, which would be characteristic of the low-temperature case with Ni-centered stripes, the configuration looks like Fig. 2.10a, where we indicate below the configuration that the net moments of neighboring spin stripes are antiferromagnetically correlated. For $\epsilon = 2/7$, we get equal numbers of Ni-centered and O-centered stripes as in Fig. 2.10b At high temperature, $\epsilon = 1/3$ has only O-centered stripes like Fig. 2.10c.

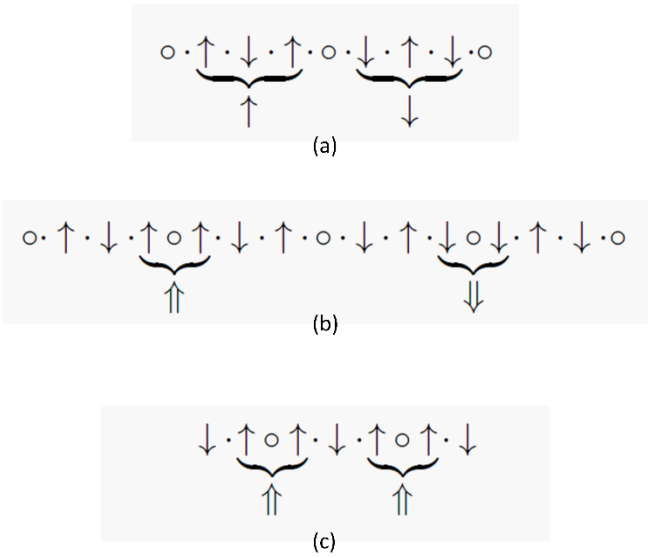

Figure 2.10: Cartoon representation of different (a) Ni- (b) combination of Ni- and O- and (c) O- centered stripes in $La_2NiO_{4.133}$ depending on Temperature. Picture taken from ref. [68].

Systematic studies on the stripe order in $La_{2-x}Sr_xNiO_{4+\delta}$ by elastic, inelastic neutron [78-80] and x-ray [72–76] scattering method show doping dependencies of the charge and spin transition temperatures of the incommensurabilities and of the inverse correlation lengths which have been shown in Fig. 2.11 and Fig. 2.12, respectively. All these experimental findings point out the stability of the stripe phase at $x = 1/3$. From the figure it is clear that particularly at this concentration $x = 1/3$ the magnetic and charge ordering transition are the highest and the correlation lengths are the longest and also the T_{CO} is always higher than T_{SO}. For $x = 1/2$, a checkerboard pattern of charge order develops at quite high temperature. The magnetic structure of the $x = 1/3$ stripe phase is commensurate and quite simple as the magnetic cell comprises only two antiparallel magnetic moments, see Fig. 2.13 (middle). The charge and spin stripes that develop in LSNO run diagonally with respect to the square lattice of Ni atoms in the NiO_2 planes. Fig. 2.13 shows the schematic of different stripe and checker board type order has been depicted for various doping concentration where it can be noticed that the magnetic unit cell is double than charge order

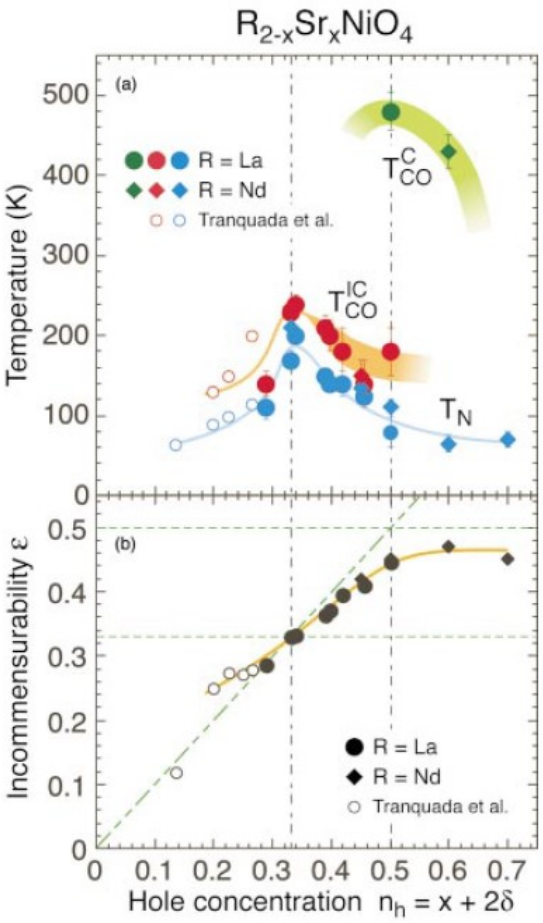

Figure 2.11: Phase diagram of $Re_{2-x}Sr_xNiO_4$: (a) Hole concentration dependence of the transition temperatures, $T_{CO}(IC)$, $T_{CO}(C)$ and T_N. (b) Hole concentration dependence of the incommensurability ϵ. Circles denote the data for $La_{2-x}Sr_xNiO_4$, while diamonds are for $Nd_{2-x}Sr_xNiO_4$. Picture taken from Fig 4 of ref. [71].

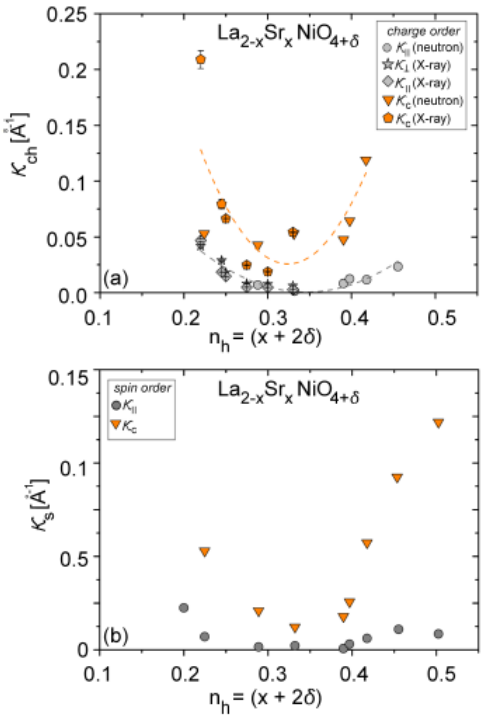

Figure 2.12: (above) the inverse charge-correlation lengths and (below) the inverse magnetic correlation lengths are given as function of hole concentration. Reproduced from ref. [14] where original refs. can be found.

unit cell and that is why we the wave vector of spin order is half of charge one. Most of doped LSNO system shows average structure as tetragonal but it is easier to characterize the stripe wave vectors in orthorhombic unit cell. With this choice, the 3D charge and spin wave vectors are $\boldsymbol{Q}_{co} = (2\epsilon, 0, 1)$ and $\boldsymbol{Q}_{so} = (1\pm\epsilon, 0, 0)$ are obtained [77, 78] where the coordinates are in reciprocal lattice units $(2\pi/a; 2\pi/b; 2\pi/c)$; there is also a stripe twin domain rotated by 90^0 in the NiO_2 plane. For the fundamental Bragg peaks, $\boldsymbol{G} = (H, K, L)$ the indices must be all even or all odd. So the allowed

superlattice peaks in the *(H, K, 0)* reciprocal plane are $\boldsymbol{G' \pm Qco} = (2m+1\pm2\epsilon,\ 2n+1,\ 0)$ and $\boldsymbol{G \pm Qso} = (2m+1\pm\epsilon,\ 2n,\ 0)$ where **G'** and **G** follow all odd and all even indices respectively. In this way it can be calculated the predicted spin and charge order superstructure reflections with any given ϵ where $\epsilon = x + 2\delta$. *Fig. 2.14 shows such calculated pattern with* $\epsilon = 0.333$ (for perfect stripe phase) and 0.46 for (checkerboard type phase). This has been found that for x=1/2 doping ϵ is not exactly 0.5 rather slightly less [79]. Evidence for significant charge modulation has also been provided by nuclear magnetic resonance studies [80, 81]. The magnetic incommensurability ϵ, is inversely proportional to the period of the magnetic modulation. It increases steadily with doping, as shown in Fig. 2.11b, staying close to the line $\epsilon = n_h$, indicating that the hole-density within the charge stripes remains roughly constant but the stripe spacing decreases with doping.

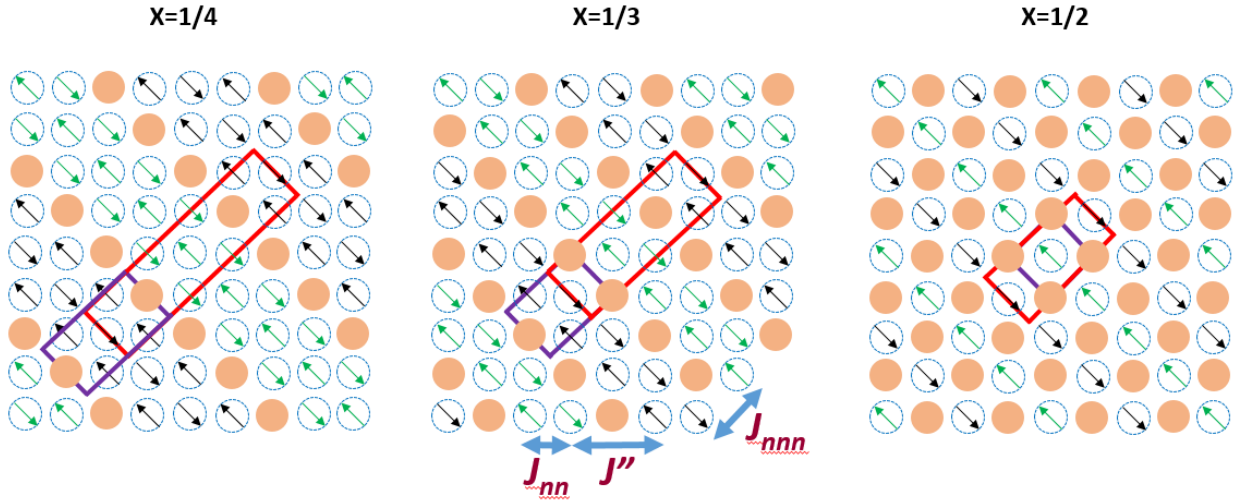

Figure 2.13: Model for the stripe and checkerboard order in NiO_2 planes for different hole density *x* (0.25, 0.33 and 0.5). Arrows indicates the S = 1 spins of Ni^{2+} sites, closed circle represents S = ½ for Ni^{3+} holes. Oxygen sites are not shown. Black and green arrows indicates that across the stripe domain spin direction change. Red rectangular box represents the magnetic superstructure unit cell, which is double the size of unit cell corresponding charge order (purple rectangle). In the middle pannel magnetic intrastripe J_{nn} (inside the stripe domain) and interstripe J_{nnn}, *J"* (across the stripe) exchange interactions between nearest and next nearest neighbor Ni^{2+} spins are depicted.

For x<0.33, ϵ_{ch} is slightly larger than x the doping suggests and 1/3 < x <1/2, ϵ_{ch} is slightly higher than x as can be seen from the Fig. 2.11b. If the hole density in the charge stripes is a constant like 1 hole per Ni sites, then there are more holes in the charge stripe region for x<1/3 than are doped into the material and to increase the hole density to level above that caused by doping electrons must have to be promoted to the conduction band so that additional holes are are

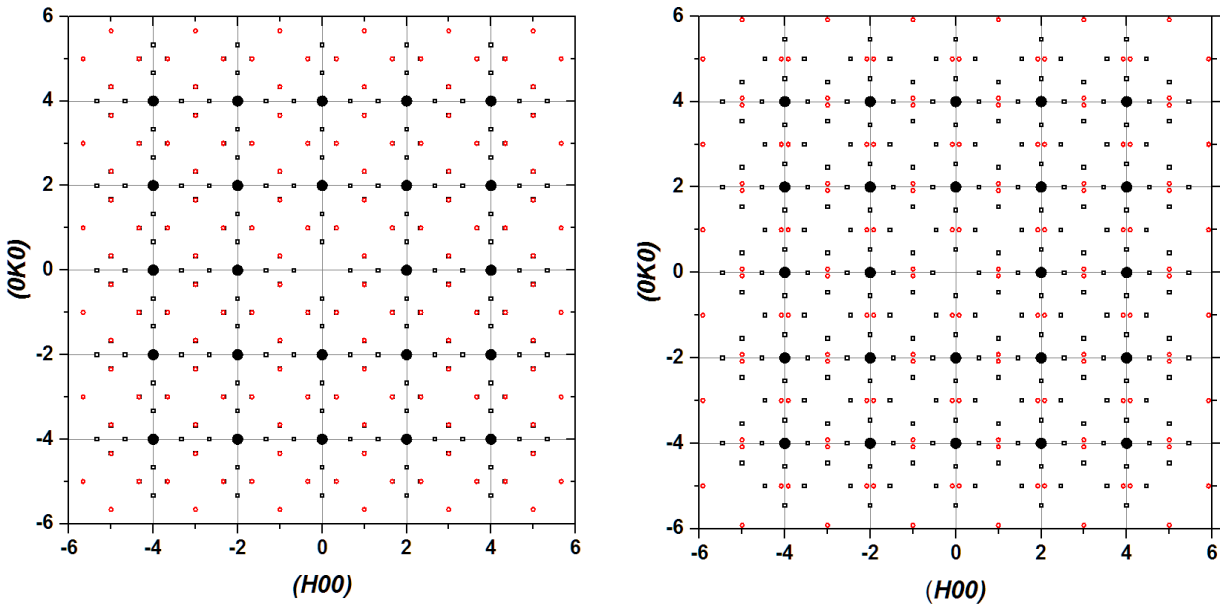

Figure 2.14: Schematic representation of calculated positions of charge (red circle) and spin (black square) order peaks along with fundamental Bragg peaks (filled black circle) in the *(HK0)* reciprocal plane in *F*-centered cell (*F4/mmm*) of $La_{2-x}Sr_xNiO_4$ for $x = 0.33$ (left) and $x = 0.5$ (right). For $x = 0.33$ spin and charge order peaks they overlap exactly because of the incommensurability ϵ.

produced therefore the free e^- are charge carrier. In other words for $x>1/3$ from doping there is an excess of holes for producing charge stripes with 1 hole per Ni sites and then holes would be the free charge carriers. This behavior points to an electronic self-doping of the charge stripes. The impact of hole-doping on the magnetic interactions has been determined from measurements of the spin-wave dispersions for crystals with $x \approx 1/3$ [82-84]. Analysis shows that the superexchange J within an antiferromagnetic region is 27.5(4) meV [85], which is only a modest reduction compared to $J =$ 31(1) meV in undoped La_2NiO_4 [86]. The effective coupling across a charge stripe is found to be $\approx$ $0.5J$, a surprisingly large value. In the spin-wave modelling, it was assumed that there is no magnetic contribution from the charge stripes; however, it is not obvious that this is a correct assumption. Combining an S = 1/2 hole with an S = 1 Ni ion should leave at least an S = 1/2 per Ni site in a domain wall. Recently, Boothroyd *et al.* [86] have discovered quasi-1D magnetic scattering that disperses up to about 10 meV and becomes very weak above 100 K. This appears to correspond to the spin excitations of the charge stripes. Inelastic neutron scattering measurements at $T > Tco$

indicate that incommensurate spin fluctuations survive in the disordered state [87, 82], implying the existence of fluctuating stripes. One might ask whether it is possible to distinguish experimentally between a model in which stripes locally run in only one direction, and one in which there is a superposition of stripes in orthogonal directions. To make this distinction, one needs a sample in which the two diagonal directions in the NiO_2 planes are inequivalent. This can be achieved by studying $Nd_{2-x}Sr_xNiO_4$, which has the same low-temperature orthorhombic structure as La_2CuO_4, with inequivalent lattice parameters along the diagonals. A careful x-ray diffraction study by Hücker et al. [1] on crystals with $x = 0{:}33$ demonstrated that the charge stripes run uniquely along the shorter a-axis.

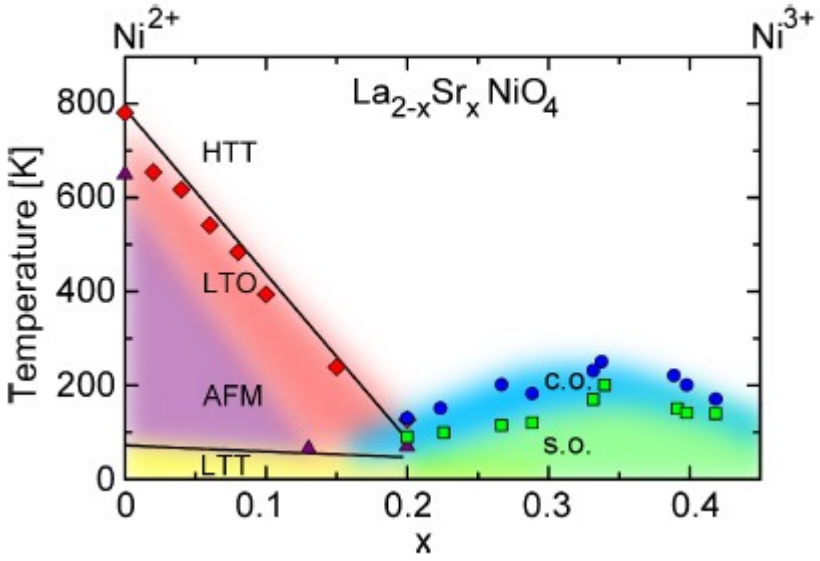

Figure 2.15: Phase diagram of $La_{2-x}Sr_xNiO_4$ concerning the structural distortion (red diamond and line), the suppression of commensurate antiferromagnetism (magenta triangles) and the appearance of the stripe phase with charge (blue) and magnetic (green) transitions. The LTT or LTLO phase is indicated in yellow. Reproduced from ref. [14] where original refs. can be found.

By recent TEM studies on $Re_{1.67}A_{0.33}NiO_4$ with Re a rare-earth element and A = Ca or Sr [1,88,89] it has been found that stripe order was stable because of the smaller ionic radius of the rare earth which stabilizes the structural tilt distortion which pins the direction of the stripes along the direction of the octahedral tilt axis. It was also found in the same work that due to the variation of of the ionic radii at the Re site in $Re_{1.67}A_{0.33}NiO_4$ reduces the correlation lengths and for $Pr_{1.67}Ca_{0.33}NiO_4$ [89] it was the longest one. From this scenario author concluded that in $La_{2-x}Sr_xNiO_4$ stripe order can coexist with the tilt distortions.

As a summary the schematic electronic phase diagram of $La_{2-x}Sr_xNiO_4$ has been shown in Fig. 2.15; the doping suppresses both the structural distortion and the commensurate *nn* antiferromagnetic order giving rise to the charge and spin stripe ordering. The crossover from the commensurate *nn* antiferromagnetism to the stripe order occurs near $x \sim 0.2$ close to the full suppression of the structural distortion, but there is overlap of the octahedron tilt distortion and the stripe phases [61]. The point here is that a nickelates system homologous to the other cobaltates, cuprates family shows a strong tendency for charge and spin to be ordered in a way that preserves the strong superexchange interaction of the undoped parent compound. It is somehow true that Ni^{2+} has S = 1 while Cu^{2+} has S = 1/2 , and this can have a significant impact on the strength of the charge localization in the vicinity of stripe ordered state of nickelates [90]. Anyway, the size of the spin cannot explain why the conventional band theory does not hold for the nickelates. The electronic inhomogeneity observed in the nickelates suggests that similarly unusual behavior might be expected also in cuprates.

References:

1. M. Hücker, M. v. Zimmermann, R. Klingeler, S. Kiele, J. Geck, S. N. Bakehe, J. Z. Zhang, J. P. Hill, A. Revcolevschi, D. J. Buttrey, B. Büchner, and J. M. Tranquada, Unidirectional diagonal order and three-dimensional stacking of charge stripes in orthorhombic $Pr_{1.67}Sr_{0.33}NiO_4$ and $Nd_{1.67}Sr_{0.33}NiO_4$, Phys. Rev. B 74, 085112 (2006).
2. J.G. Bednorz and K.A. Müller, Possible High T_c Superconductivity in the Ba- La- Cu- 0 System, Z. Phys. B - Condensed Matter 64, 189-193 (1986).
3. J.L. Bredas and G.B. Street, Polarons, Bipolarons, and Solitons in Conducting Polymers, Acc. Chem. Res. 1985, 18, 309-315.
4. E. Dagotto, Y. Tokura, Strongly correlated electronic materials: Presents and future, MRS Bulletin, Vol. 33 (2008).
5. J.B. Torrance, P. Lacorre, A.I. Nazzal, E.J. Ansaldo, Ch. Niedermayer, Systematic study of insulator-metal transitions in perovskites $RNiO_3$ (R =Pr, Nd, Sm, Eu) due to closing of charge-transfer gap, Phys. Rev. B 45, 8209 (1992).
6. J. G. Bednorz, and K. A. Müller, Perovskite-type oxides the new approach to high-T, superconductivity, Rev. Mod. Phys. 60, 585–600 (1988).
7. P. W. Anderson, The resonating Valence Bond State in La_2CuO_4 and superconductivity, Science 235, 1196 (1987).
8. J. M. Tranquada, D. E. Cox, W. Kunnmann, H. Moudden, G. Shirane, M. Suenaga, P. Zolliker, D. Vaknin, S. K. Sinha, M. S. Alvarez, A.J. Jacobson, D.C Johnston, Neutron diffraction determination of antiferromagnetic structure of Cu ions in $YBa_2Cu_3O_{6+x}$ with x = 0 and 0.15, Phys. Rev. Lett. 60, 156 (1988).
9. Y. Tokura and N. Nagaosa, Orbital physics in TMOs, Science 288, 462 (2000).
10. M. v. Zimmermann, J. P. Hill, Doon. Gibbs, M. Blume, D. Casa, B. Keimer, Y. Murakami, Y. Tomioka, and Y. Tokura, Interplay between charge, orbital and magnetic order in $Pr_{1-x}Ca_xMnO_3$, Phys. Rev. Lett. 83, 4872 (1999).
11. M. Hücker, K. Chung, M. Chand, T. Vogt, J. M. Tranquada, and D. J. Buttrey, Oxygen and strontium codoping of La_2NiO_4: Room-temperature phase diagrams, Phys. Rev. B 70, 064105 (2004).
12. P. Gopalan, M. W. McElfresh, Z. Kakol, J. Spalek, and J. M. Honig, Influence of oxygen stoichiometry on the antiferromagnetic ordering of single crystals of $La_2NiO_{4+\delta}$, Phys. Rev. B 45, 249 (1992).
13. T. Freltoft, D. J. Buttrey, G. Aeppli, D. Vaknin, and G. Shirane, Magnetic correlations and their dependence on excess oxygen in La_2CoO_4, Phys. Rev. B 44, 5046 (1991).
14. H. Ulbrich, M. Braden, Neutron scattering studies on stripe phases in non-cuprate materials, Physica C 481 (2012) 31-45.
15. C.H. Chen, S.-W. Cheong, A.S. Cooper, Charge modulations in $La_{2-x}Sr_xNiO_{4+y}$: ordering of polarons, Phys. Rev. Lett. 71, 2461 (1993).
16. J. M. Tranquada, P. Wochner, and D. J. Buttrey, Spin dynamics in an ordered stripe phase, Phys. Rev. Lett, 79 2133 (1997).

17. J.M. Tranquada, D.J. Buttrey, V. Sachan, and J.E. Lorenzo, Simultaneous Ordering of Holes and Spins in $La_2NiO_{4.125}$, Phys. Rev. Lett, 73 1003 (1994).
18. J.M. Tranquada, B.J. Sternlieb, J.D. Axe, Y. Nakamura, S. Uchida, Evidence for stripe correlations of spins and holes in copper oxides superconductors, Nature 375, 561 (1995).
19. S.A. Kivelson, E. Fradkin, V.J. Emery, Electronic liquid-crystal phases of a doped Mott insulator, Nature 393, 550 (1998).
20. J. M. Tranquada, Neutron Scattering studies of Antiferromagnetic correlation in cuprates, arXiv:cond-mat/0512115v1.
21. S. Wakimoto, G. Shirane, Y. Endoh, K. Hirota, S. Ueki, K. Yamada, R. J. Birgeneau, M. A. Kastner, Y. S. Lee, P. M. Gehring and S. H. Lee,Phys. Observation of incommensurate magnetic correlations at the lower critical concentration for superconductivity in $La_{2-x}Sr_xCuO_4$ (x = 0.05), Rev. B 60, R769 (1999).
22. M. Matsuda, M. Fujita, K. Yamada, R. J. Birgeneau, Y. Endoh and G. Shirane, Magnetic field effect and magnetic anisotropy in lightly doped $La_{2-x}Sr_xCuO_4$, Phys. Rev. B 66, 174508 (2002).
23. M. Matsuda, Y. S. Lee, M. Greven, M. A. Kastner, R. J. Birgeneau, K. Yamada, Y. Endoh, P. Boni, S.-H. Lee, S. Wakimoto and G. Shirane, Anomalous broadening of the spin-flop transition in the reentrant spin-glass phase of $La_{2-x}Sr_xCuO_4$ (x = 0.018), Phys. Rev. B 61, 4326 (2000).
24. J. B. Goodenough, Theory of the role of covalence in the perovskite-type manganites [La, M(II)] MnO_3, Phys. Rev. 100, 564 (1955).
25. J. Rodríguez-Carvajal, M. T. Fernández-Díaz, and J. L. Martínez, Neutron Diffraction study on structural and magnetic properties of La_2NiO_4, J. Phys.: Condens. Matter 3, 3215 (1991). 16, 21, 42, 46, 94, 119.
26. J. M. Tranquada, Y. Kong, J. E. Lorenzo, D. J. Buttrey, D. E. Rice, and V. Sachan, Oxygen intercalation, stage ordering, and phase separation in $La_2NiO_{4+\delta}$ with $0.05 \leq \delta \leq 0.11$, Phys. Rev. B 50, 6340 (1994).
27. W. Paulus, A. Cousson, G. Dhalenne, J. Berthon, A. Revcolevschi, S. Hosoya, W. Treutmann, G. Heger, and R. Le Toquin, Neutron diffraction studies of stoichiometric and oxygen intercalated La_2NiO_4 single crystals, Sol. State Sciences 4, 565 (2002).
28. J. E. Lorenzo, J. M. Tranquada, D. J. Buttrey, and V. Sachan, Neutron-diffraction studies on the time dependence of the oxygen ordering in $La_2NiO_{4.105}$, Phys. Rev. B 51, 3176 (1995). 21
29. O. Friedt, Präparation, Charakterisierung und Struktur von $La_{2-x}Sr_xNiO_{4+\delta}$, Diplomarbeit, Universität zu Köln, (1998).
30. J. D. Jorgensen, B. Dabrowski, Shiyou Pei, D. G. Hinks, and L. Soderholm, Superconducting phase of $La_2CuO_{4+\delta}$: A superconducting composition resulting from phase separation, Phys Rev. B 38 (1988).
31. C. N. R. Rao, Asish K. Kundu, Md. Motin Seikh and L. Sudheendra, Electronic phase separation in transition metal oxide systems, RSC. Dalton trans. 3003-3011 (2004).

32. Vijay B. Shenoy, D. D. Sarma, and C. N. R. Rao, Electronic Phase Separation in Correlated Oxides: The Phenomenon,Its Present Status and Future Prospects, ChemPhysChem 2006, 7, 2053-2059.
33. E. O. Wollan and W. C. Koehler Neutron Diffraction Study of the Magnetic Properties of the Series of Perovskite-Type Compounds [(1−x)La, xCa]MnO_3, Phys. Rev. 1955,100, 545.
34. **P. M. Woodward, D. E. Cox, T. Vogt, C. N. R. Rao, A. K. Cheetham, Effect of Compositional Fluctuations on the Phase Transitions in ($Nd_{1/2}Sr_{1/2}$)MnO_3 Chem. Mater. 1999, 11, 3528.**
35. C. Renner, G. Aeppli, B. G. Kim, Y.-A. Soh, S.-W. Cheong, Atomic-scale images of charge ordering in a mixed-valence maganite, Nature 2002,416, 518.
36. S. Mori, C. H. Chen, S.-W. Cheong, Pairing of charge-ordered stripes in (la, Ca)MnO_3, Nature 1998, 392, 473.
37. M. Uehara, S. Mori, C. H. Chen, S. W. Cheong, Percolative phase separation underlies colossal magnetoresistance in mixed-valent manganites, Nature 1999, 399, 560.
38. Phase Separation in Cuprate Superconductors (Eds.: E. Sigmund, K. A. MVller), Springer, Heidelberg, 1994.
39. J. M. Tranquada, H. Woo, T. G. Perring, H. Goka, G. D. Gu, G. Xu, M. Fujita, K. Yamada, Quantum magnetic excitations from stripes in copper oxides superconductors, Nature 2004, 429, 534.
40. K. McElroy, J. Lee, J. A. Slezak, D.-H. Lee, H. Eisaki, S. Uchida, J. Davis, Atomic -scale sources and mechanism of nanoscale electronic disorder in $Ba_2Sr_2CaCu_2O_{8+\delta}$, Science 2005, 309, 1048.
41. C. N. R. Rao, O. Parkash, D. Bahadur, P. Ganguly, S. Nagabhushana, Itinerant electron ferromagnetism in Sr^{2+}, Ca^{2+} and Ba^{2+} doped rare earth orthocobaltites ($ln^{3+}_{1-x}M^{2+}_xCoO_3$), J. Solid State Chem. 1977, 22, 353.
42. M. A. SeÇaris RodrUıguez, J. B. Goodenough, Magnetic and transport properties of the system $La_{1-x}Sr_xCoO_{3-\delta}$ ($0 \leq \delta \leq 0.5$), J. Solid State Chem. 1995, 118, 323.
43. J. Wu, J. W. Lynn, C. J. Glinka, J. Burley, H. Zheng, J. F. Mitchell, C. Leighton, Intergranular giant magnetoresistance in a spontaneously phase separated perovskite oxides, Phys. Rev. Lett. 2005, 94, 037201.
44. J. F. Mitchell , D. N. Argyriou , A. Berger , K. E. Gray , R. Osborn , and U. Welp, Spin, Charge, and Lattice States in Layered Magnetoresistive Oxides, J. Phys. Chem. B 105, 10731 (2001).
45. J. M. Tranquada, D. J. Buttrey, and D. E. Rice, Phase separation, charge-density waves, and magnetism in $La_2NiO_{4+\delta}$, Phys. Rev. Lett. 70, 445 (1993).
46. P. Lunkenheimer,a, S. Krohns, S. Riegg, S.G. Ebbinghaus, A. Reller, and A. Loidl, Colossal dielectric constants in transition-metal oxides, Eur. Phys. J. Special Topics 180, 61–89 (2010)
47. J. Zaanen and O. Gunnarsson, Charged magnetic domain lines and the magnetism of high-*Tc* oxides, Phys. Rev. B 40, 7391 (1989).

48. O. P. Vajk, P. K. Mang, M. Greven, P. M. Gehring, and J. W. Lynn, Quantum impurities in the two-dimensional spin one-half Heisenberg antiferromagnet, Science 295, 1691 (2002).
49. Louk Rademaker, Yohanes Pramudya, Jan Zaanen, and Vladimir Dobrosavljevi´, Influence of long-range interactions on charge ordering phenomena on a square lattice, Phys. Rev. E 88, 032121 (2013).
50. J. Hubbard, Generalized Wigner lattices in one dimension and some applications to tetracyanoquinodimethane (TCNQ) salts, Phys. Rev. B 17, 494 (1978).
51. V. J. Emery, and G. Reiter, Mechanism for high-temperature superconductivity, Phys. Rev. B 38, 4547–4556 (1988).
52. M. Möller, G. A. Sawatzky, and M. Berciu, Role of the lattice structure in determining the magnon-mediated interactions between charge carriers doped into a magnetically ordered background, Phys. Rev. B 86, 075128 (2012).
53. S. A. Trugman, Interaction of holes in a Hubbard antiferromagnet and high-temperature superconductivity, Phys. Rev. B 37, 1597–1603 (1988).
54. S.-W. Cheong, G. Aeppli, T. E. Mason, H. Mook, S. M. Hayden, P. C. Canfield, Z. Fisk, K. N. Clausen, and J. L. Martinez, Incommensurate magnetic fluctuations in $La_{2-x}Sr_xCuO_4$, Phys. Rev. Lett. 67, 1791 (1991).
55. K. Yamada, M. Matsuda, Y. Endoh, B. Keimer, R. J. Birgeneau, S. Onodera, J. Mizusaki, T. Matsuura, and G. Shirane. Successive antiferromagnetic phase transitions in single-crystal La_2CoO_4. Phys. Rev. B, 39 (1989).
56. D. Vaknin, S. K. Sinha, D. E. Moncton, D. C. Johnston, J. M. Newsam, C. R. Sanya, and H. E. King. Antiferromagnetism in La_2CuO_4. Phys. Rev. Lett., 58, (1987).
57. G. Aeppli and D. J. Buttrey. Magnetic Correlations in $La_2NiO_{4+\delta}$. Phys. Rev. Lett., 61 (1988).
58. T. Thio, T.R. Thurston, N.W. Preyer, P.J. Picone, M.A. Kastner, H.P. Jenssen, D.R. Gabbe, C.Y. Chen, R.J. Birgeneau, and A. Aharony. Antisymmetric exchange and its inuence on the magnetic structure and conductivity of La_2CuO_4. Physical Review B, 38 (1988).
59. G. H. Lander, P. J. Brown, J. Spalek, and J. M. Honig, Structural and magnetization density studies of La_2NiO_4, Phys. Rev. B 40, 4463 (1989).
60. S. Bakehe, Ph. D. thesis, University of Cologne, Germany (2002).
61. V. Sachan, D. J. Buttrey, J. M. Tranquada, J. E. Lorenzo, and G. Shirane, Charge and spin ordering in $La_{2-x}Sr_xNiO_{4.0}0$ with x=0.135 and 0.20, Phys. Rev. B 51, 12742 (1995).
62. S.-H. Lee and S-W. Cheong, Melting of Quasi-Two-Dimensional Charge Stripes in $La_{5/3}Sr_{1/3}NiO_4$, Phys. Rev. Lett. 79, 2514 (1997).
63. G. H. Lander, P. J. Brown, J. Spalek, and J. M. Honig, Structural and magnetization density studies of La_2NiO_4, Phys. Rev. B 40, 4463 (1989).
64. S. M. Hayden, G. H. Lander, J. Zarestky, P. J. Brown, C. Stassis, P. Metcalf, and J. M. Honig, Incommensurate Magnetic Correlations in $La_{1.8}Sr_{0.2}NiO_4$, Phys. Rev. Lett. 68, 1061 (1992).

65. K. Yamada, T. Omata, K. Nakajima, Y. Endoh, and S. Hosoya, Incommensurate magnetic correlations in $La_2NiO_{4.125}$: Magnetic phase diagram and two-dimensional hole-order, Physica (Amsterdam) 221C, 355 (1994).
66. J. E. Lorenzo, J. M. Tranquada, D. J. Buttrey, and V. Sachan, Neutron-diffraction studies on the time dependence of the oxygen ordering in $La_2NiO_{4.105}$, Phys. Rev. B 51, 3176 (1995).
67. J. M. Tranquada, J. E. Lorenzo, D. J. Buttrey, and V. Sachan, Cooperative ordering of holes and spins in $La_2NiO_{4.125}$, Phys. Rev. B 52, 3581 (1995).
68. P. Wochner, J. M. Tranquada, D. J. Buttrey, and V. Sachan, Neutron-diffraction study of stripe order in $La_2NiO_{4+\delta}$ with δ=2/15, Phys. Rev. B 57, 1066 (1998).
69. H. Yoshizawa, T. Kakeshita, R. Kajimoto, T. Tanabe, T. Katsufuji, and Y. Tokura, Stripe order at low temperatures in $La_{2-x}Sr_xNiO_4$ with $0.289 \lesssim x \lesssim 0.5$, Phys. Rev. B 61, R854 (2000).
70. Y. Oohara, R. Kajimoto, T. Kakeshita, H. Yoshizawa, T. Tanabec, T. Katsufuji, K. Ishizaka, Y. Taguchi, Y. Tokura, Physica B 329 333, 725 (2003).
71. R. Kajimoto, K. Ishizaka, H. Yoshizawa, and Y. Tokura, Spontaneous rearrangement of the checkerboard charge order to stripe order in $La_{1.5}Sr_{0.5}NiO_4$, Phys. Rev. B 67, 014511 (2003).
72. K. Ishizaka, T. Arima, Y. Murakami, R. Kajimoto, H. Yoshizawa, N. Nagaosa, and Y. Tokura, Commensurate-Incommensurate Crossover of Charge Stripe in $La_{2-x}Sr_xNiO_4$ (x~1/3), Phys. Rev. Lett. 92, 196404 (2004).
73. P.D. Hatton, M.E. Ghazi, S.B. Wilkins, P.D. Spencer, D. Mannix, T. d'Almeida, P. Prabhakaran, A. Boothroyd, S.-W. Cheong, X-ray scattering studies of charge stripes in $La_{2-x}Sr_xNiO_4$($x = 0.20-0.33$), Physica B 318, 289 (2004).
74. P.D. Spencer, M.E. Ghazi, S.B. Wilkins, P.D. Hatton, S.D. Brown, D. Prabhakaran, and A.T. Boothroyd, Eur. Phys. J. B 46, 27 (2005).
75. C. Schüssler-Langeheine, J. Schlappa, A. Tanaka, Z. Hu, C. F. Chang, E. Schierle, M. Benomar, H. Ott, E. Weschke, G. Kaindl, O. Friedt, G. A. Sawatzky, H.-J. Lin, C. T. Chen, M. Braden and L. H. Tjeng, Spectroscopy of Stripe Order in $La_{1.8}Sr_{0.2}NiO_4$ Using Resonant Soft X-Ray Diffraction, Physical Review Letters 95, 156402 (2005).
76. J. Schlappa, C. F. Chang, E. Schierle, A. Tanaka, R. Feyerherm, Z. Hu, H. Ott, O. Friedt, E. Dudzik, H.-H. Hung, M. Benomar, M. Braden, L. H. Tjeng, and C. Schuessler-Langeheine, arXiv0903.0994.
77. Ruidan Zhong, Barry L. Winn, Genda Gu, Dmitry Reznik, and J. M. Tranquada, Evidence for a nematic phase in $La_{1.75}Sr_{0.25}NiO_4$, Phys. Rev. Lett., 118, 177601 (2017).
78. S. Anissimova , D. Parshall , G.D. Gu, K. Marty, M.D. Lumsden, Songxue Chi, J.A. Fernandez-Baca, D.L. Abernathy, D. Lamago, J.M. Tranquada & D. Reznik, Direct observation of dynamic charge stripes in $La_{2-x}SrxNiO_4$, Nature, 3467 (2014).
79. R Kajimoto, M Fujita, K Nakajima, K Ikeuchi, Y Inamura, M Nakamura and T Imasato, Inelastic neutron scattering study of phonon anomalies in $La_{1.5}Sr_{0.5}NiO_4$, Journal of Physics: Conference Series 502 (2014) 012056.
80. Y. Yoshinari, P. C. Hammel, and S.-W. Cheong, Magnetism of Stripe-Ordered $La_{5/3}Sr_{1/3}NiO_4$, Phys. Rev. Lett. 82, 3536 (1999).

81. I. M. Abu-Shiekah, O. O. Bernal, A. A. Menovsky, H. B. Brom, and J. Zaanen, Similarity of Slow Stripe Fluctuations between Sr-Doped Cuprates and Oxygen-Doped Nickelates, Phys. Rev. Lett. 83, 3309 (1999).
82. P. Bourges, Y. Sidis, M. Braden, K. Nakajima, and J. M. Tranquada, High-Energy Spin Dynamics in $La_{1.69}Sr_{0.31}NiO_4$, Phys. Rev. Lett. 90, 147202 (2003).
83. A. T. Boothroyd, D. Prabhakaran, P. G. Freeman, S. J. S. Lister, M. En- derle, A. Hiess, and J. Kulda, Spin dynamics in stripe-ordered $La_{5/3}Sr_{1/3}NiO_4$, Phys. Rev. B 67, 100407(R) (2003).
84. H. Woo, A. T. Boothroyd, K. Nakajima, T. G. Perring, C. D. Frost, P. G. Freeman, D. Prabhakaran, K. Yamada, and J. M. Tranquada, Mapping spin-wave dispersions in stripe-ordered $La_{2-x}Sr_xNiO_4$ (x=0.275, 0.333), Phys. Rev. B 72, 064437 (2005).
85. K. Yamada, M. Arai, Y. Endoh, S. Hosoya, K. Nakajima, T. Perring, and A. Taylor, Complete Two-Dimensional Antiferromagnetic Spin-Wave Dispersion Relation of La_2NiO_4 Determined by Chopper Spectrometer Installed at the Pulsed Neutron Source, J. Phys. Soc. Jpn. 60, 1197 (1991).
86. A. T. Boothroyd, P. G. Freeman, D. Prabhakaran, A. Hiess, M. Enderle, J. Kulda, and F. Altorfer, Spin Correlations among the Charge Carriers in an Ordered Stripe Phase, Phys. Rev. Lett. 91, 257201 (2003).
87. S.-H. Lee, J. M. Tranquada, K. Yamada, D. J. Buttrey, Q. Li, and S.-W. Cheong, Freezing of a Stripe Liquid, Phys. Rev. Lett. 88, 126401 (2002).
88. M. Hücker, M. v. Zimmermann, and G. D. Gu, Robust charge stripe order under high electric fields in $Nd_{1.67}Sr_{0.33}NiO_4$, Phys. Rev. B 75, 041103 (2007).
89. X. Yu, T. Arima, S. Seki, T. Asaka, K. Kimoto, Y. Tokura, and Y.Matsui, Effect of Quenched Disorder on Charge Ordering Structure in $RE_{1.67}AE_{0.33}NiO_4$ (RE = La, Pr, Nd, Sm; AE = Ca, Sr), J. of Phys. Soc. Jpn 77, 093709 (2008).
90. J. M. Tranquada, Charge stripes and antiferromagnetism in insulating nickelates and superconducting cuprates, J. Phys. Chem. Solids 59, 2150 (1998).
91. B. O. Wells, Y. S. Lee, M. A. Kastner, R. J. Christianson, R. J. Birgeneau, K. Yamada, Y. Endoh, G. Shirane, Incommensurate Spin Fluctuations in High-Transition Temperature Superconductors, SCIENCE , VOL. 277, 22 AUGUST 1997.

Chapter 3

Instrumentation and Experimental Methods

After reviewing previous two chapter it is clear that dopant homogeneity, high purity single phase and good quality single crystals of TMOs with defined oxygen non-stoichiometry are very much important to have as for studying several physical properties starting from electronic-ionic conductivity, magnetism, oxygen diffusion especially when these properties are highly anisotropic with respect to crystallographic directions and structural aspect. Besides, to investigate strong electronic correlations between Sr- and oxygen doped titled compounds it is necessary to have single crystal to perform in-situ single crystal x-ray diffraction and very big single crystal roughly ~ 4 cm in length is required for neutron elastic, inelastic scattering experiments (very weak interaction between matter and neutrons) which give information about electronic, oxygen, magnetic ordering as well as lattice and spin dynamics that can't be obtained by conventional powder diffraction from polycrystalline sample. Since defects and impurities in the sample have huge effects on such above mentioned physical properties and phenomena, one must have to carry out all the pre synthesis with carefully weighing the calculated reactants to have at least single phase and good quality single crystal. Growing high quality single crystals is very difficult and complex process as it depends on several interconnected physical parameters that needs to be optimized by performing several times to get better reproducibility and the feelings. In practice, single crystal is grown by rearranging the constituents in a regular lattice site from neighboring phase which contains those constituents in form of disordered melt or solute or even solid. The conditions for single crystal growth are assumed to be non-equlibrium even tough classical thermodynamics is concerned only with equilibrium states of systems. However it can be accepted as a thermodynamic steady-state between the fluid and the crystal as long as these transient process are slow w.r.t kinetics of atoms and if the concentration gradient is not so steep [1]. In total, crystal growth combines and involves so many different areas of knowledge and studies of phase equilibria and thermodynamics, nucleation, solute partitioning,

hydrodynamics, surface tension and fluid motion, heat and mass transfer, interface attachment kinetics, interface morphology and defect generation.

Methods to analyze the progress of a solid state reaction or the quality of as grown single crystal are also important and for that in a first shot Laue backscattering and conventional powder X-ray diffraction are useful techniques. Particularly nickelates, cobaltates and cuprates all these K_2NiF_4-type oxides are very sensitive to oxygen and in practice during crystal growth it is very difficult to control the oxygen content because of the wide range of possible oxygen uptake or release that leads to ordered superstructures of excess oxygen or vacancies and might give rise to new crystal structures forming a rich phase diagram. This oxygen uptake or release depends on reaction temperature and oxygen partial pressure in the growth chamber. Determination of the oxygen content is another big problem. From X-ray diffraction it is also difficult to determine the oxygen contents as the oxygen atoms has less number of electrons and does not contribute that much in scattering factor compare to heavy atoms presents in the investigated compound. At the same time a comparably high fraction of its electrons are located in the outer shell where the corresponding energy levels strongly depend on the chemical environment as results in enormous error for the determination with the X-ray based techniques EDX and WDX. But thanks to the thermogravometry analysis (TGA) under different atmosphere from which at least it can be concluded the relative change in mass that comes only from oxygen.

In this chapter we will focus on crystal growth by traveling solvent floating zone (TSFZ) method followed by some examples showing growth and other desired direction of the crystal obtained from Laue back scattering experiment. We will discuss the technique used to determine relative mass changes by using TGA and the experiment to study magnetic properties by SQUID interface. After that we will present in details the specially designed *quartz-capillary-gas-pressure-cell* that can sustain up to 100 bar of (P_{O2}) equipped with temperature device (max. 600^0C) and also *collinear-glass-capillary-electrochemical-cell*, both were used and well adopted to perform in-situ non ambient X-ray single crystal diffraction at BM01A, ESRF also at home laboratory.

3.1 Crystal Growth by TSFZ Method Using Image Furnace

Methods like Czochralski [2] (crystal pulling) and flux growth are even tough well know and popular techniques it doesn't fulfill all the parameters to obtain optimal single crystals especially for incongruently melting materials which is our case. Czochralski method produces crystals of useful size and quality, it can only deal with materials which melt congruently whereas in flux growth process materials with a very high melting temperature, are dissolved in a solvent or "flux" and the crystal is grown below the melting temperature of the mixture and by means of very slow cooling rate, it solidifies before room temperature. The disadvantages of the flux growth is low grow rate and thus the obtained the crystals from flux is very small with eventual presence of unavoidable flux impurities from crucible. To avoid such impurities from crucible and to overcome other difficult parameter Floating Zone (FZ) technique [3] seems to be a good option. Indeed floating zone method is often more complicated and this technique requires high ability and skills to properly control the system. But it has advantages like the as grown crystal is quite bigger than compare to the crystal made by flux method, also incongruently melting material can be used to make crystal depending on the phase stability where feed rod and growing crystal have different composition from melting zone and this melting zone travels upward during growth and that is why this method is often called Travelling solvent Floating Zone (TSFZ) technique. Again main problem is these techniques were only applicable for thermal or electrical conductors, in order to avoids this paradox heating techniques along with FZ was developed using optical or mirror furnace where radiations from optical source was focused to molten zone by concave or ellipsoid gold coated mirror.

Fig. 3.1 shows the setup of the image furnace and the principle of TSFZ technique. In the FZ technique, the sample so called feed rod is hanged vertically from movable bar and the seed rod is fixed on a stationary part of the furnace below the furnace chamber. By focusing radiation from lamp to the both end of feed and seed melted at same time. This molten zone is then moved along the rod by moving the rod itself downward. A single crystal can be generated by spontaneous nucleation from polycrystalline seed rod or by using previously used single-crystalline seed crystal as the initial part of the rod. Both the feed and seed rod was synthesized by solid state reaction and

followed by several sintering and the phase purity was checked by conventional powder X-ray diffractions, the detail procedure can be found in Wahyudi et al. [4].

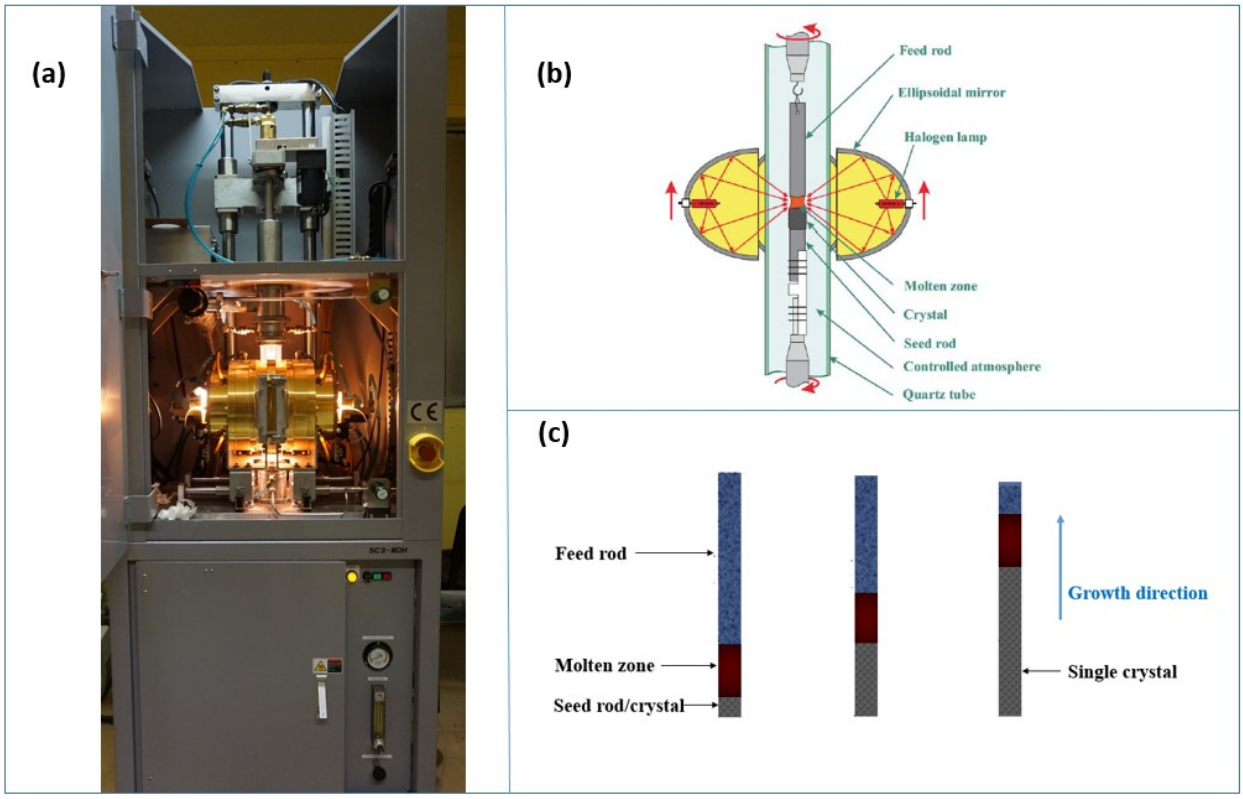

Figure 3.1: (a) Schematic representation of an Image Furnace (from NEC Machinary Corporation, Japan), inside snapshot of Image Furnace (b) and different stage during crystal growth showing growth direction.

Transporting material from the seed to the feed is another crucial process. If both rods are rotated in the same direction a large convection current will form that means material will be transported upwards on the outside and downwards on the inside, resulting in a quick connection of feed and seed rods. As the feed rod melts a fraction remains solid forming small grains that fall into the melt and through the quick connection they might sink down and deposit on the seed. This pollutes the crystal and changes melt composition. For this reason, the rods are rotated in opposite directions. The result is two convection zones and the interface is quite turbulent and prevents fast connection from top to bottom. Those solid grains have enough time to be completely solved during the slow propagation of material through the hottest part of the melt.

Growth of the strontium doped $Pr_{2-x}Sr_xNiO_{4+\delta}$ is rather more difficult, where the system becomes more and more incongruent melting with rising strontium concentration. As mentioned above, during crystal growth the melt has a different composition than the feed and seed rods, because it is enriched with a flux component which has a lower melting point than the feed rod while the temperature in the upper part of the melt is high enough to melt the feed rod. The melt climb through grain boundaries in the feed rod followed by capillary action and this brings other unwanted effects: the feed rod can be heavily enlarged and the probability that a large piece or even

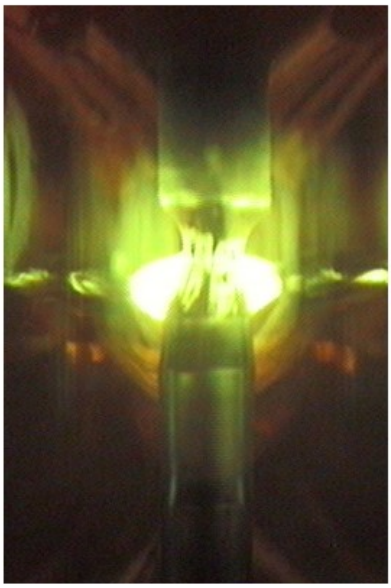

Figure 3.2: (top) Image showing feed rod, molten zone and seed rod during crystal growth, (bottom) as prepared 6 cm long single crystal of $Pr_2NiO_{4+\delta}$ oxides, top of the crystal contain flux of molt part and below unmolted feed rod.

the whole unmelted material falls into the melt and that usually breaks the melt. If smaller pieces of solid fall into the melt they might be quickly dissolved. But sometimes this fast melting can lead to the evaporation of a gaseous phase inside the melt. The excess gas will form a bubble (see Fig. 2.5 left) which will burst eventually. If it was small, the damage can be repaired but the burst of a

large bubble breaks the melt too. The size of such bubbles can be decreased with increasing pressure in the sample environment. For this reason growth in active vacuum has not been done as it amplifies the formation of bubbles in these oxygen rich compounds. Evaporation of nickel is another serious problem for the growth of nickelates. If the growth process takes too long the entire quartz glass tube will be covered with evaporated material and that prevents heating by reaching the melt. This can terminate the growth through solidification of the melt. Therefore the growth has to be finished before too much light is blocked.

As conclusion of this small survey of Traveling Solvent Floating Zone technique, we present the as grown investigated $Pr_2NiO_{4+\delta}$ and $Pr_{2-x}Sr_xNiO_{4+\delta}$ single crystal in the Fig. 3.2.

3.2 X-ray Laue Back Scattering Technique

After growing single crystal it is necessary to cut the crystal in a particular crystallographic direction followed by smooth polishing for subsequent characterization. Prior to cutting, the as grown crystals were oriented using the Laue back-scattering X-ray technique, the conditions for diffraction are fulfilled by using white X-rays beam, i.e., a continuous spectrum in *Bremsstrahlung radiation from* an unfiltered tungsten X-ray source. Since the specimen is a single crystal, the only variable necessary to meet the Bragg law $(n\lambda=2d\sin\theta)$ for different sets of planes in the crystal, is the multi- wavelengths in the white beam. In the back-reflection method, the film was placed between the X-ray source and the crystal in order to record the diffracted intensities on a film. This technique is quite strong which is also able to indicate the symmetry of the crystal. The Laue technique can also be used to study imperfections in crystals resulting from crystal growth or deformation as the Laue spots on films from perfect crystals are sharp while those from deformed crystals are elongated or splitted. Samples were mounted on goniometers that allowed rotation about all three directions and was placed at 3 cm from the films. After recording the Laue pattern it was treated and refined with help of OrientExpress [5] software that can also generate a simulated pattern which could be compared with the experimental one by eyes. This procedure tells about the directions or orientation of the crystal that is collinear with incoming beam. For example, Fig 3.3

shows the growth direction and *c*-axis of one of the as grown $Pr_{1.5}Sr_{0.5}NiO_{4+\delta}$ single crystal respectively, along with refined pattern. Once we have the oriented crystal we cut crystal using dedicated cutting machine to have defined plane which is parallel or perpendicular to desired directions. Even though it is not necessary for single crystal diffraction but it is good to have a polished surface just looks like mirror for the SIMS or conductivity measurements and this is why it was polished by using very sophisticated polishing tools. Fig. 3.3(d) shows one of the crystal surface after polishing.

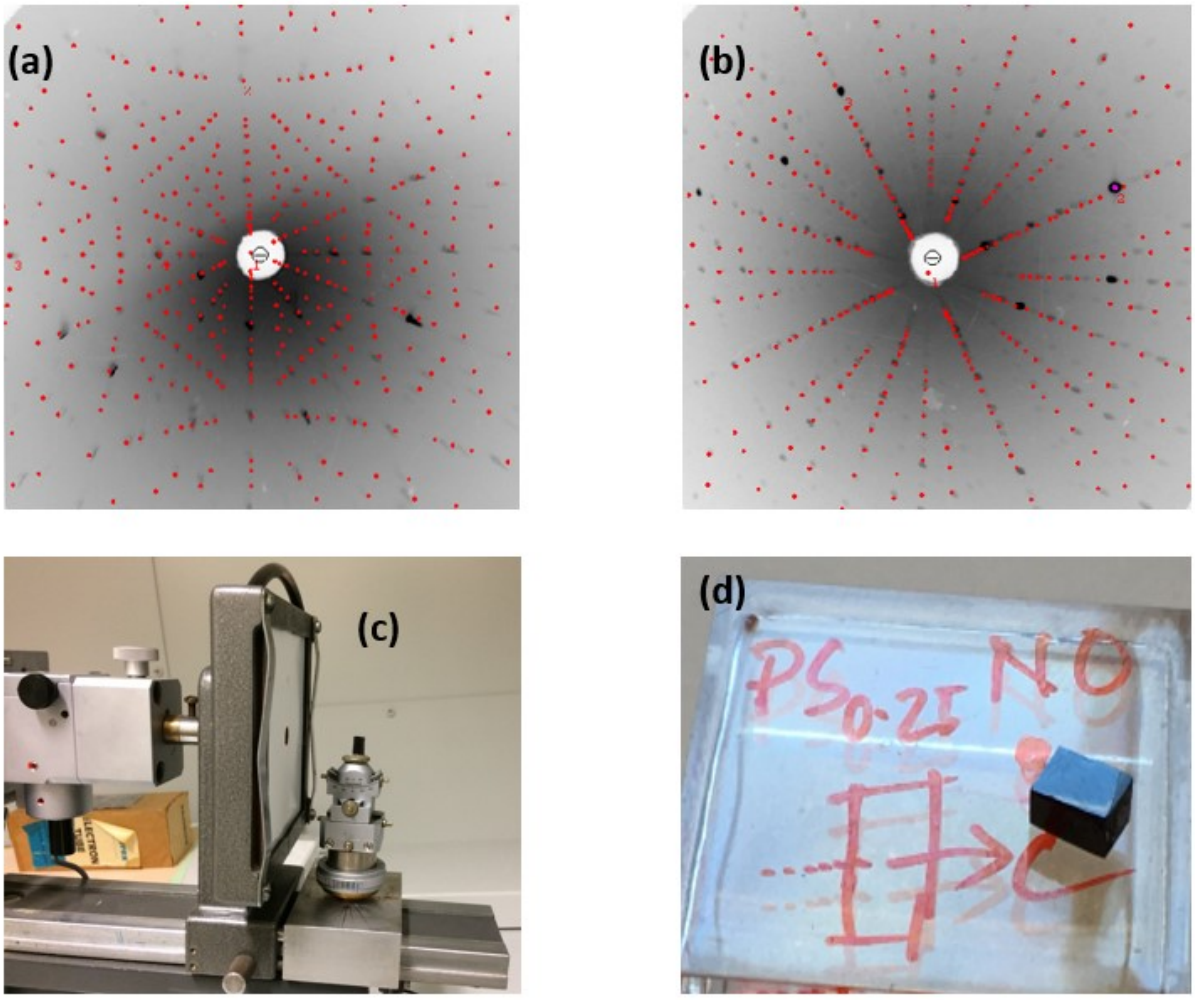

Figure 3.3: (a,b) shows experimental Laue pattern (black dots) obtained from as grown $Pr_{1.5}S_{0.5}NIO_{4+\delta}$ single crystal along with refined pattern (red dots) that corresponds to growth direction [1 0 0] and *c*-axis respectively. In (b) it is clearly visible the four fold axis in *I4/mmm* space group. (c) Laue set up showing mounted crystal on the goniometer and the film to record the Laue pattern by back scattering. (d) One of the polished surface perpendicular to c-axis obtained after orienting and cutting the crystal

3.3 Thermogravimetry Analysis (TGA) Set Up

Thermogravimetry analysis was performed to determine the mass loss due to extra oxygen in the as grown single crystal or polycrystalline sample. Crashed single crystal or powder sample was mounted in a small ceramic crucible under different gas flows and the thermogram was recorded during heating and cooling in step of 0.5, 1 and 5 ^{0}C/min up to 1150 ^{0}C. Fig. 3.5 shows the setup of the TGA in our home laboratory, the main advantages of this instrument is the resolution which means it can detect 0.1 microgram change in mass very precisely and that is the reason why in detail we see all kind of changes in the curve related to structural phase transformation, oxygen isotope exchange and even the it indicates the temperature where oxygen gets ordered differently with different modulation vector which is difficult to see such changes if the resolution is not so high. We will present those results obtained from several samples in different conditions like under nitrogen flow or oxygen flow to correlate the physical properties to oxygen non-stoichiometry i.e. change in mass and it is very important to know is the changes in results are due to change in oxygen or not.

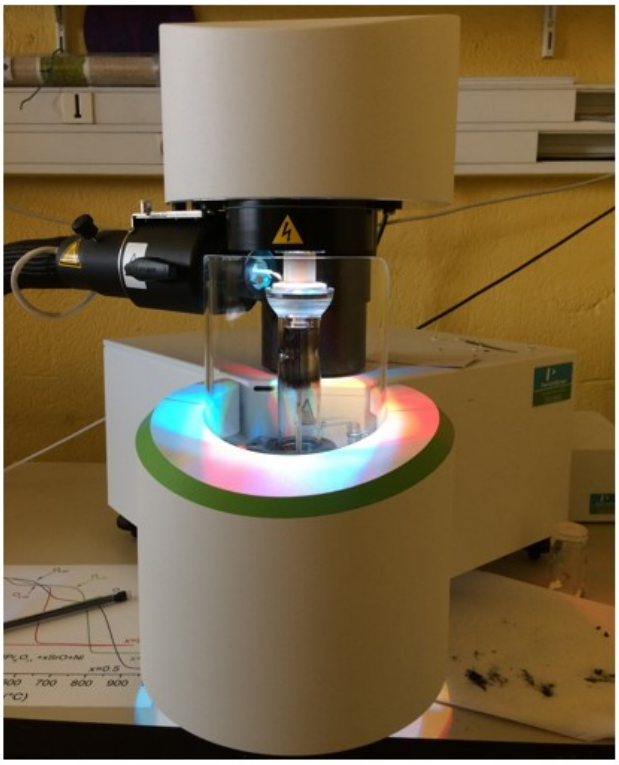

Figure 3.4: A compact instrumental set up for Thermogravimetry analysis (PerkinElmer TGA 8000)

3.4 DC Magnetometry

We have measured bulk magnetic properties of single crystalline oxygen and Sr doped Pr_2NIO_4 oxides using DC magnetometry. The experiments probed the component of the vector of the net magnetization parallel to the applied magnetic field. Complete hysteresis loops has been recorded while sweeping the field from positive to negative saturation and vice versa. Samples were mounted in such a way that the applied field was along a defined direction in the plane of the samples. Fig. 3.5 (right) depicts the sample configuration with respect to the applied magnetic field and the measured magnetization. The experiments were performed on a commercial system with dedicated option. Since we need temperatures higher than 300 K for these measurements, experiments have been conducted at the SQUID magnetometer at the University of Montpellier 2. The principles of this instruments and general details about measurements are described in the following section.

Generally, the SQUID magnetometer provides a temperature range from 2 - 800 K to measure DC magnetization. The field-cooled and zero field-cooled (FC-ZFC) temperature dependent magnetization M *(T)* curve of the investigated samples below the Néel temperature of pure stoichiometric Pr_2NIO_4 ($T_N \sim 680$ K) are of great interest since the magnetic properties are expected to be changed due to spin rearrangement and 3D spin ordering significantly at low temperature followed by charge ordering that take place always above the spin order temperature depending on the hole dope. The SQUID magnetometer is a product of Quantum Design, it is called Magnetic Property Measurement System (MPMS). The MPMS is a dedicated magnetometer (see Fig. 3.5), which uses SQUID (Superconducting Quantum Interferometer Device) technology to measure AC susceptibility and DC magnetization with a very high sensitivity. In DC experiments the sample is stepped through the superconducting detection coils, which are cooled by liquid helium. The induced voltage is measured, processed and the total magnetic moment is computed. An optional sample oven enables the MPMS to measure magnetic moments at high temperatures, in our case we went up to 400 K. The sample oven is directly installed into the probe chamber of the MPMS. A vacuum sleeve isolates the environment from the high temperature area. Thus, the probe chamber of the MPMS remains at ambient temperature.

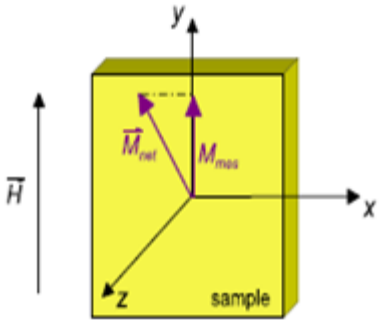

Figure 3.5: (left) Picture of MPMS instrument SQUID (Quantum Design, USA), the red & white body contains a superconducting magnet. (Right) Geometry for DC magnetometry. The applied magnetic field H is in the plane of the sample, e.g. parallel to the y direction of the sample. The experiment measures the projection M_{mes} of the net magnetization M_{net} onto the field direction.

3.5 Unconventional Capillary-Gas-Pressure-Cell

One of the main objective of this thesis was to develop phase diagram of $Pr_2NiO_{4+\delta}$ as function of oxygen pressure $P(O_2)$ and temperature (T) by using an optimized capillary-gas-pressure-cell adopted on single crystal X-ray diffractometer. Fig. 3.6 shows the schematic of the pressure cell mainly designed for single crystal diffraction. The cell used here is assembled from VICI VALCO parts. The central part is a microbore column end fitting (part No. ECEF211.0) composed of 1/8" external and 1/16" internal component which has 0.25 mm bore, inside this part two different kind of reducing ferruels were used: RF21PK which was connected to 1/8" external and other fused silica FS1.4PK was connected to 1/16" internal. These two ferruels were used to make the connections leak proof. This whole part was kept inside a metal body and was modified in order to fix in a

goniometer head. Through a hole on the metal body a PEEK (polyether ether ketone) capillary (360 µm-OD and 50 µm-ID with max. 5200 psi) was connected from end part of the column fitting to another internal reducing union (1/8' to 1/16" - ZRU21C). The advantages of this very flexible PEEK capillary is that whole pressure cell can be rotated 360^0 in phi angle during data collection without having any collision with diffractometer. An inox tube 1/8" was connected between the reducing union and the gas system by using Swagelok part. Inner quartz capillary (ϕ_{out} = 0.3mm and 0.01 mm thick) that contain the sample was glued on the inside wall but at below part of the outer quartz capillary (ϕ_{out} = 1.5 mm, ϕ_{in} = 1.1 mm) so that it does not come to heating environment. A 20 to 50µm sized crystal wad mounted on the top of the inner capillary by high temperature glue. Then the outer capillary was fixed into the standard ferruel with two component glue (Loctite). For good and fast solidification and low viscosity of the solidified glue under high gas pressure, the two components should be mixed close to the ideal 1:1 ratio. The use of a standard PEEK ferruel provides a tight and safe mounting of the capillary and allows moderately high pressures to be applied to the sample. Quartz (SiO2) capillaries were supplied by Hilgenberg GmbH (http://www.hilgenberg-gmbh.com/) with one end sealed. This Quartz capillaries can apparently withstand even higher pressures, subject to the absence of microcracks and other structural flaws. The maximum burst pressure was calculated from the equation $P_{max} = S*(K^2-1/K^2+1)$ where S is the stiffness constant of the quartz which is 48 Mpa, and K is the ratio of inner to outer diameter of the capillary and it was found P_{max} = 145 bar when K = 1.3636. The pressure was controlled by a special manometer only for oxygen and other Swagelok valve and the pressure was estimated via pressure gauge. A vacuum pump line was also connected to the gas system and the sample space in order to perform the experiment under vacuum which can reach up to 10^{-3} mbar. To avoid any contamination from air impurities in the sample space fresh oxygen was pumped several time to make sure sample is now under pure oxygen. Once the desired oxygen pressure is reached the valve connected to sample line was closed. Besides this pressure cell, a temperature device was adopted to the STOE diffractometer to perform such non ambient experiments. The temperature was calibrated in range of RT to 850 K with help of a special thermocouple provided by STOE.

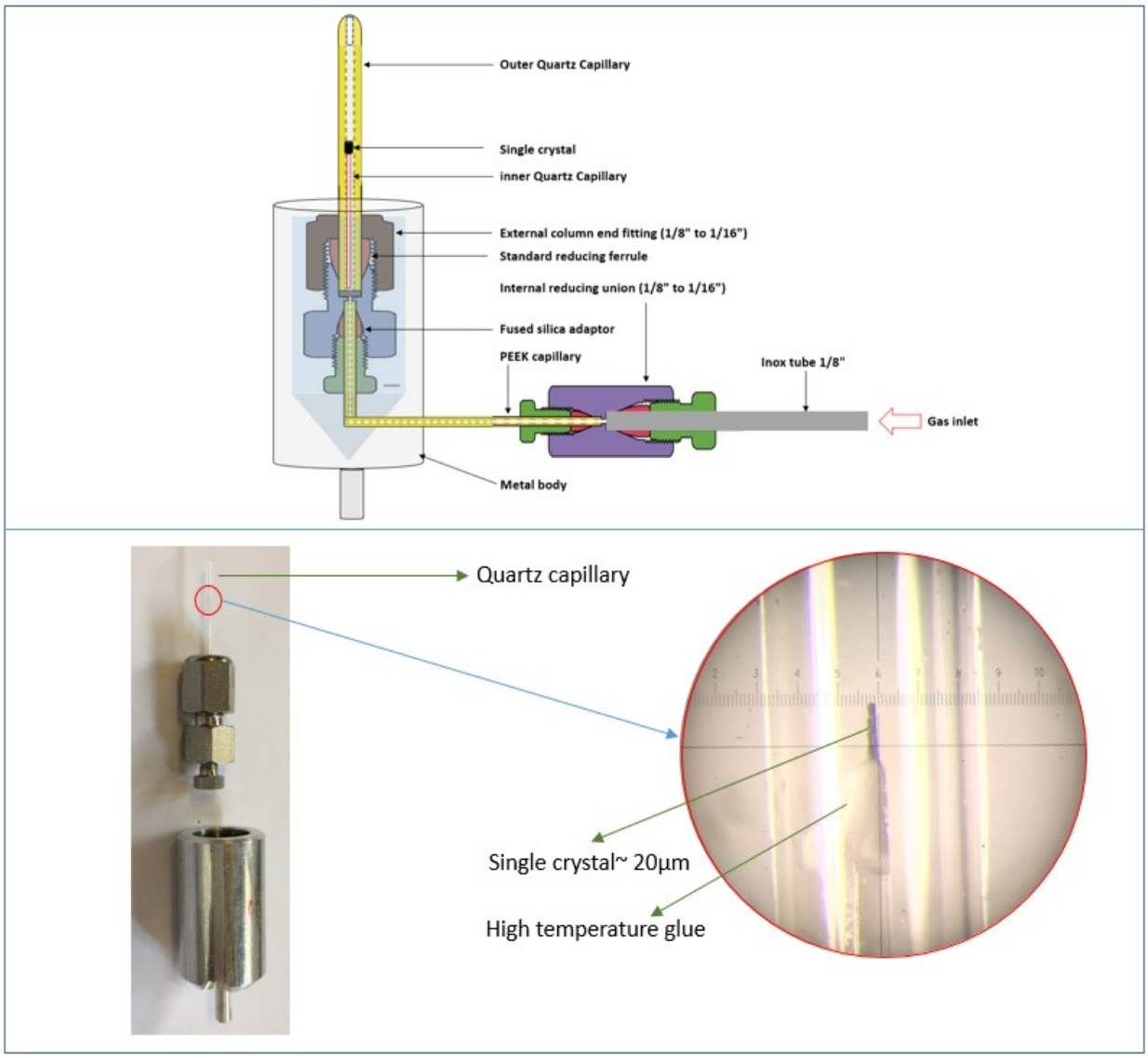

Figure 3.6: (top) Schematic representation of capillary gas pressure cell adopted for non-ambient X-ray SC diffraction and (bottom) dismounted cell to show all the components including mounted crystal on inner capillary by high temperature glue shown in zoom circle.

Heat at the sample space was generated by flowing N_2 gas passing through the temperature device and the distance from heat blower to capillary was 2 mm allowing a large opening angle for diffraction beam. This whole system was adopted also on the BM01A diffractometer at ESRF, Grenoble.

3.6 Electrochemical Cell

The design of EC cell for the *in situ* experiment is shown in the schematic diagram in Fig. 3.7. Derail reconstruction and the application of this cell can also be found in thesis of A. Maity [6] and Maity et al. [7]. As can be seen from the schematic, the design of the cell is very compact where the main body of the cell is made up of hard plastic cylinders (white part with black stripes) encapsulated with a metal cap and a metal base with 3 metal screws (only one is shown). All this blocks are connected by the co-axial central channel. Through the central channel two Debye-Scherrer glass capillaries telescoped (one inside the other) to each other are placed. Very small single crystal ~ 50 μm in size was used as electrode and was placed inside the inner capillary on the top of a gold wire ϕ = 50 μm (shown as red line) by using silver paste and carefully placing in the middle of the capillary. The inner capillary of diameter (ϕ = 300 μm) is cut at the upper end while the upper capillary of diameter (ϕ = 700 μm) is closed at the top end and the lower end is connected to the upper channel (outlet) making a close connection for the electrolyte flow. The counter electrode can be inserted anywhere in the electrolyte. 1N KOH electrolyte was steadily pumped by a peristaltic pump through thinner capillary while flowing back through the outer one. A constant current of 10 μA was applied by a KEITHLEY current source during the whole intercalation reaction. The advantage of this specially designed EC cell was its liberties of movements as it can allows 360^0 rotation in phi.

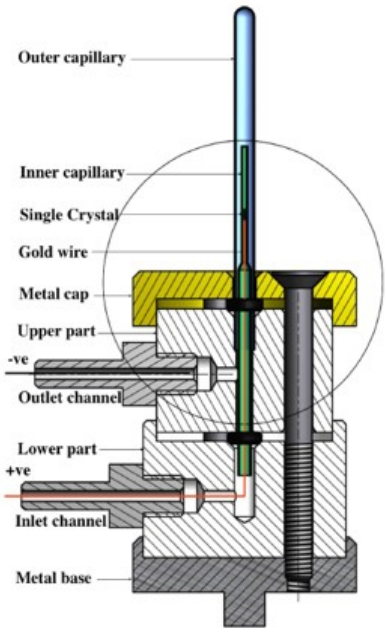

Figure 3.7: Electrochemical cell dedicated for the *in-situ* oxygen intercalation investigation in very small micron size single crystals and perfectly adapted on the BM01A diffractometer at SNBL, ESRF. Picture taken from ref. [6].

3.7 Single Crystal Diffraction

All the in-situ and ex-situ X-ray single crystal diffraction has been conducted mostly on STOE STADIVARY [8] single crystal diffractometer at home laboratory. First we performed ex-situ experiments just after preparing all the single crystal to see the as grown ground phase followed by installing pressure cell and temperature device on the STOE diffractometer to study the effect of oxygen pressure and temperature on the average structure and the microstructure. STOE STADIVARY four circle diffractometer combined with standard sealed tube Mo microfocus X-ray source (beam size ~150 μm) with energy range 3 -30 Kev and most importantly a high resolution, fast and low-noise area detector 200K 20HZ DECTRIS PILATUS detector provides always outstanding good quality data set. Read out time for each frame is quite fast and it takes 7 ms almost comparable to synchrotron case which is 2.5 ms. Sample can be mounted on a magnetic goniometer head without any adjustment tools or a lockable x, y, z and fully height adjustable goniometer head provided by also STOE, helps to center the crystal in very precise way. The detector can be moved in theta direction on a horizontal plane not vertical but it already open ups several freedoms to collect the data. One advantages of using X-ray fibre optic is gaining intensity depending on the anode material e.g. factor 2 for Mo K-alpha and comparable to a rotating anode. STOE also provides the heat stream device for non-ambient measurements with various the features: temperature range from RT to 800K accuracy within +/- 1^0 and no limitation in 2θ, ω, Φ or χ angle. The heat stream use the nitrogen medium to conduct the heat from device to sample space and was collected by ventilator on the top of the crystal. Another advantages of the setup is that there is no contamination from lambda-half harmonics as it is cut out by Zirconia foil inside the X-ray tube. Parallel, we can suppress the unwanted fluorescence from Sr K-edge (16.104 Kev) by tuning the threshold energy about 16 Kev in case of Sr-doped sample while oxygen doped samples were measure by tuning the threshold at 12 Kev. Data were collected by performing run optimizer build in the X-area software [9] mostly for ex-situ at ambient. Normally a full sphere data contains important weak superstructure reflections mostly were collected with step of 0.1^0 in phi by exposing 20 sec for each frame for but for normal average structure 3 sec gives quite good impression on reconstructed reciprocal plane. All the procedure starting from crystal mounting (using X-view

camera), creating a complete run list, data accusation and interpretation by building 3D reciprocal space along with structure refinement, has been done in one compact X-area software by STOE. This software is very helpful to handle the twin and incommensurate data set as it is the case we are dealing with. A complete setup for STOE STADIVARY single crystal diffractometer with all the necessary components and Pressure cell adopted on this goniometer are shown in Fig. 3.8.

As a big part of this thesis work, the *in situ* temperature dependent investigations on as prepared $Pr_2NiO_{4+\delta}$ have been performed on the multipurpose diffractometer BM01A [10] at (SNBL) in ESRF, Grenoble. The multifunctional diffractometer, combined with a high resolution, fast and low-noise area detector 2M DECTRIS Pilatus, opens up the opportunity for very fast and good quality

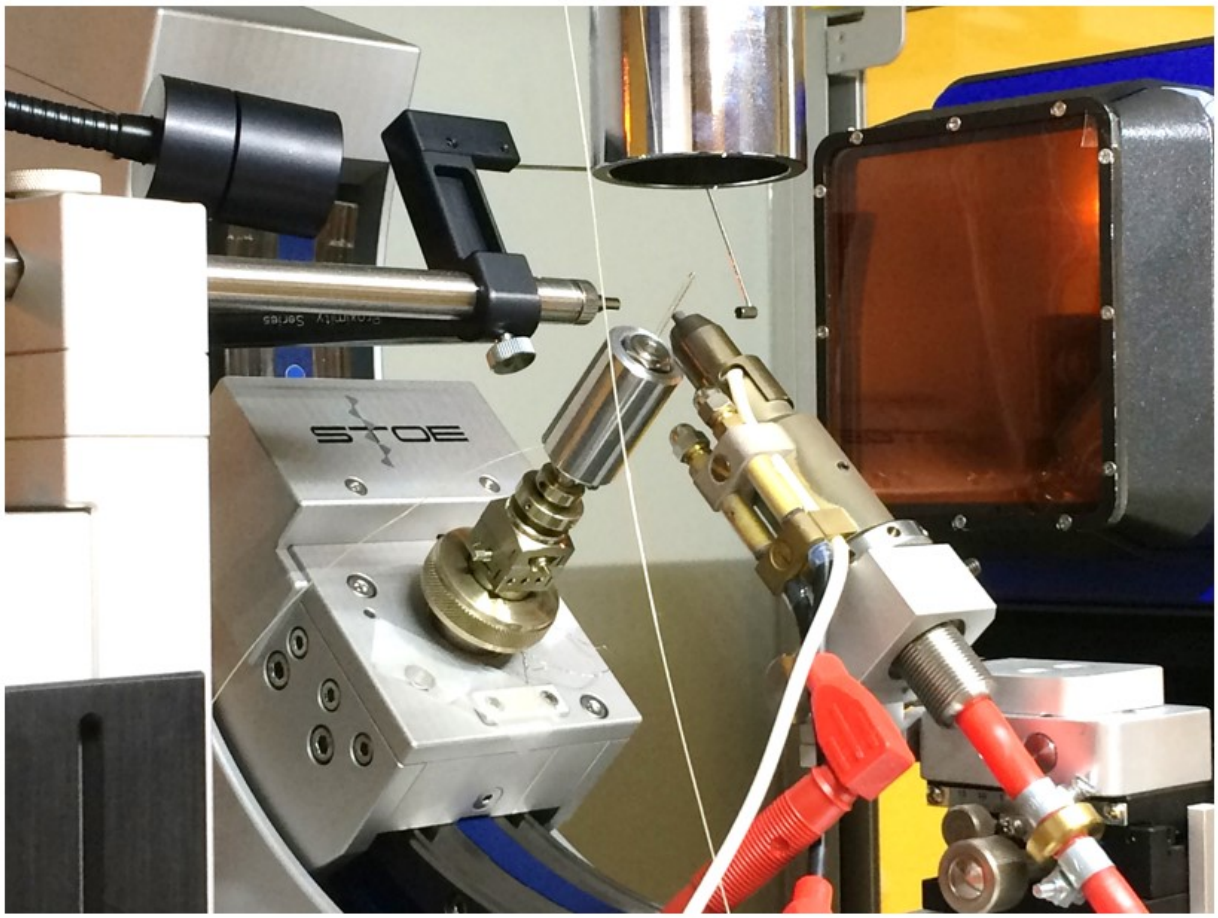

Figure 3.8: Installation of the capillary gas pressure cell under working condition, used for *in situ* single crystal diffraction studies, on STOE STADIVARY diffractometer equipped with temperature device and exhaust system allowing free rotation of 360^0 in phi.

data collection, especially important for the experiments with fast kinetics. The fast and almost zero noise data collection, which is possibly due to the combination of a sufficiently high beam intensity together with the use of a 2M Pilatus detector, having a readout time of 2.5 ms only. Similar precautions were taken to suppress the unwanted florescence like in STOE diffractometer. An important advantage of BM01A in terms of unambiguous data interpretation, is the absence of contamination by harmonics and its very narrow energy resolution, achieved via a combination of focusing beam optics with a double crystal monochromator. Data collection in BM01A is done by a user friendly and GUI-based software *Pylatus*. All the data were collected for different measurements in a timescale of 0.5 s per frame while rotating the electrochemical cell with a 0.1^{0} angular step. A full sphere data collection takes 18 min for 3600 frames (0.3 s per frame) whereas to have the exact

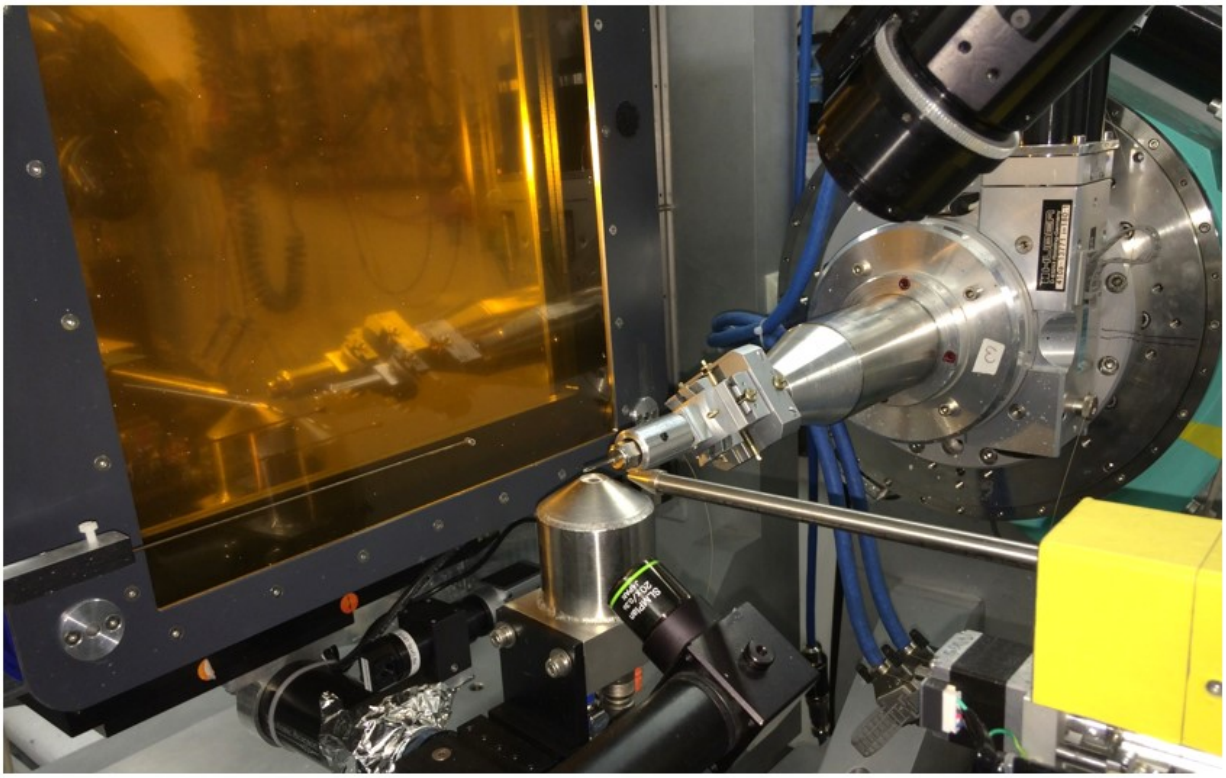

Figure 3.9: Installation of same capillary gas pressure cell under working condition, used for *in situ* single crystal diffraction studies, on BM01A diffractometer equipped with temperature blower in down from capillary allowing free rotation of 360^{0} in phi to collect full sphere data set.

same quality data set it will take 20 h using STOE diffractometer, this is the main difference between synchrotron and home laboratory diffractometer. This huge amount of data was pre-processed with an in-house-developed package SNBL Tool Box [11] and data were by using CrysAlisPro software [12]. Recently a nice tool to represent the 3D volume data has been implemented inside the SNBL Tool Box and we will show one example of that beautiful feature. Fig. 3.9 shows experimental setup on the BM01A diffractometer at ESRF with all necessary tools to perform temperature dependent experiments.

References:

1. Y. Shiohara and A. Goodilin, Handbook on the Phys. and Chem. of Rare Earths, 30 (2000) 67.
2. H.J. Scheel, J. Crystal Growth, 211(2000) 1-12.
3. D.T.J. Hurle, Handbook of Crystal Growth, 2 (1994).
4. O. Wahyudi, M. Ceretti, I. Weill, A. Cousson, F. Weill, M. Meven, M. Guerre, A. Villesuzanne, J.-M. Bassat and W. Paulus, CrystEngComm, 17, 6278-6285 (2015).
5. Laughier, J.; Filhol, A. J Appl Crystallogr **1983**, *16*, 281-283
6. A. Maity, PhD thesis, Exploring oxygen diffusion mechanism in $SrFeO_{3-x}$ and $Pr_2NiO_{4+\delta}$, followed up on songle crystal by in situ synchrotron diffraction, 2016
7. A Maity, R Dutta, B Penkala, M Ceretti, A Letrouit-Lebranchu, D Chernyshov, A Perichon, A Piovano, A Bossak, M Meven and W Paulus, Solid-state reactivity explored *in situ* by synchrotron radiation on single crystals: from $SrFeO_{2.5}$ to $SrFeO_3$ via electrochemical oxygen intercalation, J. Phys. D: Appl. Phys. 48 (2015)
8. Web reference for STOE STADIVARI Diffractometer, https://www.stoe.com/product/stoe-stadivari
9. STOE & Cie GmbH, X-Area, software package for collecting single-crystal or multi-domain crystal data on STOE area-detector diffractometers, for image processing, for the correction and scaling of reflection intensities and for outlier rejection, version 1.77, Darmstadt 2016
10. A. Perrichon, A. Piovano, M. Boehm, M. Zbiri, M. Johnson, H. Schober, M. Ceretti, and W. Paulus, Lattice Dynamics Modified by Excess Oxygen in Nd2NiO4+δ : Triggering Low-Temperature Oxygen Diffusion, The Journal of Physical Chemistry C, vol. 119, no. 3, pp. 1557–1564, 2015
11. V. Dyadkin, P. Pattison, V. Dmitriev, and D. Chernyshov, A new multipurpose diffractometer PILATUS @ SNBL, J. Synchrotron Rad., vol. 23, pp. 825–829, 2016.
12. Web reference for CrysAlis^{prc}, http://www.rigaku.com/en/products/smc/crysalis.

Chapter 4

Twinning Scheme and Structural Studies of as Grown $Pr_{2-x}Sr_xNiO_{4+\delta}$ (x = 0, 0.125, 0.25 and 0.5) by SC X-ray Diffraction

Charge Stripe has been already predicted by principle of combined charge and spin density wave [1, 2] before being observed experimentally mostly in Sr-doped Lanthanum nickelates family [3]. Remarkable attention has been drawn to the physics of stripe phases due to the discovery of a "hour-glass"-shaped magnetic spectrum in $La_{2-x}Sr_xCoO_4$ [4] similar to superconducting cuprates [5]. Besides, cobaltates a homologous system e.g. nickelates could be interesting to study such ordering state since a rather stable diagonal charge stripe order has been observed in these systems at higher hole-doping [3] as we discussed in previous chapter 2. The exact onset of stripe ordering is not known properly as function of Sr-dope and oxygen dope $Pr_2NiO_{4+\delta}$ which is equivalent system in Lanthanum nickelates family and has not been studied systematically to the best of our knowledge as the system is very sensitive to excess oxygen (δ) in a wide range from 0 to 0.25. This is one aspect, on other hand the consequences of excess oxygen ordering that might have effect on stable stripe onset region as it effects the local microstructure in long-range. Structure exhibits very complex incommensurate modulation that ordered 3-dimentionally when excess oxygen gets ordered already at RT seemingly having huge impact also on oxygen diffusion. In terms of oxygen diffusion mechanism which has been discussed theoretically and experimentally in this investigated material that excess oxygen must be present in the system in order to enhance and place the dynamically triggered phonon assisted diffusion process [6, 7]. The phase diagram of Lanthanum nickelates are well adopted but not so far for Pr-based compound in details. Doping Sr and oxygen cause the structure distortion and to go through order-disorder phase due to the NiO_6 octahedra tilting and bond length mismatch and therefore it is necessary to study or develop the phase diagram of as grown oxides as function of hole concentration before going to into other dependency in the phase diagram. It is also interested

in studying charge stripe phases in $Pr_{2-x}Sr_xNiO_{4+\delta}$ systematically but first the changes in microstructure due to excess oxygen. The orthorhombicity tells about the structural changes also in point of view of twinning that present in the studied system and makes the world more complex but in other sense it helps a lot to understand every details of those obtained complex diffraction pattern. In this way it can be realized that $Pr_{2-x}Sr_xNiO_{4+\delta}$ is a perfect model system belongs to K_2NiF_4-type oxides to investigate such complex structural aspects, electronic ordering, oxygen diffusion that open up a new window in field of strongly correlated oxides and in application of new generation SOFCs device. Hence, we have performed a whole series of as grown $Pr_{2-x}Sr_xNiO_{4+\delta}$ samples with low to high Sr-doping as well as oxygen doped samples by Single crystal X-ray diffraction on STOE STADIVARI diffractometer ($\lambda_{Mo} = 0.71073$ Å) in order to study the symmetry, lattice parameters and orthorhombicity as a function of Sr-/oxygen hole-doping.. Complementary neutron experiments besides X-ray diffraction on single crystals are needed in order to study the stripe charge and spin ordering in these nickelate compounds but we stick to the X-ray diffraction in this chapter to explain the structural features electronically only.

In this chapter we will present the RT phase diagram of hole doped as prepared $Pr_{2-x}Sr_xNiO_{4+\delta}$ oxides and having a good knowledge about the ambient phase is useful for better understanding of all the subsequent microstructural changes with temperature (T), excess oxygen concentration (δ) and oxygen pressure $P(O_2)$. Microstructure evaluation on oxygen ordering in each single domain (max. 8) related to twin and incommensurately modulated structure mostly will be focused and discussed in detail.

4.1 Phase Study by X-ray Powder diffraction

Single crystal of $Pr_{2-x}Sr_xNiO_{4+\delta}$ with x = 0, 0.125, 0.25 and 0.5 ($0 \leq \delta \leq 0.25$) have been grown by TSFZ technique using Image Furnace as discussed in chapter 3. It is importance to know the phase purity and homogeneity of the feed rod made from polycrystalline powder synthesized by solid state reaction before and after making single crystal. Single crystal of each compound were crashed into fine powder and characterized by conventional X-ray powder diffraction on PHILIPS X'pert diffractometer by taking diffraction pattern in the range $0^0 \leq 2\theta \leq 60^0$ using Cu K-alpha1,2 wavelength in Bragg-Brentano geometry. The X-ray diffraction patterns of $Pr_{2-x}Sr_xNiO_{4+\delta}$ with x = 0, 0.125, 0.25 and 0.5 have shown in the Fig. 4.1. The structure was refined by Rietveld method using FullPROF suit [8] and the refined parameters are written on each diagram.

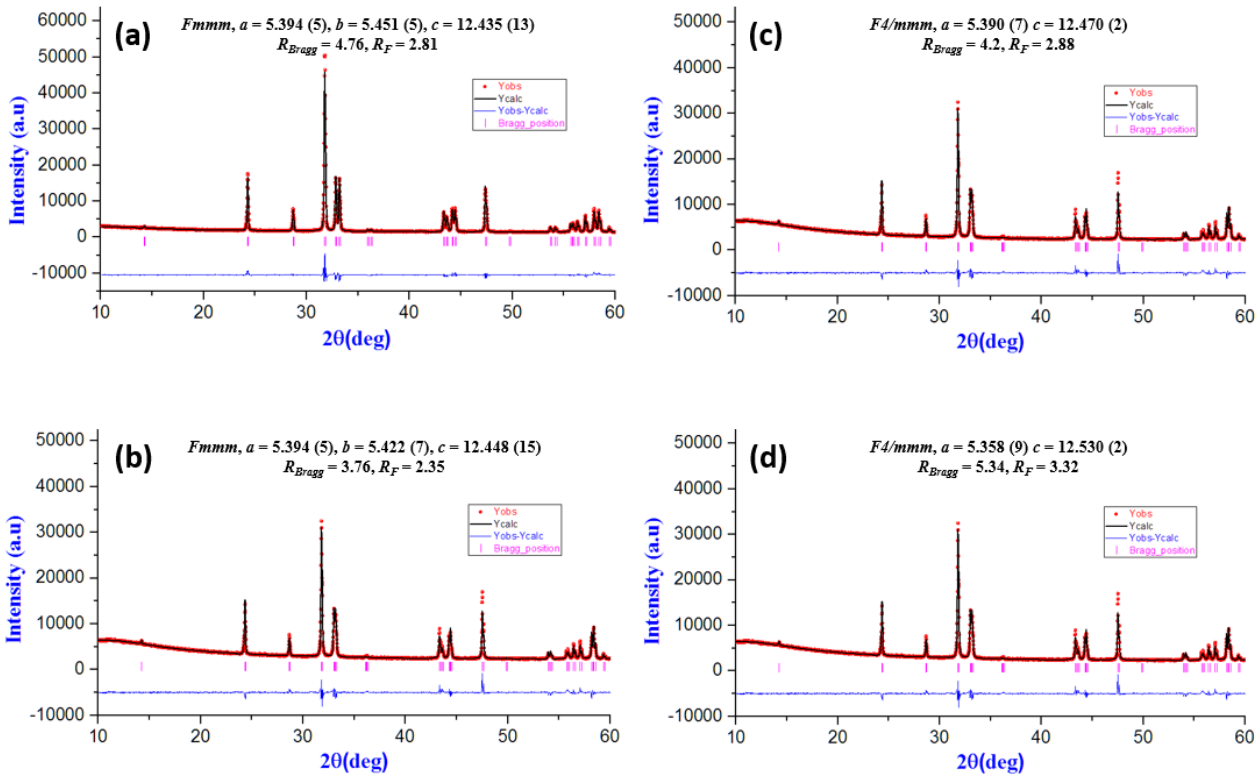

Figure 4.1: X-ray diffraction patterns of crushed PSNO single crystals after growth at RT. The patterns in (a) and (b) were obtained for x = 0 and x = 0.125 respectively (both orthorhombic *Fmmm*), while the patterns in (c) and (d) corresponds to x = 0.25 and x = 0.5 respectively with tetragonal *F4/mmm* symmetry. Refinement of these patterns clearly indicates the excellent crystalline quality of all compounds, showing FWHM close to the resolution function of the diffractometer used. Also there is no evidence for other impurity or intergrowth phase.

Phase purity of the grown single crystals was checked by through the carried out successive profile matching (Lebail mode) and the Rietveld refinement lattice parameters and the phases for each system are validated and their dependency on hole doping is studied. All PSNO crystals were found to be homogeneous and monophasic, no presence of impurities or intergrowth phase. Crystal with Sr-doped x = and 0.125 are orthorhombic (sg *Fmmm*) while it is tetragonal (*F4/mmm*) with x = 0.25 or 0.5. The values are good in agreement with those reported elsewhere [9].

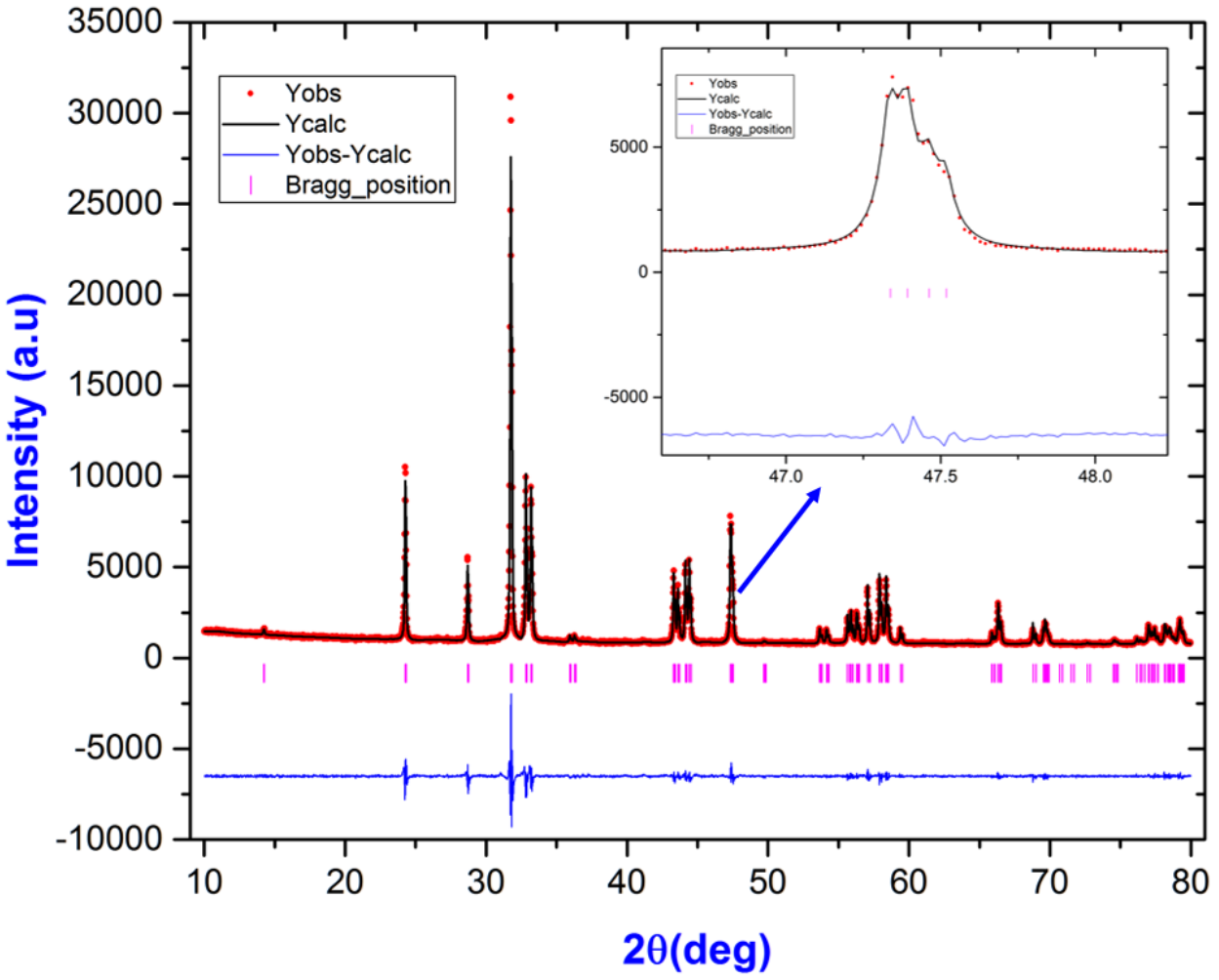

Figure 4.2: Conventional laboratory powder X-ray diffraction pattern of crashed $Pr_2NiO_{4.25}$ single crystal, pattern profile refinement carried out in profile matching mode in F12/m1 space group (a = 5.395Å, b = 5.453 Å, c = 12.439 Å and γ = 90.062^0) where inset shows the monoclinic splitting of (-220) and (220) reflections.

However, close inspection on XRD pattern presented in Fig. 4.2 shows the monoclinic phase with very small monoclinic angle $\gamma = 90.062^0$ instead of orthorhombic structure. Inset shows the splitting of *(-220)* and *(220)* reflections indexed in *F12/m1* space group and the profile refinement carried out in profile matching mode using Fullprof software. To present into a quantitative way the RT phase diagram is shown in the Fig. 4.3 below.

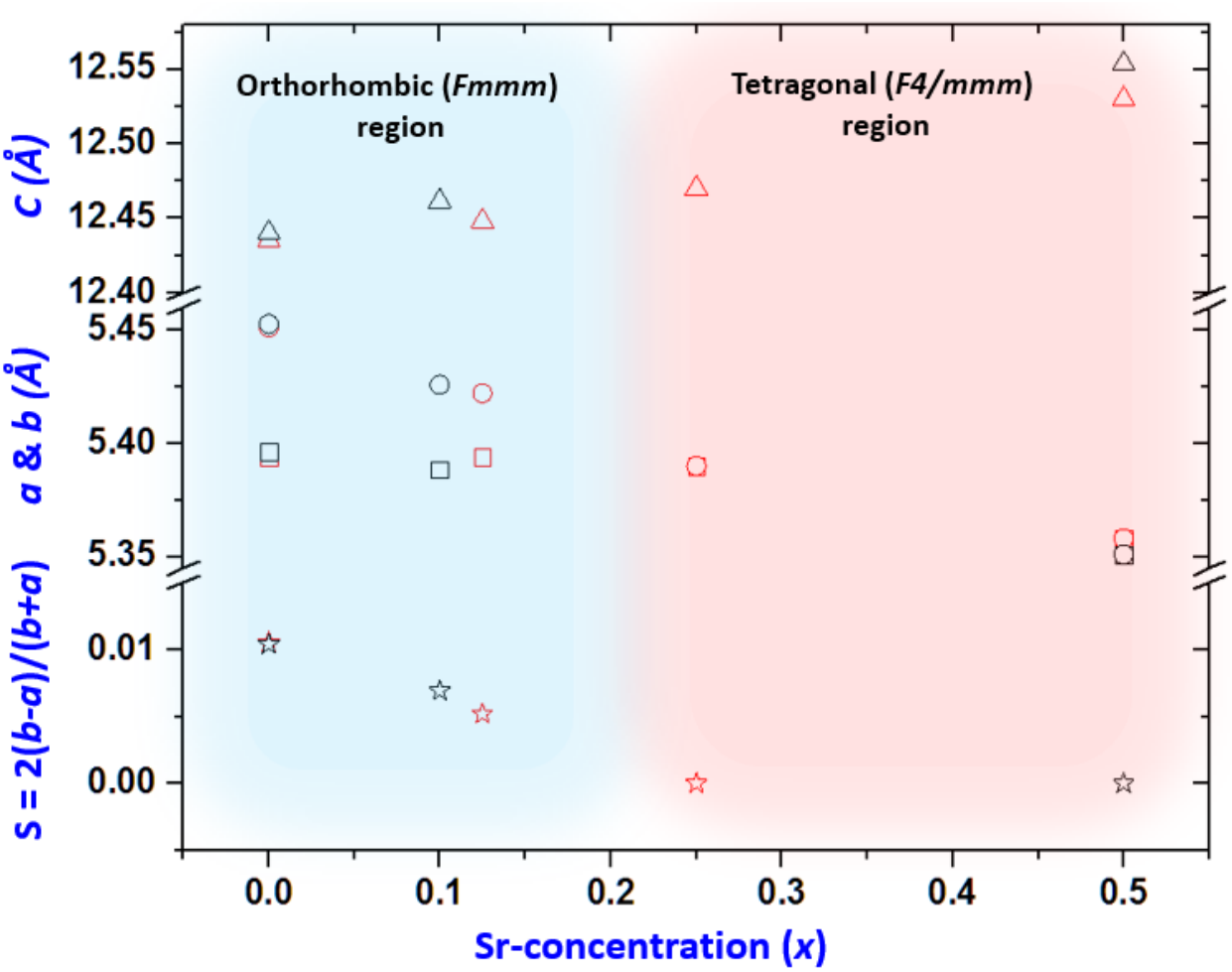

Figure 4.3: shows dependency of lattice constant a (square), b (circle), c (triangle) and orthorhombic strain (S) (star) as function of various Sr-dope and oxygen dope ($x = 0$). Note that x-axis represents only the hole concentration correspond to Sr not excess oxygen (δ). It presents two different phase region one is orthorhombic at lower Sr doping and tetragonal one with higher Sr doping. Obtained values in this work (red symbol) are in good agreement with values taken and plotted in the same figure (black symbol) from Wahyudi et. al. [9].

4.2 Investigation of Microstructure by Single Crystal X-ray Diffraction: The Beauty of Complexity

What we have seen in chapter 1 is that oxygen doped $Pr_2NiO_{4+\delta}$ oxide exhibits a high ionic-electronic conductivity and anisotropic oxygen mobility, the reason why it could be served as a good cathode material in the upcoming new generation SOFCs device which is seeking to be operated at room temperature. Besides the applications, the foundlings about low energy phonon assisted oxygen diffusion process which is dynamically activated in presence of excess oxygen already at RT has drawn a huge attention into the solid state chemistry, material physics and crystallography in order to see what are the consequences of this excess oxygen with microstructure, domain structure, electronic ordering and correlation, phase separation which is already being discussed in physics of strongly correlated materials. Here in this section we will focus not only on the structural complexity arises from the excess oxygen whereas the system is very much sensitive to the oxygen even at RT, but we will see the beauty of crystallography, the correlated electronic physics by studying the oxygen ordering as well as charge ordering using single crystal diffraction for all the Sr and oxygen doped sample to develop a understandable phase diagram at RT.

4.2.1 As Grown Oxygen doped $Pr_2NiO_{4+\delta}$ oxides

4.2.1.1 1st Impression on obtained diffraction pattern

Single crystal X-ray diffraction of as grown non-stoichiometric $Pr_2NiO_{4+\delta}$ ($\delta \sim 0.25$) was performed on STOE STADIVARI 4-circle diffractometer collecting the diffracted intensities by PILATUS area detector. Fig. 4.4 shows the 1st obtained one of diffraction pattern which represents the *(hk1)* reciprocal plane. Data was collected and reconstructed as a 3D intensity reciprocal volume and after that the desired plane was cut. In the diffraction pattern, it can be noticed that there are empty void space, it is not a pitfall but it is because of experimental condition which is called run optimization. It is also important to notice that streaks (spectral impurity) around strong Bragg reflections are coming from parts of Bremsstrahlung around K-alpha reflected by the mirror and it goes radially along 2-theta. It can be seen much more in *(hk0)* plane than *(hk1)* plane.

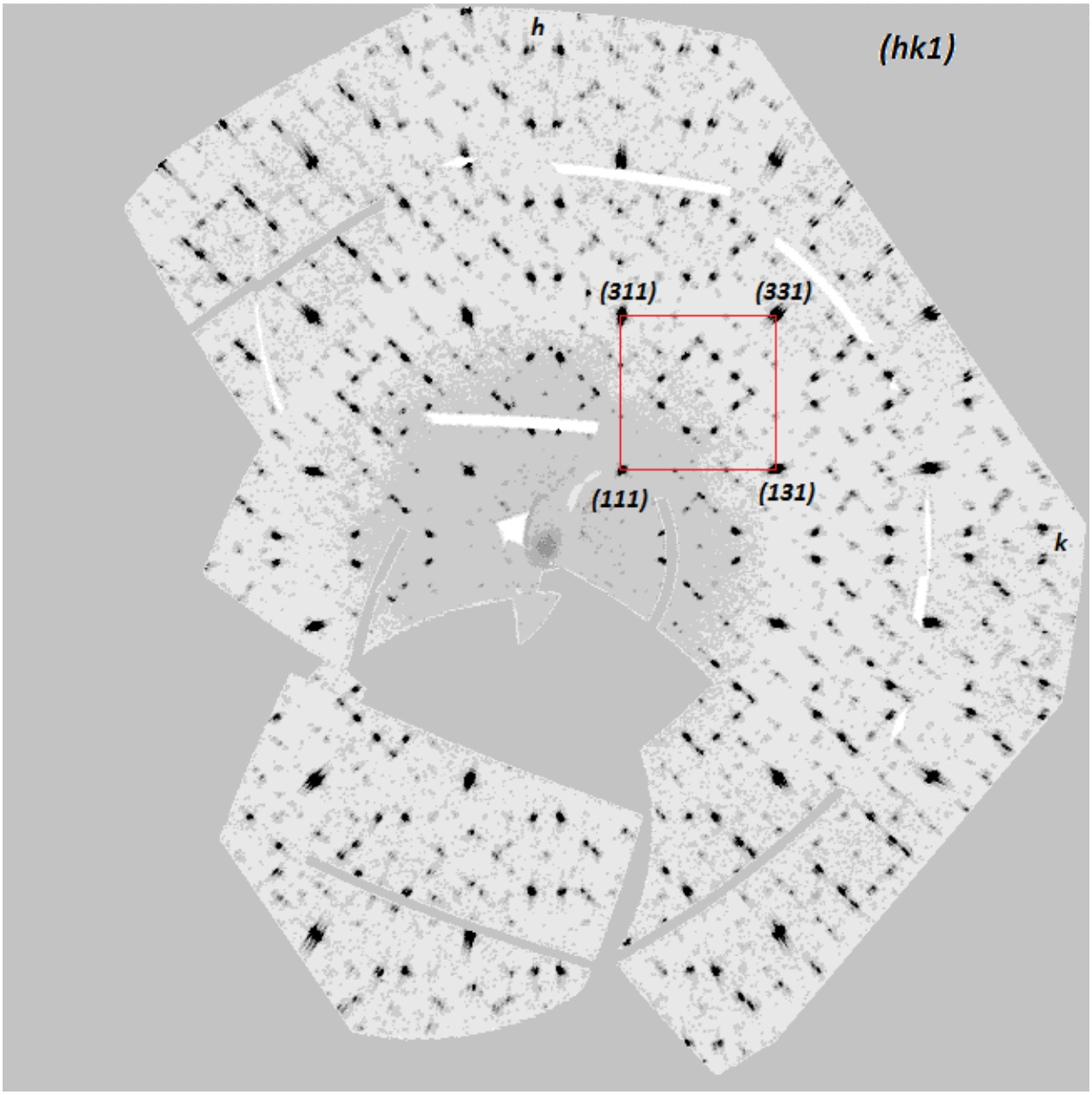

Figure 4.4: Reconstructed experimental *(hk1)* reciprocal space from laboratory X-ray diffraction data showing complex structure scenario obtained from as grown 50 µm sized $Pr_2NiO_{4+\delta}$ single crystal at RT. Red square represents the global and average orthorhombic unit cell and corresponding Bragg indexation in *Fmmm* space group.

As it can be seen in the pattern that besides the main Bragg reflections there are lot of week superstructure reflections but they appears in a periodic manner and they are coming from ordering of excess oxygen. Intercalation of such excess oxygen or presence of that (after crystal growth) in non-stoichiometric compounds such as $Pr_2NiO_{4+\delta}$ modifies the deformation of tetrahedral interlayer which contains the excess oxygen atom sites. In the low regime of oxygen concentration ($\delta < 0.1$) the induced deformation of the tilted octahedra is not pronounced and long ranged in 3D causing the structure partially disordered. But above certain critical values of $\delta \sim 0.125$ those tilted octahedra gets ordered in long range because of excess amount of oxygen are intercalation and ordering of those oxygen in 3D. This is what we see in the diffraction pattern the very complex long range order scenario just from oxygen ordering. This is not all what we see, much more complex ordering and many more week reflections are present if we look to the similar diffraction pattern of *(hk0)* or *(hk1)* plane presented in the Fig. 4.5 which is obtained by synchrotron X-ray diffraction on microdiffractometer equipped with 6M-F PILATUS area detector at ID29 MX beamline, ESRF. If we compare the both results in one shot it will be clear that the resolution of the diffracted reflections are very sharp and strong in case of data from synchrotron is due to high flux density, resolution, shorter wavelength and of course 6M Pilatus detector which is 30 times more sensitive than 200K PILATUS on STOE diffractometer. In the Fig. 4.4 the reflections which are not visible or very weak they can be seen in the Fig. 4.5 with other features like butterfly shaped strong diffuse scattering surrounding the *(h00)*-type Bragg reflections are resemble to anisotropic nuclear densities of apical oxygen atom [6] and might be from soft phonon mode at RT, we will point out this in next chapter with details. The other features concerning the modulation has been discussed in sec. 4.2.1.3. First step would be to index all the reflections in any reciprocal plane and in order to index all reflections and understand the way how all these week superstructure reflections are ordered, we need few basic ideas of crystallography in higher dimension (> 3D) e.g. (3+n)-dimensional incommensurate modulation and the twinning that is present in this single crystal.

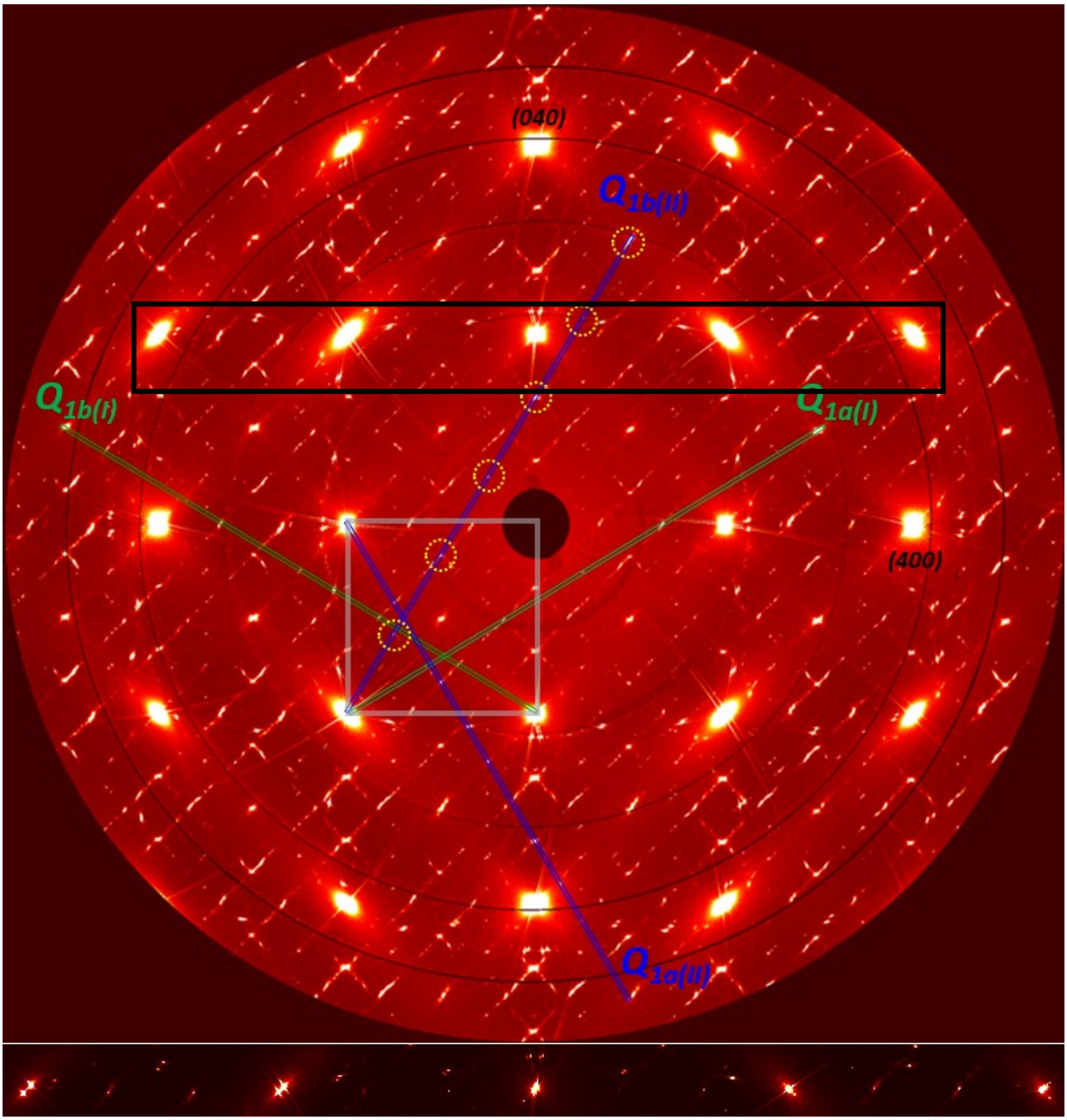

Figure 4.5: Reconstructed experimental (hk0) reciprocal map of $Pr_2NiO_{4+\delta}$ single crystal obtained from synchrotron X-ray diffraction at RT on ID29 diffractometer at ESRF. Data showing very similar pattern as Fig. 4.3 but gives much more detail information e.g. the superstructure reflections are coming out clearly and more intense, the diffuse scattering around Bragg reflections are very strong as well. Details of the modulation with simulation pattern is described in the section 4.2.1.3. (Below) shows the rectangular section where Splitting of Bragg reflections are shown by changing color and intensity scale.

4.2.1.2 Twinning of $Pr_2NiO_{4+\delta}$ oxide

Twin is a classic term mostly discussed in distorted perovskite oxides where due to higher Goldschmidt tolerance factor and huge lattice mismatch ideal perovskite cubic structure changes to lower symmetric tetragonal or orthorhombic structure either by displacing cations from their ideal positions or polyhedral tilting give rises different possible orientation of the unit cell. This way twinning can form micro- or macroscopically in the bulk material through phase transition modifying symmetry. Among different process of forming twin, in our compound it is appears as transformation twins during crystal growth the solidification of molten zone the crystal goes through HTT phase to LTO phase induced by cooperative tilting of NiO_6 octahedra and two or four twin domains can form microscopically. Different twin domains are related by so called 'twin law' which is a twin operation (also called twin elements) that brings those twin individuals or domains in a same orientation than the others. To classify the twin nature it is necessary to look on the reciprocal lattice i.e. a single crystal diffraction pattern and it was found that twin in Pr_2NiO_4 belongs to the non-merohedral family where reflections coming from twin domains are not overlapped but since there exist a partial overlapping between weak superstructure reflections as well as main Bragg reflections it is more or less pseudo-merohedral type gives problem to integrate the diffracted intensities for structure refinements. Fig. 4.6 shows the model of the observed twin domains and twin elements through experimental diffraction pattern. As it can be seen from the top panel of the figure two symmetry elements can be lost: if it is diagonal mirror plane either *(-110)* or *(110)* then it forms two twin individuals (top left) or if it is both mirror planes then it give rise four twin individuals (top right). Please follow the color code for each individuals. In case of two twin individuals the longer a^* axis and shorter b^* axis of one is flipped for other and deviated from parent tetragonal unit cell (black square) due to loss of mirror plane which is the twin element. Combing orthorhombicity with twin elements causes splitting not only the Bragg reflections but also the weak superstructure reflections. For the case of two twin individuals, the Bragg reflections split in two peaks, they can be well separated or partially overlapped depending on 2Δ; except for the *(hh0)* and *(-h-h0)* reflections which are perfectly overlapped when the *(-110)* mirror plane is lost (or *(h-h0)* and *(-hh0)* reflections if the *(110)* mirror plane vanishes).

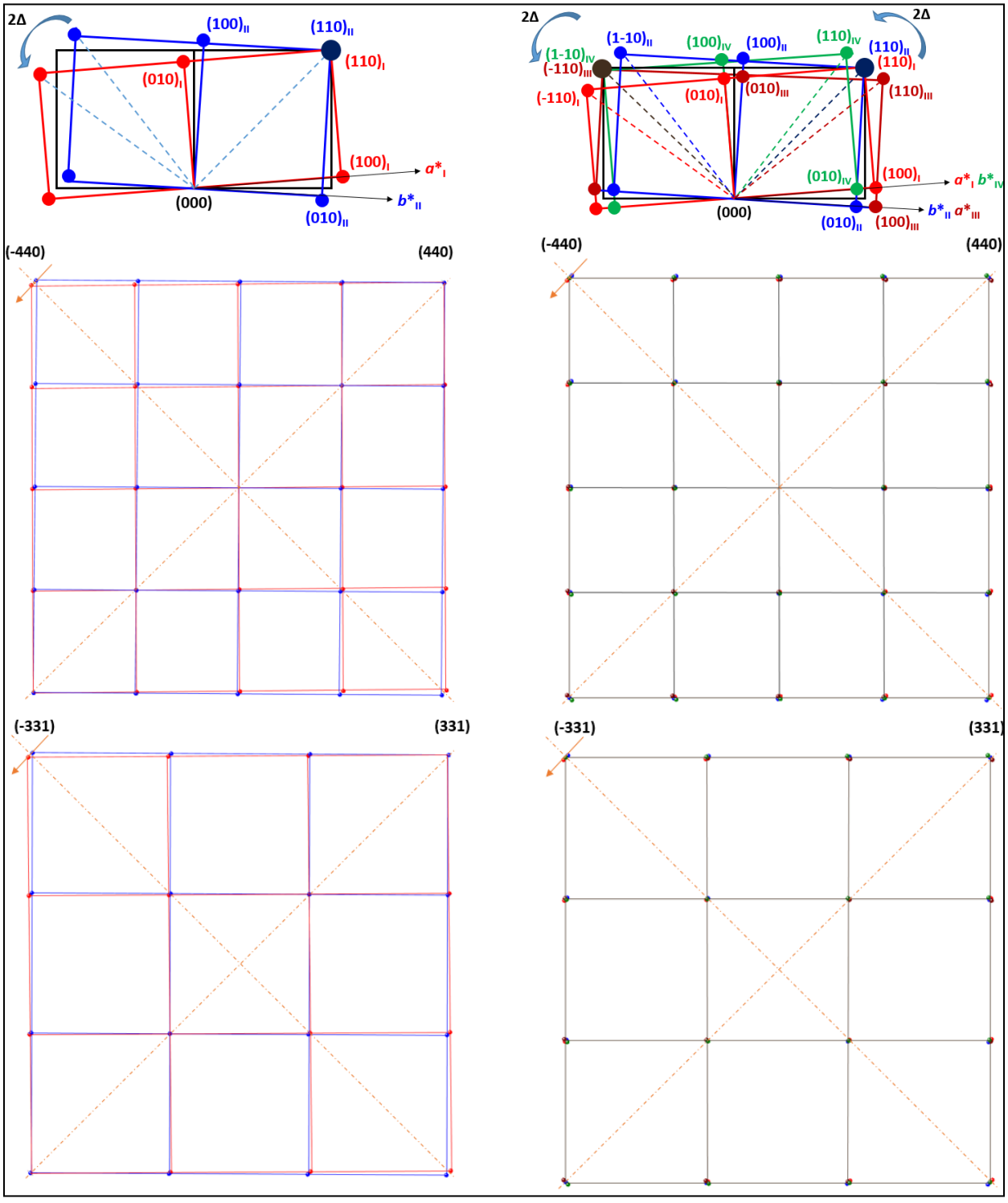

Figure 4.6: Schematic of twinning in $Pr_2NiO_{4+\delta}$ single crystals, with the loss of either [-110] or both [110] and [-110] mirror planes, resulting respectively in 2 or 4 twins individuals. (Top panel) Twin law in reciprocal space view perpendicular to c^* which is the axis shared by the two twin components; (middle and bottom panel) represents Bragg reflections in *(hk0)* and *(hk1)* plane respectively followed by both twin law (two and four domain) left and right respectively. Arrow indicates splitting in omega directions. For more see the text.

For the case of four twin domains, the Bragg reflections split in four peaks, excepted for the *(±h±h0)* reflections which split in three peaks (two of the four are exactly overlapped). The angular separation is defined as $\Delta = \tan^{-1}(a/b) - \tan^{-1}(b/a)$ where a, b are lattice parameter in orthorhombic unit cell. All the twin domains can be viewed as each set are rotated by 90^0 around c^* w.r.t others while they share common c^*-axis.

There is no way to control or alternate the number of twin domains that exists in the single crystal, it's material properties and natural effects but time to time it has been checked by X-ray diffraction that if it is kept under ambient temperature and pressure for long time (~ one year) it changes from four individuals to two individuals, the only things change during that period is excess oxygen it goes out and depending on the oxygen non-stoichiometry the microstructure changes means domain evolves. Also it has been observed that depending on externally applied oxygen pressure twin domain changes, not only number but also the nature of the microstructure, we will see in next few chapters. If we look back again to diffraction pattern in Fig. 4.4 that was taken at RT just after newly made crystal which contains four twin individuals because the all the diagonal Bragg reflections *(±h±h1)* are splitted into distinct three separate reflections and *(hk1)*-type reflections are splitted into four but as the angular separation is very small ($\Delta \sim 0.63^0$) they are highly overlapped. To distinguish the different twin individuals a Zoom section of the experimental *(hk1)* reciprocal plane has been shown in Fig. 4.7 with average *F4/mmm* unit cell (black square) where two unit cell (circle) are selected and indexation of each main Bragg reflections corresponding to different domains has been done in middle panel (Domain 1 and 2) and lower panel (Domain 3 and 4). Following the color code and subscript of each domain depicted in model (Fig. 4.6) it is clear that *(-111)* diagonal mirror is lost for domain1, 2 and *(111)* mirror plane for domain3 and 4. The crystal measured on ID29 beamline see Fig. 4.5 (below) it contains two twin individuals only one *(-110)* mirror plane is lost and in the same way with help of two twin domain model Bragg reflections can be indexed. This is how we can identify the twin elements, twin domain and corresponding main structural Bragg reflections, next step will be to assign the weak superstructure reflections with help of *(3+n)*-dimensional incommensurate modulation.

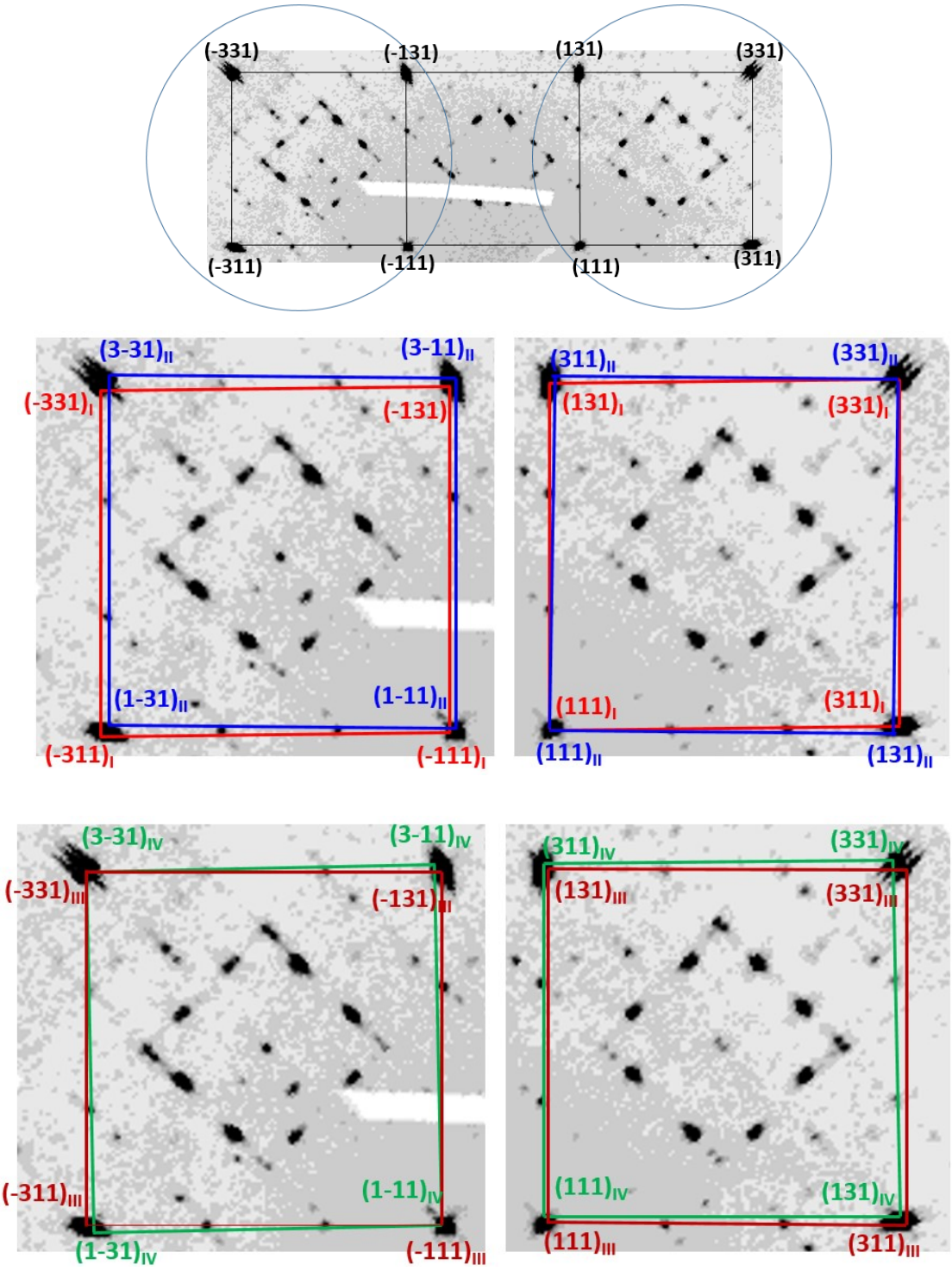

Figure 4.7: Indexation of main structural Bragg reflections in each twin individuals. (top) selected section from Fig. 4.4 where two diagonal unit cell are selected taking a average *F4/mmm* space group (black square). (middle) shows reflections under twin domain 1 and 2 where as (bottom) reflections belongs to domain 3 and 4. The reflections are highly overlapped and the angular separations for *(hk1)*-type reflections is Δ and that for *(±h±h1)* is 2Δ.

4.2.1.3 *(3+1)*-Dimensional Incommensurate Modulated Structure in *(hkn)* Plane where n = integer

The fundamental Bragg's law in X-ray physics tells us that when there is periodic arrangements of real space lattice in three dimension the whole lattice gives rise to a diffraction pattern following the law $2dsin\theta = n\lambda$ that generates a 3D reciprocal lattice and from that it can be determined the crystal structure and its lattice symmetry elements all coming from atomic ordering. But there are some situations that appears where all the diffracted reflections cannot be indexed with help of conventional any of related *Bravais lattice* means they do not belongs to that point or space group and in order to explain those unindexed reflections we need to introduce other dimension which defines the reciprocal wave vector $\boldsymbol{q}$ corresponding to those extra reflections that propagates from the main Bragg reflections forming so called "modulated structure". Structural modulation give rise to satellites that can have two origin either displacive (or positional) modulation where atoms are displaced from their regular lattice sites in a periodic manner, or occupational modulation whereas atoms occupy the sites with a periodic probability. Now if the periodicity of those modulation becomes a subset of the periodicity of basic *Bravais lattice* then it is called "commensurate modulated structure" and if not then it is called "incommensurate modulated structure". To put it in a simple way that in modulated structure the reciprocal lattice composed of two kinds of reflections, the main reflections forming a lattice which corresponds to the average unit cell, and the superlattice reflections generally of weaker intensity, also called satellites, which are generated by long range ordering of any kind, *i.e.* by the modulation waves. The mathematical derivation for modulated structure can be found elsewhere [10, 11].

Commensurate superstructures can described by a larger three dimensional unit-cell, with a volume of N times the basic one (N integer), still having usual space group, although different from the average one. Whereas incommensurate modulation does not obey the classical requirements for crystals; *e.g.* no general space group can be assigned to the symmetry of their atomic structure although their long-range order is as perfect as the one we find in ordinary crystals. In order to introduce the basic concept of higher dimensional crystallography for incommensurate phases, it is possible to start from the general expression of the reciprocal vector giving the position of Bragg

peaks in the reciprocal space given by $\boldsymbol{G} = h\boldsymbol{a}^* + k\boldsymbol{b}^* + l\boldsymbol{c}^* + m_n\boldsymbol{q}_n$, where $\boldsymbol{q}_n$ is the modulation vector in n dimension and defined as $\boldsymbol{q}_n = \alpha_n\boldsymbol{a}^* + \beta_n\boldsymbol{b}^* + \gamma_n\boldsymbol{c}^*$ and m_n is the order of the that modulation vector and it is an integer number. If at least one of the three coefficients α, β or γ of a vector $\boldsymbol{q}_n$ is irrational, the modulation is incommensurate, whereas if all are rational numbers, it exists at least one integer number N for which a new unit cell N times larger than conventional unit cell in real space (called supercell) can explain all the reflections and in this case the structure is called commensurately modulated and satellites are called superstructure reflections. Most importantly the extra dimensions *(3+n)* for such cases must be introduced to define the modulated wave vector $\boldsymbol{q}_n$, here dimension n relates the minimum number of independent wave vector that is required for integer indexing of the diffraction pattern. To define the dimensionality is bit tricky as in many cases the crystals with two dimensional modulation, two wave vectors are related also with symmetry of the average unit cell that makes them rationally independent even though they are not independent.

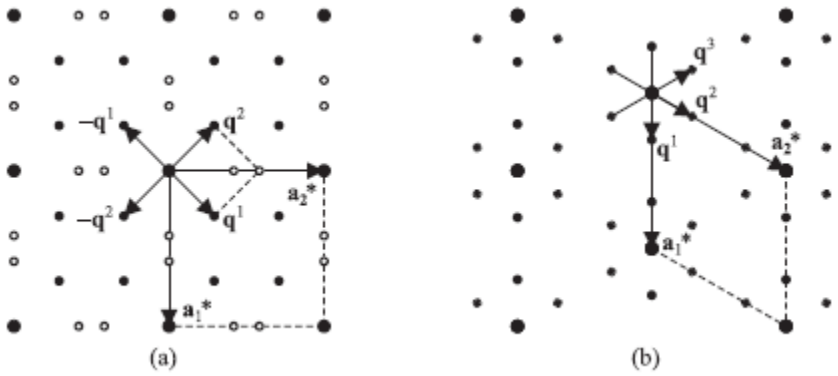

Figure 4.8: Diffraction by two-dimensionally modulated crystals. (a) *(hk0)* section of the diffraction pattern of $Ca_2CoSi_2O_7$. (b) *(hk0)* section of the diffraction pattern of 2*H*-$TaSe_2$. Large discs denote main reflections, small discs represent satellite reflections. Open circles indicate second-order satellites of the type $\boldsymbol{q1} \pm \boldsymbol{q2}$ in $Ca_2CoSi_2O_7$. Taken from Fig. 1.12 of ref. [11].

Fig. 4.8a illustrate such example where the wave vector $\mathbf{q}1 = (0.2913, 0.2913, 0)$ is mapped onto the vector $\mathbf{q}2 = (-0.2913, 0.2913, 0)$ by the fourfold rotation and is called two-dimensional modulations, because two rationally independent wave vectors suffice for an integer indexing of the Bragg reflections. Another example has shown in Fig. 47b where the diffraction pattern can be

indexed with integers on the basis of the two modulation wave vectors, ***q1*** = (0.327, 0, 0) and ***q2*** = (0, 0.327, 0). Together with ***q3*** = −***q1*** + ***q2*** = (−0.327, 0.327, 0), they form a set of three symmetry equivalent wave vectors. Any pair of them can be used for an integer indexing of the Bragg reflections, and the third vector can always be expressed as the sum or difference of the other two. From a physical point of view the modulated crystal contains three equivalent modulation waves, but for crystallographic purposes an indexing of the Bragg reflections with two wave vectors is most fruitful *(n = 2)* and 2*H*-$TaSe_2$ will be then denoted as a two-dimensionally modulated crystal.

Identifying super space group of such modulated structure in higher dimension can be done by finding the point group of basic reciprocal lattice (which brings the Bragg reflection to other with same intensities) and the propagation vector (a linear combination of basis vector of basic reciprocal lattice in 3D). Then following space group of basic average unit cell it has to look for *(3+n)* Bravais lattice for all the reflections including satellites in super space. Depending on the coefficient modulated wave vector and newly found Bravais class with experimental extinction and centering of the lattice, we have to choose the super space group that has been tabulated in ref. [10]. Finally it has to be validated among different possible solution by refining the structure. The examples that are shown in Fig. 4.8 is from crystal structure which does not exhibits twin, if the modulated structure also shows twin effects then it has to be accounted for finding modulation vector and super space group which is very difficult some time because of number of domains, overlapping of reflections and higher order satellites. Now we will be able to index all the satellites by considering both twin and incommensurate modulation in super space. Fig. 4.8 represents reconstructed *(hk1)* plane where only two reciprocal unit cell has been shown having *(110)* diagonal mirror plane which is not lost and only two twin domains are presents. Following symmetric operation of twin law each satellites can be ascribed to its specific twin domain. Therefore idealized reciprocal diffraction pattern can be simulated for two twin domains as shown in Fig. 4.9 (bottom). If we follow one twin domain e.g. domain 1 (red) then we need two modulation vectors for indexing the all satellites where those vectors are $\boldsymbol{q}_{1a} = 0.831\boldsymbol{a}^* + 0.499\boldsymbol{b}^*$ and $\boldsymbol{q}_{1b} = -0.831\boldsymbol{a}^* + 0.499\boldsymbol{b}^*$. Satellites are visible up to 6^{th} order in this commensurate modulated structure.

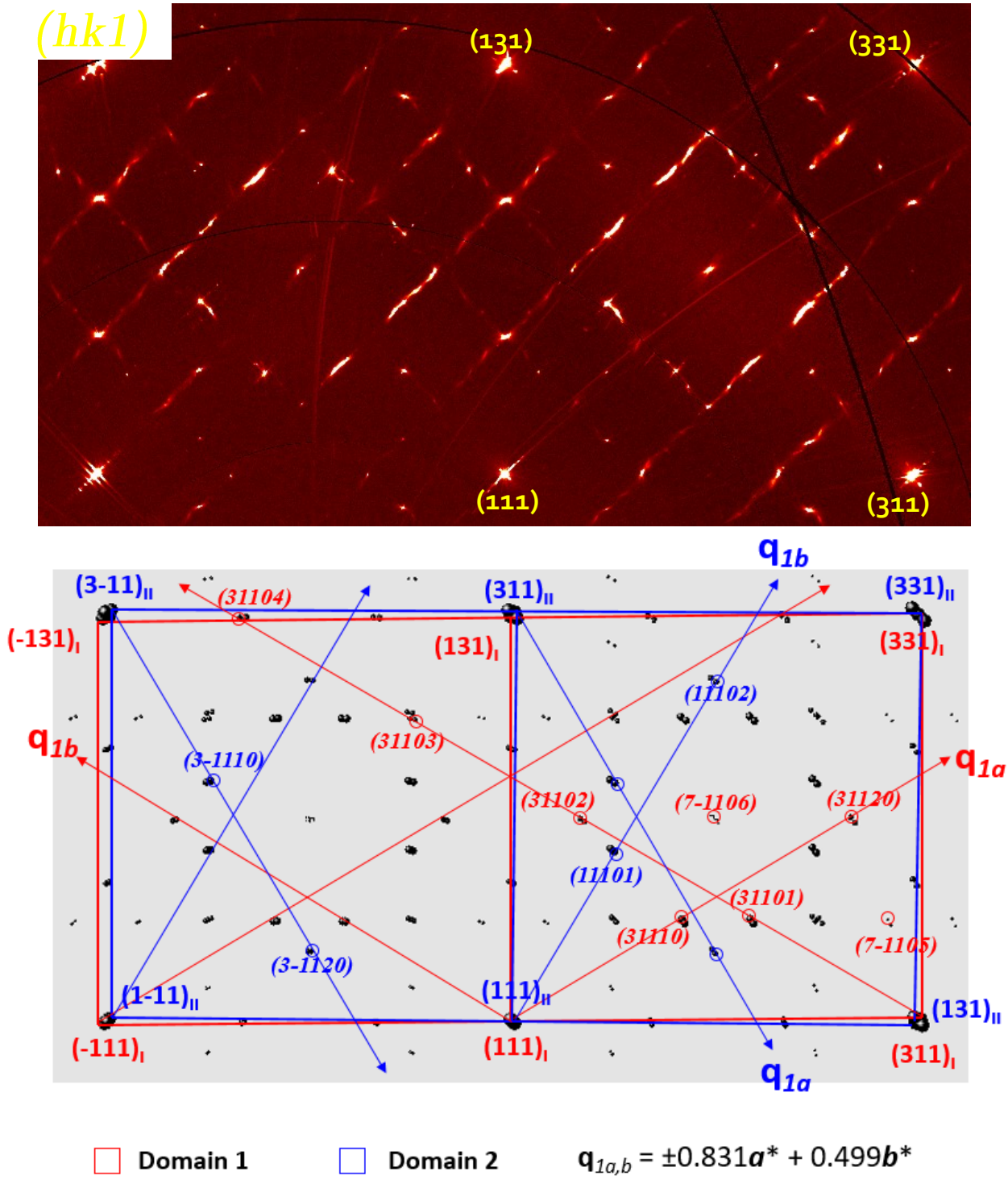

Figure 4.9: (Top) Zoom section of reconstructed experimental *(hk1)* reciprocal map of $Pr_2NiO_{4+\delta}$ single crystal obtained from synchrotron X-ray diffraction at RT on ID29 diffractometer at ESRF. (Below) illustrate the indexation on simulated pattern for *(hk1)* plane following the twin domain and commensurate modulation vector. Only two domain are considered for clarity and all the vectors are presented along positive directions. Red and blue circles indicated the satellites reflections in corresponding domain 1 and 2 respectively. Indexation has done in *(3+2)*-dimensional space with 5 miller indices. For details see the text.

We don't see the crossover satellites coming from $\mathbf{q}_{1a} \pm \mathbf{q}_{1b}$ means both vectors doesn't propagate simultaneously in the same domain. For domain 2 (blue) the satellites can be attributed in similar fashion only have to consider is the direction of a^* and b^* which is altered. In order to validate the model we have simulated the whole experimental pattern for *(hk0)* plane considering the concept of twin and modulation in higher dimension together. Figure 4.10 shows such simulated patterns for *(hk0)* plane. It says that not only this model is valid for particular one plane but also it is true for all the (*hkn*) plane where n = integer. Looking back to Fig. 4.4 where olive and blue lines represents the modulation vector for domain 1 and 2 respectively with yellow circles indicates the satellites order and it exactly similar to the simulated pattern in Fig. 4.10 where color codes are written in figure caption.

So far we have considered the space group of the each single domain is *Fmmm* as for average structure and because of orthorhombic nature the two vectors are equivalent and propagates in oblique way but they are rationally independent and it is needed to index those satellite reflections in average *Fmmm* unit cell for each domain and in that case it is called *(3+2)*-dimensional modulated structure. But if we detwin a single domain further we will see its *(3+1)*-dimensional modulated structure indeed with monoclinic symmetry *F2/m*. Each domain of basic structure is in fact twinned in two separate twin individuals (four in total in this case) because of the equivalent nature of those modulation vector. The twinning class in this case is of partial merohedral type means main reflections are almost perfectly overlapped but satellites are systematically separated. Therefore, the second twinning is only observable through satellites, but not *via* basic reflections also the intensity of Bragg reflections is ~10^3 order higher than satellites. The twin element is the mirror plane perpendicular to *a* and b**, *i.e.* this symmetry element is lost in the average structure and is applied between the twin lattices and that can be crosschecked by looking on to the satellites intensity which is not equivalent reflections. For instance, when taking into account only one pseudo merohedric domain of the basic structure e.g. domain 1, the satellites (*hklm*), (*h-klm*) symmetric by the *(100)* mirror and (*hklm*), (*-hklm*) are symmetric by *(010)* mirror plane are not equivalent; the

.

ratio between their respective intensities systematically results in the same proportion: 70-30 ± 5 % which twin's volume fraction of domain 1*a* and 1*b*.

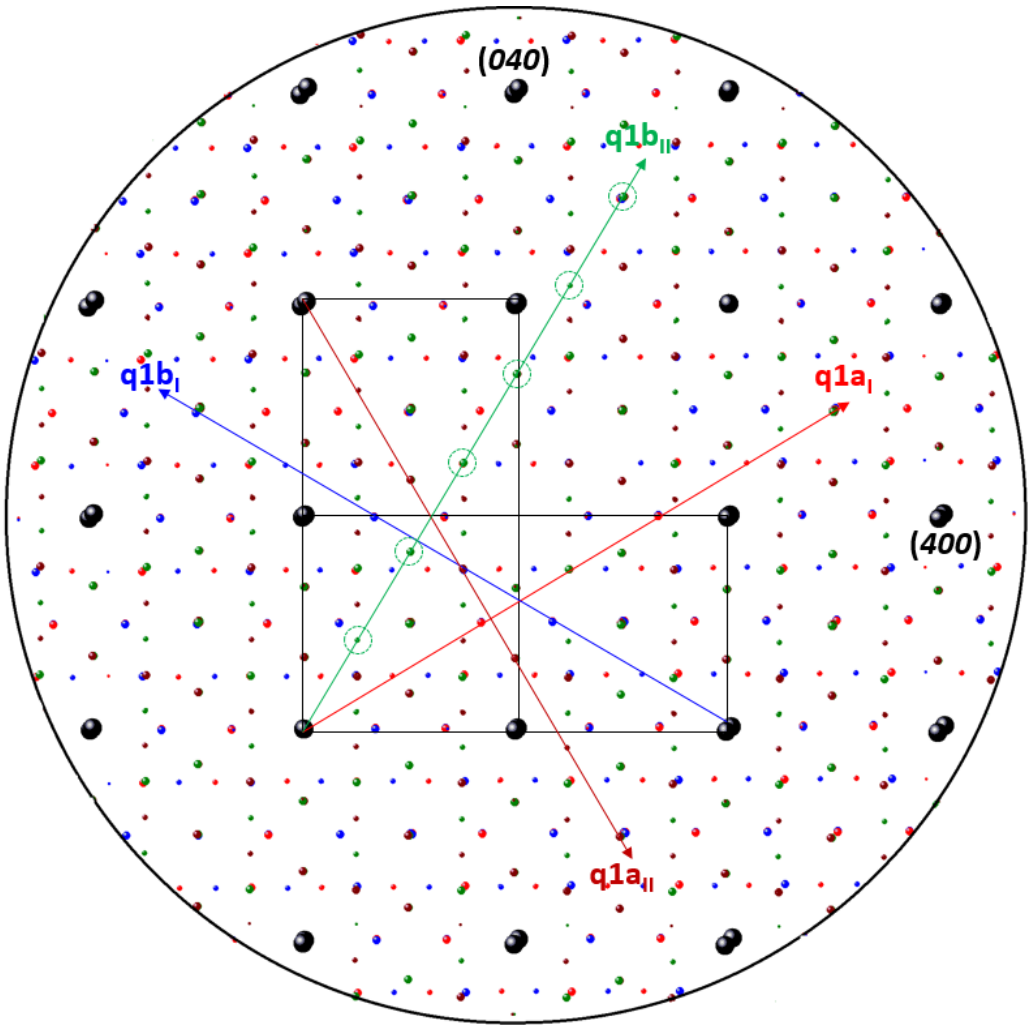

Figure 4.10: Simulated patterns for *(hk0)* plane similar to obtained experimental one in Fig. 4.4, calculated with modulation vector vectors are $\boldsymbol{q}_{1a} = 0.831\boldsymbol{a}^* + 0.499\boldsymbol{b}^*$ and $\boldsymbol{q}_{1b} = -0.831\boldsymbol{a}^* + 0.499\boldsymbol{b}^*$ for both individuals. Red and blue arrows denotes the modulation vectors in positive direction for domain one whereas olive and wine arrows for domain 2. Black box represents the average *Fmmm* unit cell with indexation. Olive circles indicates the order of the satellites and it is found to be six.

However the reflections *(hklm1)*, *(-h-klm1)*, remain equivalent by the twofold rotation axes as well as *(hklm1)* and *(hk-lm1)* by the mirror plane normal to *c**-axis. Therefore, vectors 1*a* and 1*b* shown on Fig 4.10 are invariant by the twin elements *(100)* and *(010)* mirror plane. In fact, only a single propagation vector **q1** *(α1, β1)* modulates the structure in the *a*-*b* plane, but in four distinct

twin individuals, it is called then *(3+1)*-dimensional modulated structure in *F2/m* space group. Figure 4.11 summarizes all of them, depending on their respective modulation vectors, in the left two basic pseudo merohedral twin domain *(Fmmm)* has been represented in magenta (domain1) and violet (domain2) where for domain 1 the modulation vectors are in red (q1a) and blue (q1b) whereas that in wine (q1a) and olive (q1b) for domain 2. If we separate both twin domain and there corresponding modulation then it will look like (b, c) in that figure. Further detwinning the twin domain1 give rises two other twin individuals ib space group F2/m with only one modulation vector (d, e) and similarly for domain 2 (f, g). Finally we can assign the super space group *F2/m(αβ0)(00)*, it is nonconventional *(3+1)*-dimensional superspace group can be derived from conventional *P2/m(αβ0)(00)*. The nomenclature of the superspace group can be found in ITC-vol. C [10] in detail. The monoclinic character of the modulation vector helps to simulate the diffraction pattern in *F2/m* unit cell coming from common *F*-cell after losing the both mirror plane. The quantitative analysis will be present in the next few section.

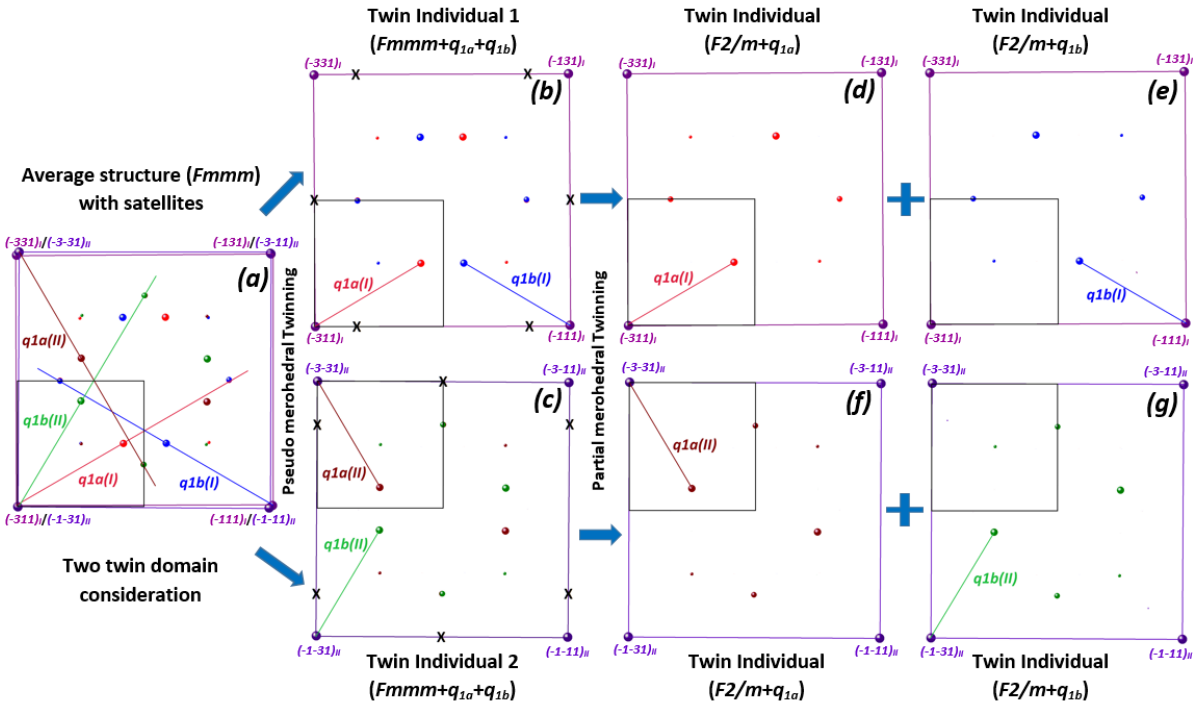

Figure 4.11: Detwin scheme to show how basic twin domain transform from average *Fmmm* to *F2/m* via intensities of satellite reflections and give rises four distinct twin individuals in total (d, e, f, and g). In case of four basic twin domain it will contain total eight twin individuals. Black square indicates basic orthorhombic unit cell.

However, depending on sample history and oxygen content complete different oxygen modulation can be obtained with different modulation vector. Fig. 4.12 shows such situation where the diffraction pattern of *(hk1)* plane which was recorded by X-ray diffraction on $Pr_2NiO_{4+\delta}$ at RT using diffractometer in ID23, ESRF. Sample history is not known but the modulation corresponds to high temperature phase which we will see in the chapter 5.

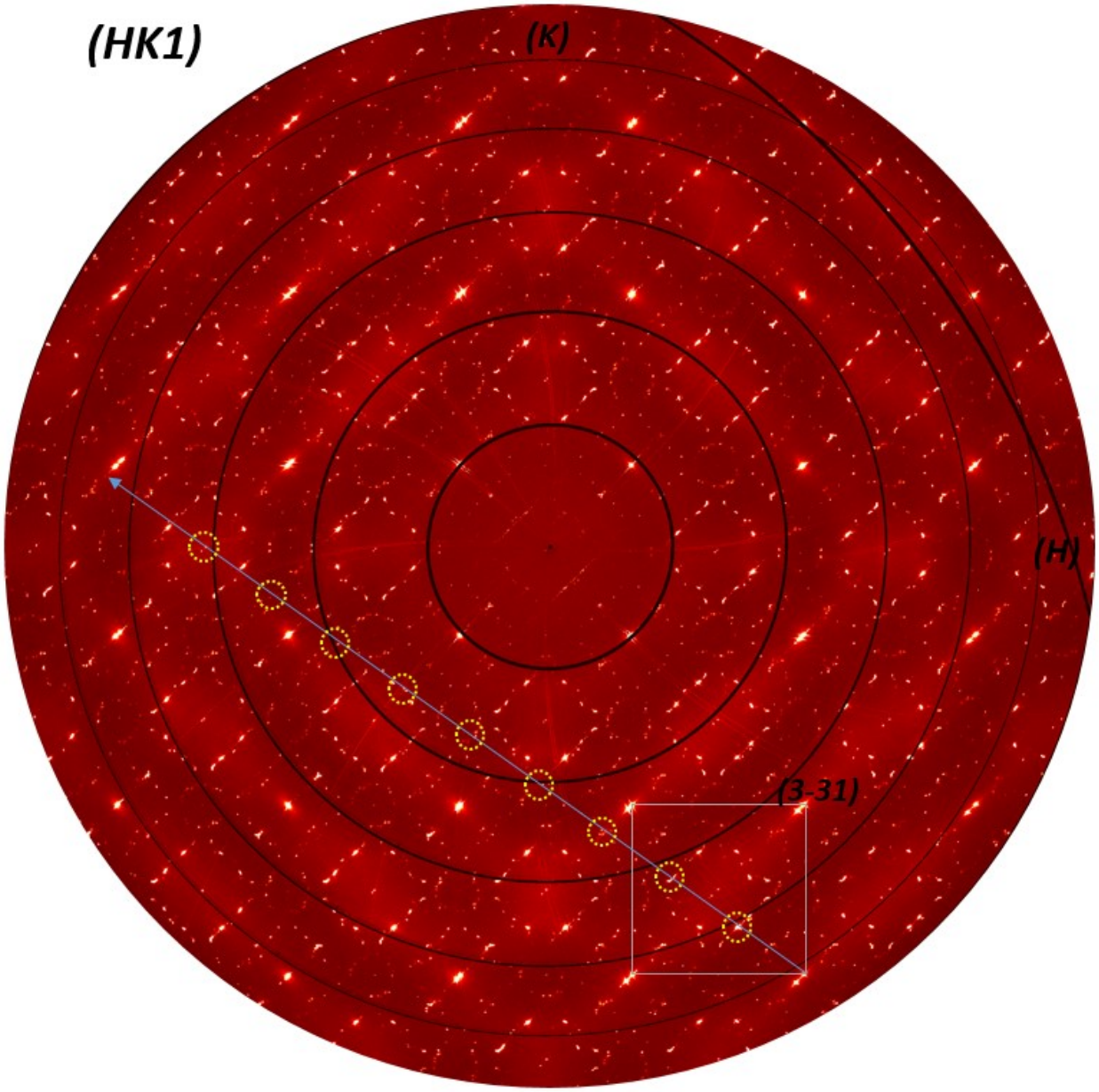

Figure 4.12: Reconstructed experimental (hk1) reciprocal map of $Pr_2NiO_{4+\delta}$ single crystal obtained from synchrotron X-ray diffraction at RT on ID23 diffractometer at ESRF. Diffraction pattern shows different oxygen modulation up to $N = 9$ order satellite with modulation vector $q = \pm 0.78a^* + 0.56b^*$ in each four incommensurate twin individuals.

4.2.1.4 *(3+2)*-Dimensional Incommensurate Modulation in *(hkn/2)* Plane where n = odd integer

The reciprocal space maps *(hkn/2)* with n = integer, *e.g. (hk1/2)*-type planes have been reconstructed. Figure 4.13 shows the *(hk½)* reciprocal plane of as grown $Pr_2NiO_{4.25}$ single crystal at RT. In this plane basic reflections are forbidden and as a consequence, all the reflections are satellites with irrational Miller indexes. A zoom on a characteristic part of the plane is shown together with the idealized positions of satellites, determined after careful observation of experimental data. The same vector $\boldsymbol{q_1}$ used to index satellites for $l = n$ (n = integer) do not have a component toward c^* ($\gamma = 0$) and even we take the component ($\gamma \neq 0$) it cannot index all satellites in this plane. Therefore, it has been chosen to introduce a second modulation vector $\boldsymbol{q_2}$ for indexing satellites with $l = ½$. Since this solution matches very well with experimental data, the results are detailed below. The reflections of the plane with $l = n + ½$ can be indexed with combination of both q_1 and q_2 commensurate vector which has component in a^*- b^* plane, $|\alpha_2| = 0.252$, $|\beta_2| = 0.249$, component along c^*, $|\gamma_2| = ½$. Only 1st order (m_2) of the $\boldsymbol{q_2}$ modulation vector has been observed. Consequently, two types of reflections are visible on the *(hk½)* plane: *i*) satellites ensuing from main reflections of *(hk0)* plane, with $m_2 = 1$; *ii*) satellites ensuing from main reflections of the *(hk1)* plane with $m_2 = -1$. So basically reflections in *(hk1/2)* plane coming from *(hk0)* and *(hk1)* plane since *(hk1/2)* does not contain basic Bragg reflections. Upon assigning each peak to its corresponding pseudo-merohedral twin domain, 1 or 2, on the basis of the twinning law and modulation vector shown in Fig. 4.13 it is possible to simulate and validate the model that has been done in Fig. 4.14 which shows both experimental (left half) and simulated (right half) are superposed in *(hk3/2)* reciprocal plane. All the *(hkn/2)* plane looks same, there is no difference in the position of satellites as they come from two planes up and down in same way. The difference of intensity between satellites generated by *(hk1)*-type main reflections ($m_2 = -1$) and by *(hk0)*-type ones ($m_2 = 1$) (small and large spots respectively on the Fig. 4.13), is proportional to the ratio of intensity between the main reflections themselves and its clearly visible. That is why, on *(hk½)* plane, intensity of satellites $m_2 = 1$ is stronger than the one of satellites $m_2 = -1$. As for the *(hk0)* or *(hk1)* plane, the reciprocal pattern of *(hk½)* plane can be indexed with vector q2a and q2b together with vector additions of

$q_{2a} + q_{1b}$ *and* $q_{2b} + q_{1a}$ (empty olive and blue circles on the Fig. 4.13) are observable whereas the reflections coming from $q_{2a} + q_{1a}$ *and* $q_{2b} + q_{1b}$ are systematically absent. For instance, for domain 1, First reflection comes from q_{2b} = (-0.252, 0.249, 0.5) with $m_2 = \pm 1$ and then follow the q_{1a} = (0.831, 0.499, 0) up to $m_1 = \pm 6$, similarly it follows for q2a and q1b, follow the disconnected black circle. For domain 2 it is solid black circle, but they can alter their position as all are connected with symmetry they will give the same results and pattern. Consequently, all satellites of the whole experimental reciprocal space can be indexed with 4 orthorhombic domains, basic space group *F*2/*m*, modulated incommensurately in two dimensions by q_1 and q_2, with $0 \leq |m_1| \leq 6$ and $0 \leq |m_2| \leq 1$ and corresponding space group is *F2/m*($\alpha_1\beta_1$0)(0*s*)($\alpha_2\beta_2$1/2)(00) in (*3+2*)-dimension.

However, the investigated $Pr_2NiO_{4.25}$ as grown crystal at RT consisting four distinct twin individuals in case of two basic twin domain and all the basic and satellite reflections on the a*-b* plane irrespective of l can be indexed in *(3+2)*-dimensional superspace with a general vector $\boldsymbol{G} = h\boldsymbol{a}^* + k\boldsymbol{b}^* + l\boldsymbol{c}^* + m_1\boldsymbol{q}_1 + m_2\boldsymbol{q}_2$ with $0 \leq |m_1| \leq 6$ and $0 \leq |m_2| \leq 1$. A superspace group approach is necessary to take into account long range ordering of oxygen and subsequent symmetries of the modulated structure. On the basis of the *F*-centered unit-cell modulated by the propagation vectors q1 (α1, β1, 0) and q2 (α2, β2, ½), and according to systematic extinctions, the general reflection conditions are the following: *(hklm*$_1$*m*$_2$*)*: $h + k = 2n$, $h + l = 2n$, $k + l = 2n$ and $m_2 = \pm 1$. According to these conditions, it can be proposed superspace group is *F2/m*($\alpha_1\beta_1$0)(0*s*)($\alpha_2\beta_2$1/2)(00). It is a non-conventional *(3+2)* superspace group derived from the conventional *P2/m*($\alpha_1\beta_1$0)(0*s*)($\alpha_2\beta_2$1/2)(00). Whereas in *(hk1)* plane it is *(3+1)*-dimensional modulated structure in *F2/m*($\alpha_1\beta_1$0)(0*s*) superspace group based on the *F*-centered unit-cell is totally legitimate and can be kept for modeling the modulation.

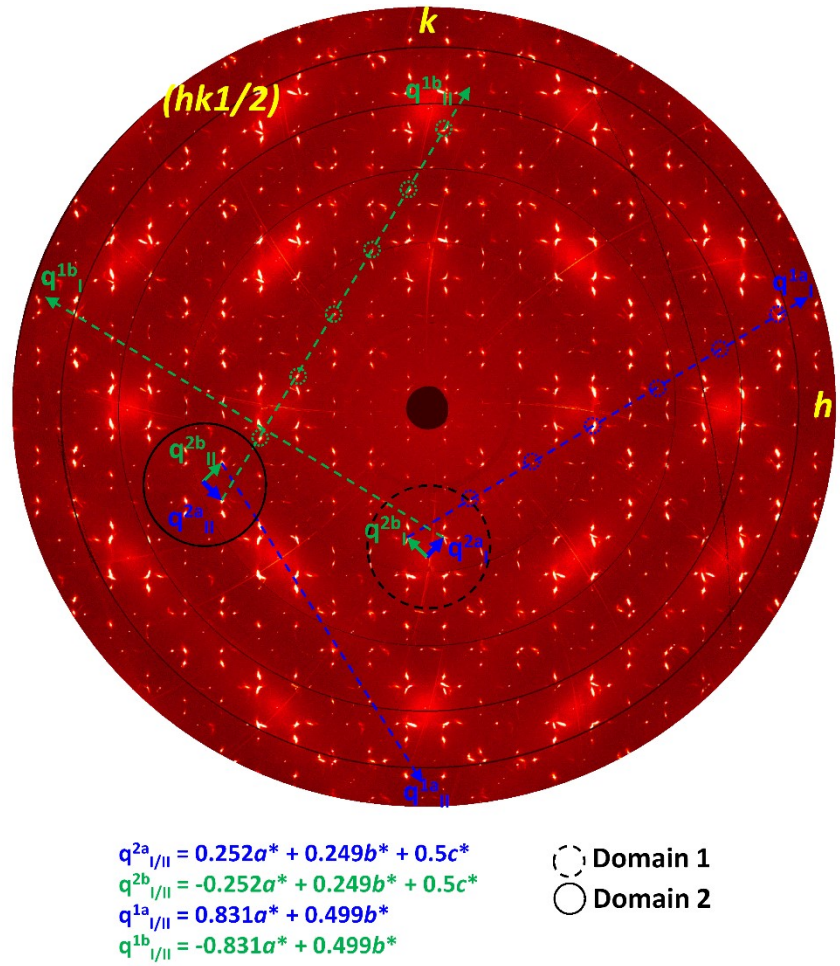

Figure 4.13: Reconstructed *(hk1/2)* plane, data obtained from same measurements and same crystal of $Pr_2NiO_{4.25}$ on ID29 diffractometer, ESRF. Bragg reflections are forbidden and only satellites are presents. Indexing is done with two modulation vector q_1 and q_2 which is written on the figure. Propagation of those modulation vector corresponding domain 1 is highlighted in disconnected black circle whereas for domain 2 in solid black circle. Small olive and blue circle represents the satellite position following vector q_1 as in *(hk1)* plane.

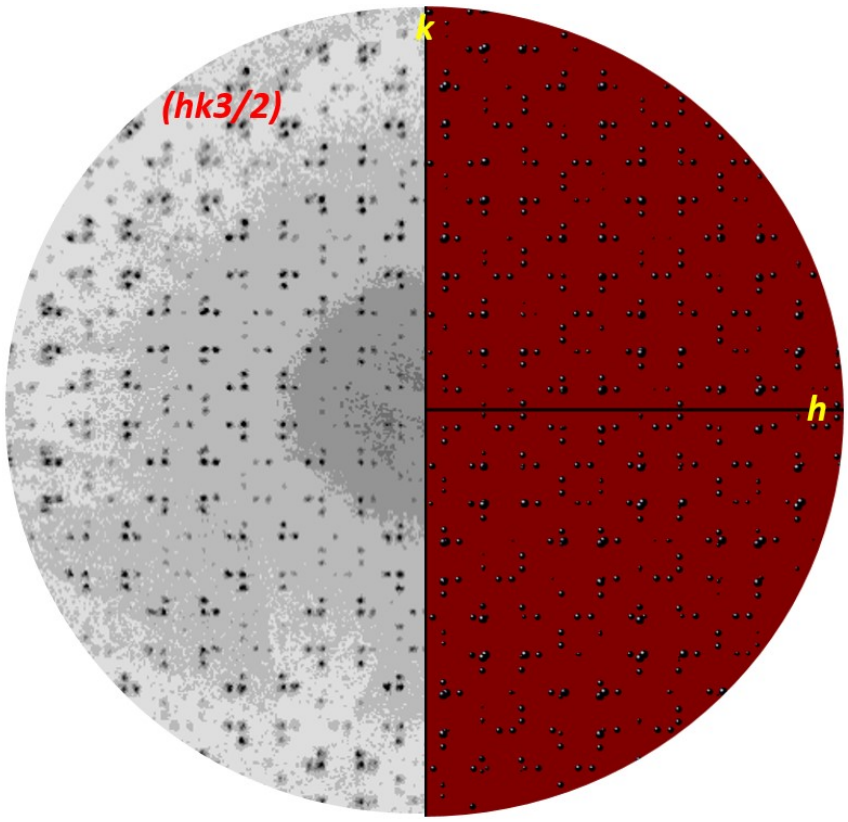

Figure 4.14: (left half) represents the experimentally obtained *(hk3/2)* plane and (right half) corresponding simulated idealized pattern following the model in Fig. 4.11. The *(hk3/2)* reciprocal plane looks same as *(hk1/2)* plane means commensurate modulation is invariant under $l = n/2$ dependence.

4.2.1.5: 3D Oxygen ordering and Diffuse Scattering in $Pr_2NiO_{4.25}$

So far we have seen *(3+2)*-dimensional modulation of oxygen ordering in *a*-b** plane perpendicular to *c**-axis and it has been described the twin domain corresponding microstructure based on observed reflection through reciprocal space map. Now we focus on other reconstructed plane perpendicular to [100], [010], [-1-10] and [1-10] directions so called *(0kl)*, *(h0l)*, *(hhl)* and *(h-hl)* plane obtained from same data set for $Pr_2NiO_{4.25}$. Fig.4.15 shows such kind of planes all together with several features like diffuse line along *c**-axis and many more different kind of oxygen ordering. For example if we look to the *(0kl)* and *(hhl)* reconstructed plane all the satellites are explained by previous section by looking to the incommensurate modulation of the oxygen ordering in *(hk0), (hk1),* and *(hkn/2)* planes except those marked in blue circles. The rectangular olive and yellow lines represents the satellites in *(hkn/2)*-, *(hkn)*-type plane respectively. The reflections marked in yellow circles are those 6^{th} order superstructure reflection falling on the diffuse line but as a strong separate reflections, so they don't come from continuous diffuse scattering this confirmed. For *(h0l)* and *(0kl)* plane diffuse lines are also splitted following the splitting of *(h00)*- and *(0k0)*-type Bragg reflections because of twin whereas only one diffuse line has been observed in (*hhl*) and (*h-hl*) plane because along *(110)* diagonal is non-splitted and *(-110)* is splitted in *(h-hl)* plane we see the projection basically perpendicular to [1-10] direction and they appears as overlapped. Interestingly those unindexed reflections marked in blue circles follows another kind of modulation particularly in these plane with non-zero component *(αβγ)* 3-dimensionally and that modulation changes with temperature. This feature will be discussed in next chapter. If we look carefully the diffuse lines actually modulated too with very small periodicity and quite high intense, a line profile corresponding to diffuse line between *(0-46)* and *(0-44)* Bragg reflections selected region has been shown in Fig. 4.16 where the intensity from Bragg reflections are omitted in order to scale the weak satellites. As it can be seen that strong *(0-45)* 6^{th} order superstructure reflection along with other very closely spaced reflections (total ~22 between main Bragg reflections) that makes it almost continuous 1D-diffuse line. However, there are still other reflections presents which could not indexed with help of the adopted modulation vector.

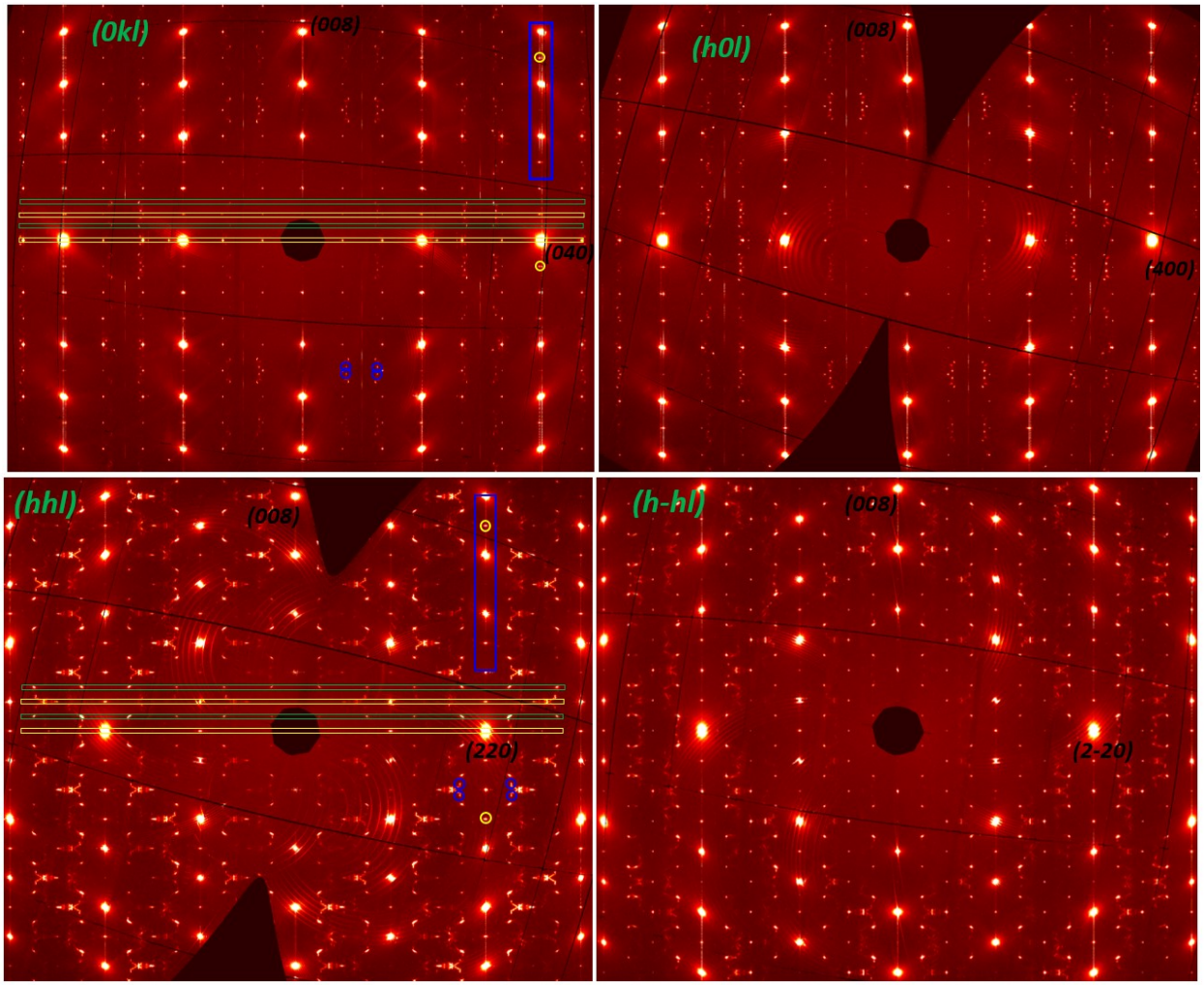

Figure 4.15: reconstructed reciprocal planes perpendicular to a^* and b^* (top), [-1-10] and [-110] direction (bottom). Blue rectangle shows the splitted and non-splitted 1D diffuse line in *(0kl)* and *(hhl)* plane respectively. Horizontal lines define the different l variation. The arc lines surrounding Bragg reflections are coming from air scattering.

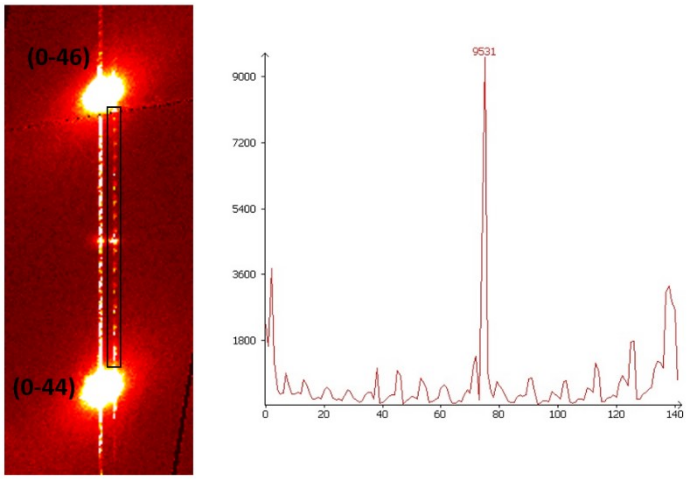

Figure 4.16: Intensity line profile for the selected regions of the 1D diffuse line in the left (black rectangle) showing weak reflections appears periodically including strong oxygen order peak.

4.2.1.6 3D volumetric representation of the oxygen ordering in $Pr_2NiO_{4.25}$ Single crystal

Representation of data is a state-of-art no matter how complex it is and sometimes important for of data treatment because it helps where to look and what to look. In this case without constructing reciprocal space map it can helps to find out how the ordering take place by walking through such 3D network and one could find out the modulations that are presents, what we all need is the information about the structure of the system. Therefore, we have presented in Fig. 4.17 such 3D volume data in reciprocal space reconstructed from same data set obtained on ID29 diffractometer. This whole data set was processed first by SNBL tool box to prepare the input file for UCSF chimera (ver. 1.11rc) which displays such big volume data set in 3-dimension basically it is made for visualizing complex structure of protein, virus, bacteria and big molecule. However, what we can see in the figure is the intensity of the each reflections are presented as volume along arbitrary direction (top left) and after suppressing the weak satellites it gives clear structural information. At first it is noticeable the high intense Bragg reflections with diffuse intensities e.g. *(200)* and *(220)* are nicely coming out along with 1D-diffuse rod along c^*-axis. Then by selecting a particular section with layer thickness (~0.05Å) we can prepare several planes having real intensity distribution of each reflections. The superstructure reflections are appeared exactly in the same position what we have seen in previous section and one can easily find out the modulation vector for any plane by rotating such volume data in 3D reciprocal space and this the advantage of such representation once you have whole network. Both way we can represents the results by visualizing or reconstructing reciprocal space map and both gives same results stating the structure is commensurately modulated.

As summary, as prepared $Pr_2NiO_{4.25}$ single crystal shows low temperature orthorhombic (LTO) phase, space group *Fmmm* for average structure and it consists of four twin individuals in basic two twin domain. Each twin individuals contain one single modulation vector q1 which explain the excess oxygen ordering in *(hkn)*-type plane in *F2/m* space group and in same way two wave vector q1 and q2 simultaneously propagates and modulate the structure in *(hkn/2)*-type plane. In general the structure is *(3+2)*-dimensional commensurately modulated where we can see the oxygen ordering

is not confined in one plane (2D) but it is 3-dimensionally ordered. The ratio of the volume fraction of two basic twin domains is about 56-44% whereas the volume fraction of corresponding twin individuals follows their parent basic domain fraction (32-24%, 26-18%). So the class of the twin belongs to partial-psedomerohedral twin highly overlapped of basic Bragg reflections has been seen this is one of the main reason not to be succeeded with structure refinement.

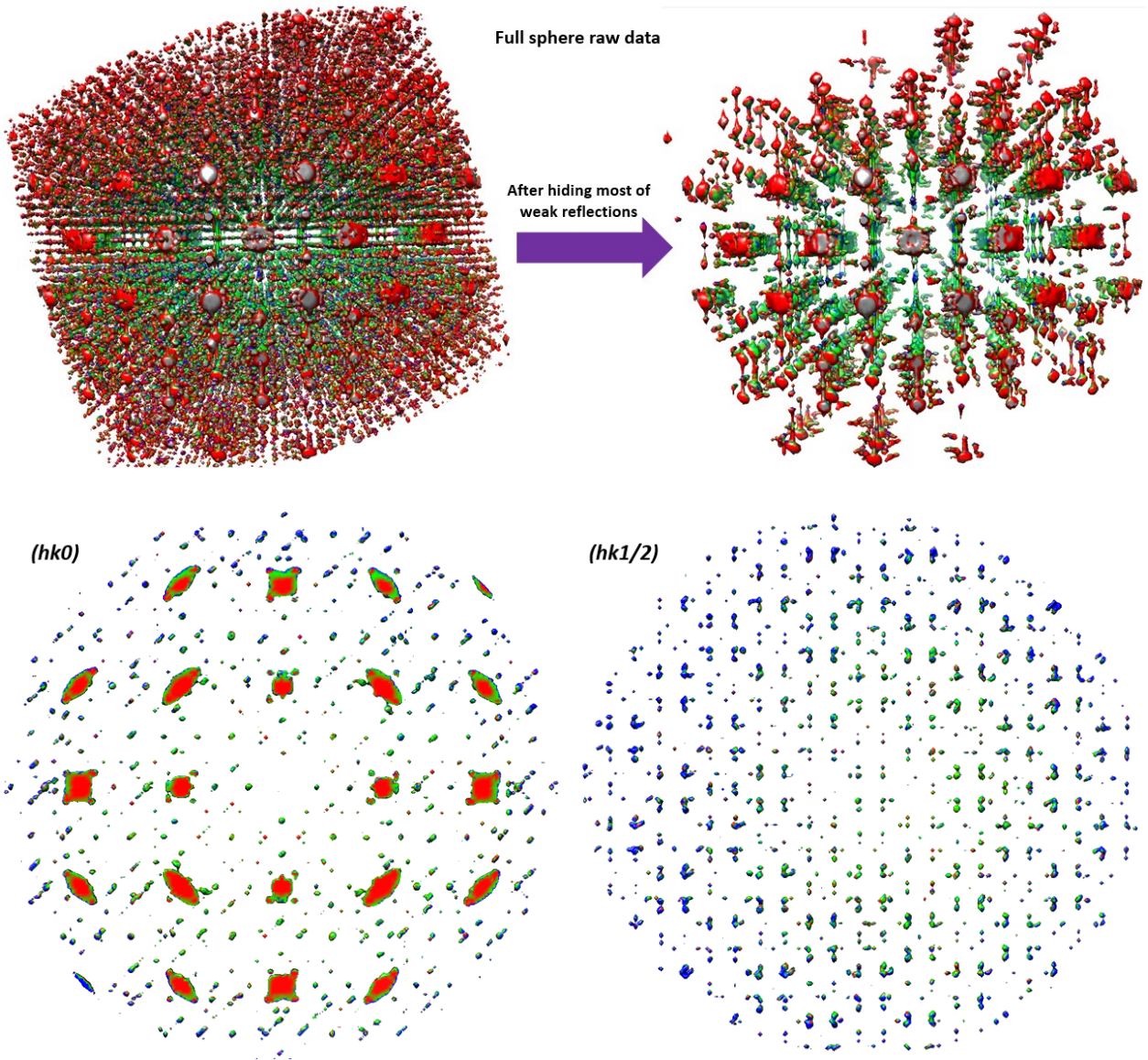

Figure 4.17: 3D-representation of volumetric single crystal data using Chimera (1.11rc) along arbitrary directions where all the reflections has been considered (top left) whereas after suppressing few of the weak reflections (top right). (Below) it shows the *(hk0)* and *(hk1/2)* reciprocal plane after cutting a slice of that 3D mesh and that resemble the obtained reconstructed map by using CrysAlisPro (Ver. 38.46)

4.3 *(3+1)*-Dimensional Modulated Structure of $Pr_{1.875}Sr_{0.125}NiO_{4+\delta}$ at RT

RT phase of as grown single crystal of $Pr_{1.875}Sr_{0.125}NiO_{4+\delta}$ ($\delta \sim 0.125$) was studied by SC X-ray diffraction on 4-circle STOE diffractometer as well as on diffractometer at ID28 (side station) high flux beamline, ESRF equipped with 1M PILATUS detector. When Sr is incorporated in the system by high temperature synthesis due to difference in ionic radius of Sr^{2+} (132 pm) and Pr^{3+} (113 pm) it gives rise to induce different tilting of NiO_6 octahedra compare to tilting in oxygen doped structure in such way that it reduce the structural distortion expected from bond-length mismatch and different Ni oxidation state it permits less oxygen atoms to get into the interstitial sites. As a results even though average structure does not change drastically but the microstructure corresponding twin domain and ordering of less excess oxygen changes. This is the main structural difference compare to oxygen doped $Pr_2NiO_{4+\delta}$ ($\delta \sim 0.25$). Fig. 4.18 represents the reconstructed reciprocal plane of *(hk1)* obtain after finding the good orienting matrix and unit cell from full sphere of single crystal data set. The intensities of weak reflections in *(hk1)* plane quite high compare to those in *(hk0)* plane and opposite for main Bragg reflections. Whole reciprocal map is invariant under two-fold rotation axis parallel to c* which confirms the orthorhombic nature. Average structure belongs to low temperature orthorhombic phase *(Fmmm)* with lattice parameter similar what has been found in X-ray powder diffraction. In the average orthorhombic structure *(-110)* diagonal mirror plane is lost and give rise two basic twin domain as in case of $Pr_2NiO_{4+\delta}$ but angular separation so called twin splitting for *(-hhl)*-type main reflections are less $\sim 0.5932^0$ as the orthorhombicity goes down making degree of overlapping higher. In the similar way all the reflection could be indexed using one general incommensurate modulation vector $\mathbf{q_1}$ and twin law. Only difference compare to oxygen doped sample is this modulation vector and order of the modulation. With help of $\boldsymbol{q_{1a}} = 0.7914\boldsymbol{a}^* + 0.5268\boldsymbol{b}^*$ and $\boldsymbol{q_{1b}} = -0.7914\boldsymbol{a}^* + 0.5268\boldsymbol{b}^*$ we have simulated the experimental pattern taking into account highest order of modulation is 4 and it is presented in the Fig. 4.19. The notation of the modulation vector was followed as before, all the higher order satellites greater than 4^{th} order are not presents and the predicted position of those absent satellites are marked as olive circle on

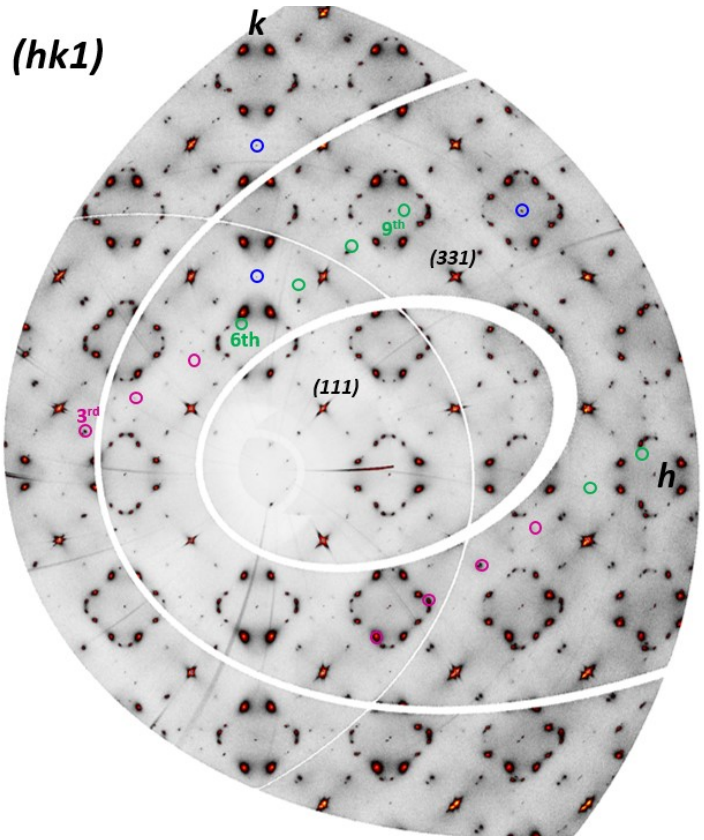

Figure 4.18: Reconstructed *(hk1)* plane, data obtained from sc X-ray diffraction of $Pr_{1.875}Sr_{0.125}NiO_{4+\delta}$ on ID28 diffractometer, ESRF. Patterns contains Bragg reflections and quite strong satellites. Indexing is done with one modulation vector $q_1 = \pm 0.7914a^* + 0.5268b^*$. Olive circles indicate the predicted reflection position higher than 4th order modulation but not present and blue circles denotes reflection coming from 1D diffuse line along c* (see Fig. 4.20)

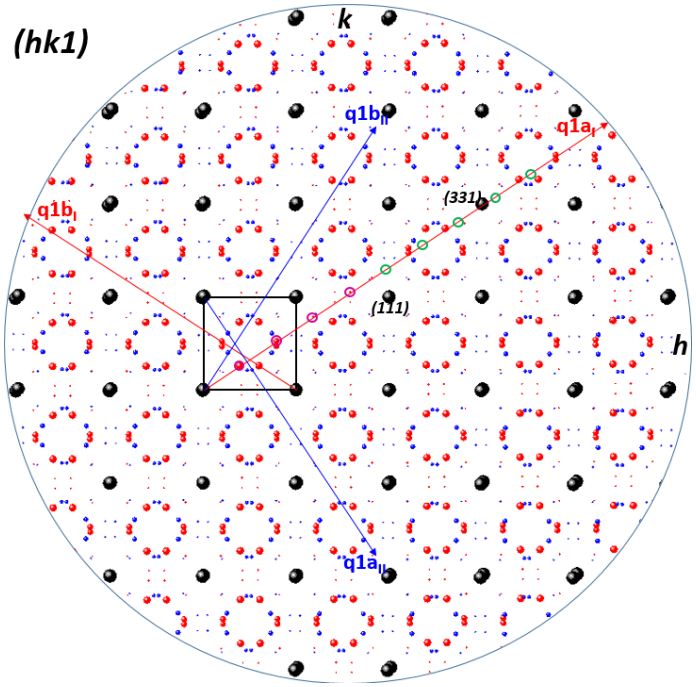

Figure 4.19: Represents simulated idealized pattern correspond to experimental *(hk1)* plane (shown above), is carried out with the modulation vector $q_1 = \pm 0.7914a^* + 0.5268b^*$ considering up to 4th order which has been observed in experimental diffraction pattern. Red and blue arrows indicated the direction of propagation vector belongs to domain 1 and domain 2 respectively. Representation of small olive circles correspond to absence of higher order satellites.

the Fig. 4.18 and 4.19. Simulation of the experimental pattern confirms the reflections marked as blue circles does not modulate and belong to modulated structure at least. If we look carefully to the experimental reciprocal plane it can be easily seen that the satellites corresponding domain 1 is way higher than satellites belongs to domain 2 and this comes from the volume fraction of the twin domain which is 56-44 %. The only reflections couldn't index with help of found modulation vector and unit cell are marked as blue circle because they are not modulated reflections they comes from the 1D diffuse lines goes along c*-axis in *(0kl)* or *(hhl)*-type reciprocal plane (see Fig. 4.20) and can be seen when the *(hk1)* plane is cut perpendicular to the diffuse line. Also the diffuse lines again splitted in twice because of the twin and does not contain string reflections in between.

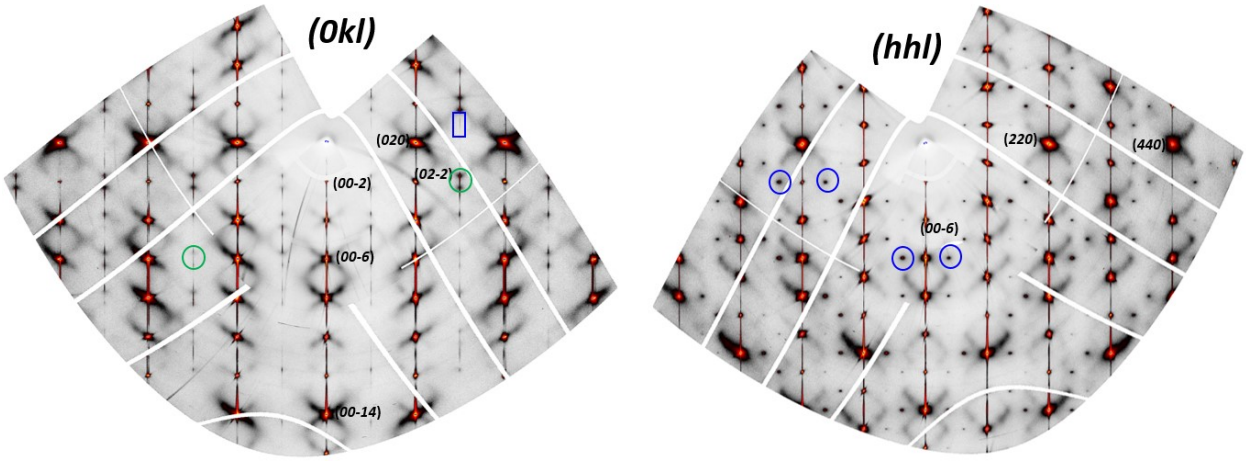

Figure 4.20: reconstructed reciprocal planes *(0kl)* perpendicular to a*. Blue rectangle shows 1D diffuse line responsible to give rise to reflections that appears on *(hk1)* plane indicated in blue circles. Olive circles shows the ordering of the satellite reflection as it does not belong to indexation of basic structure and does not fall exactly on $l =$ integer values however, in *(hhl)* all reflections are indexed and satellites in blue circle is the 3rd harmonics of the modulation.

Besides this diffuse line there is another kind of diffuse that appears surrounding the Bragg reflections sharing the corners of next Bragg peaks forming butterfly shape. This features need a further separate treatments to describe the origin and its behavior. The reflections marked in olive circle on Fig. 4.20 correspond to 3D ordering of oxygen and needs another modulation vector containing non zero component along c^* to index in that particular plane. In the *(hkn/2)* plane there is no ordering of superstructure reflection has been found, ordering of oxygen lost in the half integer plane perpendicular to c^* might because of less amount of oxygen and structural distortion.

In conclusion the LTO phase of $Pr_{1.875}Sr_{0.125}NiO_{4+\delta}$ consisting two highly overlapped basic twin domain modulate *(3+1)*-dimensionally as it needs one general incommensurate modulation vector to index all the reflections described in *F2/m(αβ0)(0s)* superspace group.

4.4 Structure of $Pr_{2-x}Sr_xNiO_{4+\delta}$ (x = 0.25 and 0.5) Explored by Single Crystal X-ray Diffraction at RT

Single crystal of as prepared $Pr_{1.75}Sr_{0.25}NiO_{4+\delta}$ (~ 0.04) was measure on STOE STADIVARI diffractometer and $Pr_{1.5}Sr_{0.5}NiO_{4+\delta}$ (~0.0) was measured on ID28 side station beamline at ESRF to see the as grown phase. Fig. 4.21 shows reconstructed *(hk0), (hk1)* and *(0kl)* reciprocal plane for each system where red and blue square in top left (hk0) plane represents the unit cell in tetragonal *I4/mmm* and non-conventional *F4/mmm* space group respectively, *F4/mmm* unit cell is derived by rotating the (3.8 x 3.8) unit cell 45^0. Reconstructed plane in the upper panel obtained from $Pr_{1.75}Sr_{0.25}NiO_{4+\delta}$ whereas those in lower panel collected from $Pr_{1.5}Sr_{0.5}NiO_{4+\delta}$. Both system exhibits pure tetragonal phase as it can be seen from the symmetry of the diffraction pattern without showing oxygen ordering as they do not incorporate excess oxygen with increasing Sr-doping. The structure is not twinned as it is tetragonal of course and lattice parameter is similar to what was found from powder XRD. From structure complexity point of view these system are quite simple compare to oxygen doped and less Sr-doped compound but they presents interesting other electronic and magnetic ordering at low temperature as well, we will see in next few chapters. Even though $Pr_2NiO_{4.25}$ and $Pr_{1.5}Sr_{0.5}NiO_{4.0}$ are electronically equivalent because of charge neutralization but not in terms of modulated microstructure, local oxygen or electronic ordering in long range but they are strongly correlated system if look to the charge or magnetic ordering at low temperature. No charge reflections are found at RT from these compound.

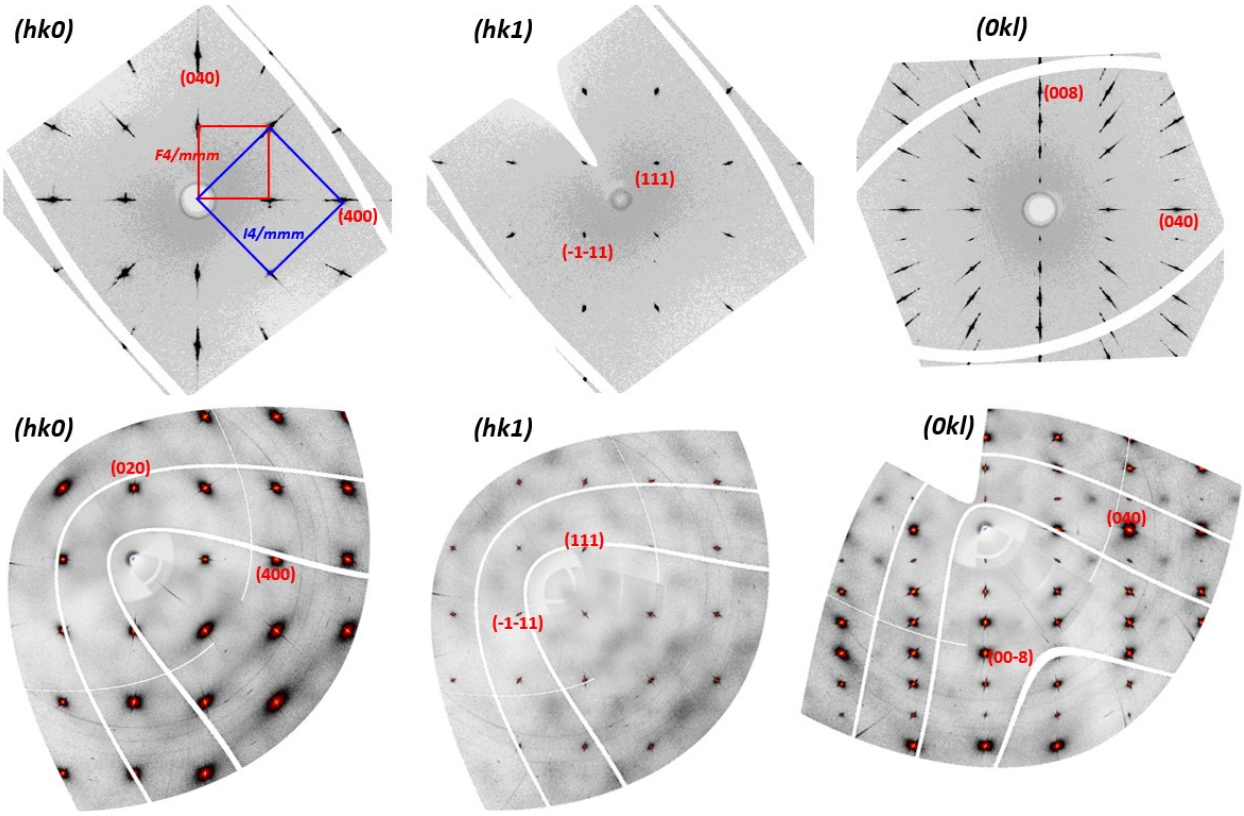

Figure 4.21: Reconstructed reciprocal *(hk0), (hk1)* and *(0kl)* space map from diffraction data of $Pr_{1.75}Sr_{0.25}NiO_{4+\delta}$ *measured on STOE STADIVARI diffractometer (top panel) whereas those of* $Pr_{1.5}Sr_{0.5}NiO_{4.0}$ measured on diffractometer in ID28 beam line, ESRF (lower panel). As it can be seen immediately the difference in intensities, resolution and diffuse scattering of the reflections measured from different diffractometer and area detector. No 1D diffuse line has been found in *(0kl)* plane as well for both system.

4.5 Summary

All the oxygen and Sr-doped $Pr_{2-x}Sr_xNiO_{4+\delta}$ (x = 0, 0.125, 0.25 and 0.5) single crystals have been investigated qualitative and intensively by powder and single crystal X-ray diffraction technique to develop the corresponding phase diagram at room temperature studying the microstructure changes based on excess oxygen ordering as function of commensurate to incommensurate modulation with twinning effects. Low temperature orthorhombic phase of pure oxygen doped $Pr_2NiO_{4.25}$ shows very complex pattern containing basic Bragg reflections along with huge amount of satellites where the average structure can be described in *Fmmm* space group. Local oxygen ordering give rise those satellites and has been indexed with help of general *(3+2)*-dimensional commensurate modulation

vector ($\boldsymbol{q}_1 = \pm 0.831a^* + 0.499b^*$) and twin law. Total 4 twin individuals makes difficulties but it helps to assign all the reflections in $F2/m(\alpha_1\beta_1 0)(0s)(\alpha_2\beta_2 1/2)(00)$ superspace group. For the $Pr_{1.875}Sr_{0.125}NiO_{4+\delta}$ system it is quite similar to oxygen doped compound only the modulation vector changes commensurate to incommensurate one ($\boldsymbol{q}_1 = \pm 0.7914\boldsymbol{a}^* + 0.5268\boldsymbol{b}^*$) which correspond to high temperature phase (we will see in chapter 5) but having different twin volume fraction and degrees of overlapping. The average structure is LTO *(Fmmm)* phase as well, all the reflections have been indexed in terms of *(3+1)*-dimensional incommensurate modulation in $F2/m(\alpha_1\beta_1 0)(0s)$ superspace group. No oxygen ordering has been found in *(hkn/2)* plane for $Pr_{1.875}Sr_{0.125}NiO_{4+\delta}$. Another difference of these two compound is the observed number of higher order superstructure reflections, maximum 6th order has been found in case of $Pr_2NiO_{4.25}$ whereas it is max. 4th order in $Pr_{1.875}Sr_{0.125}NiO_{4+\delta}$ this tells us the range of ordering is not same. It's all related to structural distortion which drives such different modulation and of course concentration of excess oxygen. To give an overview of how the intensities of different modulation order are distributed a graphical representation has been shown in Fig 4.22 for particular twin individual which is different from other individual as it depends on corresponding twin volume fractions. Other two Sr-doped nickelates (Sr = 0.25 and 0.5) both are tetragonal *(F4/mmm)* at RT with no superstructure reflections and oxygen ordering. From this it can be concluded that for certain oxygen concentration system start to show modulated micro structure in higher dimension because sample with Sr = 0.25 and 0.5) doping still contains a very low amount of oxygen and that has been verified by TGA. At least these ordering emerges once oxygen is ordered as there is no other source to give rise such satellites, there is no charge order peaks as well at RT and if there is no charge ordering take place means there is no spin order peaks as well, also not possible to detect by X-ray diffraction. To draw a conclusion on the RT phase diagram of as grown $Pr_{2-x}Sr_xNiO_{4+\delta}$ the phase diagram obtained from X-ray powder diffraction has been updated with results obtained from single crystal X-ray diffraction and shown in Fig. 4.23.

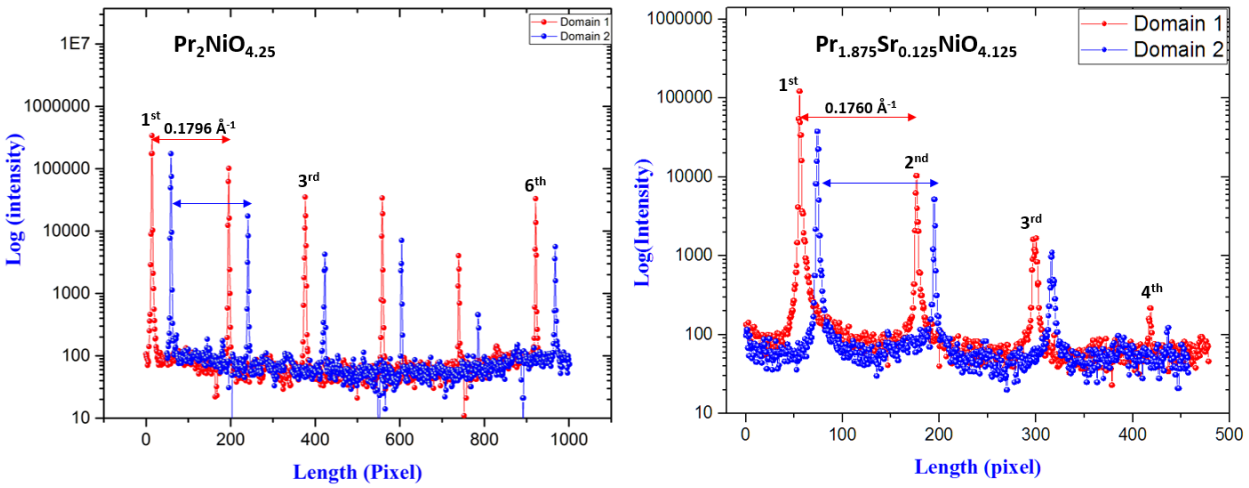

Figure 4.22: Graphical representation of line profile calculated from different satellite reflections along the modulation vector for $Pr_2NiO_{4.25}$ (left) and $Pr_{1.875}Sr_{0.125}NiO_{4.125}$ (right). Red and blue curve indicates basic domain 1 and domain 2 respectively in both plot. X-axis denotes the length in unit of pixel on the reciprocal map and Y-axis denotes intensity in logarithmic scale. Data obtained from superstructure reflections in *(hk1)* plane. For both system shows the intensity from domain 1 is higher than domain 2 as it follows the twin domain volume fraction. Red and blue arrows indicates the modulation period in reciprocal space correspond to 5.56 Å and 5.68 Å in real space for $Pr_2NiO_{4.25}$ and $Pr_{1.875}Sr_{0.125}NiO_{4.125}$ respectively. The intensities down to zero because of the detector gap which falls on the profile line during calculation. In each plot blue curve is shifted towards right side for clear vision.

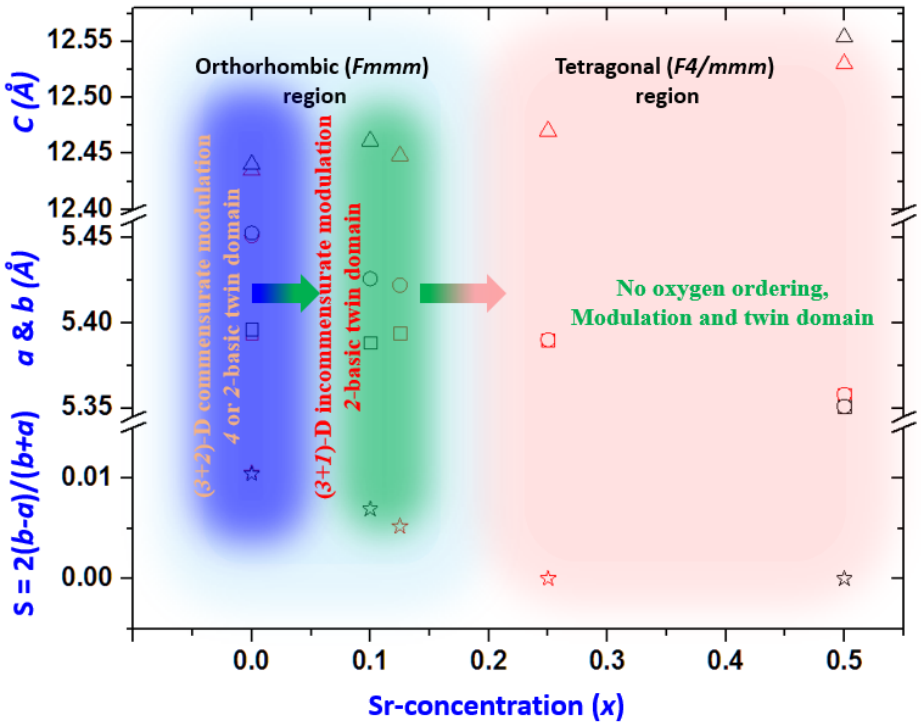

Figure 4.23: Updated RT phase diagram of $Pr_{2-x}Sr_xNiO_{4+\delta}$ which is shown in Fig. 4.3 where the phase correspond to microstructure has been added in terms of modulation and twin domain.

4.6 Difficulties

We have explained the average and microstructure of $Pr_{2-x}Sr_xNiO_{4+\delta}$ compounds from reconstructed reciprocal space map from 3D volume single crystal diffraction data set. In order to explain the structural distortion coming from bond-length mismatch and NiO6 octahedral rotation and mostly the classification of modulation is it displacive or occupational or both, we need to validate the structure by refining the structural model in *(3+n)*-dimensional superspace. For that a good data reduction is needed and here the problems come. First of all $Pr_{2-x}Sr_xNiO_{4+\delta}$ is highly X-ray absorber and anisotropic in nature. We have seen that it consists of micro twin domain up to maximum number of 8 individuals and the orientation of those domain and how much is absorbed by each domain is not known. This is the main problem for data reduction but still it can be solved in average scale if the diffraction is done on ideal spherical shaped single crystal and then spherical absorption correction could be applied or defining the face of tiny crystal followed by numerical absorption correction still not helpful because of anisotropic absorption. Even we manage the 1st step of difficulties another issues is availability of the software that can handle the incommensurate modulation together with twin domains. So far no such software is accessible, software like X-area or CryAlisPro they provide the data reduction option either considering only one domain with many more incommensurate vector or multi-domain with no modulation vector which is not our case. Still we are working in collaboration by using Eval15 software which can handle both situation (twin domain and incommensurate vectors together) but in a tricky way which works for system where the overlapping is not an issue but again our system is highly overlapped. Things are under progress to solve this kind of data reduction problem for particularly such system.

References:

1. J. Zaanen and O. Gunnarson, Charged magnetic domain lines and the magnetism of high-Tc oxides, Phys. Rev. B 40, 7391, (1989).
2. **K. Machida, Magnetism in La_2CuO_4 based compounds, Physica C 158, 192, (1989)**
3. J. M. Tranquada, D. J. Buttrey, V. Sachan, and J. E. Lorenzo, Simultaneous Ordering of Holes and Spins in La2NiO4.125, Phys. Rev. Lett. 73, 1003, (1994).
4. P. Babkevich , P.G. Freeman, M. Enderle, D. Prabhakaran & A.T. Boothroyd, Direct evidence for charge stripes in a layered cobalt oxide, Nature 471, 341 (2001)
5. J. M. Tranquada , H. Woo, T. G. Perring , H. Goka , G. D. Gu , G. Xu , M. Fujita & K. Yamada, Quantum magnetic excitations from stripes in copper oxide superconductors, Nature 429, 534, (2004).
6. M. Ceretti, O. Wahyudi, A. Cousson, A. Villesuzanne, M. Meven, B. Pedersen, J. M. Bassat and W. Paulus, Low temperature oxygen diffusion mechanisms in $Nd_2NiO_{4+\delta}$ and $Pr_2NiO_{4+\delta}$ via large anharmonic displacements, explored by single crystal neutron Diffraction, J. Mater. Chem. A, 2015,3, 21140-21148
7. Antoine Villesuzanne, Werner Paulus, Alain Cousson, Shoichi Hosoya, Loïc Le Dréau, Olivier Hernandez, Carmelo Prestipino, Mohamed Ikbel Houchati, Juerg Schefer, On the role of lattice dynamics on low-temperature oxygen mobility in solid oxides: a neutron diffraction and first-principles investigation of $La_2CuO_{4+\delta}$, J Solid State Electrochem (2011) 15:357–366
8. Web reference of FullProf, https://www.ill.eu/sites/fullprof/php/programs.html.
9. O. Wahyudi, M. Ceretti, I. Weill, A. Cousson, F. Weill, M. Meven, M. Guerre, A. Villesuzanne, J.-M. Bassat and W. Paulus, CrystEngComm, 17, 6278-6285 (2015).
10. International tables for cryatallography, Vol. C, ISBN 1-4020-1900-9
11. Sander van Smaalen, Incommensurate crystallography, ISBN - 13:9780198570820

Chapter 5

Investigation of *T*-dependent Modulated Structure of $Pr_2NiO_{4.25}$ by *in-situ* Single Crystal Synchrotron X-ray Radiation Diffraction

$Pr2NiO_{4+\delta}$ is one of the best candidates for oxygen ion conductor belonging to K_2NiF_4 family and good cathode material in SOFCs device for its high degrees of oxygen mobility at ambient. Oxygen is highly mobile in this compound at moderated temperature even down to room temperature. Compared to the other La-based oxides in K_2NiF_4 family, $Pr_2NiO_{4+\delta}$ draws more attention because of its higher structural stability and for its ability to accommodate large amount of interstitial oxygen. The recent studies by Ceretti et al. [1] and Perrichon et al. [2] have evidently shown that excess oxygen at interstitial sites plays the most important role to activate large displacements of the apical oxygen atoms towards [110]–crystallographic direction in the F–cell, and thus favoring oxygen diffusion towards interstitial sites within the rock-salt even at moderate temperature. The dynamical delocalization of apical oxygen atoms, strongly enhanced by lattice dynamics, has been identified as the prerequisite for oxygen ion diffusion in K_2NiF_4 type oxides at ambient temperature. In this regards changes in the crystal structure as function of temperature have been investigated since the phase stability of $Pr_2NiO_{4+\delta}$ with temperature becomes an important factor. Phase diagram of Sr-doped nickelates has been reviewed in chapter 2 showing successive phase transformation depending on Sr-concentration and temperature where HTT/LTO phase boundary of Nd- and Pr-nickelates shifts to higher x and T compare to La-nickelates. Structural changes of $Pr_2NiO_{4+\delta}$ with temperature has been investigated on powder sample by several neutron and X-ray diffraction studies [3-7] establishing HTT-LTO transition temperature accompanied with structural decomposition.

We are interested here to investigate the phase transitions that takes place in oxygen doped $Pr_2NiO_{4+\delta}$ single crystal as function of temperature and oxygen concentration (δ) by single crystal

synchrotron X-ray diffractions. The structural modulation in $Pr_2NiO_{4+\delta}$ single crystal corresponding the oxygen ordering has been explored at room temperature in the previous chapter. With increasing temperature from RT, structure walks through nearly-commensurate to incommensurate modulated structure which is very stable and kind of lock in phase respect to modulation keeping same twin basic twin domain all over the temperature range (100 to 400 ^{0}C) before entering to HTT phase. Recently in A. Maity PhD thesis [8] it has been discussed the phase diagram of $Pr_2NiO_{4.25}$ single crystal at ambient in the course of electrocheical reduction. The investigated was carried out to follow up the structural changes that occurs during electrochemical reduction in terms of the average structure and the changes in the microstructure by following the twin domain evolution. Analysis of commensurate superstructures revealed that the modulation did not change at all instead the intensities of the superstructures drop down to zero over the phase transition from orthorhombic $Pr_2NiO_{4.25}$ in *Fmmm* to tetragonal $Pr_2NiO_{4.12}$ in $P4_2/ncm$. We will highlight this in short to compare the results obtained from temperature dependence study. These two studies are complementary as they show different phase diagram depending on the environment in which system goes through and also important as we need to know the structural as well phase stability which is a key issue for being used in several energy applications.

There are not so many studies have been focused on the modulated structure of this titled compound by means of single crystal diffraction and hereafter we present the results in order to develop another phase diagram of $Pr_2NiO_{4+\delta}$ showing the microstructural changes (oxygen ordering, modulation vector, twinning etc.) in a wide range of temperature (RT to 1000 ^{0}C) and excess oxygen content ($0.125 \leq \delta \leq 0.25$) comparing with results from electrochemistry study along with TGA thermogram to show the variation of δ with temperature carried out on same single crystal batch. The aim of this chapter is to show the modulated incommensurability of each twin individual and corresponding modulation vector depends not only on excess oxygen content and temperature rather it is structural properties and influenced by many other parameters like structural distortions, reaction kinetics and external pressure as well.

5.1 Measurements Strategy

The temperature dependent *in-situ* investigation of $Pr_2NiO_{4+\delta}$ was performed on a needle shaped single crystal ($\phi = 50$ μm) in air atmosphere. The single crystal was mounted on the goniometer of BM01A diffractometer at ESRF. The crystal was glued on the top of a quartz capillary using high temperature resistant glue. The sample was heated from room temperature 30 ^{0}C to 1000 ^{0}C by flowing nitrogen stream focused locally on the sample. The temperature was increased with a rate of 10 ^{0}C/min. Starting from 50 ^{0}C, each data set was collected at an interval of 50 ^{0}C (*e.g.* 50, 100, 150, 200, 250, ..., 1000 ^{0}C). While collecting the diffraction data the temperature at the sample was kept fixed. The diffraction was performed with a beam orientation perpendicular to the axis of the cylindrical crystal using a wavelength of λ =0.66305 Å. For each rotation of 0.1^0 of the single crystal along its axis, the diffraction pattern was collected using the high resolution 2M–Pilatus area detector for an exposure time of 0.5 s of the SX-ray beam. In total 3600 frames were collected for 360^0 rotation in 30 minutes for each data set. During this 30 min of data collection period the temperature was fixed to a certain value.

5.2 Results and Discussion

The X-ray diffraction measurements were carried out on different batch of $Pr_2NiO_{4+\delta}$ single crystal compare to the crystal and corresponding results discussed in chapter 4. We will first present the RT phase followed by the evaluation of domain microstructure and modulation as function of temperature.

5.2.1 Structural Modulation Associated to RT Phase

Similar phase has been found already discussed in chapter 4 for the as grown $Pr_2NiO_{4+\delta}$ single crystal which shows average orthorhombic structure in *Fmmm* space group ($a = 5.394$ Å, $b = 5.459$ Å and $c = 12.438$ Å) with two basic twin domains. Fig. 5.1 shows the diffraction pattern where basic main reflections can be indexed in average *Fmmm* unit cell whereas weak satellites have been index with a nearly-commensurate modulation vector spanned by distinct individuals in a^*-b^* plane

but the observed incommensurate modulation vector was different compare to other RT phase (crystal discussed in chapter 4). In a similar fashion we can deconvolute the whole reciprocal diffraction pattern by using twin law and *(3+n)*-dimensional modulation vector in *(hkn)* plane, where n = integer specifying each satellite contribution from different individuals with their volume fraction. This structure is modulated in *(3+1)*-dimension as we don't see the ordering of excess oxygen in half-integer *(hkn)* plane and therefore with help of one general propagation vector $\boldsymbol{q}^1 = \pm 0.821\boldsymbol{a}^* + 0.493\boldsymbol{b}^*$ all the reflections can be indexed.

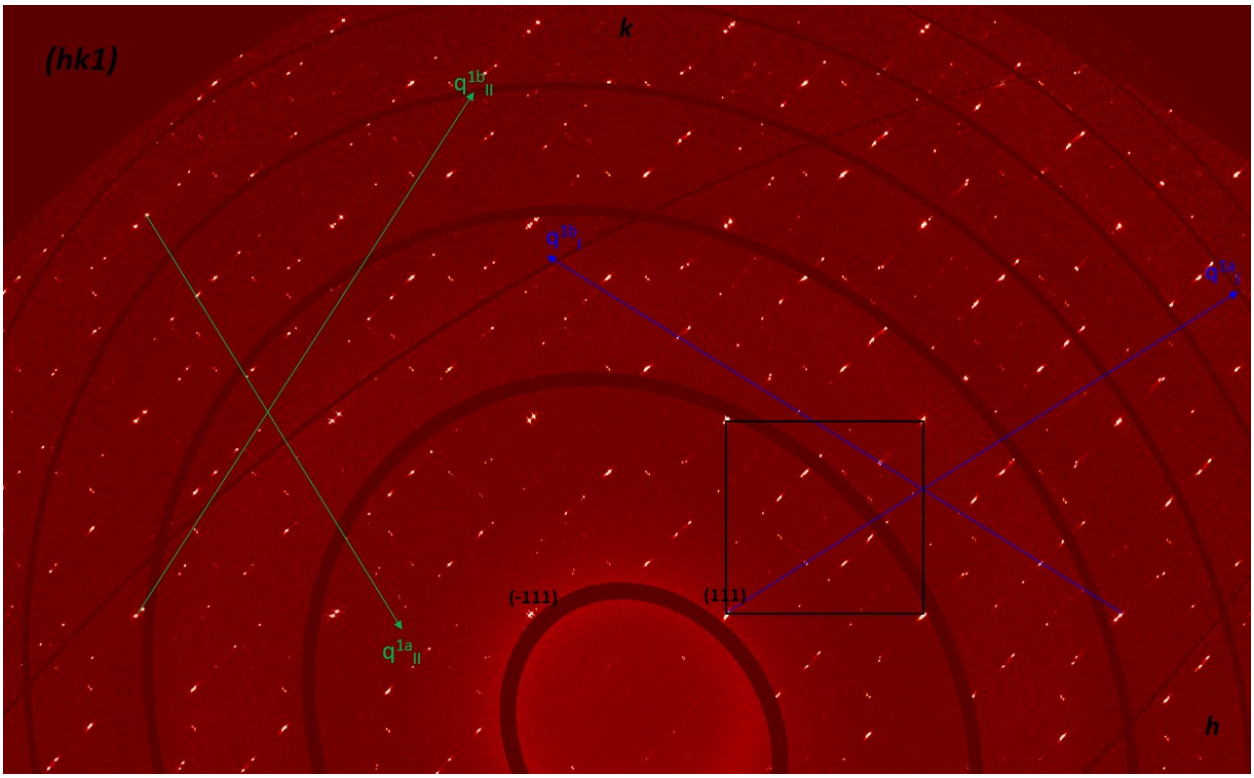

Figure 5.1: Reconstructed reciprocal *(hk1)* map of $Pr_2NiO_{4+\delta}$ obtained at RT showing *(3+1)*-dimensional nearly-commensurate modulated structure. Besides main Bragg peaks it contains weak oxygen ordered superstructure peaks in two basic twin domain where *(-110)* mirror plane is lost giving rise to splitting of *(-110)*-type reflections. Black box represents average *Fmmm* orthorhombic unit cell with modulation vector as blue and olive arrows for domain 1 and 2 respectively.

It is interesting to see that especially 4th order satellites are presents along $\boldsymbol{q}^{1b}$ vector for domain 1 (blue arrow) whereas it is along $\boldsymbol{q}^{1a}$ for domain 2 (olive arrow) in Fig. 5.1 as it can be seen the intensity of those individuals is higher than others and 5th and 6th order reflections are very weak to

be appeared. The twin volume fraction is about 44-56% for two basic domain. By studying this RT phase we can already point out that depending on the oxygen content in the starting phase of $Pr_2NiO_{4+\delta}$ structure it can modulate in different way at RT as it is evident from the propagation vector which is different from that one discussed in chapter 4 and also no ordering in *(hk1/2)*-type plane in present case.

5.2.2 Evolution of Structure and Modulation as function of Temperature

Fig. 5.2 presents the same section of reconstructed diffraction patterns where twin splitting of Bragg reflection is visible in *(hk1)* reciprocal plane by in-situ X-ray diffraction measurements on at various temperature starting from 50 ^{0}C - 1000 ^{0}C. Very sharp reflections indicates good quality crystal. In the beginning the structure is orthorhombic in two twin domains in the temperature range RT - 350 ^{0}C. Blue circles indicates the evaluation of the twin splitting of the Bragg reflections with increasing temperature and it becomes a single reflections near the temperature at 400 ^{0}C which is the boundary of the LTO/HTT phase where the phase transform from orthorhombic to tetragonal phase near 360 ^{0}C. It is important to note that even after phase transition at high temperature the oxygen ordering is still visible but appears as very weak diffuse ring indicated by olive circle in the Fig. 5.2(d). It confirms that oxygen content is lower than starting phase and highly mobile at high temperature that destroy the local ordering and transform into order-disorder phase. At very high temperature this order is completely lost and no such ring is visible means system is now completely disorder in terms of oxygen ordering. Calculated lattice parameters, volume, orthorhombic strain and angular separation so called omega splitting of Bragg peaks (2Δ) of orthorhombic domain are plotted in Fig. 5.3 and each of plot indicates the region of LTO/HTT phase transition. To give a better insight of the changes in modulation with temperature, Fig. 5.4 (a-h) represents a section of reciprocal space map that contains same one unit cell at different temperature respectively where it is clearly noticeable the intensity and sharpness of the satellite is getting lower indicating disorder state. Here in the Fig. 5.5 the evaluation of intensity and the angular separation of selected *(3-31)* reflections (blue square in Fig. 5.4 (a)) has been shown for different temperature.

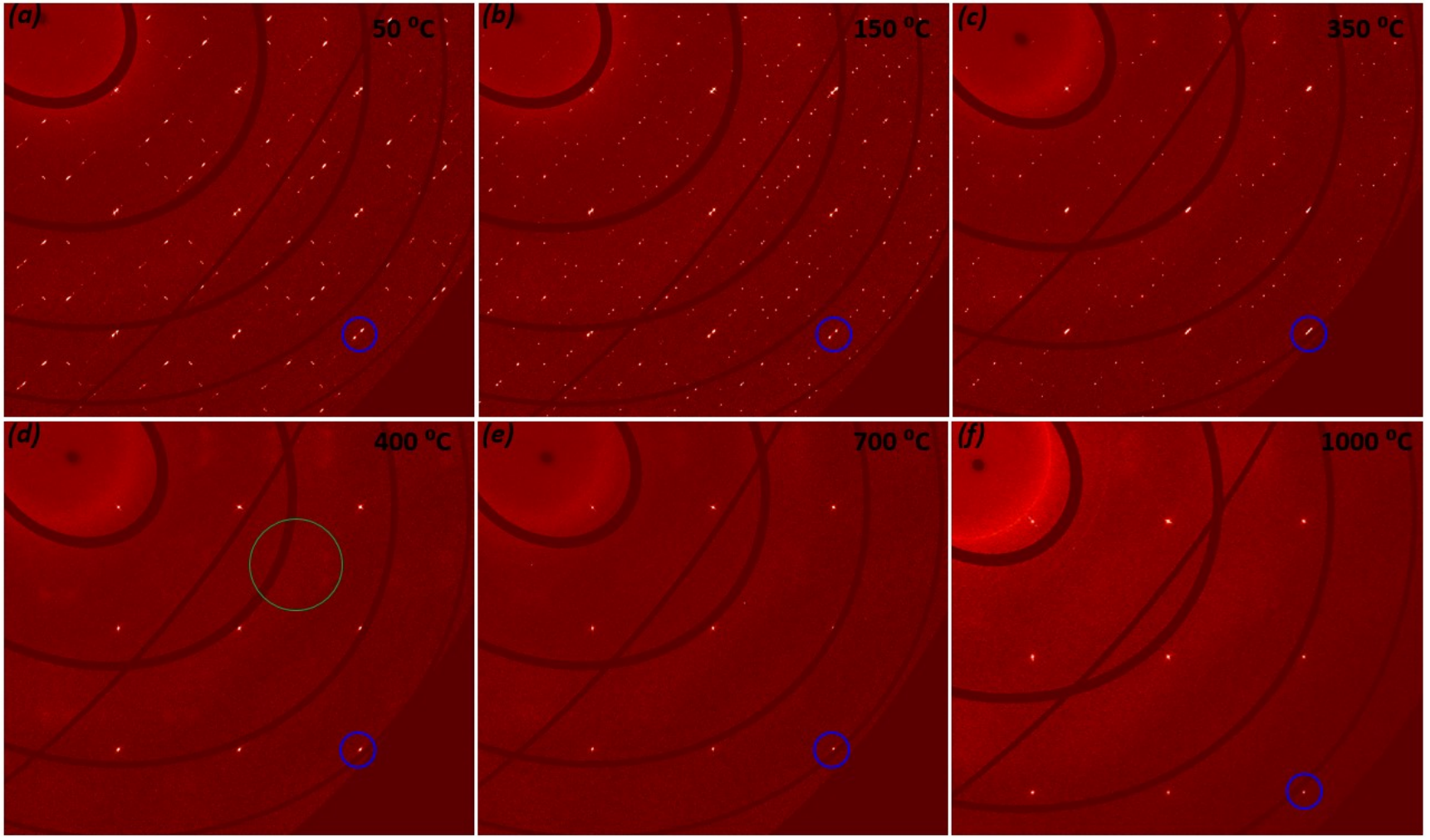

Figure 5.2: Reconstructed reciprocal *(hk1)* plane of $Pr_2NiO_{4+\delta}$ *showing the structural evaluation as function of temperature from RT to 1000 ʿC. Blue square indicated the orthorhombic twin splitting up to 350 ʿC and then one single Bragg peaks at HTT phase from 400 ʿC. Oxygen order get lost in this region of LTO/HTT phase transition. Olive Circle indicates the diffuse ring that coming from highly mobile oxygen ordering phase exactly at same position where the satellites should appear.*

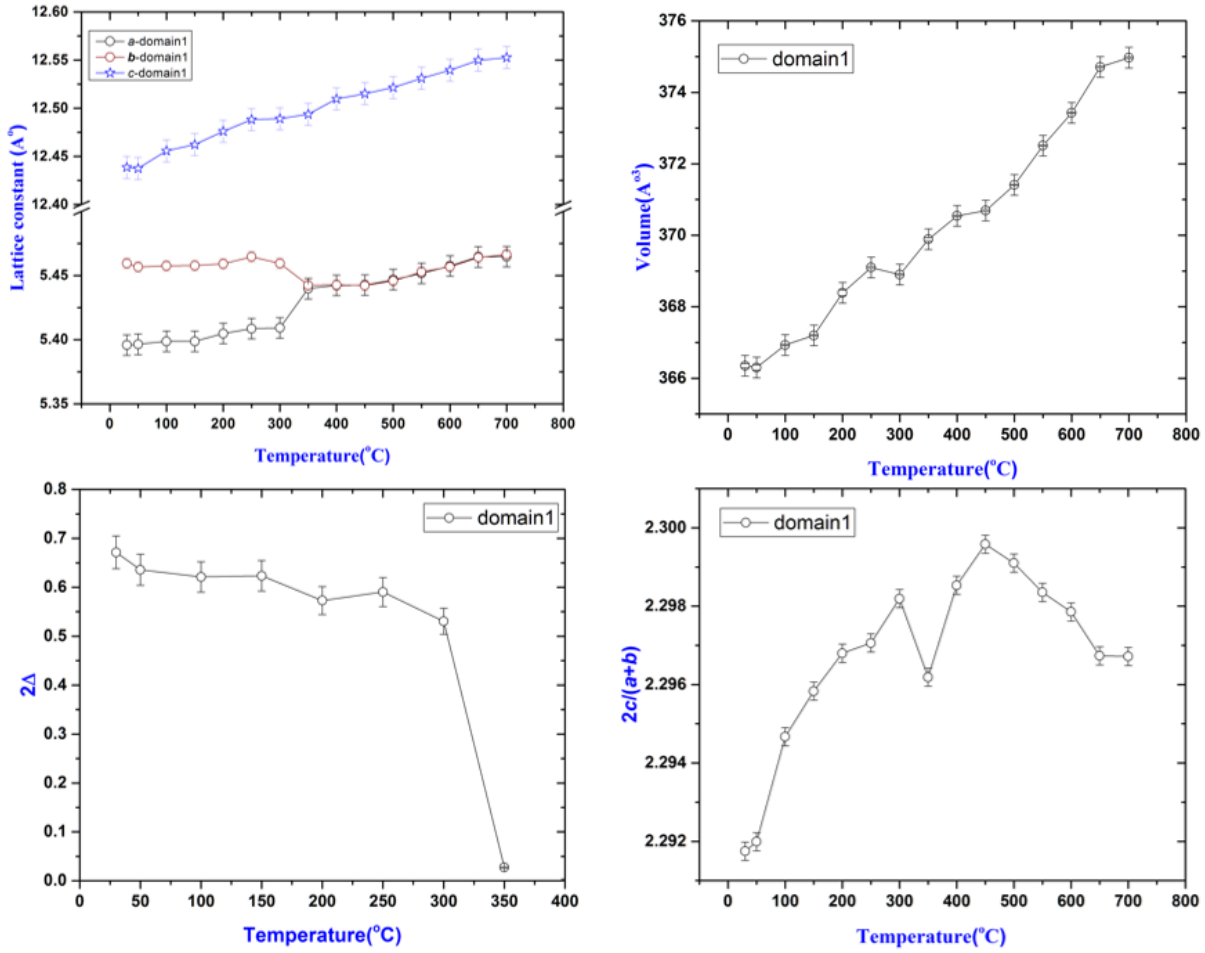

Figure 5.3: Graphs shows the variation of lattice parameters, volume of the unit cell, angular separation of splitted *(hhl)*-type Bragg reflections and orthorhombic strain as function of temperature. These are calculated from observed experimental pattern in Fig. 5.2.

One can see as the orthorhombicity goes down with temperature angular separation of the splitted *(hhl)*-type reflections become smaller as well. At temperature 300 ^{0}C (olive curve in Fig. 5.5) a new tetragonal peaks are coming and with increasing temperature it becomes stronger and become a single reflection at 400 ^{0}C (red curve) where structure transform into complete tetragonal phase. Also it gives an idea about the volume fraction which can be estimated from the intensity of each domain and it is nearly 44-56% for basic two twin domain.

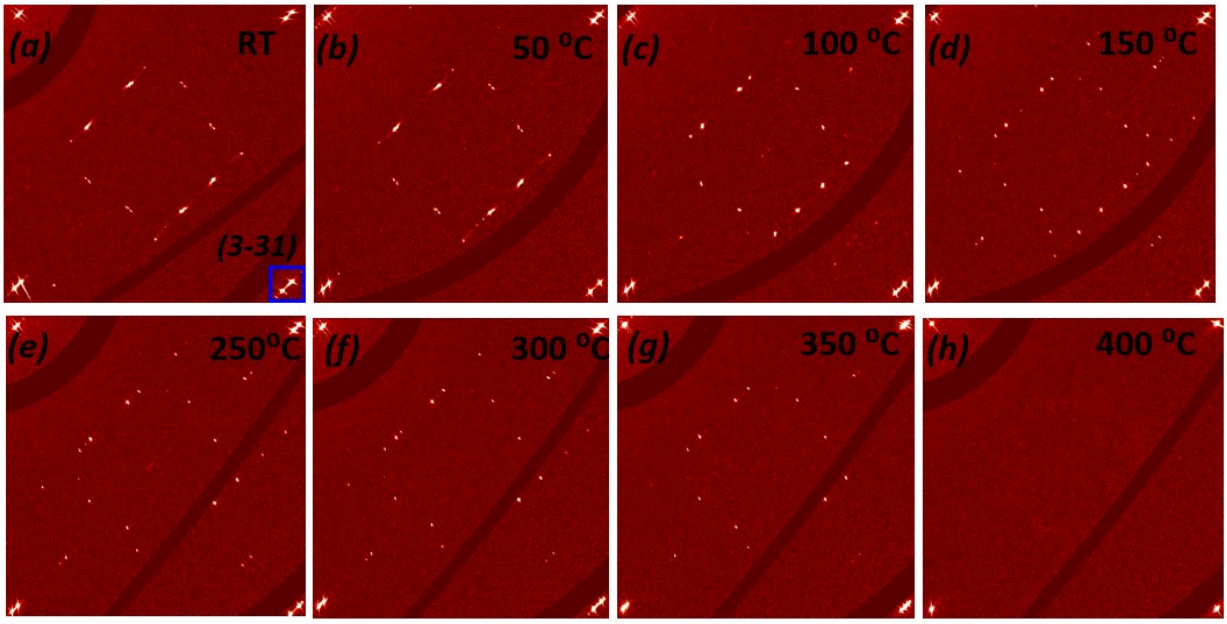

Figure 5.4: Shows continuous change in modulation vector along with intensity of the satellites as function of temperature. Each figure *(a - h)* represents the same reciprocal section contains one unit cell where blue box in (a) is a guide line to follow up the changes of *(3-31)* reflection all over the temperature range.

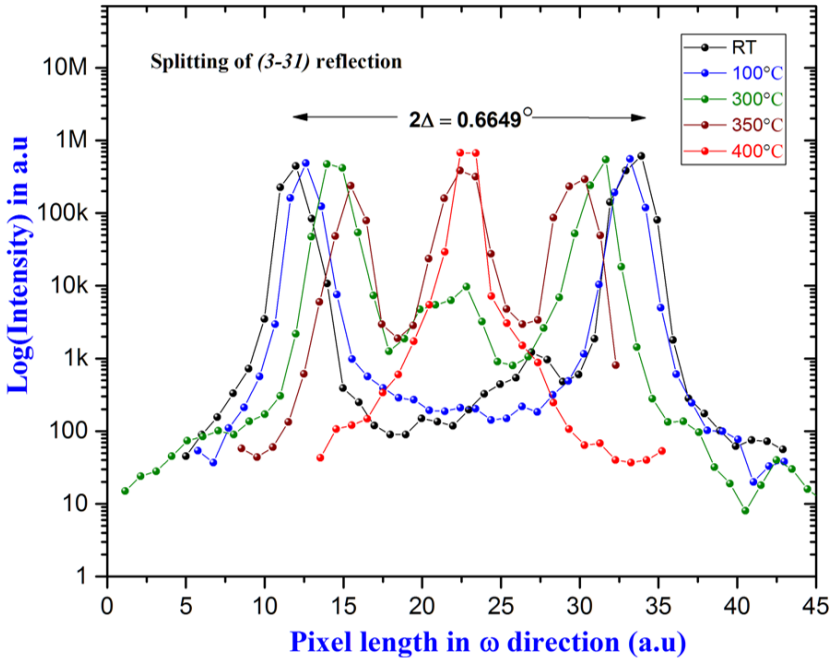

Figure 5.5: Graphical representation of logarithmic intensity of the selected reflection *(3-31)* the blue box in Fig. 5.4 with different temperature. X-axis represents indirectly the angular position in omega direction of the diffraction pattern but here it is calculated in terms of pixel length along the omega direction.

This is important to know how the modulation of oxygen ordering get changed over such wide temperature range and this only can be investigated using such sophisticated obtained X-ray 2D-diffraction pattern where very weak satellites are visible and appears as sharp peaks, this is the best part of using such giant Synchrotron radiation facilities. To illustrate such evolution a graphical presentation is given in Fig. 5.6. The components of the modulation vector for each temperature data set was determined by refining the unit cell and looking the number of indexed reflections corresponding domain. In the upper panel of Fig. 5.6 (a) shows the variation in component of the modulation vector $\boldsymbol{q}^{1a} = q_{1x}\boldsymbol{a}^* + q_{1y}\boldsymbol{b}^*$ with temperature please note that only the positive direction of the propagation is considered. After temperature 150 ^{0}C the component of the modulation vector remain constant that means the system does not modulate in any other way even up to 350 ^{0}C, it is somehow locked in to this state. In this lock in phase (150 - 350^{0}C), system continues to uptake oxygen but very less amount as can be seen from the TGA curve in Fig. 5.13. This oxygen uptake has no connection with this lock in phase as we will see in the next chapter where the effect of oxygen pressure has been discussed. The frequency range in which excess oxygen move or get ordered in the interstitial layer is higher than the detection rate of X-ray and to X-ray it appears as same modulation and after certain temperature ~ 400^{0}C this oxygen order gets destroyed. This feature is almost reversible when we cool down to RT (discussed in next chapter for PNO crystal) and that can be understood again via thermal effect. The modulation of the starting phase depends on the oxygen non-stoichiometry as well and from TGA it can be said the stable commensurate structure is favorable when $0.22 \leq \delta \leq 0.25$, below this range it enters in to incommensurate phase even at RT. This we will elaborate in the last chapter where charge and spin ordering has been discussed. Fig. 5.6 (b) illustrate how the modulation shifts to more incommensurate phase with increasing temperature.

We haven't seen the monoclinic splitting in the starting phase as the monoclinic angle ~ 0.06^0 is already in the range of error while determining angular position of *(220)* and *(-220)*-type Bragg reflection, but can be observed via measuring powder X-ray diffraction with resolution of FWHM is below 0.06^0 otherwise it will appear as a broad peaks. Recently Broux et al. [6] reported such

monoclinic phase of $Pr_2NiO_{4.22}$ at RT that retained up to 460 ^{0}C followed by HTT phase transition at 480 ^{0}C by using in-situ synchrotron X-ray powder diffraction technique. They also followed up thermal evolution of some selected satellite reflections under oxygen from RT to 900 ^{0}C.

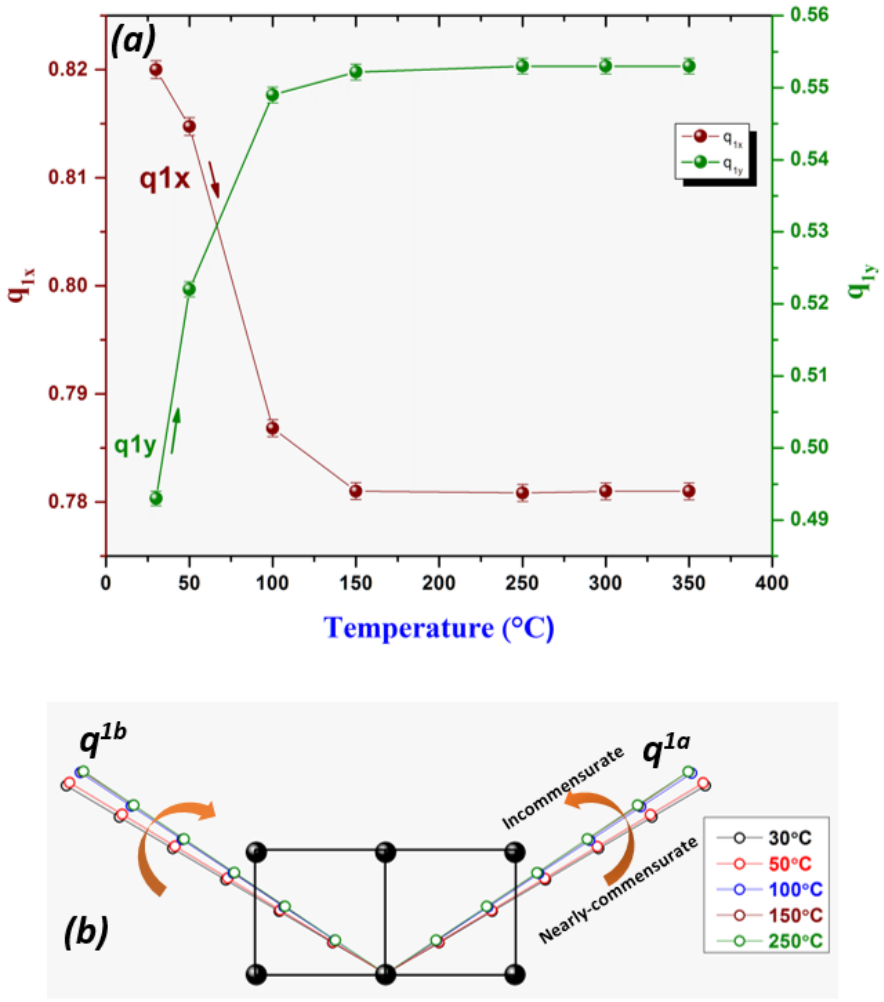

Figure 5.6: (a) Graphical representation of incommensurate modulation vector as function pf temperature, left and right axis denotes the component of that 2D vector along x and y respectively. There is sudden drop and rise of the component at 100^{0}C already indicates structure modulated in incommensurate way immediately after small perturbation of temperature and then after 150^{0}C the modulated structure is locked. (b) Another schematic where all the temperature dependent modulation vector in one unit cell are presented showing the shift from commensurate to incommensurate phase.

In the Fig. 5.7 (taken from ref. [6]) it has been shown the satellites (mark as *) are still visible up to 900 ^{0}C where complete interstitial oxygen disorder is expected as well high oxygen diffusion. Also they reported the presence of two tetragonal phase at high temperature with two different values of δ and different *a*-, *c*-lattice parameter about 0.06% which is not detectable by single crystal diffraction such close unit cell.

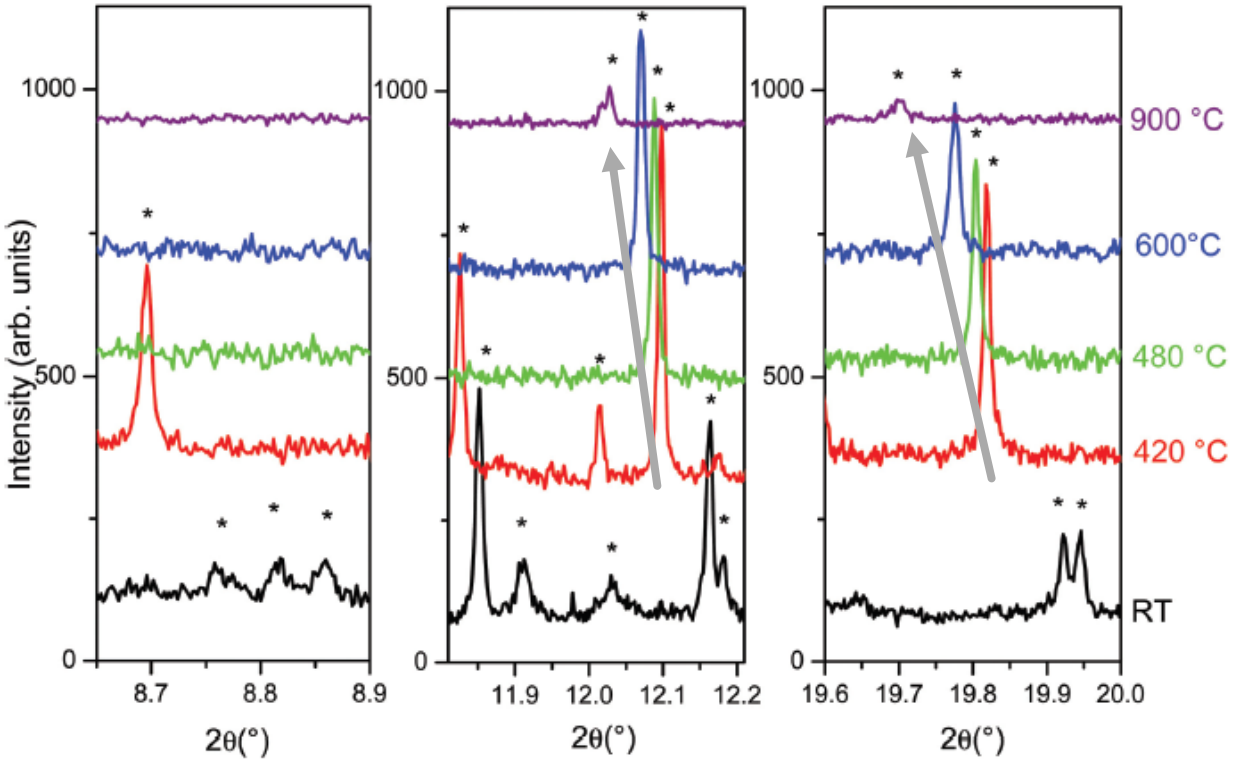

Figure 5.7: Thermal evolution of satellite reflections (marked with a*) at RT, 420, 480, 600 and 900 ^{0}C picture taken from Fig. 8 in ref. [6]. Black arrows indicates the shift of actual peaks from intergrowth phase to the lower 2θ with increase in temperature.

If we carefully look to our single crystal diffraction pattern for different temperature in *(hk0)* plane it can be seen that there are few reflections exist which retains up to high temperature 900 ^{0}C. We have calculated the d-spacing of those *(*)* marked peaks and compared to calculated *d*-spacing from single crystal diffraction patterns, it is found that the satellites in this powder pattern (Fig. 5.7) at 600 ^{0}C at an angle 2θ ~ 12.067^0 and 19.775^0 are those reflections are marked in yellow and blue circle at *(0.695, 2.133, 0)* and *(2.937, 2.182, 0)* respectively, on the *(hk0)* reciprocal plane

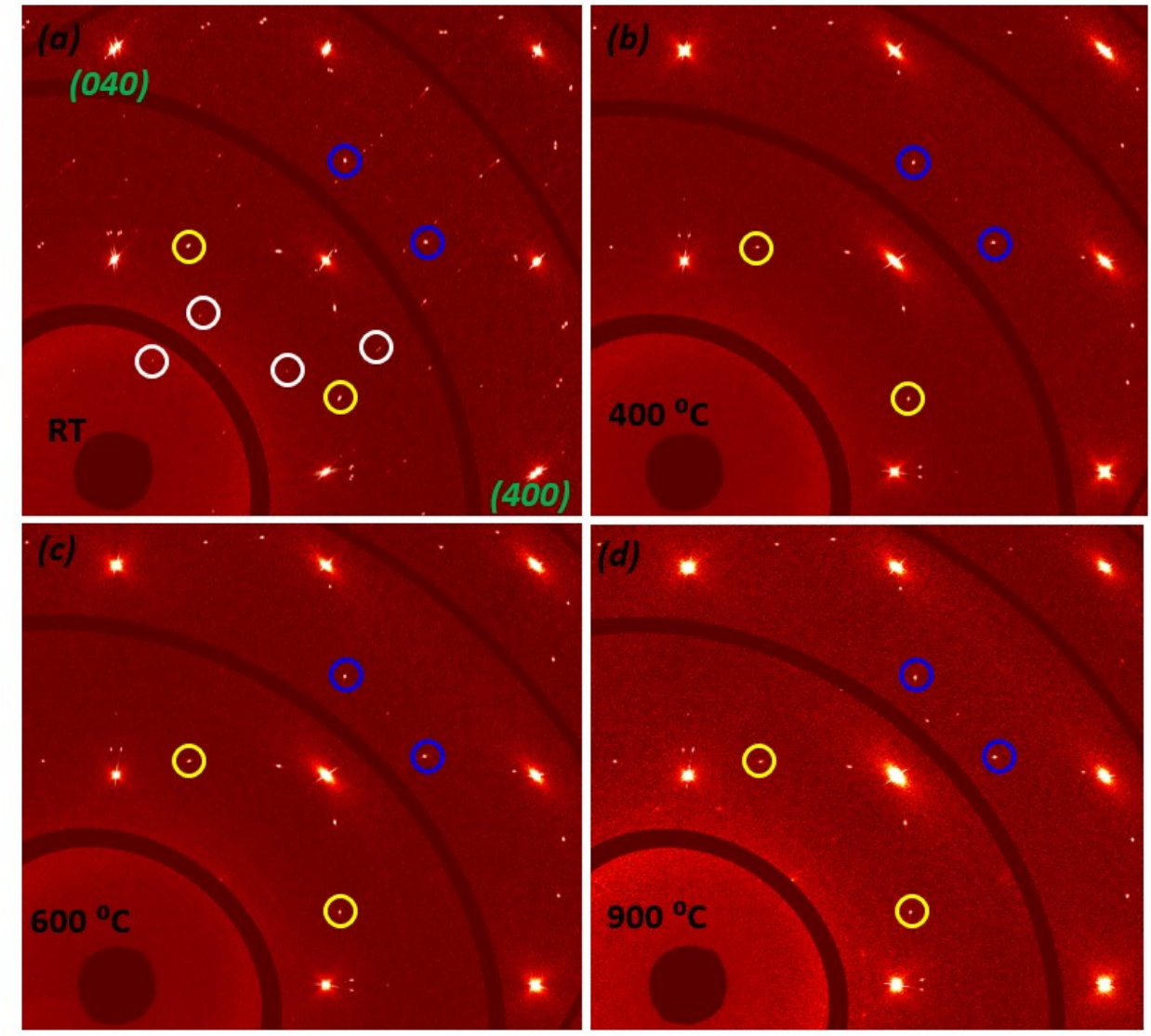

Figure 5.8: Temperature evolution of satellite from oxygen order and intergrowth parasitic reflections on *(hk0)* reciprocal plane from RT to 900 ^{0}C (a-d). In (a) Oxygen order peaks appears in as incommensurate modulation which disappear after 400 ^{0}C (b) up to 900 ^{0}C (c-d) except those parasitic peaks marked in yellow and blue circles.

obtained at 600 ^{0}C see Fig. 5.8 (c). These reflections clearly are not those satellites from oxygen ordering, rather these parasitic reflections are coming from intergrowth phase mixture that are presents from RT to 900 ^{0}C and they are quit stronger than oxygen order peaks. Increase in lattice parameter i.e. increase in inter-planner lattice distance (*d-spacing*) the position of those satellites appear at lower *2-theta* angle with increase in temperature and that is the reason why it can be seen that intergrowth peaks are shifted to lower 2-theta in the powder pattern (black arrow in Fig.

5.7). It is difficult to index those satellites in the powder pattern (black curve) w.r.t single crystal diffraction patter at RT because there are infinite number solution that can fulfill the 2-theta position of those peaks. Another interesting feature of twin is those parasitic reflections also splitted followed by twin law just like splitting of main reflections at RT and become single once it is tetragonal phase at 400 ^{0}C. However, the single crystal diffraction pattern confirms that the peaks at high temperature > 400 ^{0}C is not oxygen order satellites but they are intergrowth impurity peaks which is always present whenever make the PNO single crystals.

5.2.3 Temperature Dependent Study of Oxygen Ordering in 3-Dimension

Oxygen are not only modulated on *(hkn)*-type plane but also modulated in 3-dimension. Those modulation also change with temperature just like in *(hkn)*-type plane. One of the reconstructed *(hhl)* reciprocal section has been shown in Fig. 5.9 obtained at RT. Besides the main Bragg reflections there are defined diffuse rod as well oxygen order satellite. To index those satellite again we need one general modulation vector with all non-zero component of 3-dimensional basis vector. To differentiate this new incommensurate modulation we refer it as $\boldsymbol{q'_{1a}} = 0.317\boldsymbol{a^*} + 0.317\boldsymbol{b^*} + 0.123\boldsymbol{c^*}$ and $\boldsymbol{q'_{1b}} = -0.317\boldsymbol{a^*} - 0.317\boldsymbol{b^*} + 0.123\boldsymbol{c^*}$ also in negative direction. One advantage of this *(hhl)* section is we have non-splitted diagonal mirror along x-axis and for that we do not have to assign those modulation vector separately. We named it as $\boldsymbol{q'_{1a}}$ and $\boldsymbol{q'_{1b}}$ to define different direction. But for *(h-hl)* plane we have to cut those plane corresponding to each domain, we can't have them together as they are splitted along *(1-10)* diagonal.

Up to 3rd order of the modulation in 3D has been found (marked as broken yellow circle in Fig. 5.9) and it can be seen that there is tail coming out from 1st order satellite like comet, not clearly understood yet the reason for that. Figure 5.10 (c) shows one of the 1st order satellite at position (2.567, 2.567, 1) actually is splitted into four and only visible when the section is cut along the blue line in Fig. 5.10 (a, b). When we cut the plane along that line there is no reflection in *(hk0)* plane (olive circle) but *(hk1)* plane it contains that 1st order satellite, a zoom section of four splitting is

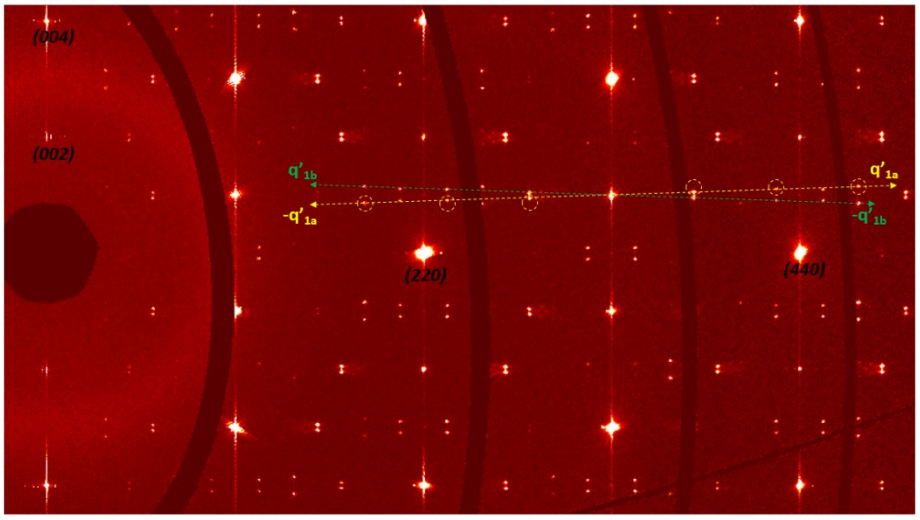

Figure 5.9: Reconstructed reciprocal *(hhl)* plane showing 3D oxygen ordering with one general incommensurate modulation vector $\boldsymbol{q'_{1a,\,1b}} = \pm\ 0.317\boldsymbol{a^*} \pm 0.317\boldsymbol{b^*} + 0.123\boldsymbol{c^*}$. Vector is drawn from *(331)* main Bragg reflections with maximum three order (yellow circle) along $\pm\boldsymbol{q'_{1a}}$ (yellow arrow) and $\pm\boldsymbol{q'_{1b}}$ (olive arrow).

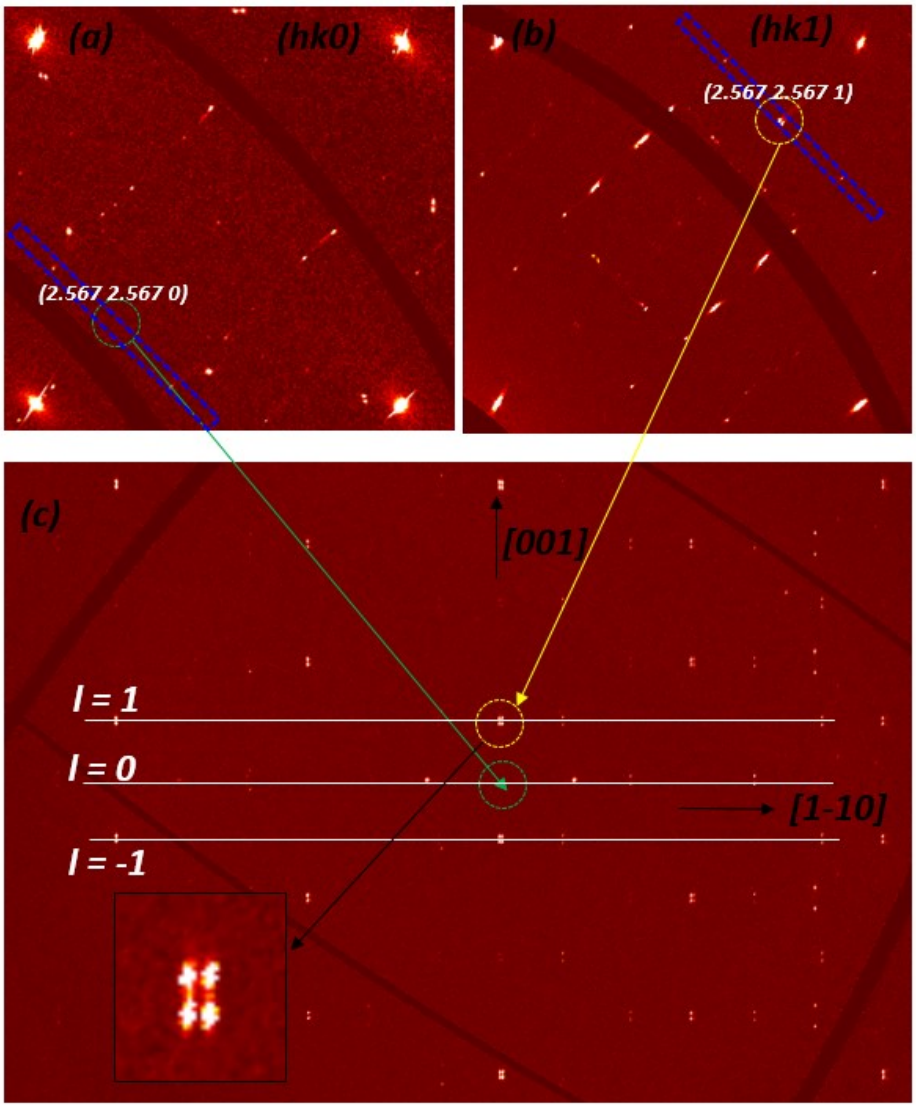

Figure 5.10: *(a)* one unit cell in *(hk0)* plane and *(b)* that in *(hk1)* plane where blue box indicates the line along which a plane in *(c)* is cut to see the 1st order modulation in the Fig. 5.9. A zoom section in *(c)* has been pointed out to show the four splitting of one of the 1st order satellite (yellow circle)

merged on the Fig. 5.10 (c). These splitting increase for 2nd order and 3rd as well and this is the reason why we need a bigger slice in reciprocal space to reconstruct by CryAlisPro software otherwise 2nd and 3rd won't be visible. Out of these four only upper two satellites appears when it is looked along vertical c^*-direction as it exactly on the top of each other. This is how satellites are ordered in 3-dimension, now we switched to the results where we see the evolution of the modulation in this plane. Figure 5.11 represents the same *(hhl)* reciprocal plane for different temperature from RT to 400 ^{0}C. The modulation change in all components not only in c*-axis rather in other two component simultaneously, this is the signature of 3D arrangement of the satellite. With increasing temperature all the component start to decrease, especially component along c* becoming small at 100 ^{0}C then becomes single reflection at 150 ^{0}C corresponding 2nd and 3rd order satellite start to disappear as diffuse spot and completely gone at higher temperature ~ 350 ^{0}C. At temperature 400 ^{0}C where HTT phase take place we don't see any more oxygen ordering which absolutely normal as they disappear in *(hkn)*-type plane also. Change in modulation for *(h-hl)* reciprocal section is similar to *(hhl)* section. We present the graphical view of those modulation evolution with temperature in Fig. 12 for *(hhl)* section. The component (α, α) of the modulation vector increases with temperature whereas component γ decreases, it follows similar trend of oxygen ordering in *(hkn)* plane in Fig. 5.6, the reason of increasing (α, α) component can be seen from Fig. 5.6(b) where 3rd order oxygen order satellite in *(hk1)* plane is actually 1st order peak in *(hhl)* plane; goes away from *(331)* Bragg reflections because of increasing α and decreasing β component of the modulation $\mathbf{q}_{1a,\ 1b}$ with temperature. Similarly, after 50 ^{0}C there is a sudden jump in modulation $(q_{x=y})$ followed by the change in modulation on *(hk1)* plane Fig. 5.6 (b) and it gets saturated nearly after 200 ^{0}C but in incommensurate phase. This again confirms that 3-dimensional oxygen ordering in *(hhl)* plane is

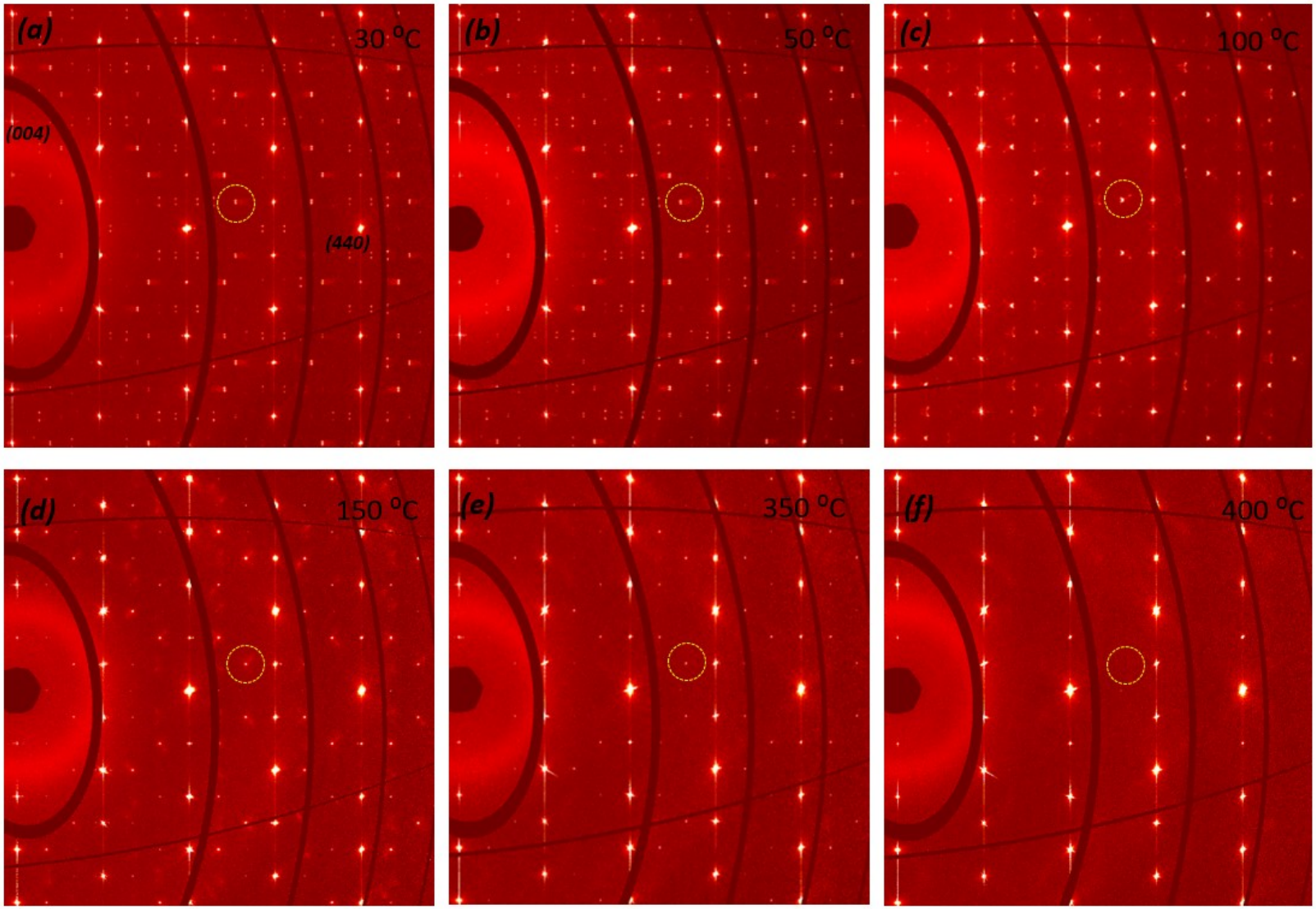

Figure 5.11: Evolution of 3D oxygen order satellite in temperature range RT to 400 ^{0}C as it can be followed via the 1st order satellite marked as yellow circle.

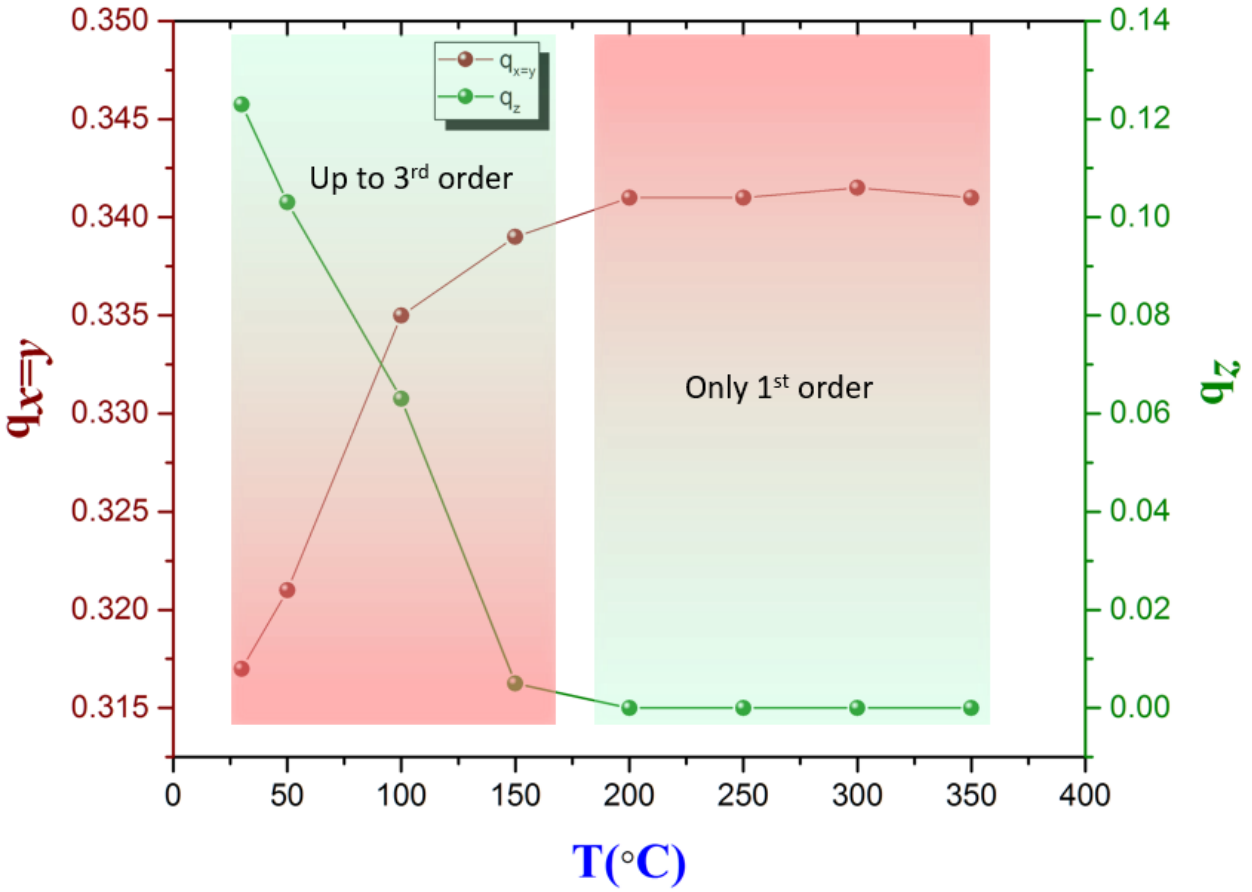

Figure 5.12: Graphical representation of the $q_{x=y}$ and q_z component of the incommensurate modulation as function of temperature where after 150 ^{0}C modulation loose the $\boldsymbol{c^*}$ component and exhibits only one order.

5.3 Thermogravimetric Analysis (TGA)

In this section we will present the TGA analysis done on as grown complete virgin $Pr_2NiO_{4+\delta}$, a piece of single crystal has been broken into very small pieces of weight ~25 mg each and three-four of them was used as starting sample for the thermogravimetric experiments. The measurements have been performed with a PerkinElmer thermobalance from RT to 1150 ^{0}C with a speed of 5 ^{0}C/min, under the gas flow 40% of Ar for balance and 20% of O_2 to the sample. Several thermogram was taken in total four run in order to see the reproducibility of oxygen uptake and release. The values of δ have been calculated according to the loss of weight and assuming that variation of oxygen concentration in the sample is the only cause of mass changing. Figure 5.13 displays the

resulting TG curve for successive four run without any interruption. Change in oxygen content is very small, at 1st run it took up ~ 0.014 amount in O_2 at 470 ^{0}C then continued to release O_2 in air up to 1100 ^{0}C. During holding at 1100 ^{0}C it continues to take up oxygen again not clear why for the moment, and reached at max ~ 0.25 at same 470 ^{0}C and come down to where it started ~ 0.230 in $\Delta\delta$.

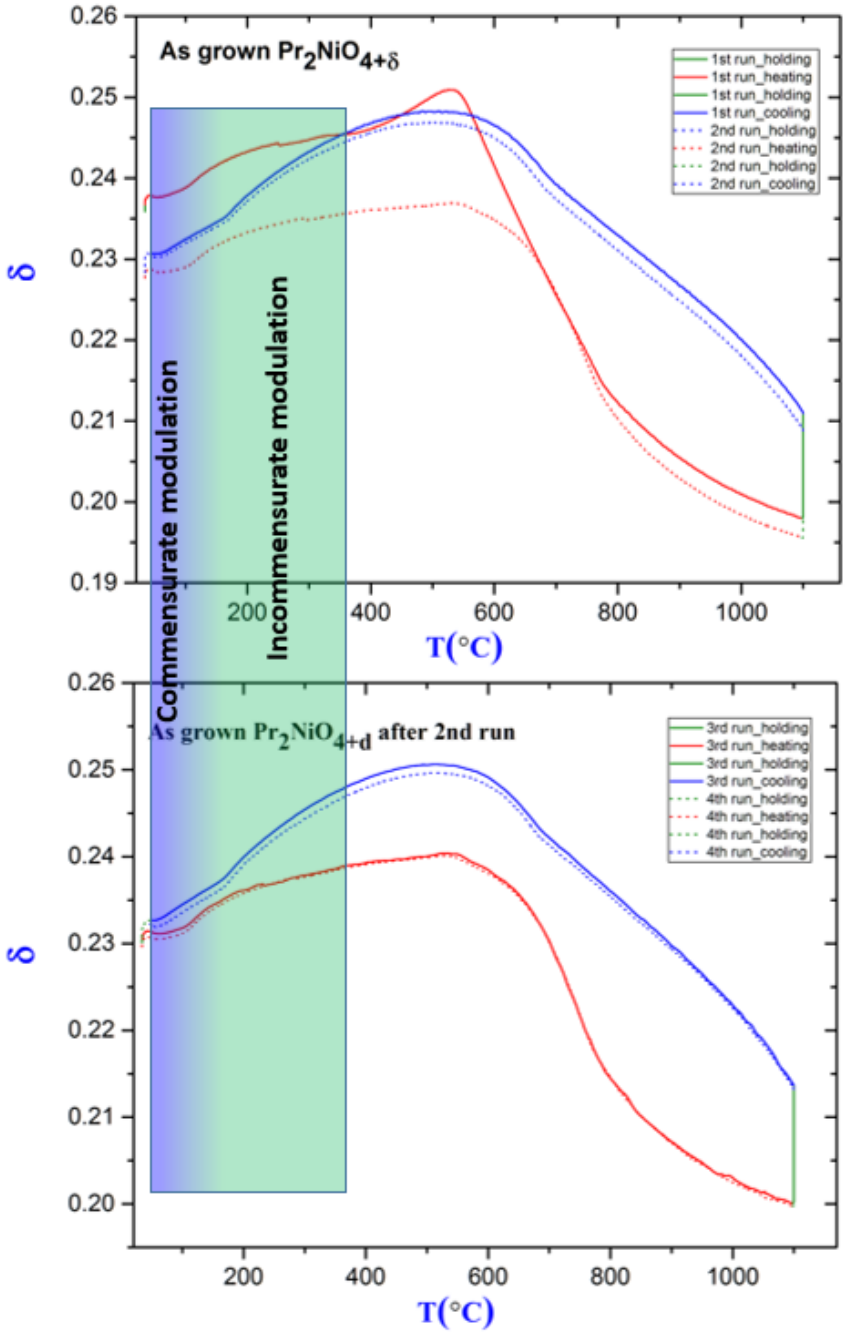

Figure 5.13: Several TGA curve under same condition (top) first two run where system stabilizes to $\delta \sim 0.23$ and in next two run (below) it is completely reversible process where commensurate to incommensurate region are same. Total change in $\Delta\delta \sim 0.014$ for O_2 uptake and $\Delta\delta \sim 0.03$ in O_2 release compare to starting phase.

In the 2nd run it stays at almost constant value then start to decrease as 1st run then come back to the initial position. For 3rd and 4th run it is completely reversible, during cooling it reaches to max. $\delta \sim 0.25$ and come back to starting phase. This is reversible in terms of oxygen uptake and release also in case of oxygen ordering as function of temperature what we will see in the next chapter. We haven't see any decomposition of such small single crystal even up to 1150 ^{0}C and at this temperature it reaches to $\delta = 0.20$. It is only possible to see such small changes with many more details inside the curve because of fine resolution ~ 0.01mg of this thermobalance. From these TGA curve it can be seen the most stable phase of $Pr_2NiO_{4+\delta}$ is with δ =0.231. During heating at temperature ~ 150 ^{0}C there is a small step of increasing δ where the incommensurability enters to the lock in constant phase and then it gets saturated at ~ 0.25 which is HTT region. During cooling again near to 150 ^{0}C it jump to lower δ values where it enters to commensurate phase.

5.4 High-*T* Vs Low-*T* reaction

We have seen the structural evolution of $Pr_2NiO_{4+\delta}$ w.r.t micro-structured domain and incommensurately modulated oxygen ordering as function of temperature, to better understand the oxygen mobility and related oxygen ordering we need to know what happens during electrochemical reduction process at ambient by in situ synchrotron X-ray single crystal diffraction method. We will present the results in short, most of the results can be found in PhD thesis of A. Maity [8]. The electrochemical reduction was carried out on $Pr_2NiO_{4+\delta}$ single crystal mounted on a dedicated electrochemical cell (discussed in chapter 3) was adopted on BM01A diffractometer at ESRF. This crystal was two times twinned in orthorhombic *(Fmmm)* structure as starting phase and during electrochemical reduction it went through several distinguished phase from intermediate $P4_2/ncm$ tetragonal to *Bmab* orthorhombic as end phase representing very structural stability. Fig. 5.14 shows the evolution of such basic structure on course of electrochemical reduction. Starting phase in Fig. 5.14 (a) was *(3+2)*-dimensionally commensurately modulated where the commensurate modulation vector was $\boldsymbol{q}_{1a,\,b} = \pm 0.833\boldsymbol{a}^* + 0.5\boldsymbol{b}^*$ used to index the satellite reflections in *(hkn)*-type

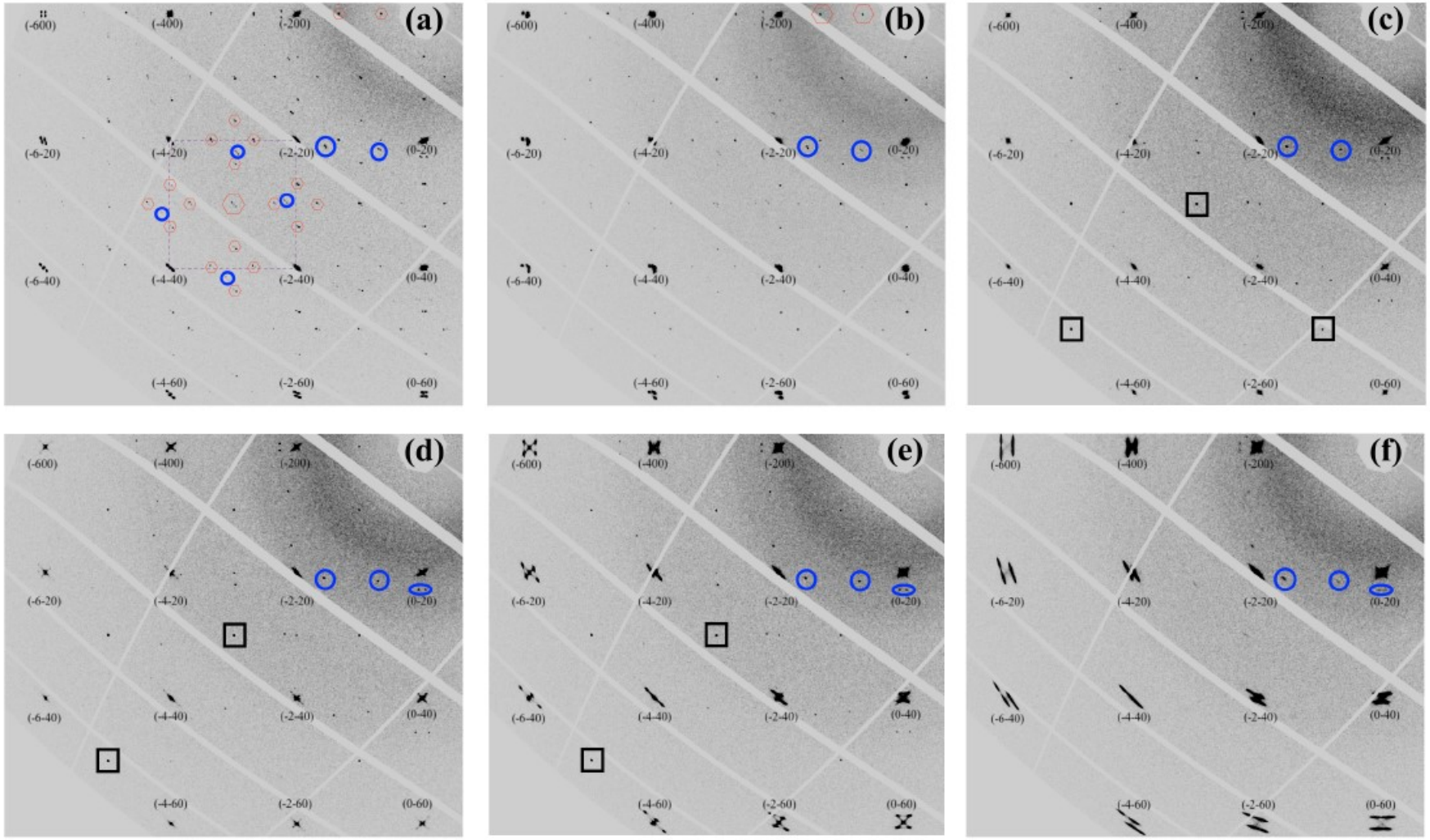

Figure 5.14: Evolution of the *(hk0)* diffraction pattern on the course of electrochemical reduction of $Pr_2NiO_{4+\delta}$. (a) starting orthorhombic phase in *Fmmm* with $\delta \sim 0.25$, (b) biphasic region *Fmmm* + *P4₂/ncm*, (c) the tetragonal phase in *P4₂/ncm* for $\delta \sim 0.12$, (d-e) biphasic region *P4₂/ncm* + *Bmab* and (f) end orthorhombic phase in *Bmab* with $\delta \leq 0.05$. The basic *Fmmm* cell outlined by the dashed square in violet in (a). The reflection enclosed in the red hexagon in (a) represents the commensurate superstructures. The *P*-type reflections of the tetragonal phase are enclosed in the black square. The blue circles show the reflections from intergrowth phase which has been observed also in the crystal investigated for T-dependent measurements. Picture taken from Fig. 9.5 in ref. [8].

reciprocal plane. Similarly, the satellite in half-integer *(hkn/2)* plane was indexed with help of other $\mathbf{q}_2$ modulation vector like before discussed in chapter 4. The main difference to the temperature dependent study is here the $\mathbf{q}_1$ modulation vector of oxygen order satellite does not change at all retain up to the entering into $P4_2/ncm$ tetragonal phase except the intensity of those satellite. In the Fig. 5.14 (c) shows the complete $P4_2/ncm$ tetragonal structure with clearly visible *p*-type reflection marked in black square then it goes to (f) *Bmab* orthorhombic as end phase which is two times twinned again but without superstructure reflection as there is no excess oxygen. The real picture of the domain evolution during electrochemical reaction that can be seen via *(-600)* one of the basic Bragg reflections and it has been shown in Fig. 5.15. This picture is a clear evidence that the phase is highly stable in terms of oxygen diffusion and ordering. Starting from (a) four twinned *Fmmm* passing through biphasic *Fmmm* + $P4_2/ncm$ region (e - g) to single $P4_2/ncm$ phase (h) followed by again another biphasic $P4_2/ncm$ + *Bmab* region (I - s) to end *Bmab* phase (t) with four twinned domain. Even after passing from a low orthorhombic *Fmmm* phase to the final orthorhombic *Bmab* phase with orthorhombicity 3 times higher can be seen from angular separation in Fig. 5.15 (a and t), the crystal and its structure was very much stable. It has been also investigated that in the course of electrochemical reduction the commensurate modulation vector $\boldsymbol{q}_1$ did not change but the intensity drops down quickly as the intermediate tetragonal phase $P4_2/ncm$ starts to grow. The intensity evolution of the *P*-type reflection corresponding to the tetragonal phase reveals that the tetragonal phase exists over a wide range of oxygen stoichiometry [8].

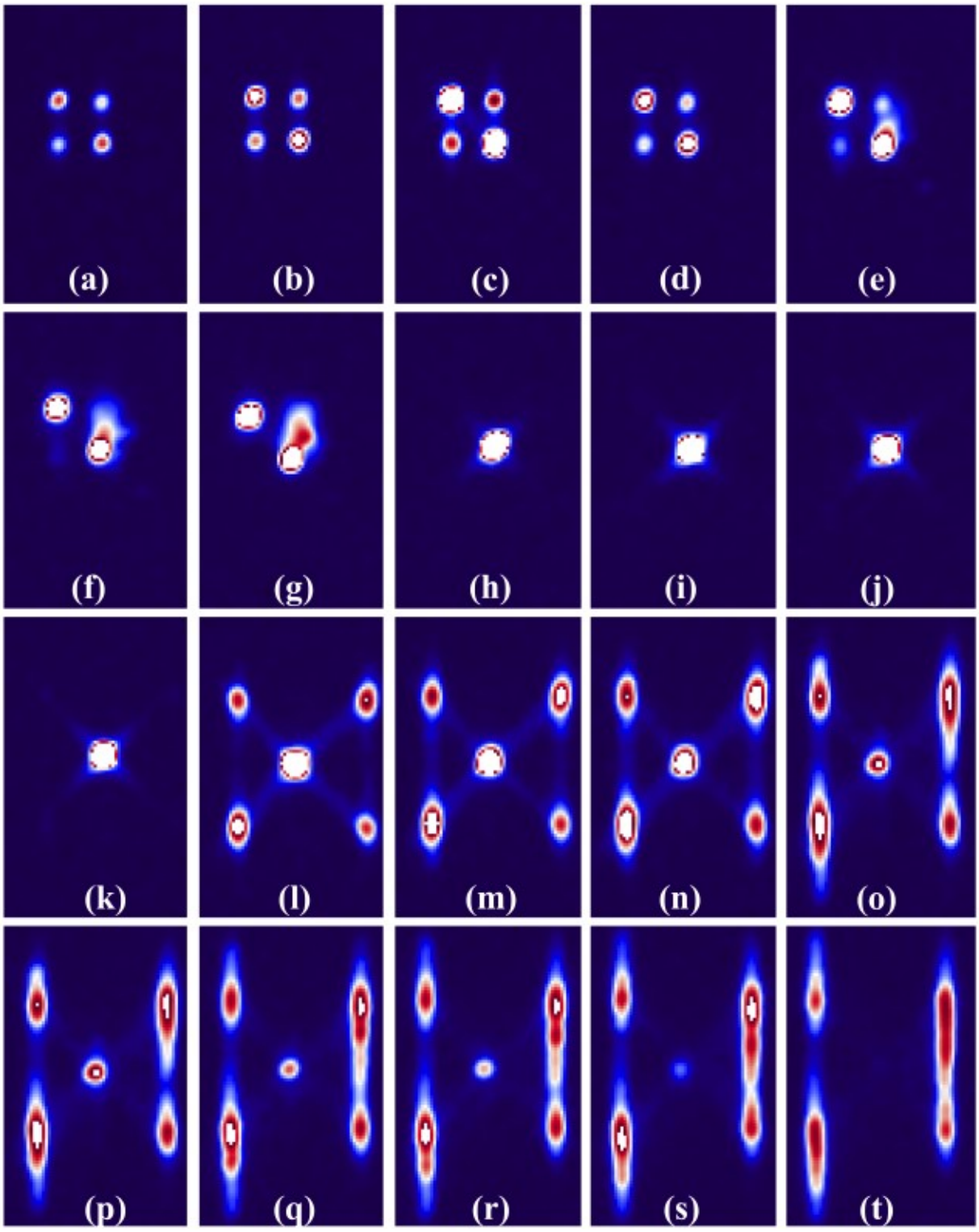

Figure 5.15: Evolution of the twin domains investigated via the observation of *(-600)* reflection. ((a)-(e)) correspond to orthorhombic *Fmmm* phase; ((f),(g)) correspond to the biphasic region of *Fmmm* + $P4_2/ncm$; ((h)-(k)) correspond to $P4_2/ncm$; ((l)-(s)) correspond to next biphasic region $P4_2/ncm$ + *Bmab* and (t) corresponds to the final *Bmab* phase. Picture taken from Fig. 9.7 in ref. [8].

5.5 Summary

As grown phase of $Pr_2NiO_{4+\delta}$ single crystal always belongs to LTO *Fmmm* structure where different number of twin domain possible to exist in the starting phase with different type of modulation. In this chapter we have shown for the high-T study the starting phase of the crystal was *(3+1)*-dimensional nearly-commensurate modulated structure ($\boldsymbol{q_1} = \pm 0.821\boldsymbol{a^*} + 0.493\boldsymbol{b^*}$) in two times twin domains where the oxygen are ordered in 3-dimension up to certain range of temperature. With increase in temperature structure start to modulate in a different way (towards more incommensurate) and oxygen order confined in 2D at ~ 200 ^{0}C. The LTO/HTT phase transition take place at 400 ^{0}C having no more oxygen ordering. HTT phase retains in the entire temperature range with small change in lattice parameters. Compare to low temperature phase system passes through several distinct and define phase. To summarize all the different phases that take place depending on the reaction condition we have presented the phase diagram during electrochemistry reduction and high-T study in Fig. 5.16, where left y-axis denotes the change in excess oxygen content on course of reduction electrochemically and corresponding RT phase diagram is shown in left colored rectangle. In the staring *Fmmm* phase we have found *(3+2)*-dimension exact commensurate modulation ($\boldsymbol{q_1} = \pm 0.833\boldsymbol{a^*} + 0.5\boldsymbol{b^*}$) of oxygen order satellite which persists up to before entering in to $P4_2/ncm$ tetragonal phase. At the end it enters to another LTO *Bmab* phase with higher orthorhombicity. Right y-axis denoted the change in excess oxygen content during high-T diffraction study and the values are taken from TGA curve assuming for all crystals have the same stable phase and oxygen content ~ 0.23. During high-T reaction system gets perturbed immediately with small increase in temperature and huge change in modulation vector has been observed. It stayed always in *(3+1)*-dimensional structure but with different propagation vector making the oxygen order 3D to 2D. Finally at High temperature system becomes tetragonal phase passing through biphasic *Fmmm* + *F4/mmm* phase. This is clear that the way oxygen gets ordered in the structure is different for low- and high-T reaction, for low-T electrochemical reaction the release of oxygen via interstitials diffusion mechanism is periodic without any thermal disturbance the reason why X-rays sees it the same modulation unless the periodicity is lost by releasing oxygen

at certain limit $\delta_c \sim 0.125$. This phenomena also confirms there must be minimum number of excess oxygen to modulate the structure. In case of high-T reaction oxygen uptake and releasing is associated with thermal effect that manifest the oxygen modulation and even though excess oxygen content is quite rich at high temperature region it is already in tetragonal phase and due to structural distortion and NiO_6 tilting modulation gets lost. In conclusion it is said that phase diagram is rather simple but it is complex in terms of oxygen modulation whereas the system already exhibits different distinct phase at different environment.

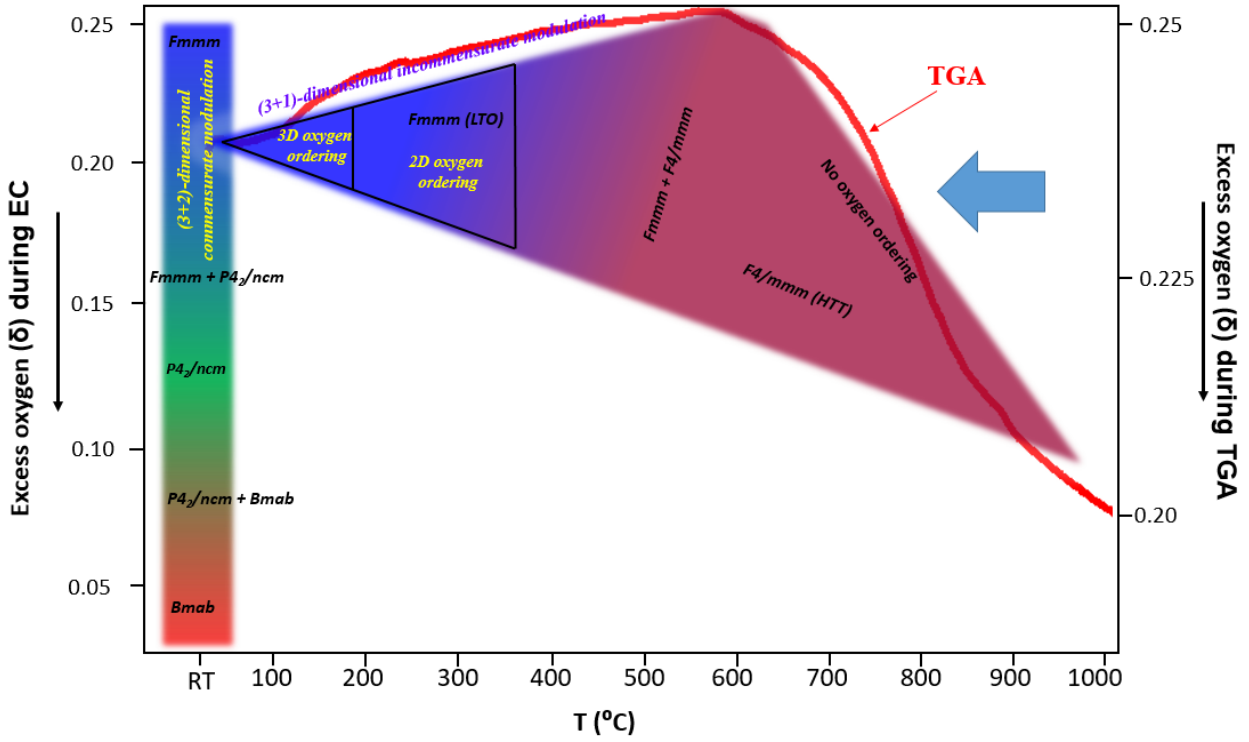

Figure 5.16: Phase diagram of $Pr_2NiO_{4+\delta}$ single crystal in two different reaction condition. (Left) shows the low-T phases as function of excess oxygen content during electrochemical reduction process at RT. (Right) shows the high-T phase diagram correlated with excess oxygen content as function of temperature. In both kinetics system goes through several phases consciously modified with different oxygen modulation scenario.

References:

1. M. Ceretti, O. Wahyudi, A. Cousson, A. Villesuzanne, M. Meven, B. Pedersen, J. M. Bassat, and W. Paulus, Low temperature oxygen diffusion mechanisms in $Nd_2NiO_{4+\delta}$ and $Pr_2NiO_{4+\delta}$ via large anharmonic displacements, explored by single crystal neutron diffraction, J. Mater. Chem. A, vol. 3, no. 42, pp. 21140– 21148, 2015.
2. A. Piovano, A. Perrichon, M. Bohem, M. Johnson, W. Paulus, Positional Recurrence Maps: a powerful tool to decorrelate static and dynamical disorder in distribution maps from molecular dynamics simulations, PCCP, The Royal Society of Chemistry, 2013.
3. J.D.Sullivan, D.J.Buttrey, D.E.Cox, J.Hriljac, A Conventional and High-Resolution Synchrotron X-Ray Diffraction Study of Phase Separations in $Pr_2NiO_{4+\delta}$, Journal of Solid State Chemistry, 1991, 94, 337.
4. M.T.Fernandez-Diaz, L. Martinez, J. Rodriguez-Carvajal, Solid State Ionics, 1993, 63065, 902.
5. C. Allancon, J. RodriguezCarvajal, M. T. FernandezDiaz, P. Odier, J. M. Bassat, J. P. Loup, J. L. Martinez, Zeitschrift Fur Physik B-Condensed Matter, 1996, 100, 85.
6. Thibault Broux, Carmelo Prestipino, Mona Bahout, Serge Paofai, Erik Elkaïm, Vaibhav Vibhu, Jean-Claude Grenier, Aline Rougier, Jean-Marc Bassat and Olivier Hernandez, Structure and reactivity with oxygen of $Pr_2NiO_{4+\delta}$: an in situ synchrotron X-ray powder diffraction study, Dalton Trans., 2016, 45, 3024–3033.
7. PhD thesis, Exploring oxygen mobility in $(Pr/Nd)_2NiO_{4+\delta}$: Single crystal growth, isotropic exchange depth profiling and structural characterization by X-ray, neutron and electron diffraction, Olivia Wahyudi, 2011.
8. A. Maity, PhD thesis, Exploring oxygen diffusion mechanism in $SrFeO_{3-x}$ and $Pr_2NiO_{4+\delta}$, followed up on single crystals by in situ synchrotron diffraction, 2016.

Chapter 6

In Situ Investigation of *T*-dependent Modulated Structure of $Pr_2NiO_{4+\delta}$ Under Different Oxygen Pressure $P(O_2)$ by Single Crystal Laboratory *μ-focused* X-ray Diffraction

$Pr_2NiO_{4+\delta}$ is good electron and ion conductor showing high oxygen diffusion coefficient even at room temperature compare to other homologous nickelates and excess interstitials oxygen must be present in the interstitial layer even in small amount to have such high oxygen mobility [1-6] which makes it to serve as a cathode material in application of SOFCs devices at moderate temperature. In terms of cell performances of SOFCs devices the pressurized operation as catalytic reactors has been proposed [7-10] but few works has been carried out on electrochemical characteristics at high pressure [11-13]. Recently, Railsback et al. [14] reported high pressure performances of mixed-conducting oxygen electrodes including $Pr_2NiO_{4+\delta}$ showing electrochemical responses under oxygen partial pressure $P(O_2)$ up to 10 bar. The polarization resistance decreased with increasing pressure in all cases, but the nickelates decreased more rapidly than the perovskites and they proposed that this difference is a direct result of the different $P(O_2)$ dependences of the defect concentrations – the oxygen vacancy concentration decreases with increasing $P(O_2)$, whereas interstitial concentrations increase. But there are no reports, to our knowledge, showing the effects of high oxygen pressure $P(O_2)$ on local microstructure of $Pr_2NiO_{4+\delta}$ by studying oxygen modulation using *in situ* single crystal X-ray diffraction. The phase diagram of $Pr_2NiO_{4+\delta}$ is extremely complex and the related structures are strongly depending on the reaction conditions. We have described earlier the strong dependence of the incommensurate modulation vector with temperature, while keeping the oxygen partial pressure constant. Correlating these structural studies with the oxygen stoichiometry, especially when explored by thermogravimetric studies, it becomes clear that d becomes maximum, i.e. 0.25 at around 450°C when heated in air, while the stoichiometry at ambient temperature is less and around $\delta = 0.22$. Since DFT type simulations have shown that the amount of the interstitial

oxygen atoms sensitively triggers the diffusion behavior and especially at ambient temperature, the interest to possibly obtain and stabilize stoichiometric $Pr_2NiO_{4.25}$ at ambient temperature is challenging. We therefore aimed to investigate the phase diagram of $Pr_2NiO_{4+\delta}$ as a function of pressure and temperature, not only with the aim to synthesize stoichiometric $Pr_2NiO_{4.25}$ at high pressure and to study if this possible modification can be stabilized down to ambient temperature, but also to develop a sophisticated tool to explore more generally phase diagrams of non-stoichiometric oxides as a function of Temperature and $P(O_2)$ by in situ studies on tiny single crystals. The use of small crystals is mandatory for kinetical reasons, but equally possible at laboratory diffractometers, due to recent developments as μ-sources and "zero-noise"-type pixel detectors. The aim was therefore to develop an "easy to use"-device which allows to explore the phase stability of oxides up to 100 bars and 700°C, while being able to collect full data sets of the reciprocal lattice.

Both doped and undoped Nickelates are the good reference systems compare to high-Tc cuprates showing similarities with cuprates such as antiferromagnetic state, metal-insulator transition and charge and spin stripe phase [15]. However, at ambient pressure Sr-doped La_2NiO_4 is insulator and at high pressure it is expected to become either metallic or some excotic ground state [16, 17]. MI transition in nickelates takes place at higher sr-doped concentration where stripe phase falls into insulating phase. From the resistivity data of nickelates at high pressure it is know that MI transition drops to lower sr doped concentration and consequently at high pressure needs to push it all way down to stripe phase. From stripe point of view it could be also interesting to perform such high pressure experiments on such tiny crystal at low temperature. Recently, Hucker group [18] they reported charge stripe order in $La_{1.67}Sr_{0.33}NiO_4$ single crystal at high pressure (4 GPa), T =190 K created by Diamond envil cell using X-ray diffraction but the cell was not suitable for in situ pressure change at low temperature and due to less available cryostat stability the range of wide angular sweeps was limited. These are the real experimental obstacle during measurements can take place. Our aim would not be only to focus the results obtained from our X-ray diffraction experiment performed using specially designed pressure cell but also to show the reliability of the optimized

measurements with less obstacle at least for high temperature and could be use this kind of pressure cell for low temperature measurements as well.

In this chapter we will present first time the evolution of structure by investigating lattice parameter, microstructure twin domain and oxygen modulation of as prepared $Pr_2NiO_{4+\delta}$ single crystal ($\phi \sim 20\text{-}30\ \mu m$) inside a dedicated compact quartz gas capillary pressure cell mounted on laboratory STOE μ-focused X-ray ($\lambda = 0.71073$ Å) diffractometer under different oxygen pressure $P(O_2)$ up to 75 bar including vacuum (0.01 mbar) in a temperature range from RT to $T_{max} = 500\ ^0C$.

6.1 Experimental Strategy

A small single crystal of $Pr_2NiO_{4+\delta}$ ($\phi = 20\ \mu m$) was glued inside a quartz capillary ($\phi_{out} = 1.5$mm, $\phi_{in} = 1.1$ mm) using high-temperature ceramic glue on the top of another quartz capillary ($\phi_{out} =$ 0.3mm) keeping at middle position of outer capillary in order to center the crystal without spherical aberration. Bottom of the inner capillary was sealed using epoxy glue in order to avoid capillary burst due to high pressure. Set up for the pressure cell is described in details in section 3.5 of chapter 3, beside a specific oxygen manometer, allowing to reach 150 bars, it essentially contains thin and flexible peek-tubes, which are generally used for high pressure gas chromatography. Due to the high temperature device we need to optimized the chi motor of the STOE diffractometer to -45^0 in angle (see the Fig. 3.8 in chapter 3) but we had full freedom in omega motor where we rotated 360^0 in angle to collect the full sphere 3D data set and this was only possible because of very flexible PEEK capillary. Such cells have been developed especially at large scale facilities and high pressure *in situ* reaction cells were usually made of single crystalline sapphire capillaries of small diameters, which can resist pressures up to several hundred bars at high temperatures, i.e. 1000°C. The special need in our case is not only to explore the whole reciprocal space, but equally to detect superstructure reflections of weak intensities, which are up to 4-5 orders of magnitude less compared to the basic reflections. Since single crystalline sapphire capillaries yield a significant amount of additional

reflections, we therefore optimized to use quartz capillaries which have a significant lower tensile strength compares to sapphire. The big advantage, however, is that they do not yield additional reflections, which would render any data analysis of the complex patterns obtained for PNO, quasi impossible

We have carried out all the measurements without any obstacle. To perform the measurements in a systematic way we followed the steps as below:

(i) Normal measurement at ambient pressure and temperature.

(ii) Then we applied our desired oxygen pressure and measured again at RT.

(iii) After that we started heating the sample up to where we found the LTO/HTT phase transition and took the data set at every increasing temperature.

(iv) Come back to RT by measuring at successive lowering temperature with step.

(v) Measured again at RT still under pressure and then

(vi) We released the pressure and measured at ambient pressure and temperature.

Following these above steps we carried out several measurements at different oxygen pressure of 50 bar and 75 bar. Besides these two applied pressure we took the data sets just by increasing temperature at ambient pressure to see the actual effects of pressure on the structure. Similarly, we went for the vacuum (0.01 mbar) even though it was not so high level we performed the diffraction at different temperature. We have now four different parameters to check the stability and evolution of the structure under vacuum, ambient pressure, oxygen pressure of 50 bar and 75 bar respectively. Most of the data set was taken by rotating the crystal 360^0 in step of 0.1^0 with exposure time 10 sec after stabilizing the each desired temperature. This is the reason why (short exposure time compare to synchrotron resolution) satellite peaks would be appear on the reconstructed plane as very weak reflection. Only the RT data set was taken with longer exposure time where we will see those satellites as quite strong as it was exposed to X-ray beam for ~20 sec.

6.2 Exploring Structure of $Pr_2NiO_{4+\delta}$ as function of Temperature under different Oxygen Pressure $P(O_2)$

6.2.1 Phase diagram of $Pr_2NiO_{4+\delta}$ during Heating and Cooling at Ambient Pressure

We have already seen the RT and T-dependent phase diagram $Pr_2NiO_{4+\delta}$ only during heating where the RT phase consisting of *(3+2)*-dimensional incommensurate modulated structure and continue to change into *(3+1)*-dimensional incommensurate modulated structure with increasing temperature. In this study we have also performed X-ray diffraction during cool down to RT. Fig. 6.1 shows reconstructed reciprocal *(hk1)* plane of $Pr_2NiO_{4+\delta}$ obtained at ambient pressure and in the temperature range from RT *(a)* to 400 ^{0}C *(d)* and cooling down to 350 ^{0}C *(e)* finally to RT *(f)*. First thing to notice is the intensity of the weak satellites which is 10-4 times main Bragg reflections and ambient phase shows average *Fmmm* orthorhombic structure with one time twined and *(3+1)*-dimensional incommensurate modulated structure as we do not have other modulation in *(hkn/2)* plane where n=integer with starting modulation vector $\boldsymbol{q_1} = \pm 0.80719\boldsymbol{a^*} + 0.52316\boldsymbol{b^*}$ at RT. Second thing to notice is the modulation $\boldsymbol{q_{1a}}$ (blue arrow) associated to domain 1 and that $\boldsymbol{q_{1b}}$ (wine arrow) of domain 2 becomes very weak almost invisible at high temperature (see Fig. 6.1 (b)). With increasing temperature structure changes to more incommensurate modulated one and at 400 ^{0}C it becomes tetragonal *(F4/mmm)*. Again down to RT it come back to same orthorhombic phase with same lattice parameter and slight different in incommensurate vector, the reaction or phase transition is reversible in terms of structure as function of temperature at ambient pressure. Fig. 6.2 shows graphical representation of evaluated lattice constant, orthorhombic strain and component of modulation vector associated to structure of $Pr_2NiO_{4+\delta}$ as function of temperature. If we correlate the incommensurate modulation vector of the present system to our previous measurements done at BM01A (chapter 5) we can evaluate the temperature corresponding to this current modulation at RT which is $T \sim 60$ ^{0}C and from the TGA curve (Fig. 5.13) we can obtain the value of $\delta \sim 0.234$

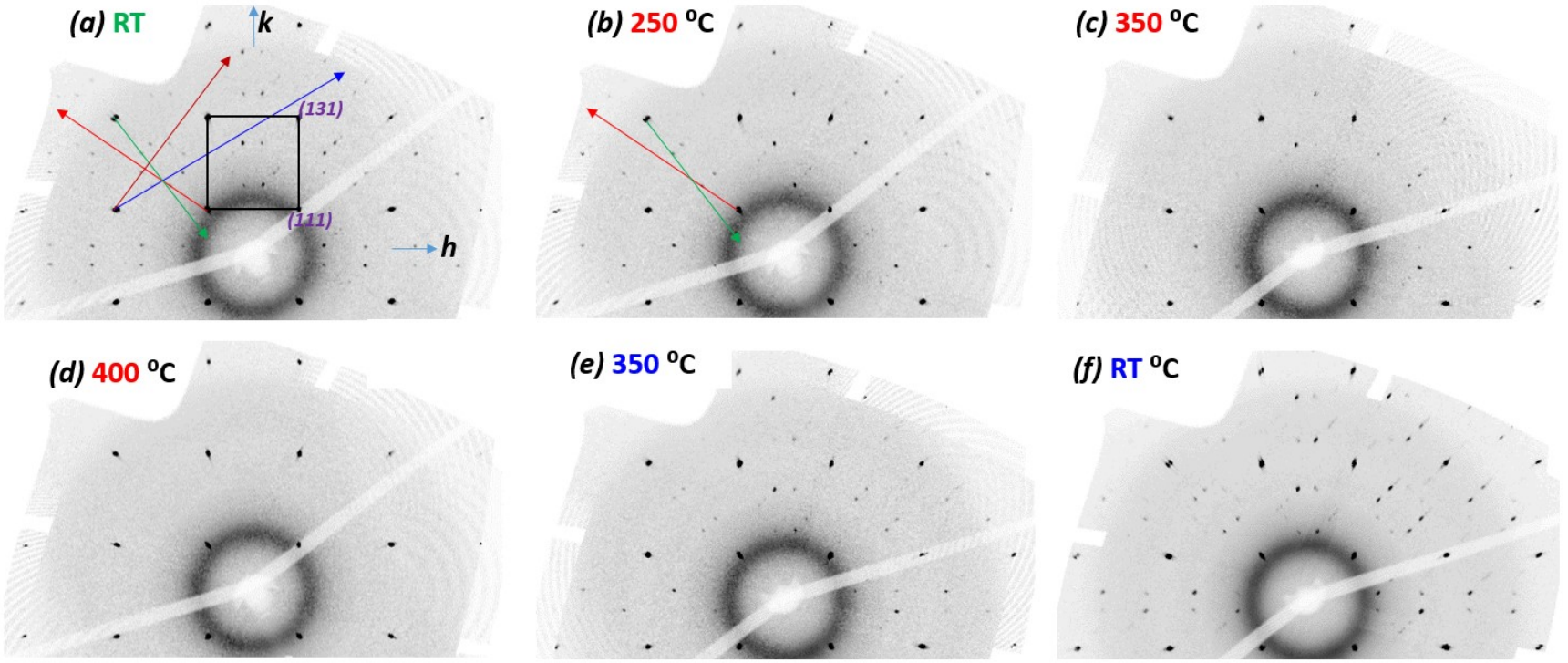

Figure 6.1: Reconstructed reciprocal *(hk1)* plane of $Pr_2NiO_{4+\delta}$ obtained at ambient pressure and temperature range from RT to 400 °C *(a - d)* and cool down to RT *(e - f)*. Inside the black powder ring is coming from quartz capillary. In (a) red and blue arrows indicated the modulation vector of one twin domain 1 and olive and wine arrows that of domain 2. Black box represents *Fmmm* average unit cell.

± 0.02. It again reproduce the LTO/HTT transition temperature at ambient pressure which is $T_{LTO/HTT} = 400\ ^{0}C$ compare to the previous results in chapter 5.

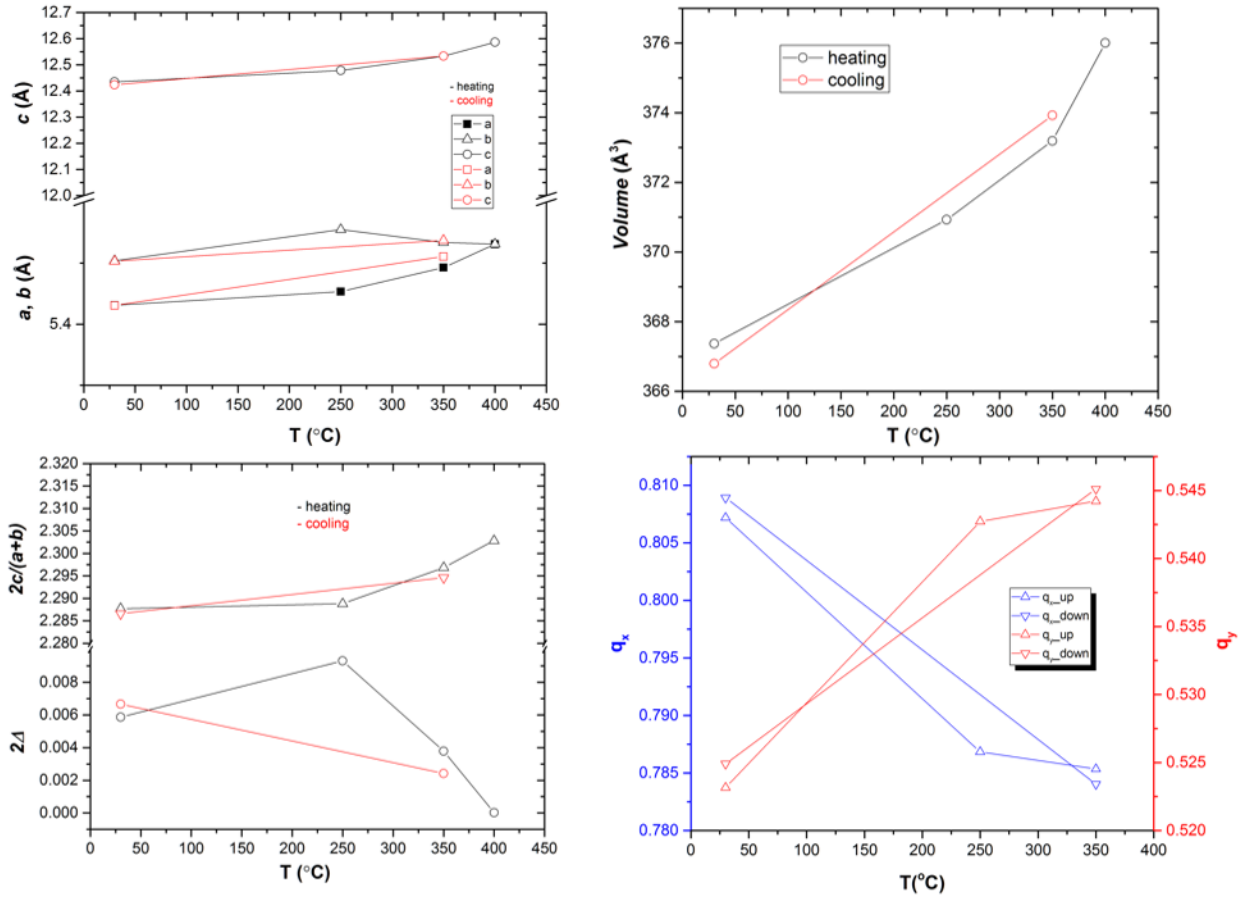

Figure 6.2: (Top left) lattice constants, (top right) volume of the unit cell of $Pr_2NiO_{4+\delta}$ as function of temperature is plotted. Corresponding angular separation of *(h-hl)*-type reflections and orthorhombic strain (bottom left) is presented. The component of the modulation vector as function of temperature is shown in (bottom right). Each plot shows the reversibility of the structural transition with temperature.

6.2.2 Phase diagram of $Pr_2NiO_{4+\delta}$ during Heating and Cooling under Oxygen Pressure of 50 and 75 bar

To see the initial effect of the oxygen pressure on the structure of $Pr_2NiO_{4+\delta}$ at RT we performed two diffraction measurements one is under ambient pressure and other under pressure of 50 bar and the corresponding diffraction patterns of *(hk1)* plane is shown in Fig. 6.3 (a & b). Immediately it can be seen in Fig. 6.3 (a) that the spacing between 1st order satellite along vector $\boldsymbol{q_{1a}}$ and $\boldsymbol{q_{1b}}$ is not same as in Fig. 6.3 (b) and this clear when we see the graphical plot of the component of $\boldsymbol{q}$ vector as function of temperature in Fig. 6.4 (a). We cannot say about the change in oxygen content (δ) but it is true that oxygen pressure $P(O_2)$ modify the order of interstitial oxygen and make more commensurate structure. In Fig. 6.4 (a) continuous blue and red arrows indicate this deviation of the modulation vector to the more commensurate just after applying the pressure (50 bar). After that we changed the temperature up to 450 ^{0}C keeping the pressure fixed and followed up the reconstructed reciprocal map, the corresponding *(hk1)* plane is shown in Fig. 6.3 (c & d). LTO/HTT phase transition take place at 450 ^{0}C that can be seen in (d) where the *(-331)* Bragg reflections is no more splitted and no satellite is observed. During cooling at temperature 420 ^{0}C satellite start to appear again as very weak reflection marked in blue circle in Fig. 6.3 (e) could be also related to kinetics of the reaction means system might needs time to get ordered and give intense reflections. At 50 ^{0}C we can see the *(-331)* reflection is now splitted in three not two (zoomed area in Fig. 6.3 (g)) and that must be due to the introduction of the other twin domain, this is clear that new twin domain formation is related to effect of the 50 bar of oxygen pressure together with different oxygen content that presents particularly at this temperature and also the rate of cooling how fast or how slow it was. Since it was started to grow the other twin domain and after releasing the pressure it continues to grow and as results the volume fraction of the new domain increased. This was the effect of the pressure on domain structure of $Pr_2NiO_{4+\delta}$ as function of temperature. Now what are the others effect of high pressure on the structure: to see this we look back to the Fig. 6.4 (a) where one big difference needs to be noticed first that modulation vector does not follow the same trend

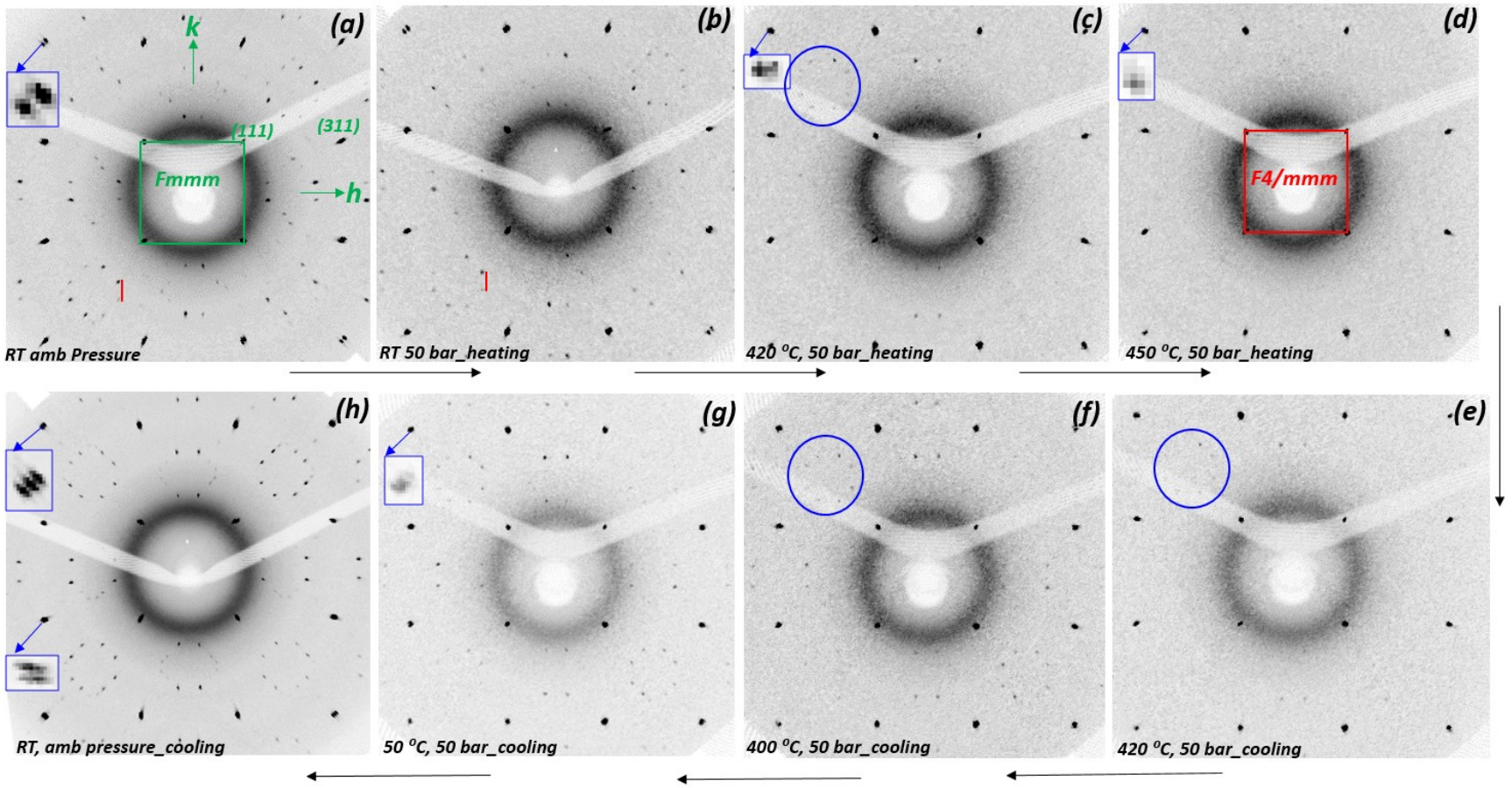

Figure 6.3: Reconstructed *(hk1)* plane of $Pr_2NiO_{4+\delta}$ at different temperature under oxygen pressure of 50 bar. (a) diffraction pattern obtained at ambient where average structure is *Fmmm* orthorhombic where blue box shows zoomed of the splitted (-331) Bragg reflections indicates one time twinned. (b and c) Shows the same diffraction pattern but obtained at RT and 420 ^{0}C after applying pressure respectively. (d) Represents the reciprocal *(hk1)* plane where structure is tetragonal and red box is *F4/mmm* unit cell where zoomed reflection is unique no splitting. (e - g) Shows the obtained same *(hk1)* plane during cooling the sample at 420, 400 and 50 ^{0}C. (h) At the end after releasing the pressure sample was measure at RT and blue box shows splitting of the Bragg reflections indicating crystal is now two times twinned which started already at 50 ^{0}C in (g). Black arrows indicated the sequences of the measurements.

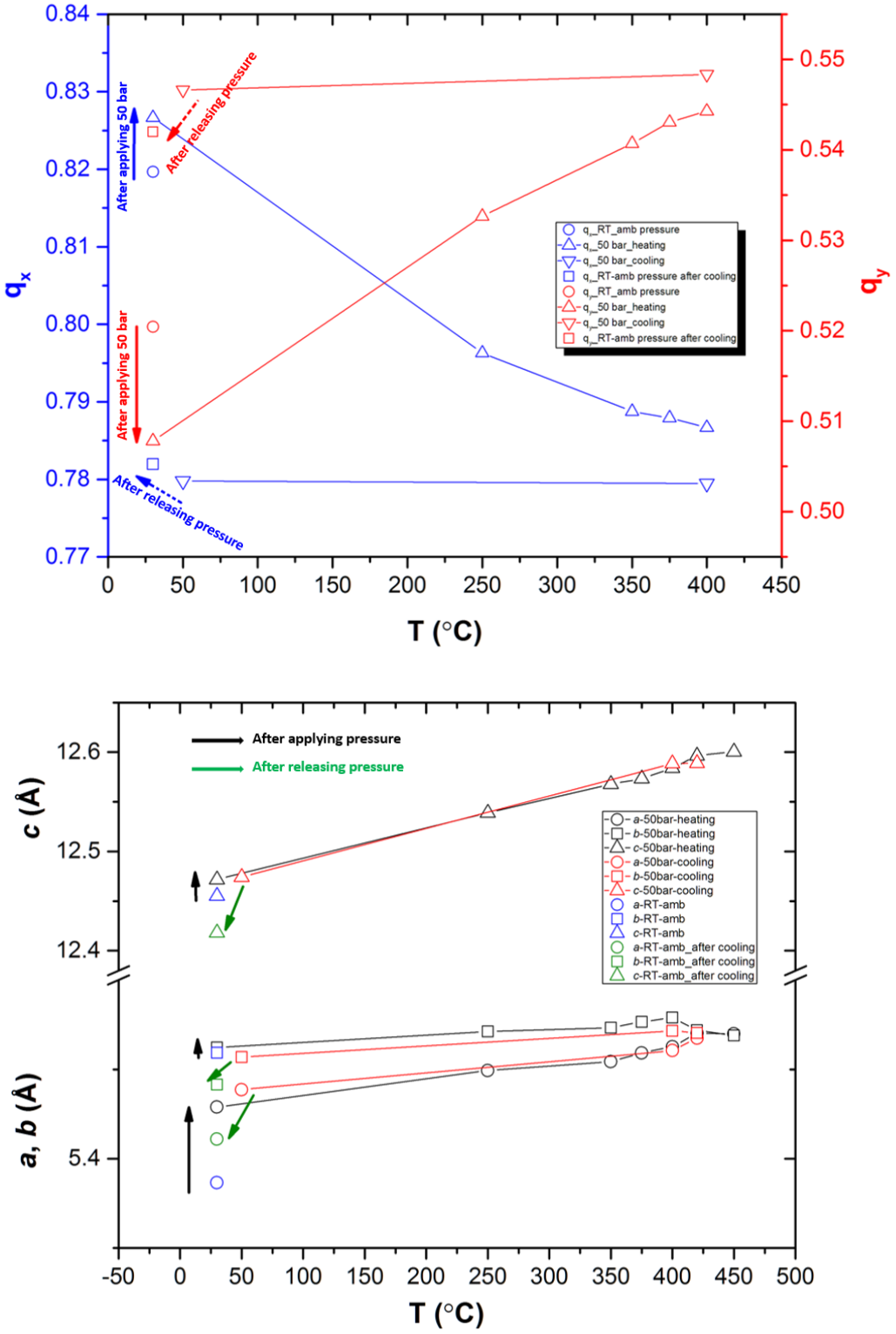

Figure 6.4: (a) Evolution of modulation vector as function of temperature at oxygen pressure of 50 bar, heating and cooling curve shows the irreversibility of the modulation. (b) Variation of the lattice parameters as function of temperature under pressure of 50 bar.

as we have seen during modulation vector evolution as function of temperature only in Fig. 6.2 (bottom right) and Fig. 5.6 (a). Here in the present study component q_x *(q_y)* start to decrease (increase) continuously very slowly with temperature under pressure of 50 bar and there is no saturation take place. Secondly, during cooling the modulation remains at almost same values kind of another lock in phase like memory effect and this is reason why even after releasing pressure it goes to the value where the pressure was just applied (see the broken blue and red arrows in Fig. 6.4 (a)). Incommensurability is shifted to higher temperature value. The evolution of the modulation is irreversible compare to only temperature study where it is reversible. This is again confirmed the real effect of the oxygen pressure of 50 bar by studying the change in the lattice parameters of the $Pr_2NiO_{4+\delta}$ structure as function of temperature. Starting *a, b* and *c* parameters differ from that values just after release the pressure at RT (see the green arrow in Fig. 6.4 (b)).

For the next measurements under oxygen pressure of 75 bar we took another tiny single crystal of $Pr_2NiO_{4+\delta}$ from the same batch and proceeded in the same way we did for oxygen pressure of 50 bar. Fig. 6.5 shows respective *(hk1)* reciprocal plane obtained at different temperature under oxygen pressure of 75 bar. Initial LTO orthorhombic phase exhibits *(3+2)*-dimensional commensurate modulated structure at ambient pressure with modulation vector $\boldsymbol{q1}_{a,b} = \pm 0.832\boldsymbol{a^*} + 0.508\boldsymbol{b^*}$ in the a^*-b^* plane (Fig. 6.5(a)). This is the first time we have observed *(3+2)*-dimensional incommensurate modulated structure when the system is under oxygen pressure of 75 bar at RT and associated modulation vector was $\boldsymbol{q1}_{a,b} = \pm 0.821\boldsymbol{a^*} + 0.516\boldsymbol{b^*}$ in the a^*-b^* plane whereas still we have the satellite in *(hkn/2)* plane, n = integer see Fig. 6.5 (I, J). With increase in temperature structure loose the long range order along c*-direction and it shows only (3+1)-dimensional incommensurate modulation Fig. 6.5(c), followed by LTO/HTT phase transition at 475 ^{0}C (d). During cooling down under oxygen pressure of 75 bar it does modulation vector does not change like the case for 50 bar and this time we did not see the twin domain evolution. A graphical representation of the modulation vector has been shown in Fig. 6.6 (a), here again it is irreversible phase transformation during cooling under high pressure and even after releasing pressure it stays almost same values. Also, we have presented evolution of the lattice parameters as function of temperature at 75 bar of oxygen

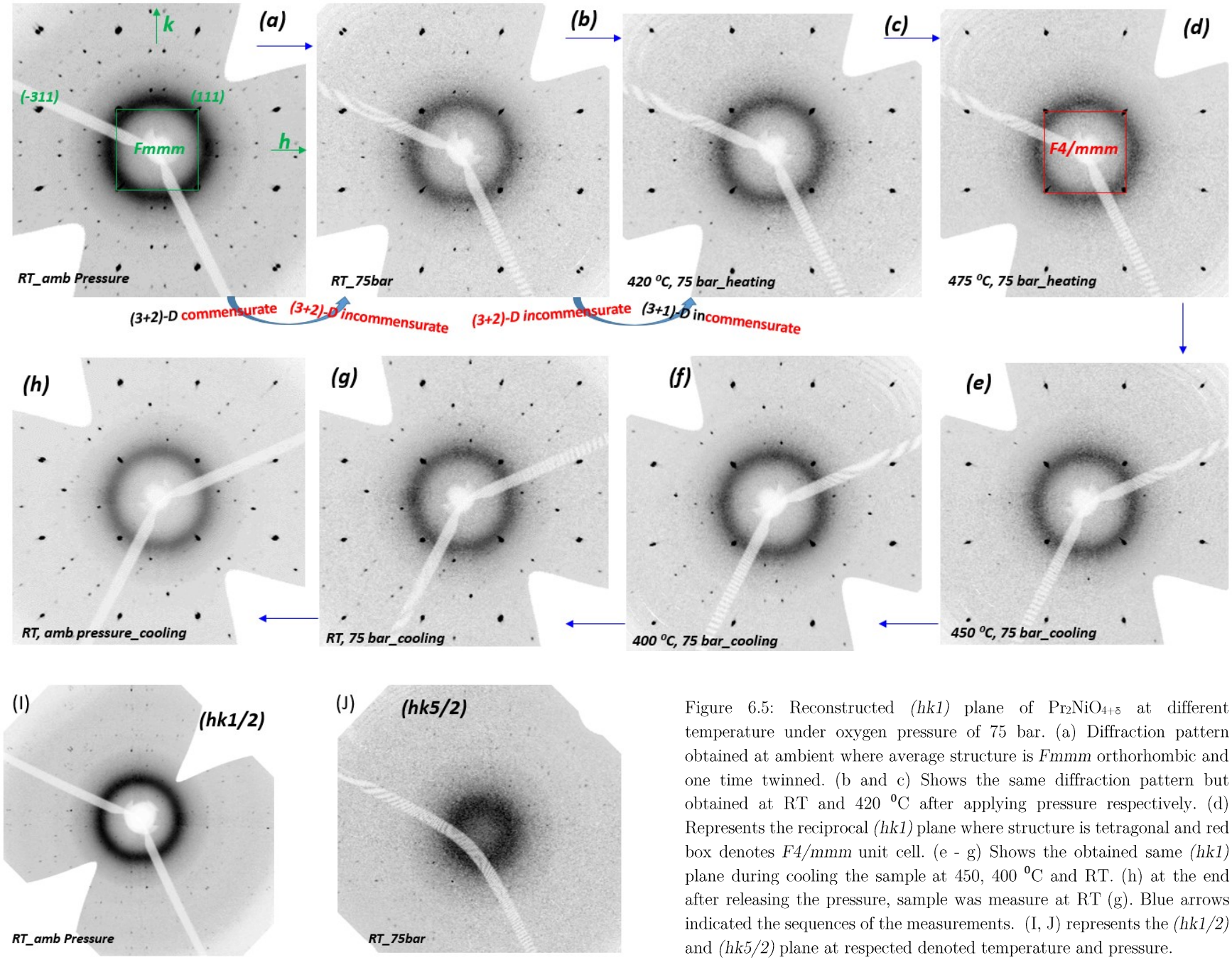

Figure 6.5: Reconstructed *(hk1)* plane of $Pr_2NiO_{4+\delta}$ at different temperature under oxygen pressure of 75 bar. (a) Diffraction pattern obtained at ambient where average structure is *Fmmm* orthorhombic and one time twinned. (b and c) Shows the same diffraction pattern but obtained at RT and 420 ^{0}C after applying pressure respectively. (d) Represents the reciprocal *(hk1)* plane where structure is tetragonal and red box denotes *F4/mmm* unit cell. (e - g) Shows the obtained same *(hk1)* plane during cooling the sample at 450, 400 ^{0}C and RT. (h) at the end after releasing the pressure, sample was measure at RT (g). Blue arrows indicated the sequences of the measurements. (I, J) represents the *(hk1/2)* and *(hk5/2)* plane at respected denoted temperature and pressure.

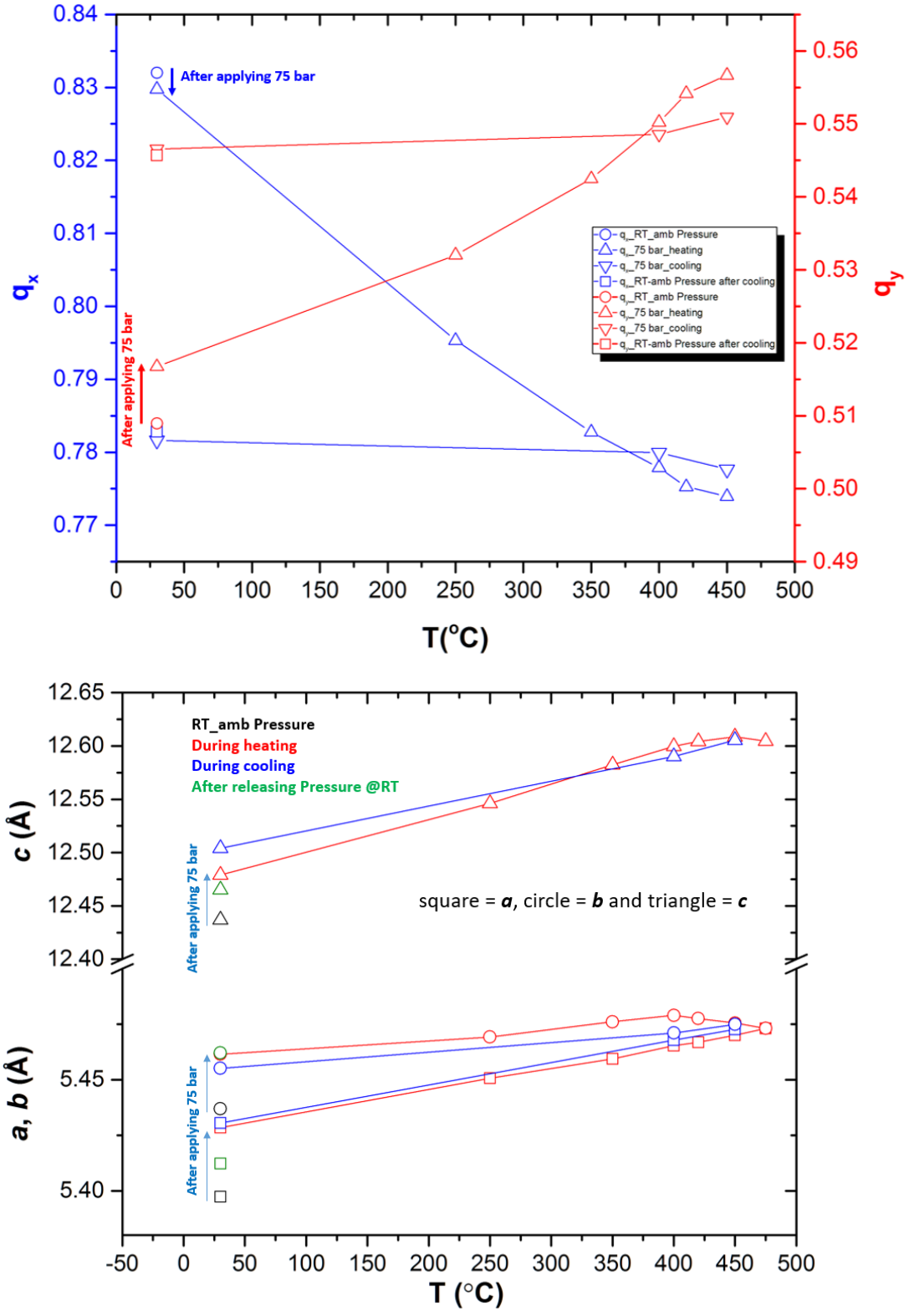

Figure 6.6: (a) Evolution of modulation vector as function of temperature at oxygen pressure of 75 bar, heating and cooling curve shows the irreversibility of the modulation. (b) Variation of the lattice parameters as function of temperature under pressure of 75 bar.

pressure in Fig. 6.6 (b) and it can be noticed that just after applying pressure a huge amount of changes in all the *a, b and c*-lattice constant takes place. With these results we confirm only the effect of oxygen pressure on not only average structure but also on the microstructure, twin domain and the modulation of the oxygen ordering as we consider oxygen stoichiometry is constant under such high pressure. In other words in terms of modulation of the oxygen ordering the phase transformation is irreversible compare when it is under pressure compare to reversible case under ambient pressure.

6.2.3 *ex situ* studies at oxygen pressure of 75 bar

To get an overview of the oxygen content changes just after releasing pressure we performed an ex situ measurements where we put small amount of crystallites in the same pressure cell and applied oxygen pressure of 75 bar. Only outer part of the capillary containing the sample was kept inside a small furnace followed by heating up to 600 ^{0}C and cooled down to RT under pressure. Then after releasing pressure immediately some part of the sample was taken to measure TGA under oxygen. One of tiny crystal was taken for the X-ray diffraction to see the phase and ordering pattern of the oxygen. Fig. 6.7 (a) and (b) shows the *(hk1)* reciprocal plane obtained by performing *ex situ* and *in situ* X-ray diffraction after releasing oxygen pressure coming from high temperature to RT, respectively. Both are *(3+1)*-dimensionally incommensurate modulated structure with slight change in modulation vector which can be seen by looking on the 1st and 2nd order satellite position marked in olive circle for both pattern. In Fig. 6.7 (a) the modulation vector $\boldsymbol{q}_{1a,1b} = \pm 0.802\boldsymbol{a^*}+0.525\boldsymbol{b^*}$ whereas in Fig 6.7 (b) it is $\pm 0.7816\boldsymbol{a^*}+0.546\boldsymbol{b^*}$. If we look to the TGA curve it indicates the immediate oxygen huge amount of oxygen uptake ~ 0.04 and this means after releasing pressure system lost 0.02 amount of interstitial oxygen from stable starting phase. This might be due to rapid cooling from 600 ^{0}C and it forces the system to loose oxygen to equilibrate with ambient oxygen partial pressure. Perhaps this might be the reason to the change in modulation take place in case of *ex situ* data compare to *in situ* at least at RT under ambient pressure since we cannot determine the oxygen content when it is under pressure. This is also evident from values of lattice parameters.

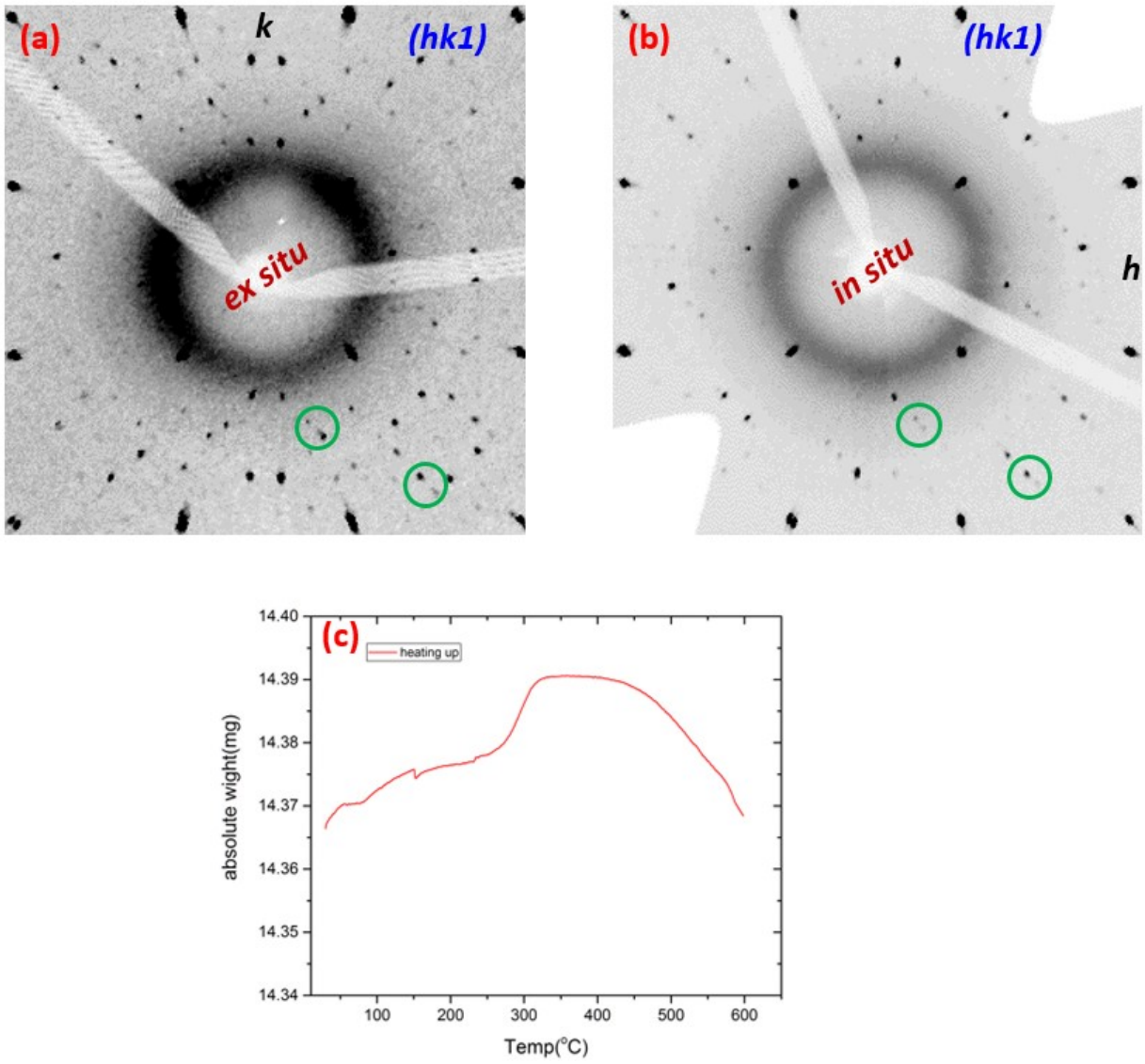

Figure 6.7: Comparison between *(hk1)* reciprocal plane: *ex situ* (a) and *in situ* (b) diffraction results obtained after releasing high oxygen pressure at RT showing slight change in modulation vector associated to their different *c*-lattice parameter and (c) obtained TGA curve (after cooling down to RT and releasing pressure) from the sample used for ex situ measurements indicated lower oxygen content at starting phase compare to normal stable phase ($\delta \sim 0.22$)

When we come down slowly during in situ measurements and release the pressure at RT the obtained $c = 12.4552$ Å where as in ex situ during rapid cooling it is 12.5039 Å and this pretty much reflect the consequences in TGA curve. This is also verified that during slow cooling in case of *in situ* experiment it has been crosschecked the same crystal after 20 days and we have seen no changes in modulated structure and *c*-lattice parameter. We have presented *(hk1)* plane of crystal which was

measured after 20 days in Fig 6.8 (a) together with same one from Fig. 6.7 (b). We will again show this kind of phenomena the differences that coming from rate of cooling where sample is treated under vacuum in the following section.

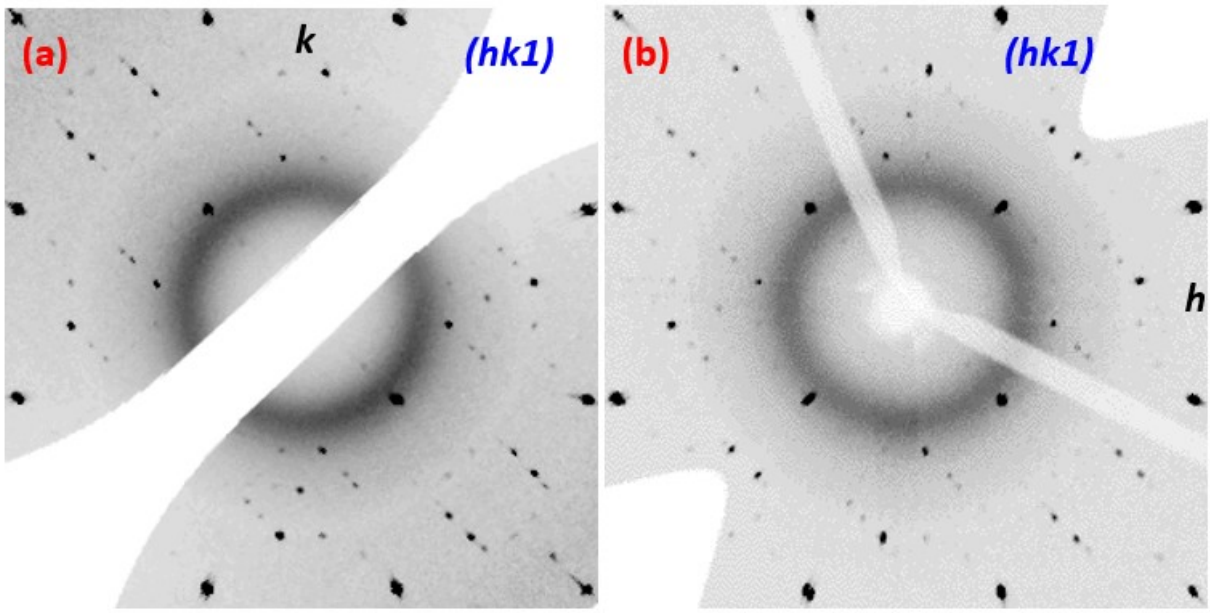

Figure 6.8: (a) Represents the *(hk1)* plane of the same crystal measure after 20 days compared to crystal in (b) showing no differences in the modulation vector except the intensity and that is because of longer exposure of X-ray beam in (a).

6.2.4 Structure of $Pr_2NiO_{4+\delta}$ under Vacuum (*in situ* and *ex situ*)

Results obtained from $Pr_2NiO_{4+\delta}$ treated under vacuum (0.01 mbar) by performing *in situ* and *ex-situ* X-ray diffraction is much more interesting and complex. We took another sample of $Pr_2NiO_{4+\delta}$ from same batch and mounted inside the pressure cell. Vacuum was applied via laboratory secondary pump which is connected to the gas-system to the sample keeping oxygen gas channel closed. We followed the same strategy: went up to 500 ^{0}C from RT under vacuum and come down to RT and then vacuum was released. The results are presented in Fig. 6.9 for different temperature starting from ambient (a) to 500 ^{0}C (not shown) then to RT (c and d). Starting ambient phase was

orthorhombic (a = 5.413 Å, b = 5.4467 Å and c = 12.456 Å) in one time twinned and shows *(3+2)*-dimensional commensurate modulated structure with modulation vector $\boldsymbol{q}_{1a,b} = \pm 0.834\boldsymbol{a^*} + 0.502\boldsymbol{b^*}$ (see Fig. 6.9(a)). At temperature 350 ^{0}C structure goes immediately to tetragonal phase ($a = b$ = 5.453 Å and c = 12.558 Å) without having superstructure reflections and it stays in this phase even up to 500 ^{0}C with little change in lattice parameters (Fig. 6.9(b)). After coming back to RT under vacuum structure transforms into orthorhombic phase (a = 5.397 Å, b = 5.488 Å and c = 12.465 Å) reversibly with same modulation $\boldsymbol{q}_{1a,b} = \pm 0.834\boldsymbol{a^*} + 0.497\boldsymbol{b^*}$. Orthorhombicity increases little bit as it can be seen from the twin splitting (Fig. 6.9(c)). Once we release the vacuum average structure remains same as twinned orthorhombic (*Fmmm*) but the modulation gets changed completely compare to starting phase. Superstructure reflections are now appeared as circle in between two strong Bragg reflections (see blue circles in Fig. 6.9(d)). Here we have presented *(hk2)* plane as the satellite appears as strong w.r.t Bragg one. We will show in the next section that with the help of newly found commensurate modulation vector $\boldsymbol{q''}_{1a,b} = \pm 0.6\boldsymbol{a^*} + 0.2\boldsymbol{b^*}$ all the satellite can be indexed. As soon as vacuum is released system takes up oxygen again and c-axis (12.414 Å) gets shorted as the stress is removed and these extra oxygen order themselves separately (which is not strong to see) and combined with those O_{int} already present at the interstitial position give rise this new modulation. It can be viewed as two separate cluster of modulation: modulation 1 ($\boldsymbol{q}_{1a,b} = \pm 0.834\boldsymbol{a^*} + 0.502\boldsymbol{b^*}$) from the O_{int} before releasing vacuum and modulation 2 ($\boldsymbol{q'}_{1a,b} = \pm 0.233\boldsymbol{a^*} + 0.302\boldsymbol{b^*}$) from extra added O_{int} after releasing vacuum. Combining these two modulation domain structure can modulate in this new propagation vector $\boldsymbol{q''}_{1a,b} = \boldsymbol{q}_{1a,b} + \boldsymbol{q'}_{1a,b} = \pm 0.6\boldsymbol{a^*} + 0.2\boldsymbol{b^*}$. Now the question can arise: why don't we see the ordering from those two different modulated domain 1 and 2? Intensity from modulated domain 1 (Fig. 6.9 (c)) already very weak from domain 2 could be also weak enough to see as less number of 2nd O_{int} but there combined effect can be more pronounced and order make them those two separate domain disorder. In order to validate this arguments we need proper structure refinements and the order-disorder scenario w.r.t also NiO_6 octahedra tilting as we will see now actually structure adopt new NiO_6 octahedra tilting or orientation of that when we cool down the system rapidly under vacuum and releasing pressure at RT by means of *ex situ*.

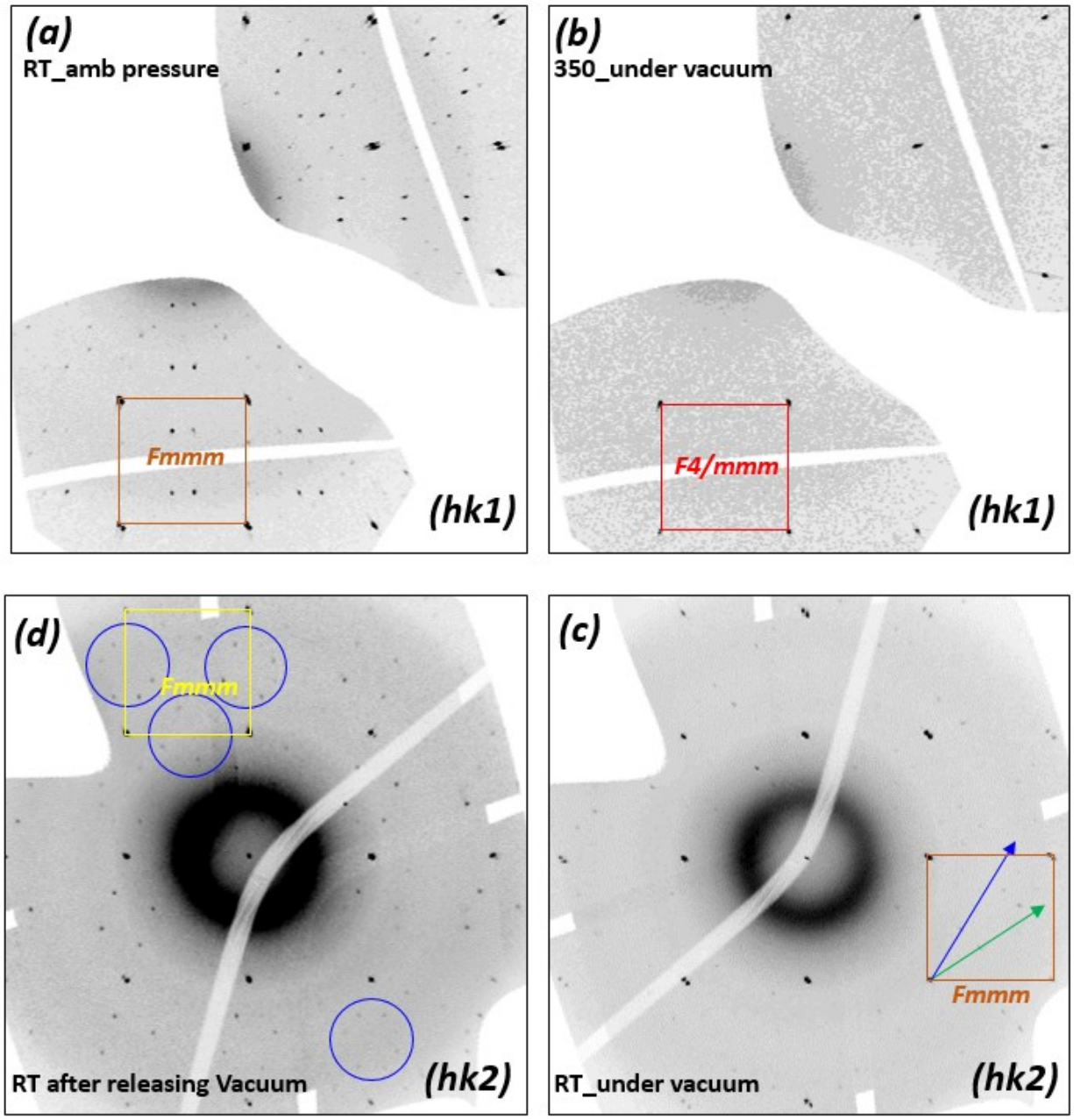

Figure 6.9: Represents the evolution of average structure and modulation of oxygen ordering of $Pr_2NiO_{4+\delta}$. (a) Show reconstructed *(hk1)* plane obtained at RT and ambient pressure showing *Fmmm* structure with *(3+2)*-dimensional commensurate modulated structure. (b) Shows the tetragonal phase without satellite. (c) After coming back to RT under vacuum exhibits same structure as starting phase and (d) *(hk2)* plane with complete different commensurate modulation in *Fmmm* cell. Blue circle indicates new arrangements of satellite between two strong Bragg reflections.

To emphasize the structure in more details we have performed *ex situ* X-ray diffraction measurements on $Pr_2NiO_{4+\delta}$. Crystal was heated to 500 ^{0}C under vacuum and cooled down to RT

under vacuum followed by releasing vacuum. Fig. 6.10 shows reconstructed *(hk0), (0kl)* and *(h0l)* reciprocal plane at RT after releasing the pressure. Three things are noticeable 1st, nicely defined sharp oxygen ordering peaks what we have seen previously in Fig. 6.9(d), 2nd in *(h0l)* plane reflections are splitted and 3rd average structure is orthorhombic (a = 5.407 Å, b = 5.482 Å and c = 12.329 Å) with high orthorhombicity and small c-axis. No twinned splitting was found in *(hk0)* plane indicated single orthorhombic domain. Splitting of Bragg reflections in *(h0l)* plane can be due to monoclinic angle between a- and c-axis. From the reflection conditions: no condition in *(hk0)* plane, l = 2n in *(0kl)*, l = 2n in *(h0l)* and l = 2n along *(00l)* space group can be assigned as orthorhombic *Pccm* again it needs to refine the structure to validate the space group. We now switched to the modulation that we have in *(hkn)*-type plane, n = integer. Fig. 6.11 shows the experimental and corresponding idealized pattern obtained at RT after releasing vacuum. All the satellite reflections can be indexed with the found commensurate modulation vector $\boldsymbol{q}''_{1a,b} = \pm 0.6\boldsymbol{a}^* + 0.2\boldsymbol{b}^*$. In this plane satellite and p-type reflections are very sharp but 10^{-4} order of magnitude less than main Bragg reflections. Up to 4th order satellite are presents and all the 1st and 2nd order satellite are stronger than 3rd and 4th order in ant positive or negative direction. Here only two individuals (q''_{1a} and q''_{1b}) are needed to modulate the structure even though it is not twinned. The origin of the new kind of modulation can be argued like before that two separate domains from two different type of O_{int} ordering modulate together. This can be also related to different NiO_6 octahedra tilting in the *Pccm* phase as we mentioned before and the orientation could be slight different from LTLO *Pccn* phase. The argument of oxygen uptake is validated and can be seen from the TGA curve (Fig. 6.7) which was performed in Ar atmosphere (even it contains O_2) and then change to oxygen flow. Shorter c-axis is also a consequences of such oxygen uptake just after releasing vacuum and the kinetics is different from heat treatment under ambient pressure and high oxygen pressure.

Most interestingly this is the first time we have seen the modulation appears twice in non-integer *(hkn/3)* plane where n = integer, along c^* at with period of $0.33c^*$. Fig. 6.12 illustrate the complex ordering in *(hkn/3)*-type plane with n= integer.

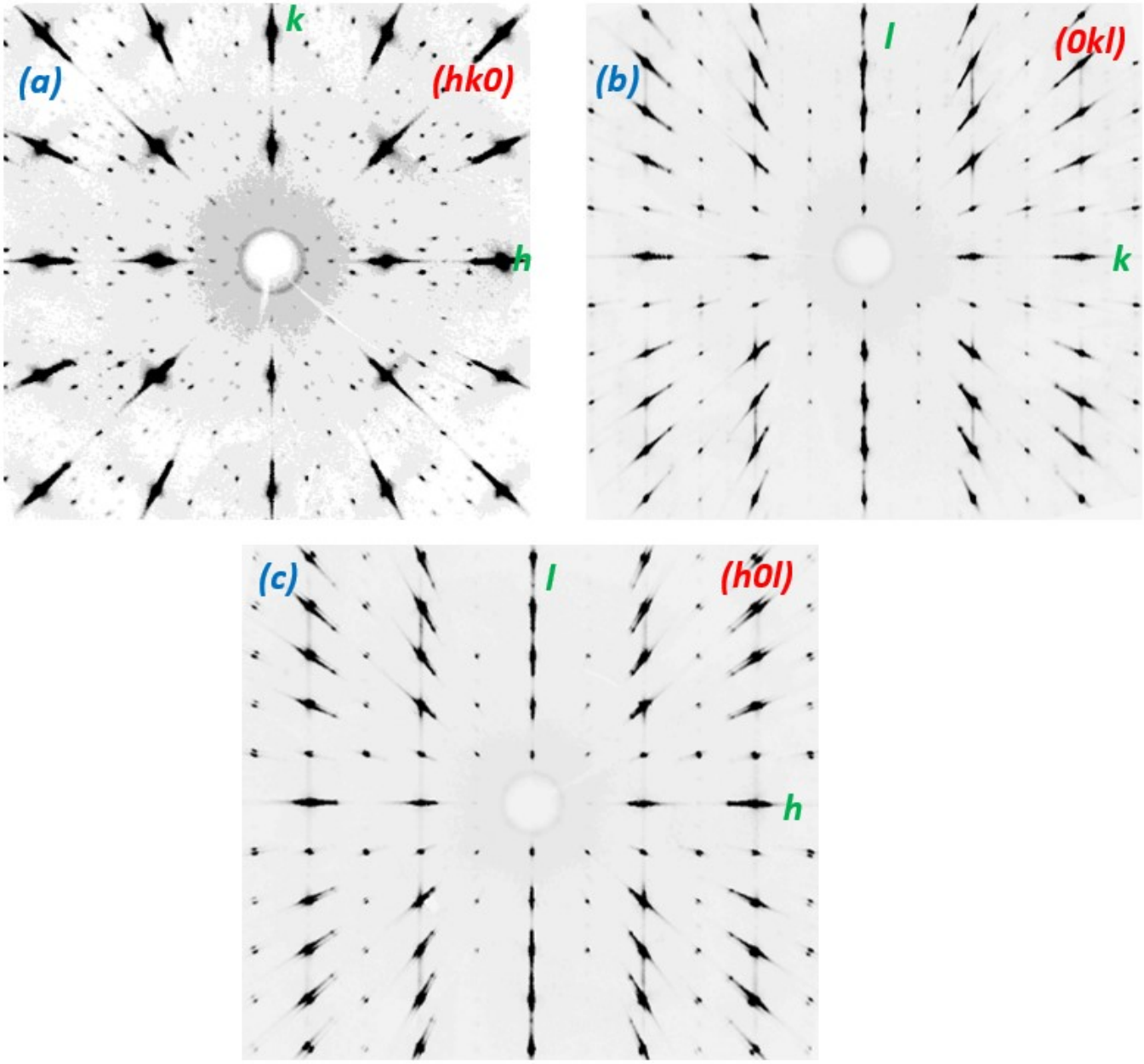

Figure 6.10: Reconstructed reciprocal plane of *(hk0), (0kl)* and *(h0l)* obtained from *ex situ* vacuum treated $Pr_2NiO_{4+\delta}$ after coming back to RT from 500 ^{0}C and releasing vacuum.

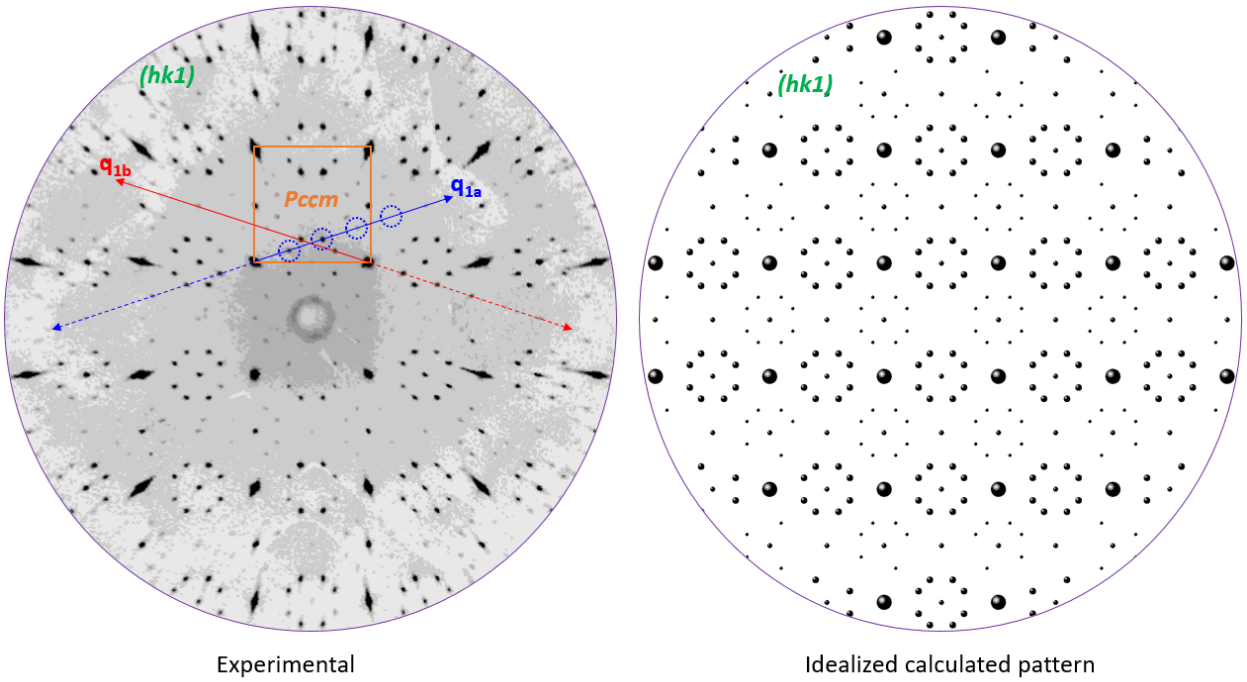

Figure 6.11: (Left) experimentally obtained *(hk1)* plane from same measurements in Fig. 6.10 and corresponding calculated idealized pattern with modulation vector $\boldsymbol{q}^{\prime\prime}{}_{1a,b} = \pm\, 0.6\boldsymbol{a}^{*} + 0.2\boldsymbol{b}^{*}$ in blue and red arrows. Orange box represents average orthorhombic unit cell in *Pccm* space group.

Even though *(hk0.33)* and *(hk0.66)* look similar but they are not equivalent in terms of intensities: then how to correlate this modulation? If we look on the upper plane like *(hk1.33)* and *(hk1.66)* reciprocal plane there is similariities between pair of planes like *(hk0.3)-(hk1.33)* and *(hk0.66)-(hk1.66)*. Also Fig. 6.13 shows comparison between those plane by looking the section (olive rectangle) indicates *(hk0.33)-(hk0.66)* and *(hk1.33)-(hk1.66)* are not equivalent. The point is how ever they modulate, the contribution from *(hk1)* and *(hk0)* is not same, at least it can be said that satellite in *(hk-0.33)* and *(hk0.33)* plane is modulated from *(hk0)* plane, similarly saltellite in *(hk0.66)* and *(hk1.33)* plane is modulated from *(hk1)* plane and so on. So far the exact modulation vector is not found to index all these satellite. This special modulation is now under investigation.

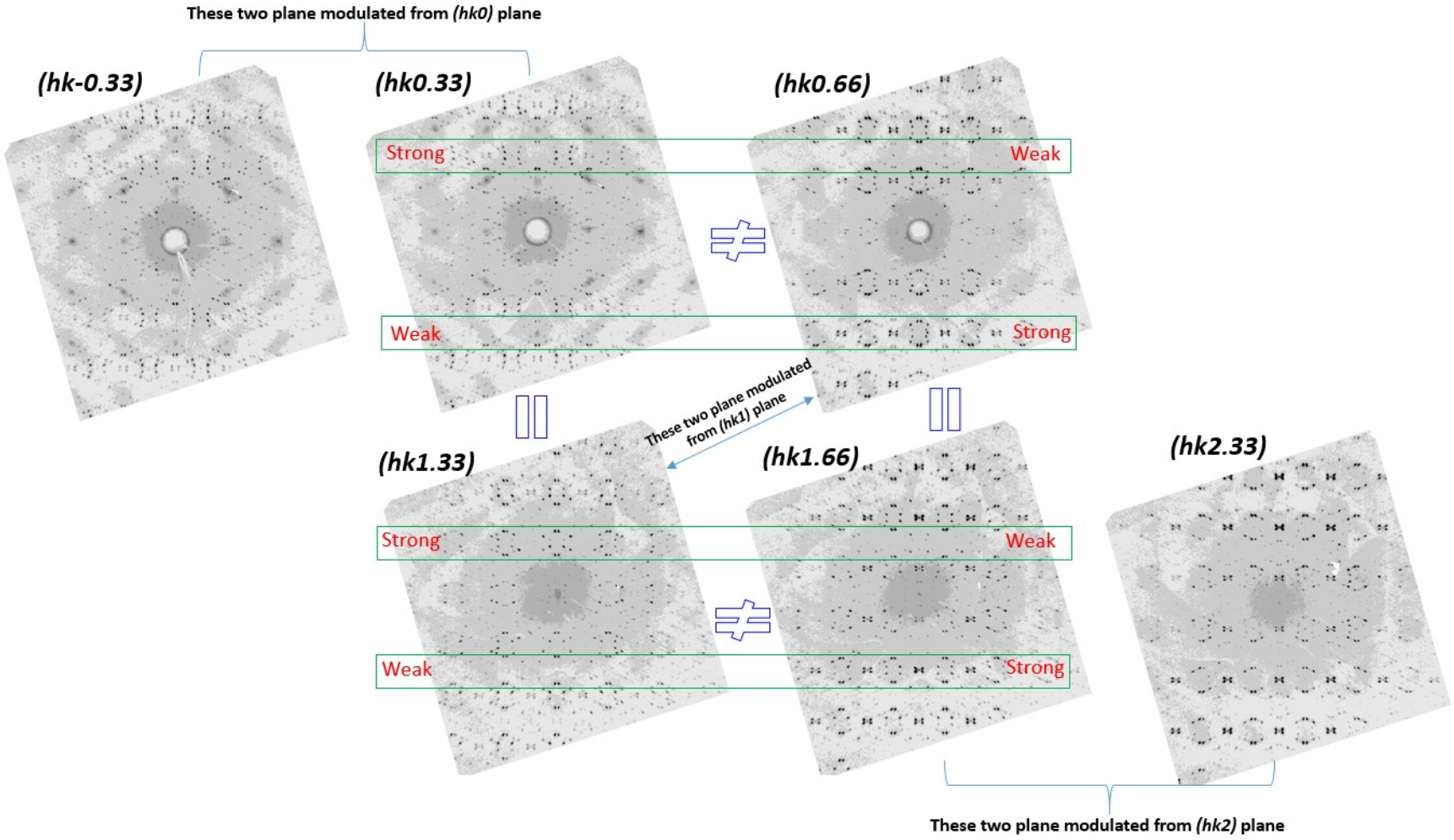

Figure 6.12: Represents the equivalency between modulation in those plane where the contribution comes from *(hkn)* plane where n= even and non-equivalent where the satellite modulate from *(hkn)* plane where *n* =odd. Also represents the equivalent plane of *(hk0.33)* and *(hk1.33)*. Suitable modulation is not found yet. Some tools need to be adopted to index such continuous modulation as they don't alter the position rather intensity and the way they appear (movement from left to right).

6.3 Study of Thermogravimetric analysis at different Atmosphere

We have seen the evolution of phase and modulation of oxygen ordering in $Pr_2NiO_{4+\delta}$ under vacuum at different temperature by means of ex situ and in situ X-ray diffraction measurements. In order to see the change in oxygen content to compare the vacuum study we have taken successive thermogram under Ar atmosphere and at last step we changed the Ar to O_2 flow to see the oxygen uptake. For each curve we kept the same condition of heating rate 5 ^{0}C/min and holding time at RT and 1100 ^{0}C. Fig. 6.13(a) shows the obtained TGA curve for different run; run 1 and 2 corresponding to measurements under Ar flow and in run 3 it was carried out in O_2 flow. During 1st heating oxygen uptake was quite small $\delta \sim 0.01$ (as the Ar bottle contain little amount of O_2, was not pure) and it losses $\delta \sim 0.08$ amount of oxygen at high temperature then it stays almost in the same oxygen level for the 2nd heating in Ar flow. Cooling process is reproducible (blue curve) for both run and there is some changes that take place at same temperature for heating (red rectangle) and cooling (blue rectangle) respectively. Since LTO/HTT transition already took place very earlier at 350 ^{0}C (which we have seen from X-ray diffraction Fig. 6.9) and there is no structural ordering, this specific changes could be associated with internal modification which is not clear yet. But what we want to know is that just after switch to O_2 flow system start to take up oxygen immediately (see the black encircle at time 1050 min Fig. 6.13(b)). This $\delta \sim 0.01$ amount of oxygen uptake cause the reason to make change in modulation as soon as we release the vacuum what we have seen in X-ray diffraction patter (see Fig. 6.9(d)). Once again the vacuum level even tough is not same for both measurements we cannot make a confirm conclusion but at least it gives an idea what's happening with oxygen content. In run 3 as usual once it start to heat again in O_2 flow it increase very sharply and reach to the maximum oxygen content $\delta \sim 0.25$ at temperature 360 ^{0}C with same small change around 800 ^{0}C similar to what we found in previous thermogram in Fig. 5.13.

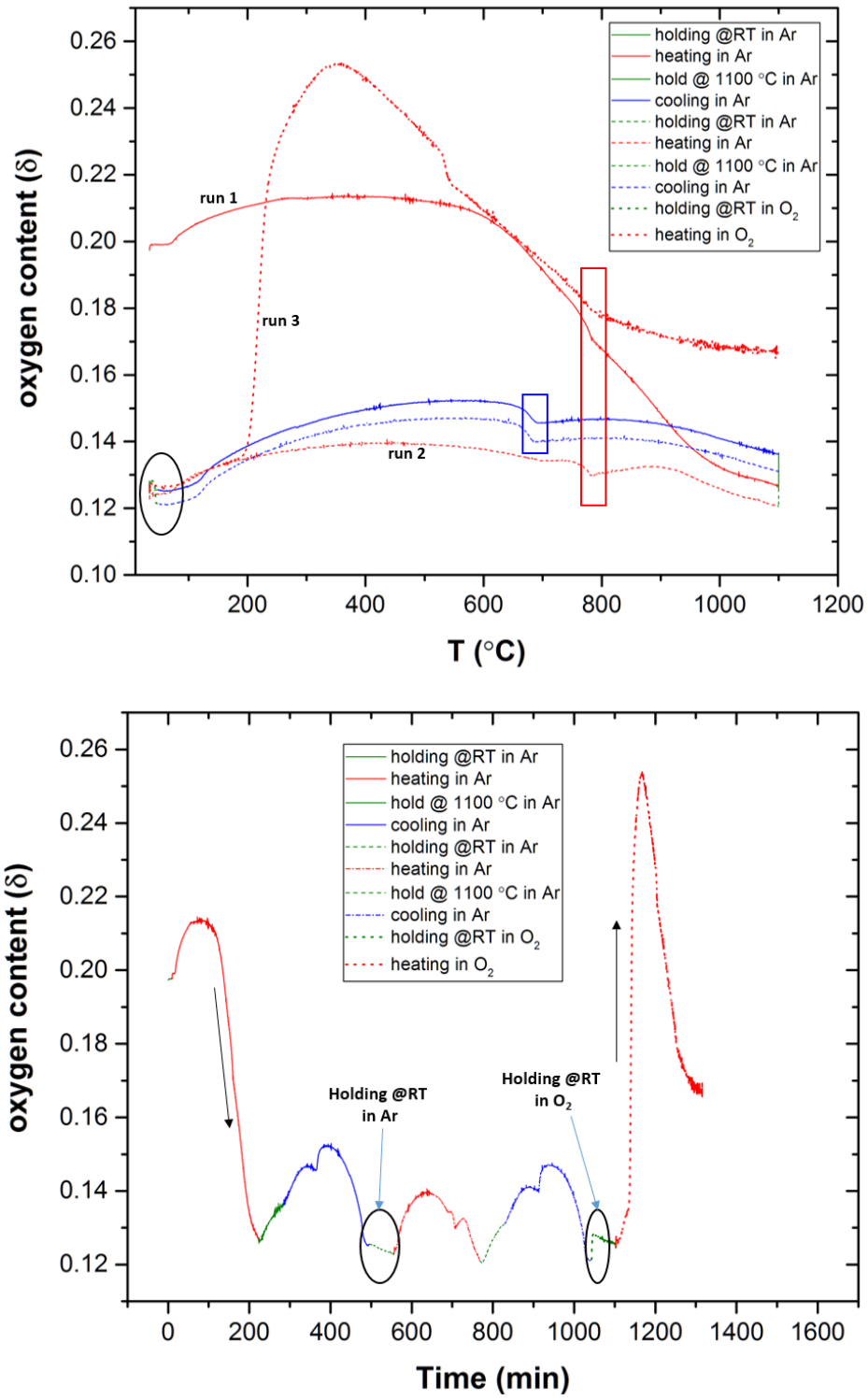

Figure 6.13: (Top) shows TGA curve of $Pr_2NiO_{4+\delta}$ under Ar flow (run 1 and 2) and O_2 flow (run3), indicates different scenario of oxygen release and uptake with temperature. (Bottom) represents the same curve plotted with time along x-axis to show the change in oxygen content during holding at RT encircled in black oval.

6.4 Summary

In this chapter we have explored the evolution of average structure and modulation of oxygen ordering in $Pr_2NiO_{4+\delta}$ as function of temperature under different oxygen pressure and vacuum. As the system incorporate oxygen atom at interstitial site by oxidizing from $Pr_2NiO_{4.0}$ to $Pr_2NiO_{4.25}$ or treating thermally under oxygen or ambient pressure it give rises different type of complex 3D oxygen ordering starting from RT to high temperature, it is important to know the associated complex phase diagram combining all the ordering scenario with phase transition as function of temperature and pressure in order to better understand the correlation between such structural changes in microscopic region with phonon assisted oxygen diffusion mechanism at ambient. In Fig. 6.14 and Fig. 6.15 we have presented the phase diagram separately in terms of lattice parameter evolution and modulation vector from x-ray single crystal diffraction measurements during heating and cooling the sample under certain condition of pressure. One important point should be noted that starting modulation vector for each four measurements are different because of the oxygen stoichiometry of each starting phase might not be same, it completely depends on the oxygen stoichiometry of the sample and the age of it. However, only temperature dependent study at ambient pressure gives an idea about the one part of phase diagram where change in microstructure and oxygen uptake-release is reversible kinetically. Same kind of temperature dependent X-ray diffraction study under 50 bar of oxygen pressure is completely different where during heating it does not go to stable incommensurate phase rather slowly and before saturating that lock in phase it enters to tetragonal phase which is similar to case of study under 75 bar of oxygen pressure but still follow the trend as like ambient pressure. On the other hand during cooling it gets locked in to that high temperature incommensurate phase and does not change by means of modulation vector up to RT. This is another aspect of pressure effects, just after releasing pressure not only it change the oxygen ordering in higher dimension but also twin domain gets modified it becomes two time twinned from one time twinned. So far these are the basic changes we have observed and we haven't discover all the reason behind such changes yet. But at least it would help a lot once we have structural model microscopically considering all the effects to describe several physical phenomena e.g. low temperature charge, spin and electronic phase separation. All the answer is hidden behind

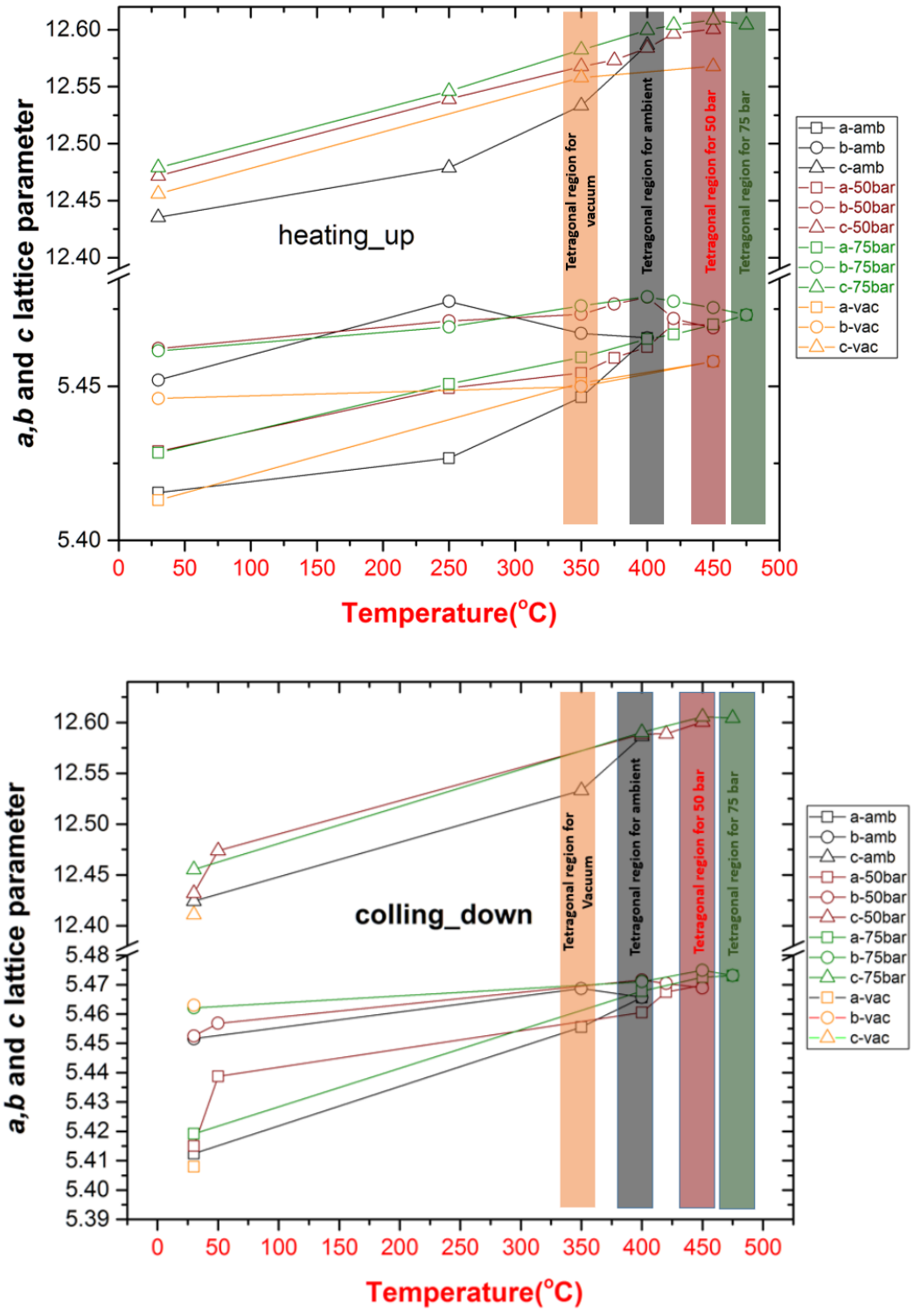

Figure 6.14: Graphical representation of lattice parameter evolution of $Pr_2NiO_{4+\delta}$ as function of temperature under different oxygen pressure. Data obtained from in situ X-ray single crystal diffraction during heating (top) and cooling (bottom) the sample. Four superimposed different color bar indicates LTO/HTT phase transition temperature for four different pressure.

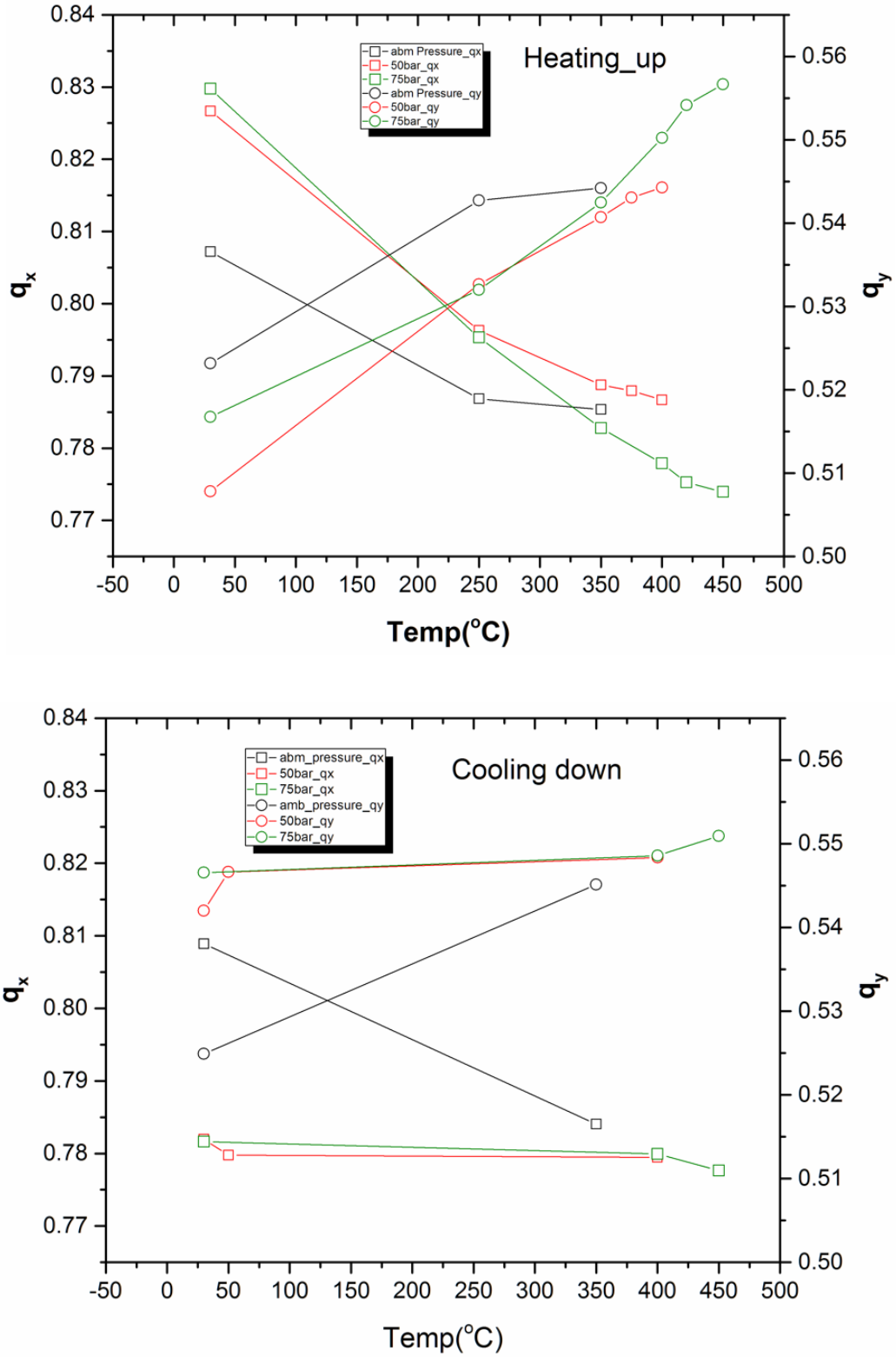

Figure 6.15: Graphical representation of component of modulation vector of oxygen ordering in $Pr_2NiO_{4+\delta}$ as function of temperature under different oxygen pressure. Data obtained from in situ X-ray single crystal diffraction during heating (top) and cooling (bottom) the sample. It show the irreversibility of the modulated structure except at ambient pressure.

this oxygen ordering screening which is the key of the complex structure of $Pr_2NiO_{4+\delta}$. Another complex ordering of oxygen interstitials has been observed which prefers to be appeared once we heat the sample under vacuum and coming back to RT followed by releasing vacuum, here again, what we have seen before is different vacuum level can alter the oxygen ordering along with average structure in different way. Most importantly, it is interesting to know that LTO/HTT transition temperature shifts to higher temperature with increasing oxygen pressure, this is an another effect of oxygen pressure which tells us the NiO_6 octahedra are forced to rearrange at higher temperature where we consider no change in oxygen interstitials atoms as it is under high pressure. In conclusion, structure responds completely different way under different external parameters e.g. pressure, temperature and vacuum basically means the oxygen ordering that take place microscopically and locally can be influenced either by changing the oxygen stoichiometry electrochemical reaction at ambient or by applying high oxygen pressure. These are the most important effects of external parameters on the structure globally and locally which might have direct consequences with other physical phenomena which we will see in the next chapter, also since all the physical properties in this titled compound are related and dependent on the oxygen stoichiometry 1^{st} and 2^{nd} highly anisotropic crystal structure one can tune the microstructure by applying desired temperature and pressure for studying e.g. low temperature charge and spin ordering in the strongly correlated TMOS like $Pr_2NiO_{4+\delta}$.

References:

1. Villesuzanne, A.; Paulus, W.; Cousson, A.; Hosoya, S.; Le Dréau, L.; Hernandez, O.; Prestipino, C.; Houchati, M. I.; Schefer, J. On the role of lattice dynamics on low-temperature oxygen mobility in solid oxides: a neutron diffraction and first-principles investigation of $La_2CuO_{4+\delta}$. Solid State Electrochem. 2011, 15, 357−366.
2. Perrichon, A.; Piovano, A.; Boehm, M.; Zbiri, M.; Johnson, M.; Schober, H.; Ceretti, M.; Paulus, W. Lattice Dynamics Modified by Excess Oxygen in $Nd_2NiO_{4+\delta}$: Triggering Low-Temperature Oxygen DiffusionJ. Phys. Chem. C 2014, 119, 1557−1564.
3. W. Paulus, H. Schober,S. Eibl, M. Johnson, T. Berthier,O. Hernandez,M. Ceretti, M. Plazanet, K. Conder and C. Lamberti, Lattice Dynamics To Trigger Low Temperature Oxygen Mobility in Solid Oxide Ion Conductors, *J. Am. Chem. Soc.*, 2008, 130 (47).
4. M. Ceretti, O. Wahyudi, A. Cousson, A. Villesuzanne, M. Meven, B. Pedersen, J. M. Bassat, and W. Paulus, "Low temperature oxygen diffusion mechanisms in Nd2NiO4+δ and $Pr_2NiO_{4+\delta}$ via large anharmonic displacements, explored by single crystal neutron diffraction," J. Mater. Chem. A, vol. 3, no. 42, pp. 21140– 21148, 2015.
5. W. Paulus, A. Cousson, G. Dhalenne, J. Berthonc, A. Revcolevschi, S. Hosoyad, W. Treutmann, G. Heger, R. Le Toquin, Neutron diffraction studies of stoichiometric and oxygen intercalated La_2NiO_4 single crystals, Solid State Sciences 4 (2002) 565–573.
6. O. Wahyudi, M. Ceretti, I. Weill, A. Cousson, F. Weill, M. Meven, M. Guerre, A. Villesuzanne, J.-M. Bassat and W. Paulus, CrystEngComm, 17, 6278-6285 (2015).
7. S. H. Jensen, X. F. Sun, S. D. Ebbesen, R. Knibbe, and M. Mogensen, Hydrogen and synthetic fuel production using pressurized solid oxide electrolysis cells, International Journal of Hydrogen Energy, 35(18), 9544 (2010).
8. X. Sun, M. Chen, S. H. Jensen, S. D. Ebbesen, C. Graves, and M. Mogensen, Thermodynamic analysis of synthetic hydrocarbon fuel production in pressurized solid oxide electrolysis cells, International Journal of Hydrogen Energy, 37(22), 17101 (2012).
9. D. M. Bierschenk, J. R. Wilson, and S. A. Barnett, High efficiency electrical energy storage using a methane–oxygen solid oxide cell, Energ Environ Sci, 4(3), 944 (2011).
10. C. Drevet, M. Henault, and J. Fouletier, Oxygen electrode reaction on stabilized zirconia under high oxygen pressure (up to 100 bar), Solid State Ionics, 136, 807 (2000).
11. T. Matsui, M. Futamura, R. Kikuchi, and K. Eguchi, in Solid Oxide Fuel Cells 10, K. Eguchi, S. C. Singhai, H. Yokokawa, and H. Mizusaki, eds., Vol. 7, p. 851–858, Electrochemical Society Inc, Pennington, (2007).
12. L. Zhou, M. J. Cheng, B. L. Yi, Y. L. Dong, Y. Cong, and W. S. Yang, Performance of an anode-supported tubular solid oxide fuel cell (SOFC) under pressurized conditions, Electrochim. Acta, 53(16), 5195 (2008).
13. E. C. Thomsen, G. W. Coffey, L. R. Pederson, and O. A. Marina, Performance of lanthanum strontium manganite electrodes at high pressure, J. Power Sources, 191(2), 217 (2009).

14. Justin Railsback, Gareth Hughes, Liliana Mogni, Alejandra Montenegro-Hernandez, and Scott Barnett, High-Pressure Performance of Mixed-Conducting Oxygen Electrodes: Effect of Interstitial versus Vacancy Conductivity, Journal of the Electrochemical Society, 163 (13) F1433-F1439 (2016).
15. M. Hücker, M. v. Zimmermann, R. Klingeler, S. Kiele, J. Geck, S. Bakehe, J. P. Hill, A. Revcolevschi, D. J. Buttrey, B. Büchner, and J. M. Tranquada, Phys. Rev. B 74, 085112 (2006).
16. E. Kaneshita and A. Bishop, J. Phys. Soc. Jap. 77, 123709 (2008).
17. L. Simonelli, V. M. Giordano, N. L. Saini, and G. Monaco, Phys. Rev. B 84, 195140 (2012).
18. Web reference https://photon-science.desy.de/annual_report/files/2013/20132962.pdf.

Chapter 7

Incommensurate Charge and Spin Stripe order in Oxygen and Sr-doped $Pr_{2-x}Sr_xNiO4_{+\delta}$ explored by Neutron and X-Ray Diffraction Technique

Both oxygen and Sr-doped $Pr_{2-x}Sr_xNiO_{4+\delta}$ belongs to strongly correlated electron system with basic orthorhombic (x = 0 and 0.125) and tetragonal (x = 0.25 and 0.5) unit cell consisting of square planner NiO_2 layer separated by Pr/Sr spacer layer as shown in Fig. 7.1 (left). This structure is homologous to high-T_c superconductor cuprates and other cobaltites but the nickelates does not show any superconductivity over entire Sr-doping, especially ground state of undoped Pr_2NiO_4 oxides is insulator and antiferromagnetic. In order to understand the peculiarity of this oxide investigation on $Pr_{2-x}Sr_xNiO_{4+\delta}$ single crystal upon oxygen and Sr doping is essential.

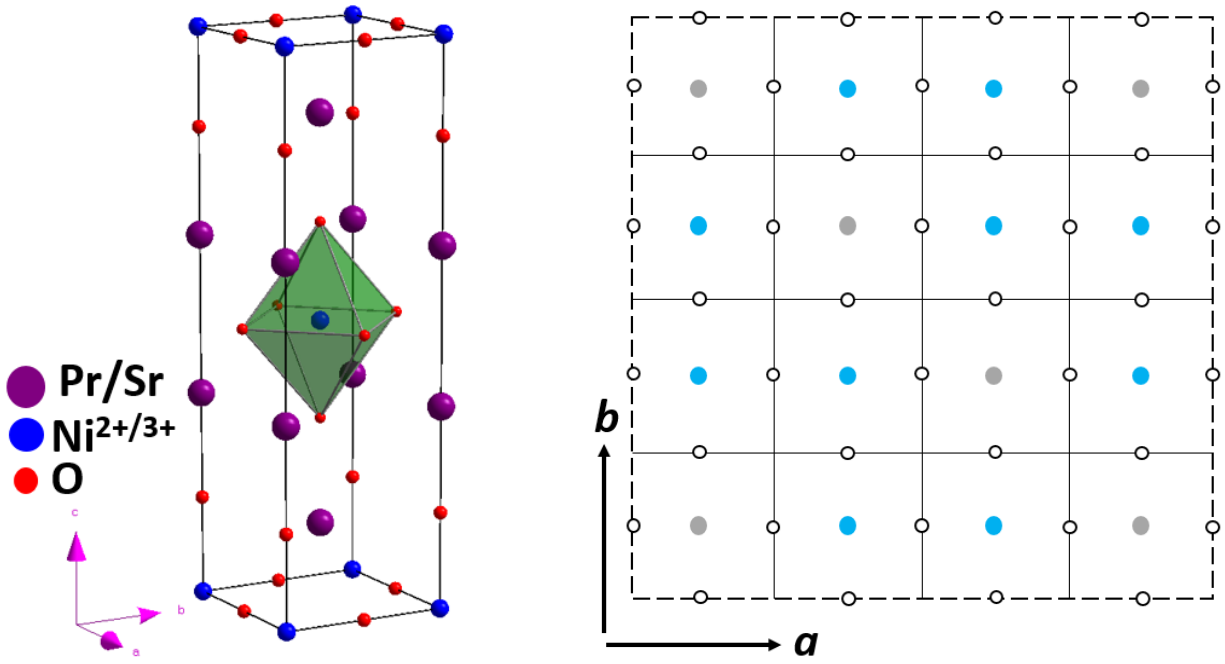

Figure 7.1: (Left) shows the basic tetragonal *(I4/mmm)* unit cell of $Pr_{2-x}NiO_{4+\delta}$ excluding excess oxygen and (right) a schematic representation of Ni^{2+} (grey), Ni^{3+} (sky blue) and oxygen (open circle) arrangement in stripe charge order phase.

Depending on the electronic configuration and oxidation state of Ni^{2+}/Ni^{3+} transition metal ions in octahedral crystal field (HS or LS) electronic phenomena may vary system to system and may give rise different competing state between oxygen, charge and spin ordering. Simultaneous oxygen, hole and spin ordering was first observed using neutron diffraction in $La_2NiO_{4.125}$ single crystal [1]. We have seen in chapter 2 pure undoped La_2NiO_4 is antiferromagnetic $T_N \sim 650K$ with ordered moment 1.6 μ_B [2], doping with Sr (at the cost of disordered dopant potential) or excess oxygen (certain concentration leads to long range stripe ordered state) in NiO_2 plane gradually reduce the Neél temperature T_N. and it can be induced the metallic behavior with higher doping concentration. Also structural distortion is suppressed by the Sr doping [3-4] due to the bond-length mismatch coming from large ionic radius of Sr and the oxidation of Ni similar and the reason why HTT/LTO phase boundary shifted to higher x and T for Pr and Nd compare to La. In the previous chapter we have seen also this LTO/HTT transition temperature shifted further to higher T with higher oxygen pressure in $Pr_2NiO_{4+\delta}$. This already gives an idea that Sr- and oxygen doping influence the internal structure distortion which might relates the electronic ordering in the sample and affects the reliability of the linear relationship of charge concentration $n_h = x + 2\delta$. In our recent studies it has been found the incommensurability ε of charge and spin ordering is highly sample dependent in terms of oxygen concentration, similar situation also has been confirmed by several measurements where it is reported the fluctuation in incommensurability arising from the oxygen concentration in $La_{2-x}Sr_xNiO_{4+\delta}$ materials with the stripe order of charges and spins associated with structural distortion [5-6]. Besides the nonlinearity of incommensurate charge concentration another interesting feature has been found that in oxygen doped $Pr_2NiO_{4+\delta}$ ($\delta \sim 0.25$) sample both checker board and stripe charge order exists at low temperature whereas checkerboard retains up to RT. It has been shown spontaneous rearrangement of checkerboard to stripe charge order ($\varepsilon = 0.44$) but in $La_{1.5}Sr_{0.5}NiO_4$ single crystal where with decreasing temperature, a checkerboard-type charge order is formed below $T^C_{CO} = 480K$ [7]. So far to our knowledge, nickelates doped with oxygen and Sr simultaneously is not highlighted in details. To better understand the picture of connected charge and spin ordering with oxygen ordering, a model system should be introduce by studying X-ray and neutron diffraction on only oxygen doped $Pr_2NiO_{4+\delta}$ separately with Sr doped $Pr_{2-x}Sr_xNiO_{4+\delta}$.

Herewith, in this chapter we present the interplay of oxygen ordering together with charge and spin ordering in $Pr_{2-x}Sr_xNiO_{4+\delta}$ (x = 0, 0.125 and 0.5) explored by X-ray and neutron diffraction from RT to low temperature and magnetic properties measurements by using SQUID. We wanted to see the combined effect of equivalent hole doping (oxygen or Sr), for that we did not reduce the sample to take out the excess interstitial oxygen in Sr-doped sample and this is reason why the interpretation was quite complex but it gives us a new insight of such strongly correlated electronic material.

7.1 Experimental Strategy

Magnetic properties of as grown $Pr_2NiO_{4+\delta}$ is highly anisotropic along different crystallographic direction as the coupling along *c*-axis is less dramatic than coupling in *a*-*b* plane. Two small piece of oriented crystal of dimension *4 mm* × *4 mm* × *2 mm* was taken for SQUID magnetometry measurements where the magnetic field was applied along c-axis and perpendicular to c-axis. *M*-*T* curve was taken from 400 - 2 K under ZFC and FC mode. To see any ferromagnetic signal is present or not we also measured the *M*-*H* loop up to 7 tesla of magnetic field at 5 and 10 K. Single crystal X-ray diffraction measurements for all the sample (x = 0, 0.125 and 0.5) were carried out only at RT and 80 K which is far below from both charge and spin ordering temperature where low temperature was obtained by very stable liquid nitrogen flow. Fast data sets were collected from 1M PILATUS area detector using the wavelength $\lambda = 0.7$ Å at insertion device beamline ID28 (side station), ESRF, Grenoble.

Similarly, single crystal neutron diffraction measurements on the big size crystal (x = 0 and 0.5) were performed at RT, 100 and 2 K. Measurements were carried out with the diffractometer (λ = 2.45 Å) at DMC, SINQ, PSI and data were collected by 2D area detector. We will presents all the results obtained by local and global technique in the following section.

7.2 SQUID Magnetometry

Magnetic susceptibility and isothermal magnetization of $Pr_{2-x}Sr_xNiO_{4+\delta}$ at various temperature and magnetic field applied parallel and perpendicular to c^*-axis are obtained to investigate overall

picture of magnetic properties. Fig. 7.2 shows inverse molar susceptibility $\chi_m^{-1}(T)$ curve after zero-field cooling at applied magnetic field of 50 Oe perpendicular and parallel to c*-axis of as grown $Pr_2NiO_{4+\delta}$. At temperature range over RT a linear fit has been performed with Curie-Weiss law and from that $\boldsymbol{\mu}_{eff} = 4.46\ \boldsymbol{\mu}_B$ was obtained and the calculated negative Curie -Weiss temperature was $\boldsymbol{\theta}_{CW}$ = -257 K indicates clearly antiferromagnetic ordering. Also several segment of that inverse susceptibility curve was fitted with Curie-Weiss law and it shows different effective magnetic moment from 4.46 μ_B to 3.44 μ_B that means at higher temperature range Pr^{3+} is in paramagnetic state and Ni^{2+}/Ni^{3+} sub lattices are partially ordered. Once the temperature decreased Ni^{2+} and Ni^{3+} sub lattice gets ordered and only the contribution in effective magnetic moment $\boldsymbol{\mu}_{eff} = 3.74\ \boldsymbol{\mu}_B$ comes from Pr^{3+} only even though little bit higher value than calculated one. Further decreasing temperature Pr^{3+} lattice start to order partially and as a results effective magnetic moment decrease $\boldsymbol{\mu}_{eff} = 3.44\ \boldsymbol{\mu}_B$. The calculated and experimentally observed effective magnetic moments are given in table 1. Another feature is that Commensurate and incommensurate charge order temperature can be seen as small hump in the inverse susceptibility curve at T^C_{CO} = 334 K and T^{IC}_{CO} = 170 K respectively. Tso = 99 K is the temperature where the spin start to get order once after the incommensurate charge are ordered at T^{IC}_{CO} = 170 K. Then at very low temperature spin rearrangement take place perhaps at T_{SR} = 8K which can be seen as small knee. Besides to see all these spin and charge order temperature $\chi_m T$ vs T and 1st derivative of molar susceptibility ($d\chi_m/dT$) vs T has been plotted in the inset of the same Fig. 7.2 where different colored arrow indicate those temperature. The black circle in the derivative curve indicates some kind of arrangement or ordering of spin but still not clear yet. It has been reported on stoichiometric Ln_2NiO_4 (Ln = Pr, Nd and La) single crystal that decreasing temperature crystal structure goes through LTO *(Bmab)* to LTT *($P4_2/ncm$)* phase transformation with new spin arrangement and give rise to ferromagnetic out-of-plane interaction and upon oxygen doping this 3D magnetic ordering get lost [8-11].

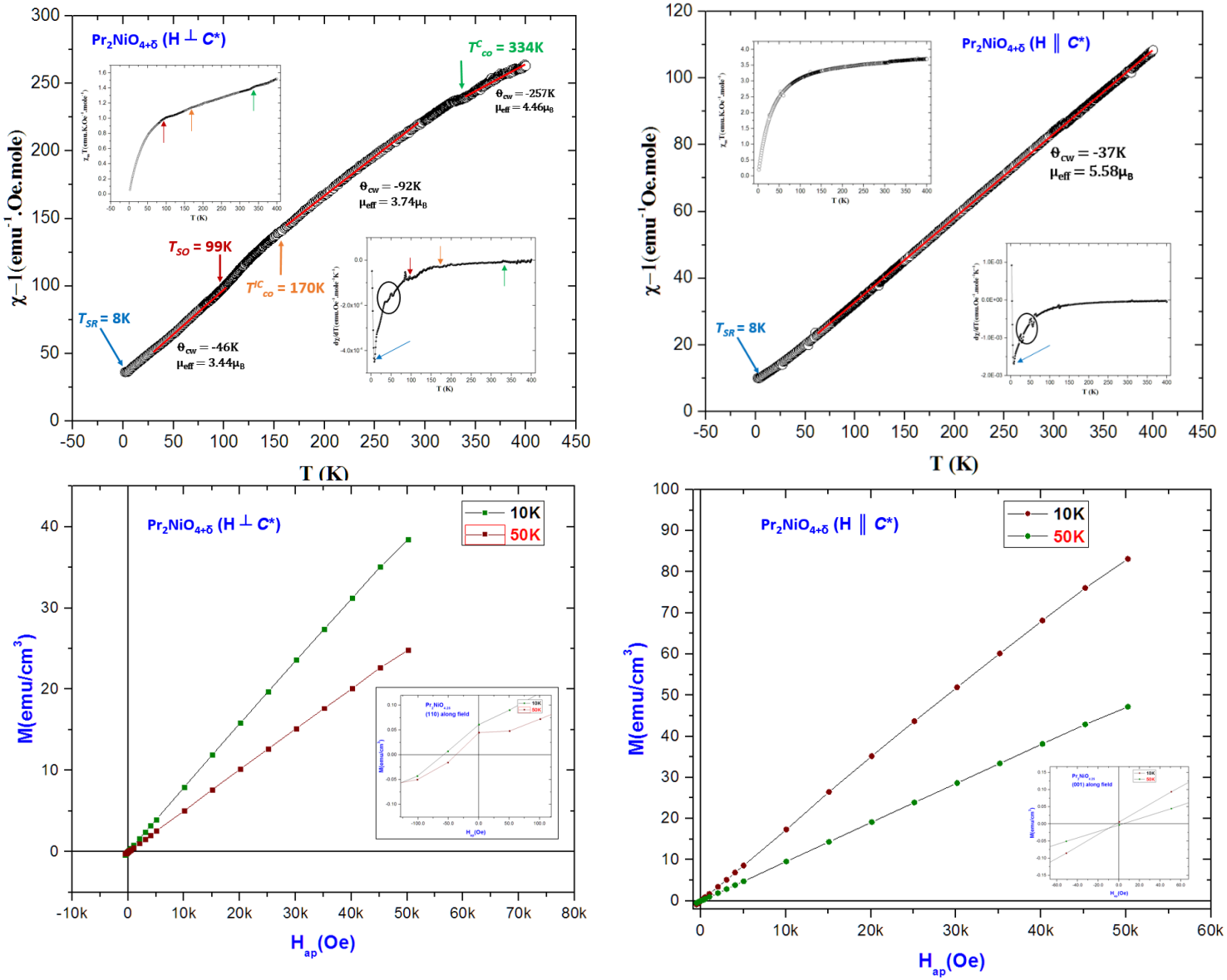

Figure 7.2: *(a-b)* inverse molar susceptibility curve of $Pr_2NiO_{4+\delta}$ with applied field of 50 Oe perpendicular and parallel to c*-axis respectively. Inset shows the $\chi_m T$ *vs* T and 1st derivative of χ_m *vs* T to identify clear different charge and spin order temperature. *(c-d)* Isothermal magnetization $M(H)$ curve for both oriented crystal at 10 and 50 K shows weak ferromagnetic signal in case of sample exposed to field perpendicular to c*-axis.

In our study we have not observe 3D magnetic ordering as the inverse susceptibility curve when applied magnetic field parallel to c*-axis does not show any long range ordering down to 60K. But interestingly in a*-b* plane ferromagnetic singnal in isothermal M*(H)* curve at 10 and 50 K as it can be seen very weak magnetization (0.05 emu/cm^3) persist at extrapolated zero magnetic field see Fig. 7.2 *(c)*. It could be associated with new spin ordering below T_{SO} = 99K where magnetic spin are canted but in the a*-b* plane, this is somewhat new feature which haven't reported yet for non-stoichiometric sample where as parallel to c*-axis there is no such hysteresis (Fig. 7.2 *(d)*). Besides, present studied compound $Pr_2NiO_{4+\delta}$ is an orthorhombic in structure which has different NiO_6 octahedral distortion compare to LTO *(Bmab)* phase of Pr_2NiO_4 and down to 2K we have not observe any phase transition like stoichiometric case. This could be somehow related with the fact to observe weak ferromagnetic interaction in *Fmmm* structure. We will show later the diffraction pattern obtained at low temperature which confirms no evidence of change in average structure as well the oxygen ordering. In order to determine the temperature where this weak ferromagnetic signal appear we have measured on the same sample after six month followed by ZFC and FC temperature dependent magnetization in a*-b* plane. Fig. 7.3 *(a)* shows the M(T) curve for FC and ZFC measurements and it shows the clear deviation of those two curve at T = 190K which is the most likely the incommensurate charge order temperature after spin order temperature the separation becomes larger which can be seen in the difference curve Fig. 7.3 (b). Clear indication of this ferromagnetic interaction in plane can be observed though isothermal magnetization curve M*(H)* in Fig. 7.3*(c)* where the remanent magnetization is quite strong (M_{rs}~ 0.18 emu/cm^3) at 5K and the curve is not straight. This remanent magnetization M_{rs} goes down with increasing temperature as it can be seen from Fig. 7.3 *(d)*. Also the hysteresis curve shows two sudden change in the slope at magnetic field of 18KOe and 65KOe respectively. Similar scenario has been reported for stoichiometric Pr_2NiO_4 single crystal where the applied magnetic field is parallel to c*-axis, two transition are observed at 16 and 42 KOe [10]. But the difference is in our case the applied field is perpendicular to c*-axis. The higher zero-field extrapolated magnetization for magnetic field higher than 60 KOe is obtained with a value of 10.5 emu/cm^3. However since the relative orientation between spin and applied field is not known, no more details can be obtained from current data.

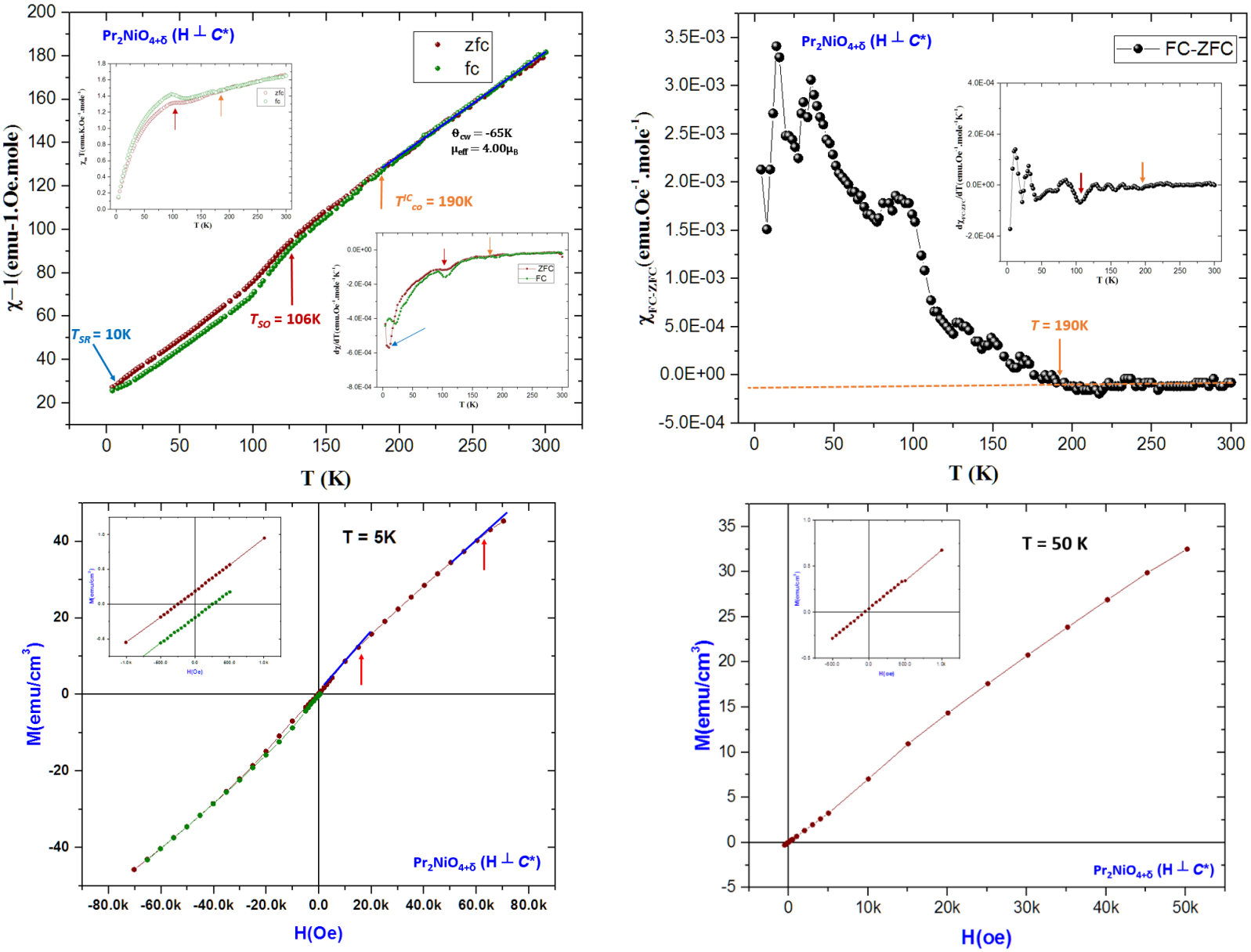

Figure 7.3: *(a-b)* shows FC, ZFC inverse molar susceptibility and difference FC-ZFC molar susceptibility curve of $Pr_2NiO_{4+\delta}$ with applied field of 50 Oe perpendicular to *c**-axis respectively. Inset shows the $\chi_m T$ *vs* T and 1st derivative of χ_m *vs* T to identify clear different charge and spin order temperature. *(c-d)* Isothermal magnetization M*(H)* curve for both oriented crystal at 5 and 50 K shows weak ferromagnetic signal in case of sample exposed to field perpendicular to *c**-axis at 5 K.

In case of electronically equivalent compound $Pr_{1.5}Sr_{0.5}NiO_4$ the picture of magnetic ordering is more dramatic. Here we have observed 3D magnetic ordering below $T = 100$ K. Fig. 7.4 *(a-b)* shows the inverse molar susceptibility as function of temperature with applied field perpendicular and parallel to c^*-axis respectively. Both curve shows huge anomaly corresponding charge and spin ordering at different temperature denoted by arrows on the curve and inserted 1st derivative of the magnetic moment to see clearly those discontinuity. The calculated effective magnetic moment at high temperature paramagnetic region correspond to paramagnetic moment of Pr^{3+} lattice. For both oriented crystal isothermal magnetization curve at temperature 5, 100 and 350 K reveals antiferromagnetic characteristic as the straight curve pass through the origin with small gap at zero field for the temperature 5 and 100 K could be again weak ferromagnetic but M_{rs} is very small ~ 0.003emu/cm^3 see Fig. 7.4 *(c-d)*. Unless we have the picture of $Ni^{2+}/^{3+}$ spin arrangement in and out of a^*-b^* plane it is difficult to conclude the origin of such ferromagnetic interaction in the cluster of antiferromagnetic one. But 3D nature of magnetic ordering reveals the differences in the magnetic structure between oxygen and Sr doped single crystal even though they are electronically equivalent. Once we have the nuclear and magnetic structure locally, the distortion and orientation of NiO_6 octahedral it will be more clear the origin of such deviation. However, it is also confirmed again the influences of oxygen doping which change the 3D ordering in $Pr_2NiO_{4+\delta}$ and introduce weak ferromagnetic interaction in a^*-b^* plane. We will see switch to the interplay between spin and charge ordering locally by means of 2D X-ray/neutron diffraction to see is there any consequences with ferromagnetism and 3D ordering of magnetic spin for both sample.

Table 1: Magnetic parameters for $Pr_{2-x}Sr_xNiO_{4+\delta}$ (x = 0 and 0.5)

compound	Calculated μ_J (B.M) for Pr^{3+}	Exp. μ_{eff} (B.M) High temp region	Exp. μ_{eff} (B.M) Low temp region	θ_{CW} (K) High temp region
$Pr_2NiO_{4+\delta}$	3.58	4.44	3.44	-257
$Pr_{1.5}Sr_{0.5}NiO_4$	3.58	3.67	3.49	-276

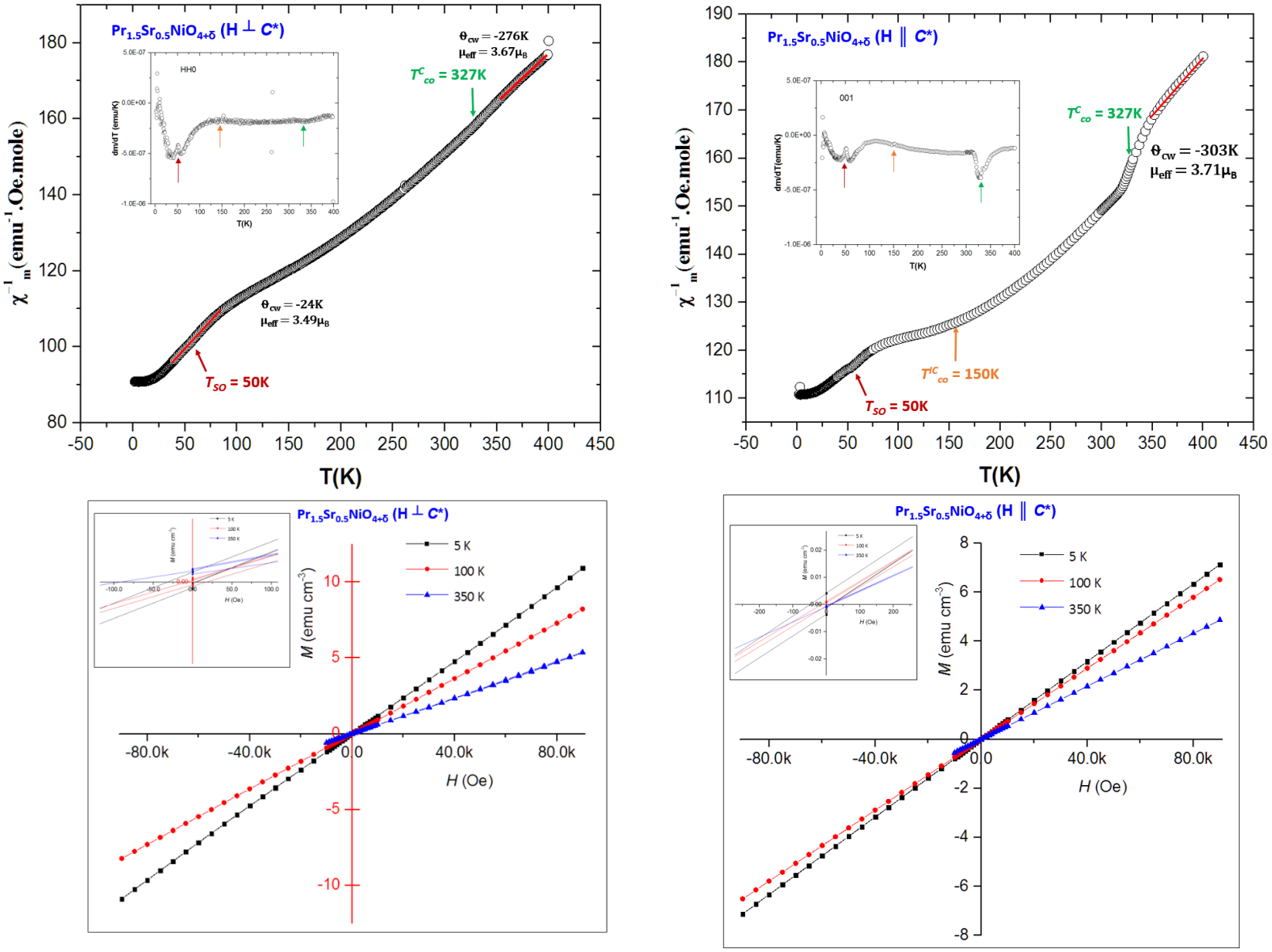

Figure 7.4: *(a-b)* inverse molar susceptibility curve of $Pr_{1.5}Sr_{0.5}NiO_4$ with applied field of 50 Oe perpendicular and parallel to c*-axis respectively. Inset shows the 1st derivative of χ_m *vs* T to identify clear different charge and spin order temperature. *(c-d)* Isothermal magnetization M*(H)* curve for both oriented crystal at 5, 100 and 350 K shows weak ferromagnetic signal in case of sample exposed to field perpendicular to c*-axis.

7.3 Charge and Spin stripes in Oxygen doped $Pr_2NiO_{4+\delta}$ Single Crystal

Hole doping by oxygen intercalation in Pr_2NiO_4 destroy the commensurate antiferromagnetic order *(100)*-type magnetic Bragg reflection and form spin charge stripe or checkerboard ordering depending on hole concentration and their arrangements in the lattice. Similar to lanthanum nickelates, simultaneous static stripe and checkerboard charge order has been found in praseodymium nickelates in the range of hole concentration $0.375 \leq n_h \leq 0.5$ where $n_h = x + 2\delta$ and it is 0.5 in case of oxygen doped $Pr_2NiO_{4.25}$. Normally, below the charge ordering temperature, T_{CO}, the holes order to form static charge stripes and below T_{SO}, the spins order in the region between the charge stripes. The hole rich stripes act as π domain walls for the local antiferromagnetic order, existing in the hole deficient regions with nickel moments perpendicular to the stripe propagation direction. Such stripes run parallel to a/b-axis in F-centered cell in NiO_2 plane and are found to be two dimensional in nature. A schematic of charge and spin stripes and checkerboard ordering in the $(a - b)$ plane in the *F4/mmm* setting for is shown in Fig. 7.5 for two orthorhombic twin domain. The wave vectors for the charge and spin stripes are $\boldsymbol{Q}_{CO} = (\pm 2\varepsilon, 0, \pm 1)$ and $\boldsymbol{Q}_{SO} = (1 \pm \varepsilon, 0, 0)$ respectively, where the incommensurability ε is the splitting from the nuclear and magnetic Bragg reflections respectively. For the nuclear Bragg reflections must be all odd or even, e.g. to have charge order satellite in *(HK0)* plane, modulation wave vector will propagate from *(HK1)/(HK-1)* plane where all reflections are odd to reach on *(HK0)* plane with $l = 1$ component. Following this rule we can write the reflection conditions for all charge and spin satellite on *(HK0)* plane as follows:

$$\boldsymbol{G'} \pm \boldsymbol{q}_{CO} = (2m + 1 + 2\varepsilon, 2n + 1, 0) \text{ and } \mathbf{G} \pm \mathbf{q}_{SO} = (2m + 1 + \varepsilon, 2n, 0);$$

where G' and G refers fundamental Bragg reflections in *(HK±1)* and *(HK0)* respectively and m, n = integers. The stripe order is most stable at $\varepsilon = 1/3$ where it shows the highest charge and spin ordering temperatures and the longest correlation length. Moreover, ε exhibits a systematic deviation from the linear relation see Fig. 2.11. However, another well-known ground state of a hole-doped system is the so-called checkerboard-type charge order with the doping concentration of 50% holes. From our recent studies on the oxygen doped $Pr_2NiO_{4+\delta}$ system, however, we haven't detect

any commensurate charge order peaks instead we have observed an incommensurate spin and charge order with an incommensurability ε = 0.38 from neutron diffraction studies. But, from synchrotron X-ray diffraction reveals simultaneous existence of both checkerboard (ε = 0.5) and stripe order (ε = 0.328) whereas checkerboard commensurate order persists even up to room temperature.

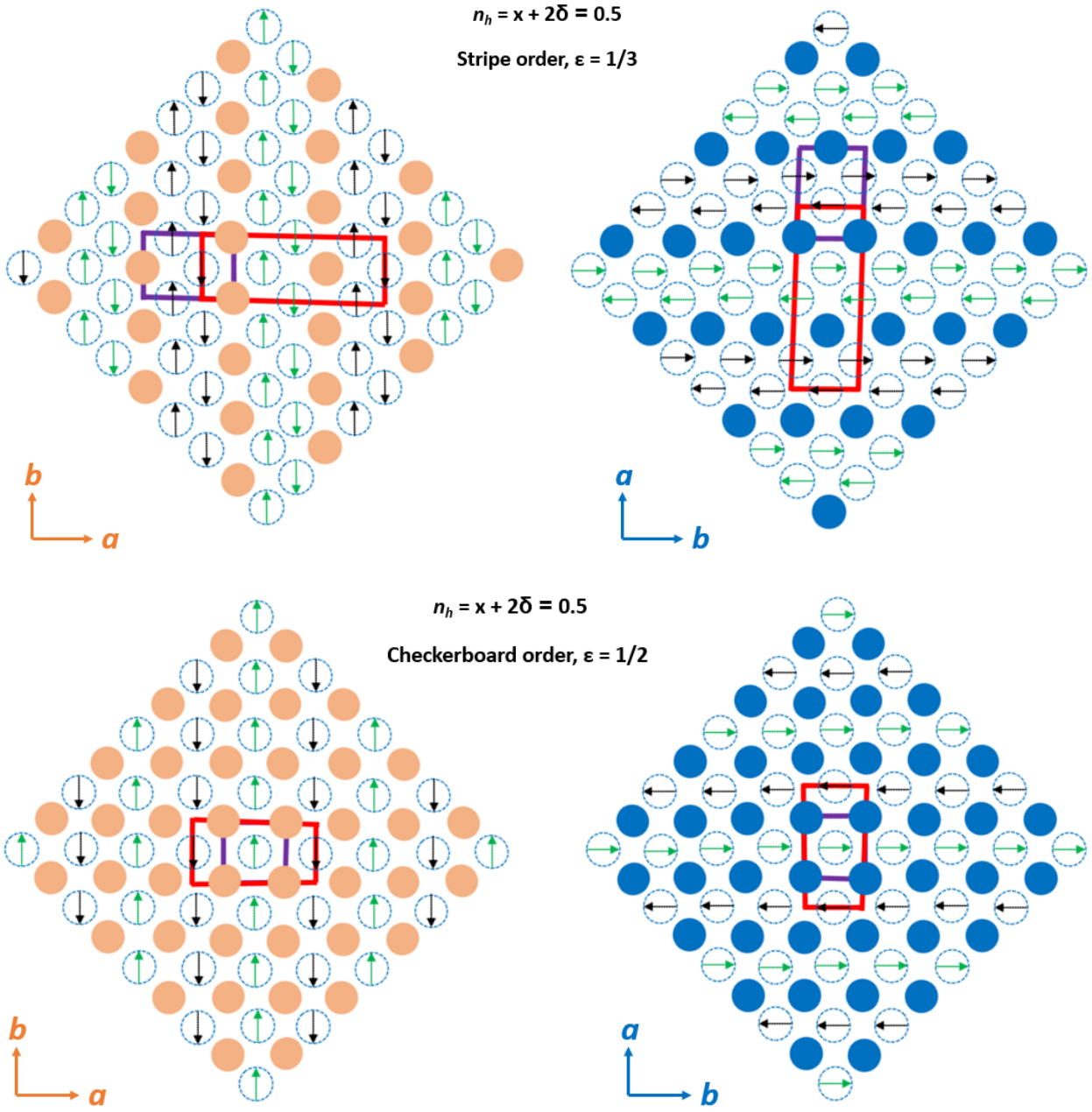

Figure 7.5: (Top) and (below) shows schematic of stripe and checkerboard-type order of charge and spin in twin orthorhombic lattice where the stripes runs along the *a*/*b*-axis.

The discrepancy between two different incommensurability of charge order peaks in case of neutron and X-ray diffraction could be due to different oxygen stoichiometric as the measured sample was not the same for both measurements.

7.3.1 Single Crystal Neutron 2D diffraction

Fig. 7.6 shows reconstructed reciprocal *(hk0)* and *(h0l)* plane at 300 and 2K obtained from neutron single crystal diffraction on as grown $Pr_2NiO_{4+\delta}$ single crystal. At both temperature system shows average orthorhombic twinned structure with oxygen order satellite where modulation vector for oxygen ordering does not change even after lowering the temperature could be due to the oxygen are freeze and persist the same modulation as at RT. In Fig. 7.6 *(b)* several charge (red circle) and spin (orange circle) order peaks are present on the *(hk0)* plane at low temperature T = 2K with incommensurability $\varepsilon = 0.38$, theoretically that correspond to oxygen concentration about $\delta \sim 0.19$. However, this is interesting to see that both charge and spin modulate only along a^* from fundamental nuclear and magnetic Bragg reflection in their corresponding twin domain, also in the higher *d*-value region the modulation is not visible for charge order peaks and might be related to relation between intensity and *q* in reciprocal space. Spin ordering has also *l*-dependence modulation as it can be seen from the diffraction pattern Fig. 7.6 *(d)*, on the position (1.38, 0, $l = 0$ to 2) (yellow rectangle) there are strong five peaks are located at $l = 0$, 0.5, 1, 1.5 and 2 with continuous diffuse intensity. This indicates strong correlation of spin order along c^*-axis where the modulation period is $1/2c^*$. From SQUID measurements see Fig. 7.2 *(b)* we haven't seen long range order down to 10K but there is spin reorientation at 8K and perhaps this ordering along c^* make the changes in inverse susceptibility curve. Similar scenario has been reported in Hucker et al. [12] in stoichiometric $La_{1.875}ba_{0.125}CuO_4$ for charge stripe order where they confirmed due to LTT octahedral tilt pattern stripes are parallel in every other CuO_2 plane and coulomb repulsion between charge stripe introduce additional shifts by half the charge order period but they did not talk about spin order in that compound. In our case structure is still LTO *(Fmmm)* perhaps with same NiO_6 octahedral tilting as RT *(Fmmm)* phase, so the question is what the reason could be for that spin modulation along c^*-axis. This is confirmed that those modulations are not from oxygen or any nuclear Bragg peaks

as they don't show up at RT. Is this related to oxygen ordering that manifest the spin stripe at low temperature or 3D magnetic ordering which has *c*-axis double of that in average unit cell. To get the answer it needs further experiment specially temperature dependent magnetic and nuclear structural study locally to see the NiO_6 octahedral arrangement. We haven't the evidence for *l*-dependent charge stripe order because of limited accessibility to measure and reconstruct the reciprocal plane like *(H1L)* or *(1KL)* where the charge order peaks from *(HK0)* can be seen. But charge order reflections falling nearly to the 2nd order of oxygen ordering in *(hkn)* plane where n = odd integer. Fig. 7.7 *(a)* shows a proposed spin arrangements in NiO_2 layer with spin periodicity c^* and corresponding idealized diffraction pattern in *(H0L)* plane with $\varepsilon = 0.38$ whereas Fig. 7.7 *(b)* displays same pattern when periodicity becomes larger $2c$ and give rise additional spin order peaks at *l*-half integer. In order to keep the periodicity of charge stripe along the *c*-axis same and periodicity of spin order double along *c*-axis only possibility would be different orientation of spin of Ni^{2+} in $z = c$ compare to $z = 0$ plane. This is a model, it needs to be verified by experiment the actual spin alignment in NiO_2 layer.

7.3.2 Single Crystal X-ray diffraction

Synchrotron X-ray diffraction on the same compound $Pr_2NiO_{4+\delta}$ but different batch has been carried out to see the evolution of charge order and oxygen order at RT and 80K. First time we have seen the commensurate checkerboard ($\varepsilon = 0.5$) and stripe ($\varepsilon = 0.328$) charge order presents at low temperature. Fig. 7.8 *(a-b)* shows reconstructed *(hk0)* plane with full of oxygen and charge order peaks along with main Bragg reflections at 80K whereas at RT stripe charge order peaks disappeared rest of the peaks remain at same reciprocal space without changing the modulation vector for oxygen ordering. Blue circle enclose the stripe charge order reflections in Fig. 7.8 (a). In details one section (blue rectangle) of *(hk0)* plane has been presented for both temperature in Fig. 7.8 (c-d). Fig. 7.8 (c-d) shows structure again consists of two orthorhombic twin domains (red and blue unit cell) labeled with corresponding *h,k*- directions. Usually it is expected to have two charge order reflections followed by vector *(h±2ε, 0, 1)* which we have for each domain red and blue circle. But we do not have charge order peak spanned along k-direction marked as cross (X).

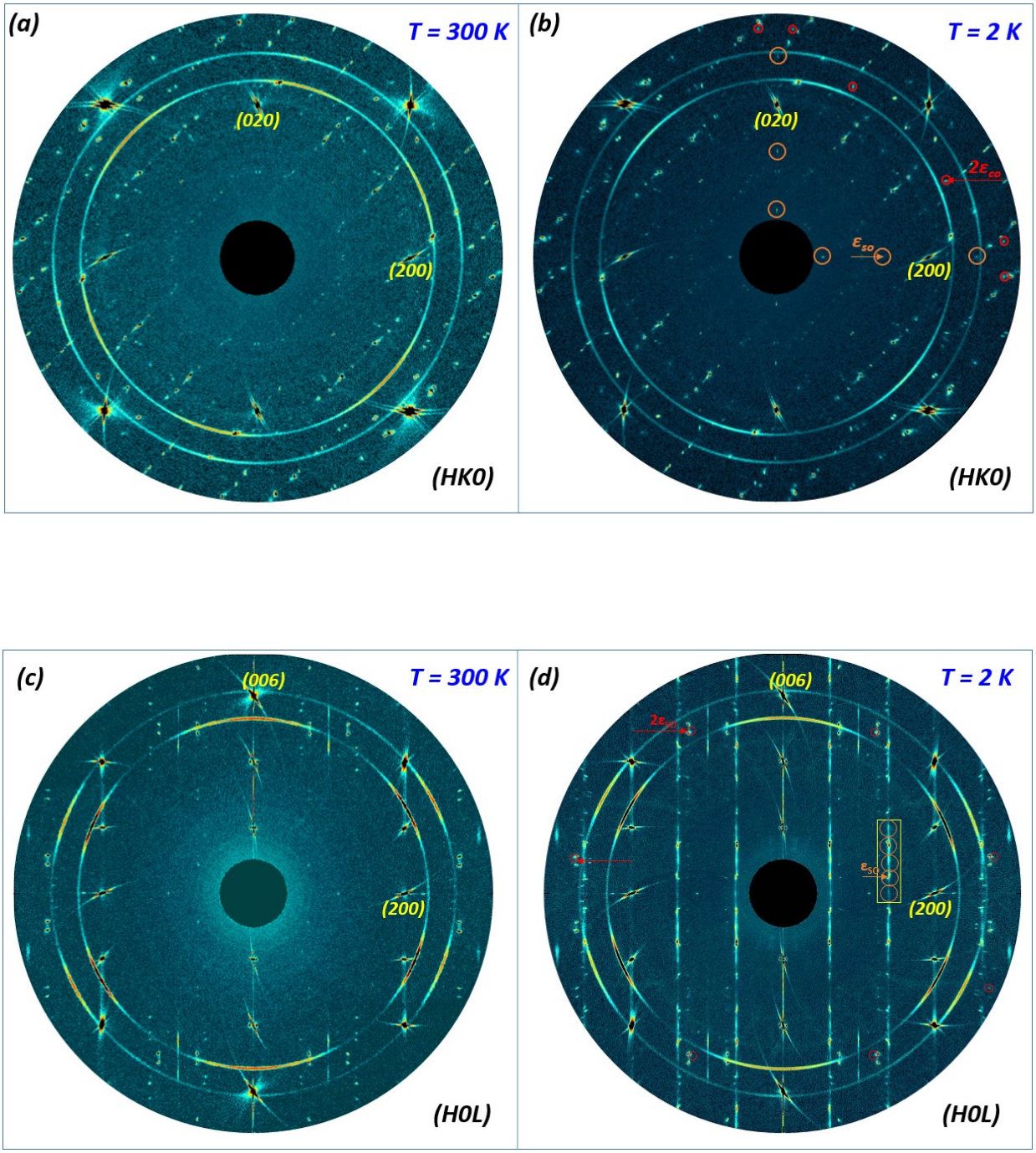

Figure 7.6: *(a-b)* Reciprocal space map of *(hk0)* and *(c-d) (h0l)* plane at 300 and 2K respectively obtained from neutron single crystal diffraction on $Pr_2NiO_{4+\delta}$. Spin and charge order satellite ate marked in orange and red circle in *(b)* propagate from nuclear and magnetic Bragg reflections with $\varepsilon = 0.38$. Spin order correlation along c^*-direction (yellow rectangle). Rest of the satellite are coming from oxygen ordering like discussed in section 4.

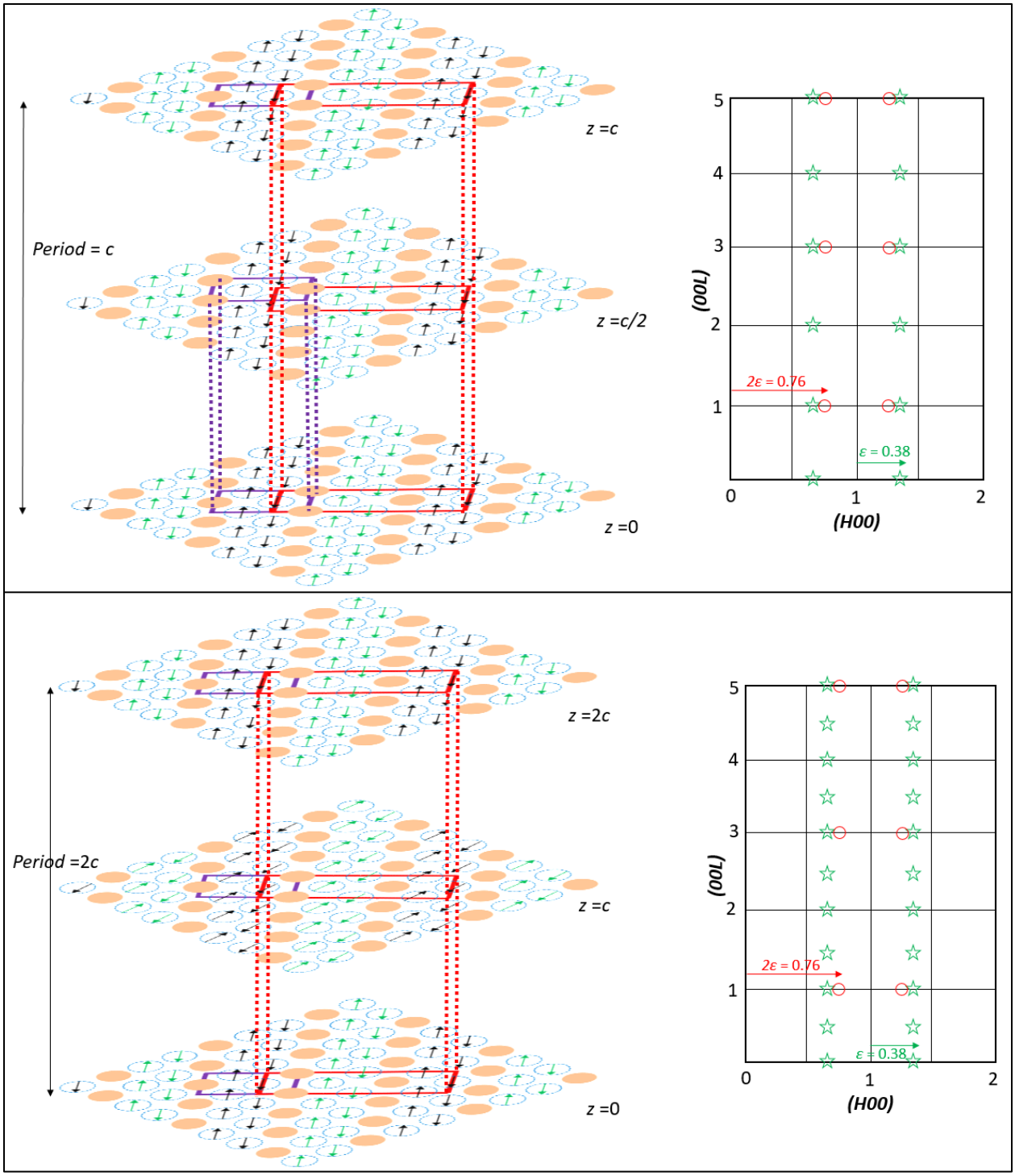

Figure 7.7: (Top) schematic representation of spin arrangement of Ni^{2+} in NiO_2 layer with spin modulation period c and corresponding idealized *(h0l)* section where green star and red circle represents spin and charge satellite. (Bottom) same schematic view when magnetic unit cell become double in c-direction showing strong correlation in 3D whereas the Ni2+ spin at z = 1 are different from that at z = 0 to keep the charge order unit cell unchanged. Idealized *(h0l)* plane shows extra spin order satellite at l= 0.5, 1.5 so on which is similar to obtained experimental pattern in Fig. 7.6 *(d)*, oxygen ordered are excluded in the calculated pattern.

Basically we have another extra peaks next to the each charge order peak. First we thought this might be due to twin domain but if it does follow the twin law it would also follow the same twin angular separation but this not the case, the angular separation is different not along omega nor two-theta. Surprisingly they are absent at 300K only appeared at low temperature with those stripe charge order peaks. The origin of those extra peaks is not clear, to better understand we need a measurements decreasing temperature slowly from RT to 2K in order to see they appear at same temperature or not also needs to be investigated by elastic/inelastic to see if it dynamic origin or static. They might be coming from some other phase following the feature electronic phase separation in nano scale. But this is clearly some other kind of nuclear reflections and not the oxygen order peaks because oxygen order peaks are described in the same manner with the modulation vector $\boldsymbol{q} = \pm 0.83\boldsymbol{a^*} + 0.5\boldsymbol{b^*}$ and there is no change in the modulation vector between these two measured temperature. This is not all, if we cut the plane *(-3.65, k, l)* flowing the rectangle section in Fig. 7.8 *(a)*, we can see those two reflections are basically four with small $\gamma \sim 0.02c^*$ component, this is what has been shown in Fig. 7.9 *(a)*. When we on the *(hk0)* plane they appear as two. So if it is from several nano phase they might be strongly correlated in 3D as they appear very sharply not as diffuse scattering in the plane with $\Delta l = 4$. Actually they should also appear in the plane with l = even if it follows the charge modulation vector but they are absent in between plane with *l* =even, e.g. alt *l* = 2 and 6 they are absent means they do not modulate from all *(hkn=odd)* plane. Besides, commensurate CB-type charge order reflection are present at both RT and 80K only intensity differ but a part of the system changes to stripe type charge order with decreasing temperature. Matsuda et al. [13] revealed that for lightly doped $La_{2-x}Sr_xCuO_4$ with x ~ 0.02 shows a phase separation between nondoped Néel ordered state from this matrix stripe order modulation emerges whereas Kajimoto et al. [14] showed in half-dope nickelates stripe emerges from matrix of CB-type charge order. This complex behavior might emerges from phase separation and is a consequences of strong correlation of coupling between charge and spin degree of freedom.

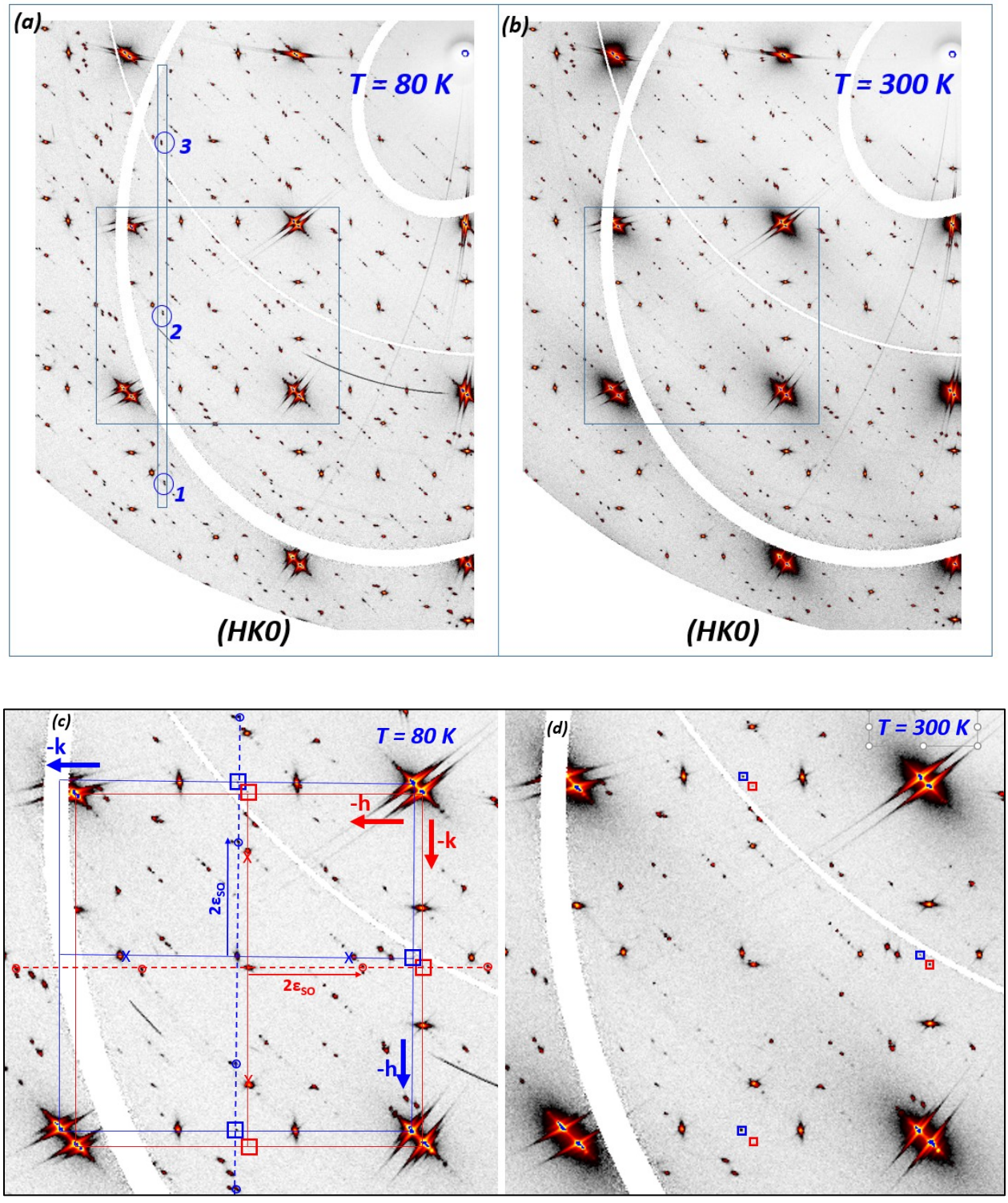

Figure 7.8: *(a-b)* shows the experimental reciprocal *(hk0)* plane obtained from X-ray diffraction on $Pr_2NiO_{4+\delta}$ single crystal at 80 and 300K. Blue rectangles in *(a-b)* are represented as zoomed section in *(c-d)*. Blue and red circles enclose are stripe charge order peaks in the corresponding twin domain. Blue and red small box represents the position of checkerboard-type charge order peaks along both directions. Unobserved charge order peaks are marked as cross.

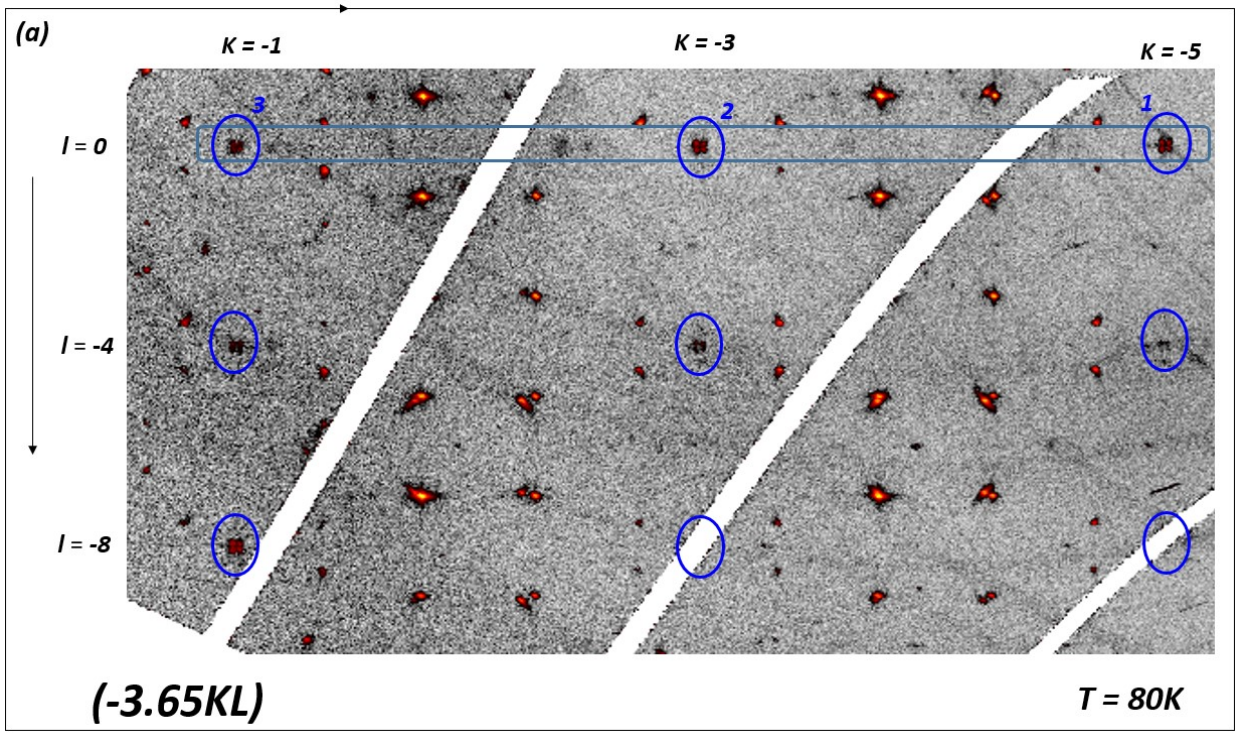

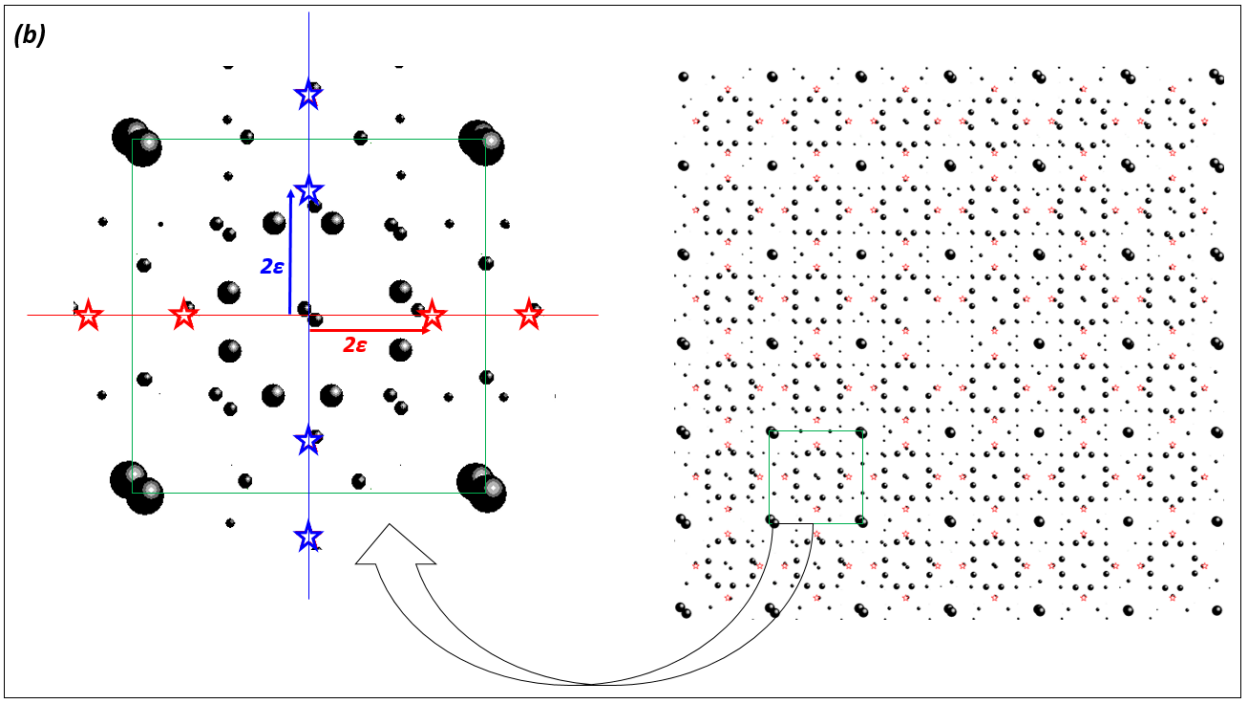

Figure 7.9: *(a)* shows (-3.65kl) reciprocal plane cut along the thin blue rectangle in Fig. 7.8 *(a)*. Blue circles enclose stripe charge order peaks as well as other three peaks. (b) Schematic representation of idealized *(hk0)* plane contains all the main Bragg reflections together with oxygen order and stripe charge order peaks. CB charge order satellite is not included.

Fig. 7.9 *(b)* represents the idealized *(hk0)* pattern which has been calculated considering the oxygen ordering with its corresponding modulation vector in total four twin individuals and superimposed with stripe charge order peak which is calculated only for one average unit cell. Twin law also can be applied for charge stripe order similarly as oxygen order only difference would be the modulation vector. Due to the commensurability effect 2nd order oxygen satellites are closely located to the stripe charge order peaks.

7.4 $Pr_{1.875}Sr_{0.125}NiO_{4+\delta}$ Single Crystal

7.4.1 Charge Stripe studied by X-ray Diffraction

Sr-doping in $Pr_2NiO_{4+\delta}$ introduce the hole in NiO_2 layers as oxygen doped sample and depending on concentration level charge stripe order take place. Here we will present the results from such Sr-doping $Pr_{2-x}Sr_xNiO_{4+\delta}$ (x = 0.125) single crystal obtained from synchrotron X-ray diffraction. This compound still intercalates interstitial oxygen in to the interstitial sites even after Sr-doping and estimated oxygen content $\delta \sim 0.125$, so from this calculated hole concentration will be $n_h = x + 2\delta = 0.375$. Fig. 7.10 *(a-b)* shows one of the reconstructed *(hk0)* reciprocal plane at 80 and 300K respectively. At both temperature structure is orthorhombic and one time twinned, at RT besides fundamental Bragg reflections there are satellite from oxygen ordering as we have seen that at critical $\delta_c \sim 0.125$ oxygen start to get ordered and the found modulation vector was $\boldsymbol{q} = \pm 0.7914\boldsymbol{a^*} + 0.5268\boldsymbol{b^*}$ with having maximum 4th order satellite. The description of calculated and experimental pattern has been given in Fig. 4.16 and 4.17 in chapter 4. We have same oxygen modulation vector at 80K in addition the stripe charge order peaks marked in blue circle in Fig. 7.10 *(a)* are present with the incommensurability $\varepsilon = 0.354$ quite lower than calculated value and higher than stable stripe ground state ($\varepsilon = 1/3$). Solid blue and red box shows such two charge order peaks at higher two-theta value where the actual twin splitting can be seen (zoomed area bottom of that figure) where arrow indicates the direction of splitting. But this again similar situation like oxygen doped

sample what we have seen in previous section. Even though charge order peaks are splitted one of them belongs to one twin domain. In Fig. 7.11 all those charge order satellite corresponding each orthorhombic domain (blue and red unit cell) has been identified and for each domain charge order modulate following the vector $\boldsymbol{q}_{CO} = (h\pm 2\varepsilon,\ 0,\ 1)$ not along k-direction which does not appear marked as cross (X). Only difference from oxygen doped sample is 1st the incommensurability (ε), 2nd the splitting follows the twin angular separation (green arrow) even though one of them does not belong to any of two domain and 3rd in the *l*-direction they appeared as diffuse with strong intensity not like four what we have seen Fig. 7.9 *(a)*. One of the reconstructed *(h1l)* plane cut through the section following the thin rectangle in Fig. 10 (a) has been presented for both temperature in Fig. 7.12 *(a-b)*. It can be seen as we mentioned above that at temperature 80K charge order satellite appears strong central peak having small diffuse tail (blue circle) and there are no four reflection even not two. We haven't any evidence for actual charge order temperature T_{CO} perhaps they will appear as much more strong peaks at further low temperature. But at this temperature 80K this small diffuse tail indicated disorder state of holes in stripe region and that might be due to different structural distortion (NiO_6 octahedra tilting) for Sr doping which is not same as in case of oxygen doping and this is the case actually when we will see when we dope more Sr doping in the system. At least this different scenario can be considered as introducing Sr-doping suppress the long range charge stripe along c^*-axis (from 4 distinct satellite to one satellite with diffuse tail) but do not modify in plane correlation and both type of hole doping play vital role differently in this strongly correlated electronic system. Lastly besides all this electronic ordering at low temperature one more interesting feature is the strong diffuse scattering around the fundamental Bragg reflections which even presents at low temperature, could be related to low energy phonon modes but not surely thermal diffuse at least for this two temperature and this low energy lattice distortion becomes more stronger down to 80K that also supports the arguments with local structural disorder responsible for changing the stripe matrix.

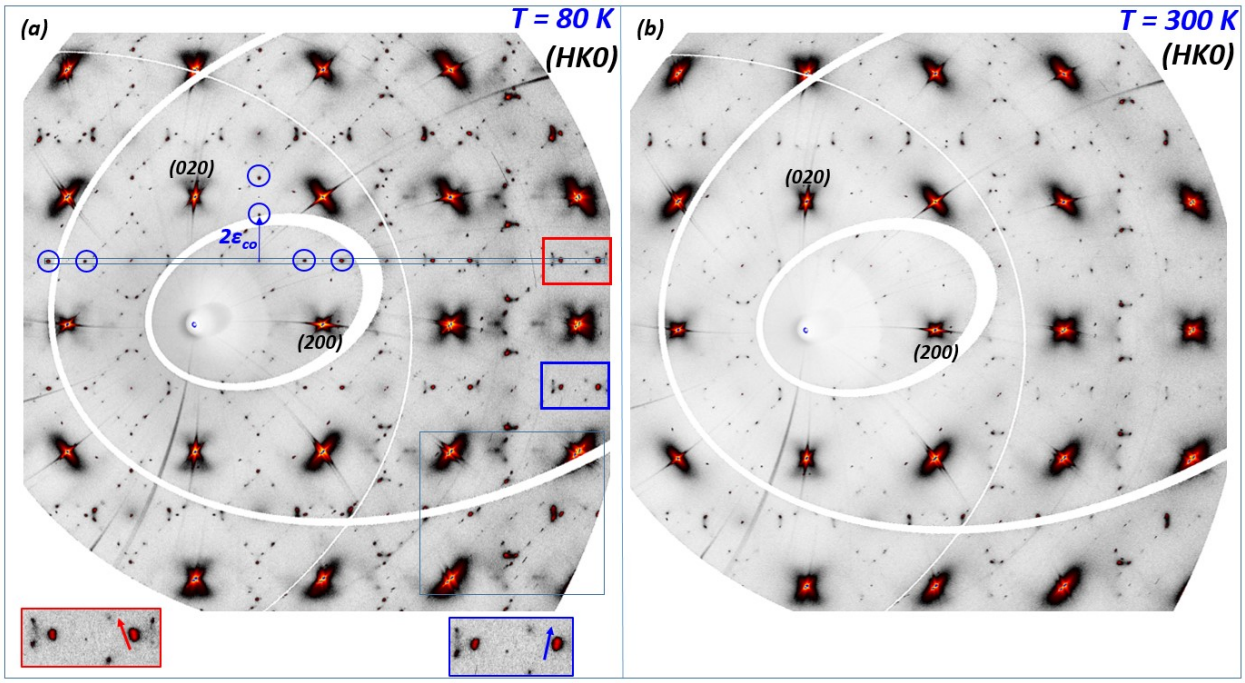

Figure 7.10: *(a-b)* shows the experimental reciprocal *(hk0)* plane obtained from X-ray diffraction on $Pr_{1.875}Sr_{0.125}NiO_{4+\delta}$ single crystal at 80 and 300K. Blue circle represents the charge order peak. Blue and red box shows charge order peak splitting along indicated direction.

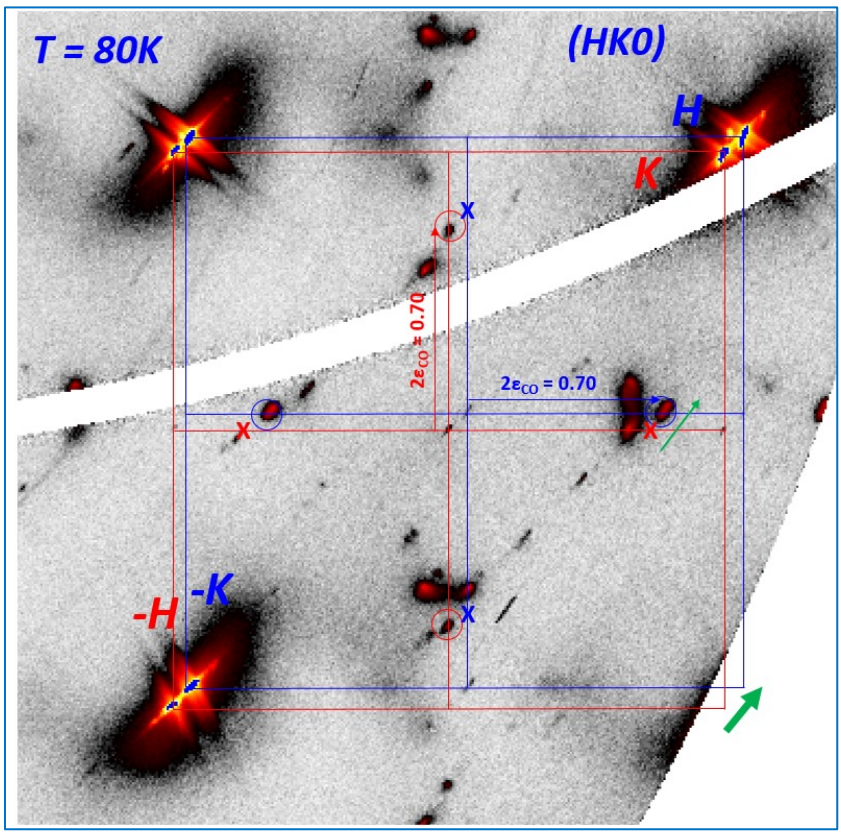

Figure 7.11 shows selected section as indicated by light blue rectangle in Fig. 7.10 (a) at temperature 80K. Each charge order satellite has been indexed according to the modulation vector in their respective twin individuals. Green arrows shows the direction of splitting of CO peaks and cross indicates the expected position of charge order peak modulate along *k*-direction.

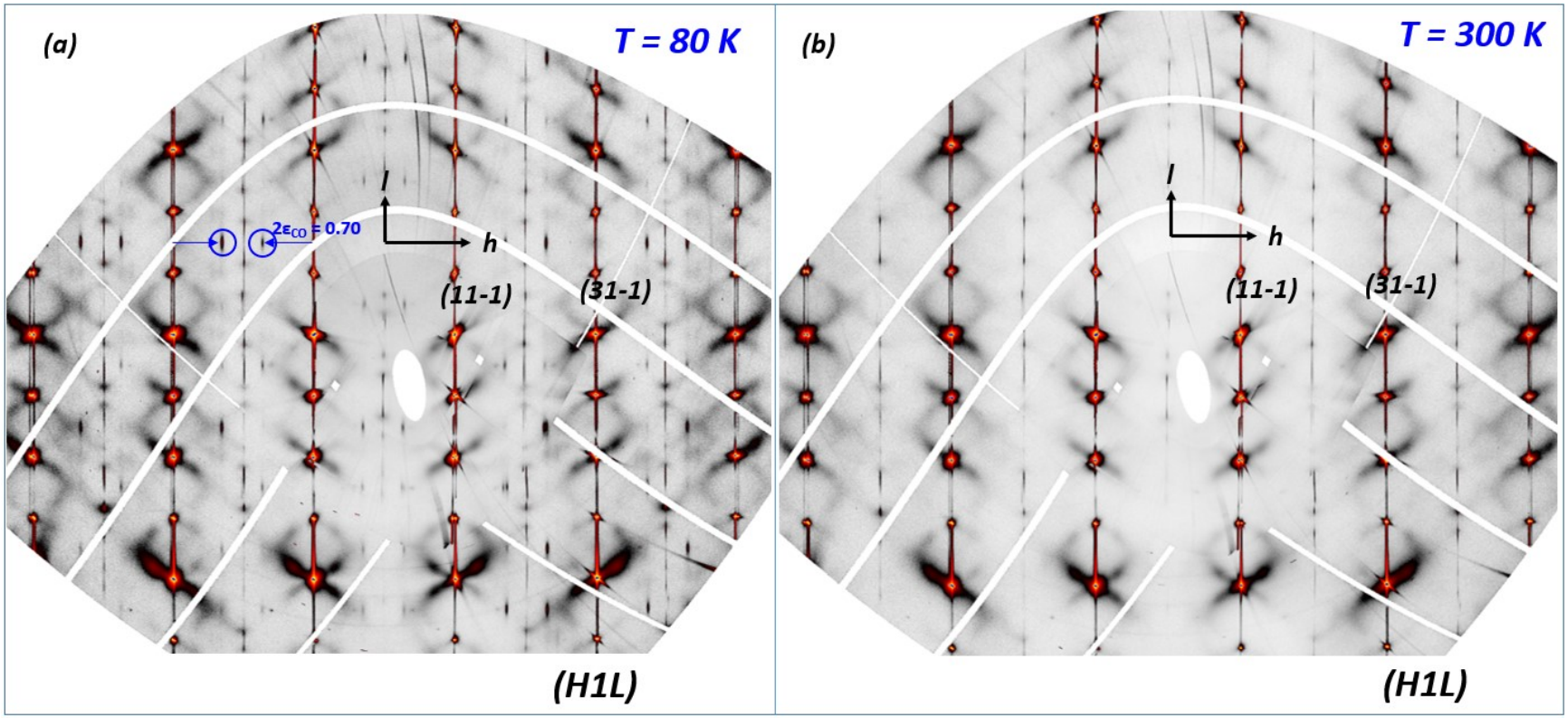

Figure 7.12 *(a-b)* shows reconstructed *(h1l)* plane from the same measurements at 80 and 300K where at left picture blue circles indicated the diffuse like charge order peaks modulate from *(-11-1)/(-111)* with vector *(±2ε,0,±1)* indicated by one of the blue arrow.

7.4.2 Charge and Spin Stripe studied by Neutron Elastic Scattering

Charge and spin ordering temperature has been determined by performing elastic neutron scattering on the same crystal batch which was measured on beam line ID28 at ESRF in a range of temperature from RT to 5K. The neutron scattering experiment was carried out on thermal triple axis spectrometer PUMA at MLZ, Neutron source FRMII Garching, Munich. We found the incommensurability $\varepsilon = 0.33$ exactly the ground state of stripe phase but different from X-ray measurement again. However, since $\varepsilon = 1/3$ spin and charge order satellite overlap and difficult to separate their contribution to the scattering intensity. But it is possible to determine both ordering temperature by scanning the reciprocal space along *(h00)* direction where we have only spin order peaks and scanning along *(h-10)* through *(π, π)* point of orthorhombic unit cell we can deter mine charge order temperature as it is normally higher than spin order temperature *($T_{CO} > T_{SO}$)*. A schematic has been given to the right side of the each diagram to show the direction of corresponding scan and predicted satellite positions. Fig. 7.13 *(a-b)* shows such scan profile at different temperature. Scanning through *(h00)* reveals the spin melting temperature as it can be seen the stripe spin order peaks start to appear at *(0.66, 0, 0)* and *(1.33, 0, 0)* reciprocal position in green and blue curve not so strong but $T_{SO} = 180$K can be evaluate in between this two temperature. In between this two peaks there is also negligible peaks is present which is from nuclear diffuse line that can be seen in the previous X-ray diffraction pattern. For the scanning profiles along *(h-10)* contains both charge and spin order reflection at *(-0.33, -1,0)* and *(0.33, -1, 0)* position, 1st charge start to order at $T_{CO} = 225$K the red bottom curve in Fig. 7.13 *(b)* and then spin start to get ordered at 180K which is getting stronger at 185K. The peak at *(1, -1, 0)* correspond to another diffuse line passing through this *(π, π)* point.

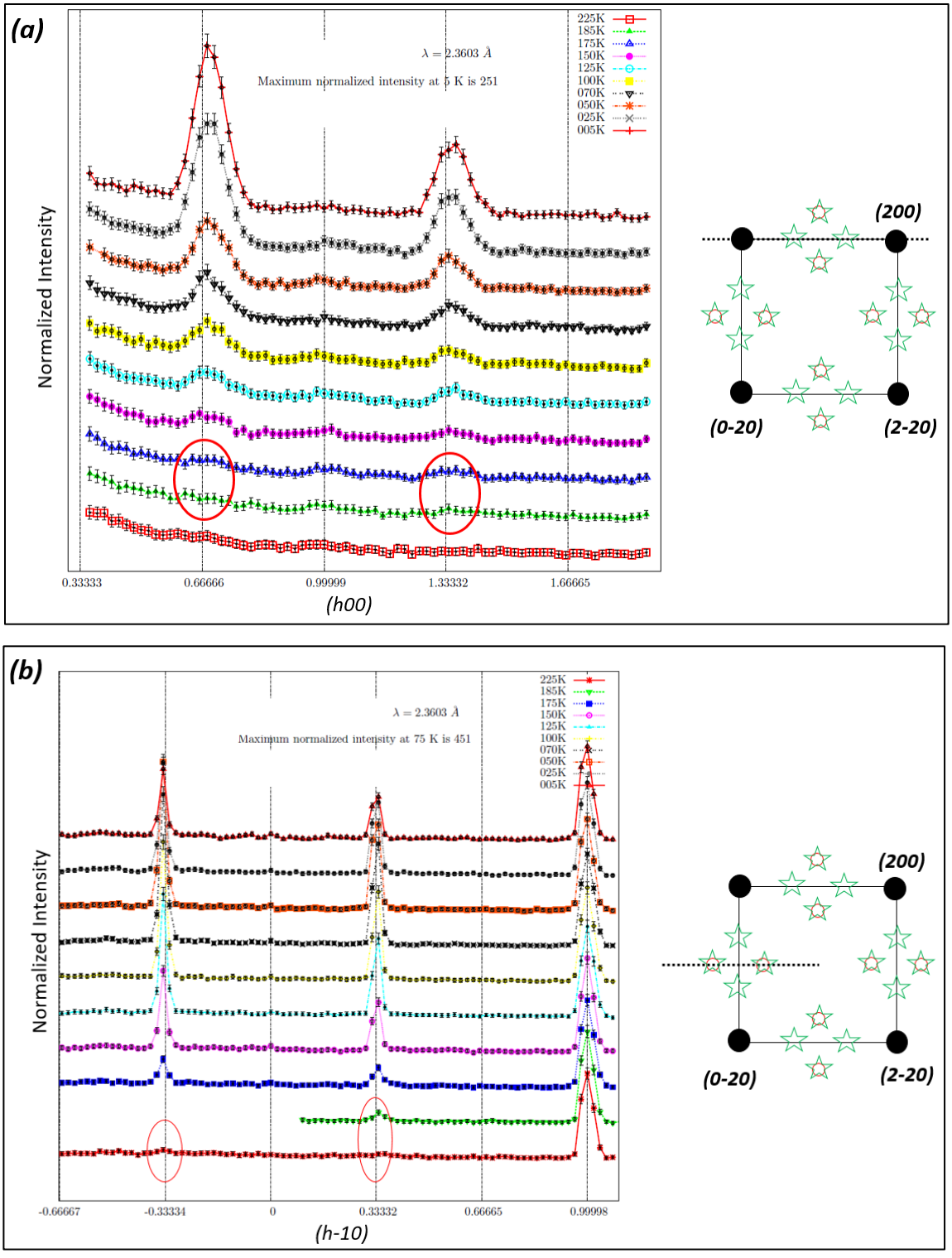

Figure 7.13: (a-b) shows the scan profiles at different temperature obtained by elastic neutron scattering experiments on $Pr_{1.875}Sr_{0.125}NiO_{4.125}$ single crystal along *(h00)* and *(h-10)* direction respectively. Red ellipse indicated the appearing of satellite peaks. The schematic on the right sides are guideline to scanning direction with predicted charge (red circle) and spin (green star) order peak position.

7.5 Correlation between Charge and Spin stripes in $Pr_{1.5}Sr_{0.5}NiO_{4+\delta}$ Single Crystal

In this section we present combined results from neutron and synchrotron single crystal diffraction on half-doped $Pr_{1.5}Sr_{0.5}NiO_4$. Further Sr-doping in $Pr_2NiO_{4+\delta}$ introduce more hole per Ni sites in NiO_2 layers and reduce the oxygen intercalation but still structure contains $\delta \sim 0.04$ amount of excess oxygen. We expect same kind of competition between CB-type and stripe charge ordering in this half-doped region where $n_h = x = 0.5$ neglecting excess oxygen.

7.5.1 Single Crystal Neutron 2D diffraction

Fig. 7.13 shows reconstructed reciprocal *(hk0)* and *(h0l)* plane at 300 and 2K obtained from neutron single crystal diffraction on as grown $Pr_{1.5}Sr_{0.5}NiO_{4+\delta}$ single crystal. At both temperature system shows tetragonal *(F4/mmm)* structure without any oxygen order satellite because there is no sufficient δ_c amount of interstitial oxygen to get ordered. Fig. 7.14 *(b)* represents *(hk0)* plane at 2k where spin and CB-type charge satellite are marked in orange and red circle respectively. Spin stripe follows the incommensurate modulation ($\varepsilon = 0.44$) whereas charge satellite follows commensurate CB order ($\varepsilon = 0.5$). However we did not found any incommensurate stripe charge order reflections from this measurements, the expected position are marked as small red circle. This might be because of small atomic displacement, neutrons detect the presence of charge order via the induced atomic displacements and for small scattering intensities varies roughly as Q^2. This small atomic displacements are because of large amount of Sr doping. Reciprocal position for *(210)* and *(1.88 1 0)* is at small Q from which the charge contribution is negligible and this true for both stripe and CB-type charge order. It can be seen that CB-type order is not present at (210) but it is there at higher Q-value *(310)*. Similarly as oxygen doped ($n_h = 0.5$) sample CB-type CO peaks are present even from RT to 2K. At very lower Q values spin order satellite are absent along *[h00]* and *[0k0]* direction marked as orange cross (X). This not the Q values issue because we can see other spin order peaks at lower Q-values could be related to magnetic symmetry elements that extinct those

reflections. Marked reflections by yellow circle are from some impurity phase which presents at both temperature 300 and 2K.

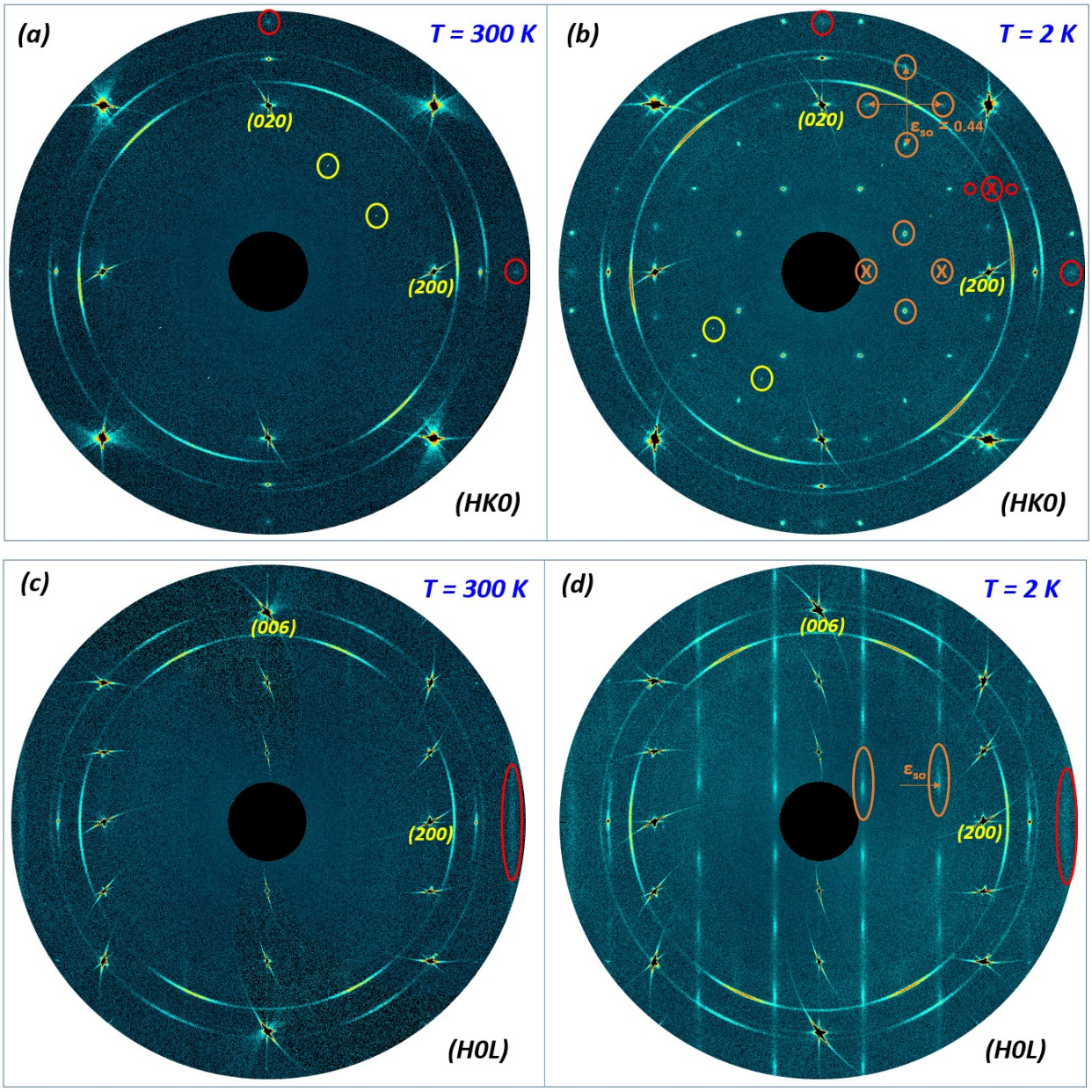

Figure 7.14: *(a-b)* Reciprocal space map of *(hk0)* and *(c-d) (h0l)* plane at 300 and 2K respectively obtained from neutron single crystal diffraction on $Pr_{1.5}Sr_{0.5}NiO_{4+\delta}$. Stripe spin and CB-type charge order satellite are marked in orange and red circle following the modulation with $\varepsilon = 0.44$ for stripe and $\varepsilon = 0.5$ for CB. Spin order correlation along c^*-direction (orange ellipse) is lost almost appears as diffuse line showing disorder pattern. Red ellipse shows the diffuse line arising from short range and disorder CB-type charge modulation.

Another arguments can be made in the picture of stacking faults separating structural domains that has been reported to explain the origin of incommensurate short range magnetism independent of stripe charge order in half doped cobaltate $La_{1.5}Sr_{0.5}CoO_4$ [28]. Simultaneous incommensurate magnetic and charge ordering was probably first observed in a doped nickelate, a simple model of real-space static ordering of holes and spins for different incommensurability has been described in section 7.7, where doped charges segregate into lines separating magnetically ordered stripe domains. In such a superlattice, e.g. such as associated with polaron ordering, atomic positions and/or alignment of magnetic moments do not vary in the direction perpendicular to the propagation vector, presenting superlattice modulation as a periodic arrangement of lines of parallel spins and/or identical atomic displacements. Fig. 7.25 shows ideal CB charge and spin order *(a)*, stacking faults giving rise to short range incommensurate spin order *(b)*. Stacking faults have no 1D rigidity and give rise to isotropic disorder. Savici et al. [28] confirmed such scenario of short range nano-sale spin correlation indicating the structure of faults in CB charge order in the form of magnetic disclinations with stripe stacking fault. Short range incommensurate magnetism in nickelates arise from discommensuration (mixture of CB and stripe see section 7.7) but in case of stripeless incommensurate magnetism it appears from stacking fault at least strongly evident in ref. [28] for $La_{1.5}Sr_{0.5}CoO_4$ Fig. 7.25 *(b)*. CB charge order in this $La_{1.5}Sr_{0.5}CoO_4$ material occurs independently of incommensurate stripeless magnetic order mainly driven by lattice electrostatics and local spin entropy competing with the crystal field splitting of Co ion's energy levels. Magnetic incommensurability in this picture can result from an inhomogeneous exchange modulation induced by CO [28]. In this regard we can say the system $Pr_{1.5}Sr_{0.5}NiO_4$, where we see the CB charge ordering independent of stripe magnetic ordering and do not show associated the stripe charge (ε =0.44) fron neutron diffraction, it could be due to stacking faults that truncate the super-lattice coherence, resulting in a diffuse peaks in place of both charge and magnetic peaks Fig 7.14 *(c-d)* instead of normal discommensuration as shown in Fig. 7.23 *(f)*.

However the twin domain of spin modulation is not same as the intensities are not equivalent when they modulate 90^0 in angle from main antiferromagnetic Bragg reflections. This has been elaborated pictorially in Fig. 7.15 considering two domain rotated by 90^0 in angle and spin stripe is modulated in their respective domain following spin modulation vector $(\pm\varepsilon, 0, 0)$ we can plot each reflection separately. Sky blue and red corresponding domain 1 and 2 respectively where small and bigger filled circle indicates the weak and strong peaks. The reflections along *(0k0)* with k = odd integer are stronger than that along *(0k0)* with k = even inter and finally when both are superimposed we have similar pattern as experimental one in Fig. 7.13 *(b)*. Green star represents the position of the fundamental magnetic Bragg peaks from which spin modulate but in practice it is not there it is just a guideline. Fig. 7.14 *(d)* shows the *(h0l)* plane obtained at 80K where the spin order peaks appear as much more diffuse (orange-ellipse) along c*-axis and CB-type charge order as well diffuse line not a distinct peak (red ellipse) indicates more disordered scenario because of higher Sr doping.

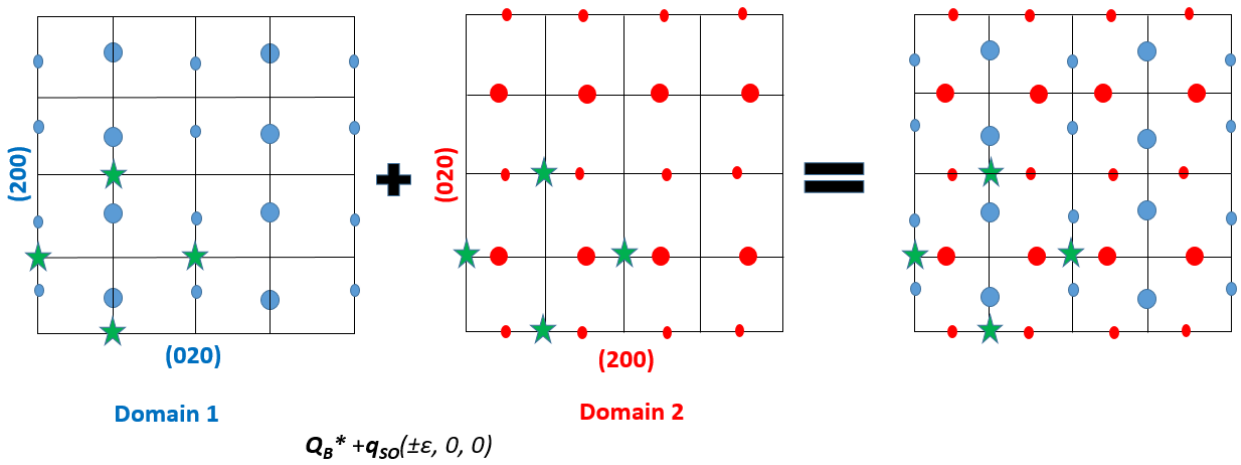

Figure 7.15: Schematic presentation of *(hk0)* plane of two magnetic domain rotated by 90^0 where spin modulation take place following the mentioned vector with $\varepsilon = 0.44$ from AF Bragg reflections (green star). This pattern shows that intensity of every spin order peaks along *(0k0)* with k = odd integer is stronger than that along *(0k0)* with k = even integer. This indicates the average magnetic modulated structure is not equivalent respect to their domain and the loss or change in some magnetic symmetry elements.

To visualize stripe spin order peak together with predicted stripe charge ordering peaks a schematic of ideal *(hk0)* plane has been shown in Fig. 7.16 with mentioned modulation vector on the figure. Red circle and Black Square represents the charge and spin order peaks, following this pattern one can perform elastic or inelastic scattering experiments for any desire reflections all over the reciprocal space.

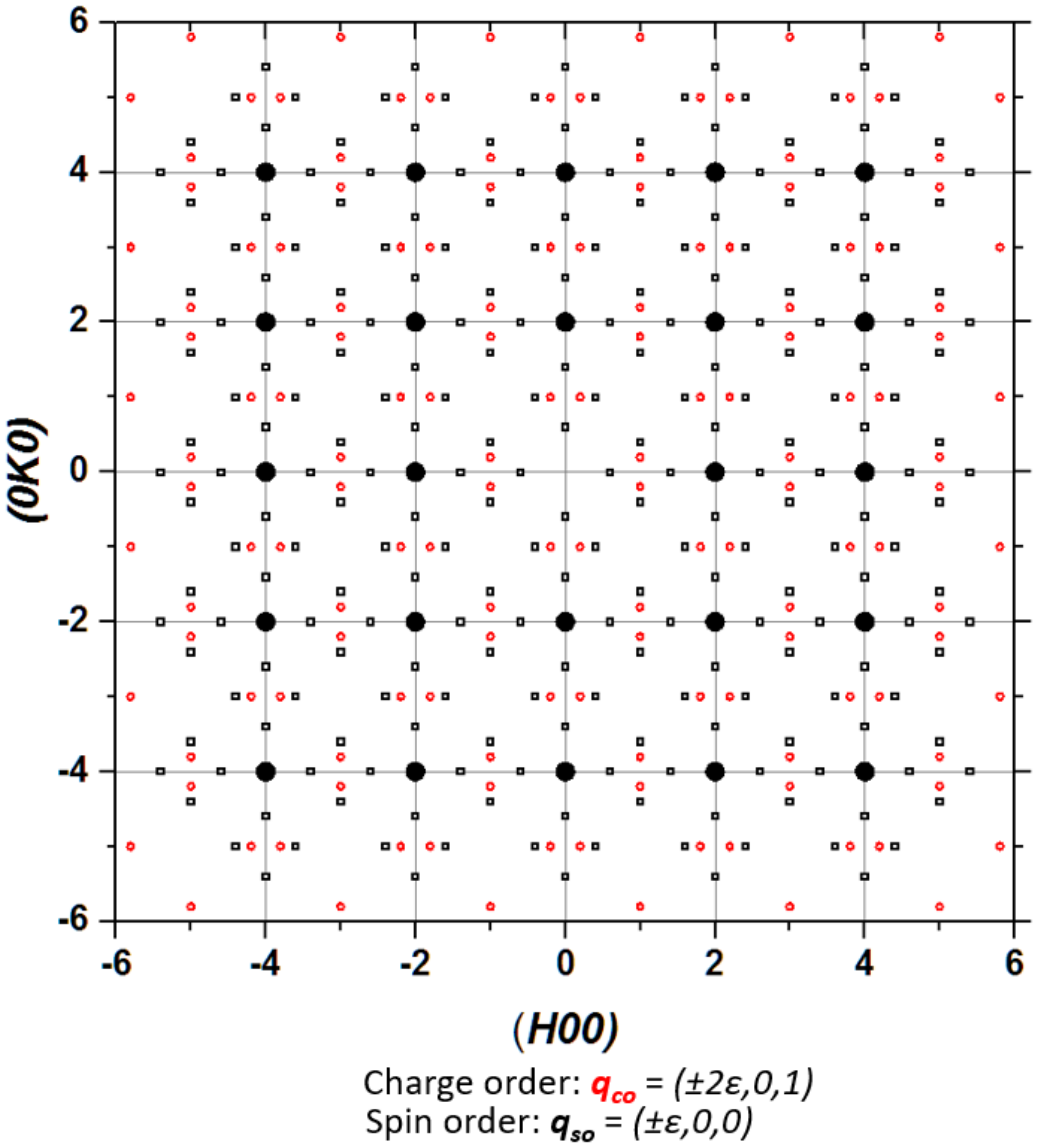

Figure 7.16: Calculated idealized *(hk0)* plane showing expected stripe charge order and spin order peaks following the modulation vector with ε = 0.44 whereas red circle and black square represents the CO and SO satellite.

7.5.2 Single Crystal X-ray diffraction

Even though we haven't detect the stripe charge order peaks from the single crystal neuron diffraction measurements due to the small atomic displacements issues we can see them by synchrotron high flux X-ray diffraction. Fig. 7.17 *(a-b)* shows the reconstructed *(hk0)* plane at 80 and 300K obtained from synchrotron X-ray diffraction on $Pr_{1.5}Sr_{0.5}NiO_{4+\delta}$ where structure is tetragonal *(F4/mmm)* for both temperature and at 80K the plane does not contain any oxygen ordered peaks only the stripe charge order reflections along with fundamental nuclear Bragg peaks are present. No LTT *(P4/2ncm)* phase has been detected for this compound at 80K. Blue circle represents the stripe charge order peak modulate from nuclear Bragg reflection following the modulation with $\varepsilon = 0.40$ which is different from what we obtained in case of neutron diffraction. This discrepancy might originate from slight deviation in Sr-content about ~ 0.04 or oxygen deficiency ~ (4-δ) if we consider same Sr concentration then. Even though it has been also reported elsewhere such arguments with observed different incommensurability obtained from X-ray and neutron diffraction. But in our case we cannot argue with the error coming from different experimental techniques because the sample measured for neutron diffraction was different from sample measured in synchrotron x-ray diffraction. However, our aim was to see the existence of such stripe order charge modulation in half-doped sample. If we take the $\varepsilon = 0.40$ and calculate the charge order peak position it will look like the Fig. 7.16 with slight different position. Also we have not detect any commensurate CB-type charge order in this sample what we saw in neutron measurements. This also a hints that might be Sr content is less and to determine the actual value of Sr concentration we need perform further high resolution TEM/SEM or EDS measurements. Anyhow from the current results we can confirm the charge modulation even though incommensurability is slight different and most interestingly we can correlated the fact of short range order of charge modulation with CB-type charge order and stripe spin order from neutron measurements. There we have seen continuous diffuse line for both SO and CO which is similar to diffuse intensities for CO in X-ray diffraction.

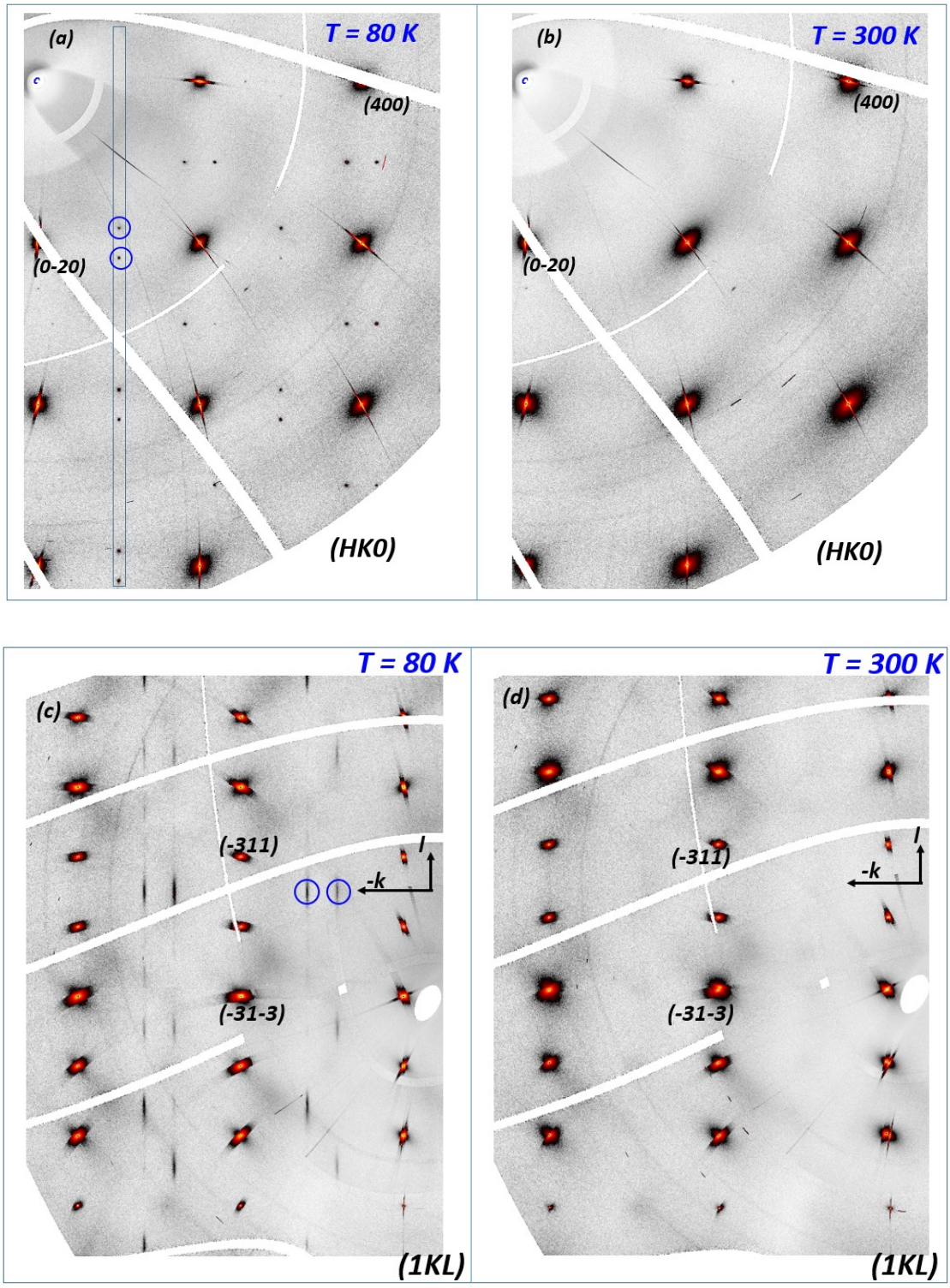

Figure 7.17: *(a-b)* shows the experimental reciprocal *(hk0)* plane obtained from X-ray diffraction on $Pr_{1.5}Sr_{0.5}NiO_{4+\delta}$ single crystal at 80 and 300K. Blue circle represents the charge order peak. Blue and red box shows charge order peak splitting along indicated direction

Fig. 7.17 *(c-d)* shows one of the reconstructed *(1kl)* plane cut along the thin blue section in *(a)* for both temperature. Blue circle enclose the one of the diffuse area from CO peaks at 80K. The diffuse scattering around the nuclear Bragg reflection is not that much dramatic or strong compare to sample doped with Sr ~ 0.125, the lattice or atomic displacements are hardly suppressed by large Sr-doping. Besides, there are few reflection might be some artifacts or impurity phase that present at both temperature. From this two measurements it can be concluded that at certain amount of Sr-doping nearly or exactly to half-dope region, a part of the system shows stripe incommensurate charge stripe emerges from matrix of commensurate CB-type charge order region showing strong correlation between short range stripe charge and spin degrees of freedom.

7.6 Charge Modulation in the Picture of Polaron Ordering

The phase separation and existence of mixture of both static charge stripe and CB charge ordering could rise the question that is it distinct charge order only from arrangements of holes or is it an ordering that coming from interaction of low energy breathing phonon with holes which is called polaron. $Pr_{2-x}Sr_xNiO_{4+\delta}$ is isostructural with $La_{2-x}Sr_xCuO_{4+\delta}$ having comparable physical properties where for stoichiometric parent compound with Sr doping introduce holes in to the NiO_2/CuO_2 planes (x^2-y^2) band. The difference is $(3z^2-r^2)$ orbitals on the ions of Cu^{3+}/Cu^{2+} remain filled whereas they are half filled on the ions of Ni^{3+}/Ni^{2+}. Winkler et al. [15] confirmed that a sharp drop in the T_N of La_2CuO_4 with initial Sr doping can be understood as due to an unusually large dilution of the antiferromagnetic interactions of the matrix by the large itinerant-electron correlation bags which is called multicenter polarons. In similar fashion they expected the drop of T_N with x occurs in $La_{2-x}Sr_xNiO_4$ on initial doping, which implies formation of multicenter polarons in this system also. From our SQUID magnetometry also proves that at higher Sr ($x = 0.5$) $Tso = 50$K becomes lower compare to ($x = 0$) sample where $Tso = 106$K. They first time reported evolution of such multicenter polaron size in $La_{2-x}Sr_xNiO_4$ in the range of $0.2 \leq x \leq 0.55$. We have seen already that $Pr_{2-x}Sr_xNiO_{4+\delta}$ forms static stripe charge ordering consisting of the mixture of $\varepsilon = 1/3$ stripe order and $\varepsilon = ½$ CB order similar to $La_{2-x}Sr_xCuO_{4+\delta}$, this is what Yoshizawa et al. [16] have shown with neutron diffraction

that commensurate, charge-ordered stripes of static small polarons appear below a T_{CO} at x = 1/3 and x = ½. Winkler et al. [15] also confirmed that appearance of such phase separation in nickelates the coulomb repulsion between polaron are responsible to become small polarons at larger value of Sr doping (x) instead of condensation into multihole and spin bags. In this regards we can expect in the homologous $Pr_{2-x}Sr_xNiO_{4+\delta}$ structure that polaron also plays an important role that take place due to the interaction of local lattice distortion and itinerant electron.

We have seen the X-ray and neutron 2D diffraction pattern evidence for the presence of charge and spin ordering along with enormous complicated oxygen ordering in $Pr_{2-x}Sr_xNiO_{4+\delta}$ at low temperature for the first time. Changes of the modulation wave vector means the incommensurability as function of hole doping *(x, δ and n_h)* also has been determined and presented in Fig. 7.18 and the interpretation can be drawn based upon the polaron ordering. So far we have noticed that all the charge and magnetic superlattice reflections are present up to 1st order only no 2nd or higher order harmonics has been detected which indicates the modulation are essentially because of sinusoidal lattice distortion. For Sr (x = 0) doped sample charge satellite are much sharper and becomes more diffuse along *c**-axis with increase in Sr content. The correlation of superlattice modulation perpendicular to NiO_2 plane means along *(00l)* direction becomes quasi-2D ordering. .The existence of stripe charge order in the matrix of CB charge order phase would have consequence with physical properties of this system. Even though for $Pr_{2-x}Sr_xNiO_{4+\delta}$ oxides the infrared anomaly is not so evident in the literature but for $La_{2-x}Sr_xNiO_{4+\delta}$ it has been shown for x = 0.5 infrared spectra revealed a phonon breathing mode near 670 cm^{-1} which is almost invisible for x > 0.5 [17]. But it has been reported in Ceretti et al. [18] for oxygen doped $Pr_2NiO_{4.25}$ that at low temperature low energy phonon modes are already presents that induce the large displacement amplitude to activate oxygen mobility. Similarly assuming the same hole concentration in x = 0.5 dope sample which is electronically equivalent there might be such low energy phonon modes exists. If it is the case then from theoretical first principle calculation point of view studied by Anisimov and Zannen et al. [19] on cuprates it can be shown the interaction of charge (holes) with the breathing mode phonons which involve four nearest oxygen atoms surrounding Ni atom on the NiO_2

square plane. Together with another infrared absorption band observation reported by Xiang et al. [20] on cuprates and nickelates, they showed the interaction between holes and phonon in nickelates is much stronger than cuprates leading to localized breathing polarons.

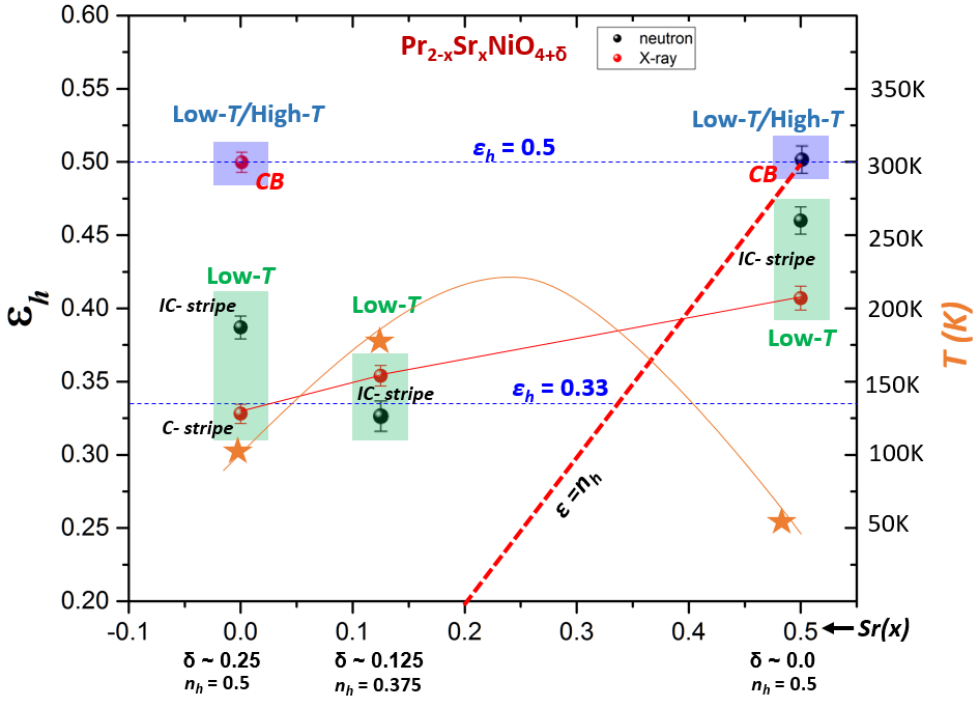

Figure 7.18: experimentally observed incommensurability vs Sr *(x)* content for both X-ray and neutron measurements. *X*-axis represents the Sr *(x)* content marked as black arrow and since there is also extra oxygen the amount of that is written as δ and the total hole concentration *(n_h)*. Left *Y*-axis denotes the experimentally observed incommensurability for both neutron and X-ray diffraction as black and red bullets with the error bar, corresponding stripe and CB region are mentioned and highlighted with different colored region. Right *Y*-axis denotes the spin order temperature obtained from neutron 2D diffraction and 1D scattering experiments.

Similarly we can propose the appearance of doublet charge satellite emerging from singlet CB satellite is results of 2D ordering of localized polarons on NiO_2 square plane for x= 0.5 and δ = 0.25 sample where one hole per Ni site is introduced and could be localized polarons give rise such singlet ordering like regular AF *(100)*-type and this ordering is essentially 2D as there is no correlation along *(001)* direction. In order to support our findings, we have shown similar electron diffraction pattern for x = 0.2 from the paper of Chen [21] where the author reported such polaron ordering in

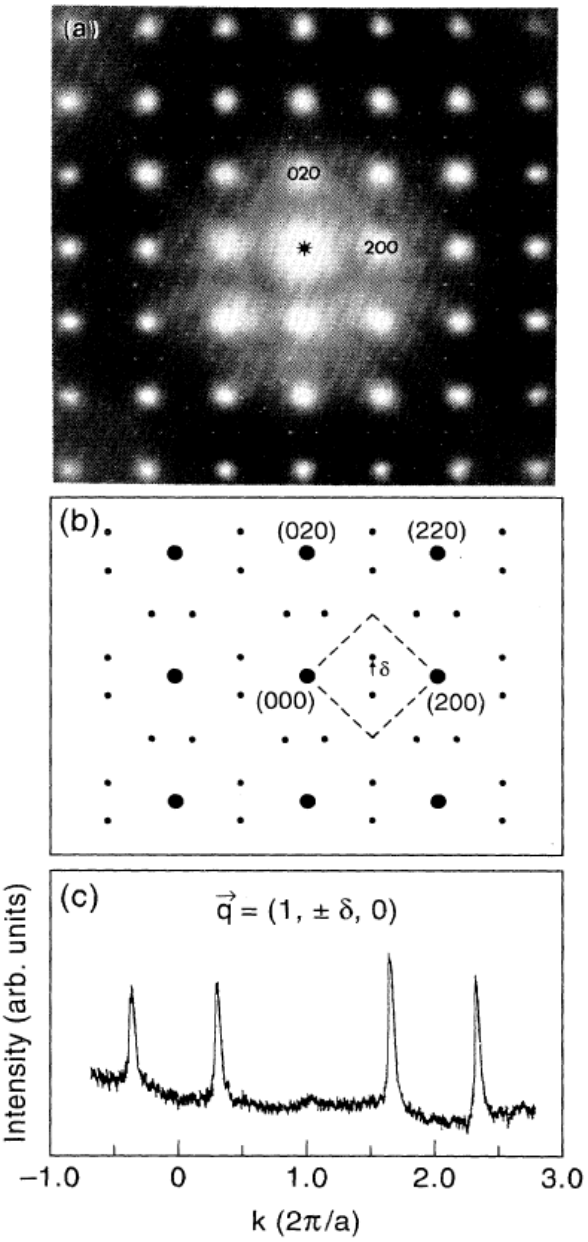

Figure 7.19: (a) [001] zone-axis electron diffraction pattern obtained at 93 K from a high-pressure oxygenated sample with x =0.2. Fundamental diffrraction spots are indexed with an orthorhombic cell. Presence of superlattice spots is evident. (b) A schematic representation showing the locations of the superlattice spots (small closed circles) in the reciprocal lattice. For comparison, a tetragonal unit cell is also indicated. (c) A microdensitometer trace showing the superlattice reflections along the *(1k0)* direction. The peak width is limited by the selection aperture of the microdensitomer. Figure has been taken from Fig. 1 of ref. [21].

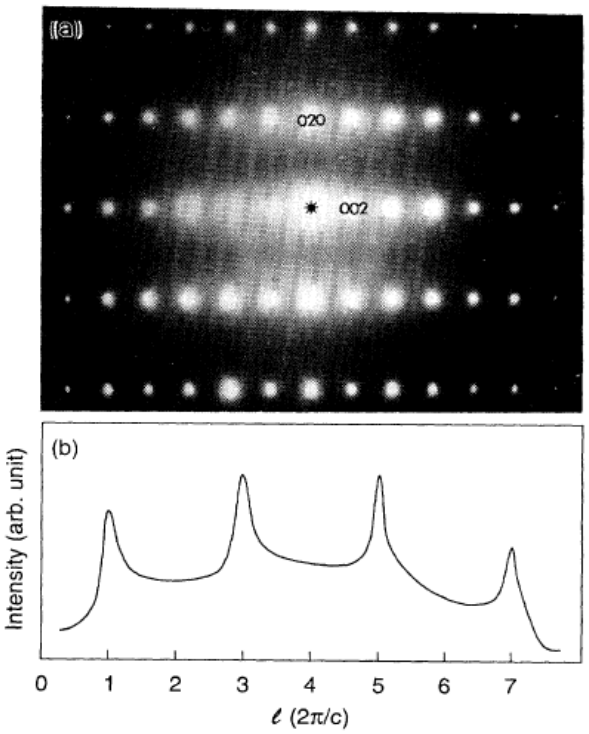

Figure 7.20: (a) [100] zone-axis electron diffraction pattern showing the elongation of superlattice reflections along the c^*-axis. (b) A microdensitometer trace through the diffuse streaks along the *(00l)* direction. Figure has been taken from Fig. 2 of ref. [21].

$La_{2-x}Sr_xNiO_{4+\delta}$ with x = 0.5. First thing to notice is that patterns in Fig. 7.19 and 7.20 they used the notation different from our notation of modulation vector. They have taken the ordering modulation from *(π, π)* point of tetragonal unit cell where as we have chosen the modulation from *(π, π)* point of orthorhombic unit cell. That is why they claimed the incommensurability is decreasing with increasing Sr-doping but this is correct if we consider our notation we see it is increasing with Sr-doping as shown in Fig. 7.17. Similar kind of pattern we have in case of stripe charge order for all the composition x = 0, 0.125 and 0.5. They have shown nicely the broadening of satellite as diffuse along *(00l)* which is true for in our case. They also claimed that for For $\varepsilon = 1/3$ polaron lattice, considerations of antiferromagnetic spin configurations of polarons with net spin $S = 1/2$ interlaced with an antiferromagnetic $S = 1$ lattice suggest a magnetic ordering characterized by a wave vector ε_{SO} which is half of the lattice modulation wave vector, i.e., $\varepsilon_{SO} = \varepsilon_{CO}/2$ which is true always for any Sr doping case as the magnetic unit cell is double of that charge order unit cell. This occurs because the spin order parameter changes sign across a polaron/charge domain wall and might be frustrated. It also can be understood considering the strong coupling between the breathing polarons which leaves little possibility for ordering defects that cause the charge and magnetic diffuse intensities along *(00l)*.

7.7 Possible Incommensurate Stripe Models and Stripeless Spin Order

In our present study all the composition shows incommensurability $\varepsilon \geq 1/3$ determined from both X-ray and neutron diffraction measurements for all the composition. In Fig. 7.18 observed rational fraction of incommensurability (ε) can be expressed by the equation $\boldsymbol{\varepsilon = \frac{n+m}{3n+4m}}$ for $n_h \leq 1/3$ and $\boldsymbol{\varepsilon = \frac{n+m'}{3n+2m'}}$ for $n_h \geq 1/3$ [14, 23-26], where n_h is the total hole concentration given by $n_h = x + 2\delta$. Following this equations we have found the combination of n and m' for the experimentally obtained incommensurability as tabulated in Table 2. In order to understand the meaning of m, n and m' we have to see the models for stable stripe ($\varepsilon = 1/3$) and checkerboard ($\varepsilon = ½$) charge ordering at least for our case we do not need to take account for another stable stripe ($\varepsilon = ¼$). The indices m, n and m' refers the ideal model for $\varepsilon = ¼$, $1/3$ and ½. If the all combination of m, n and m' is possible then it can be described the all the discommensuration by taking combination of those indices. Fig. 21 shows the deviation of incommensurability from linear relation where ε has been expressed following the rule mentioned on the picture for $n_h \leq 1/3$ and $n_h \geq 1/3$. Fig 7.22 *(a-b)* shows the ideal stripe and checkerboard-type spin and charge arrangements in orthorhombic unit cell (blue box). In Fig. 7.22 *(b)* for CB ordering green shaded box represents a one charge stripe unit cell of width a, note that for $\varepsilon = 1/2$, there is one charge stripe per two columns of Ni atoms (fundamental unit cell) and this correspond to indices m', similarly for stripe Fig. 7.22 *(a)* red shaded box indicates one charge stripe unit cell of width $3/2a$ ($\boldsymbol{a = a_O}$ = **width of fundamental orthorhombic unit cell**) per three columns of Ni atoms and this refers to indices n. Finally for stripe $\varepsilon = ¼$ it can be seen as one charge stripe per four columns of Ni atoms of width $2a$ and refers the indices m. The black dashed outline indicates magnetic unit cell in the corresponding stripe or checkerboard configuration. The possible stripe and CB charge order unit cell as well magnetic unit cell has been depicted in those figure. Blue shaded box represents the same charge stripe unit cell of width a, but they are not allowed. For stripe case it does not repeat in the real space unit and in CB there is no net spin moment. Note that For CB each possible charge order unit cell contains one hole and one Ni^{2+} atom and magnetic unit cell consist of zero magnetic moment and two holes. Similarly, in case of stripe charge order each stripe unit cell contains one hole and no net magnetic

spin. Black cross represents the oxygen site in orthorhombic unit cell. Here we will consider the site centered charge order not bond centered.

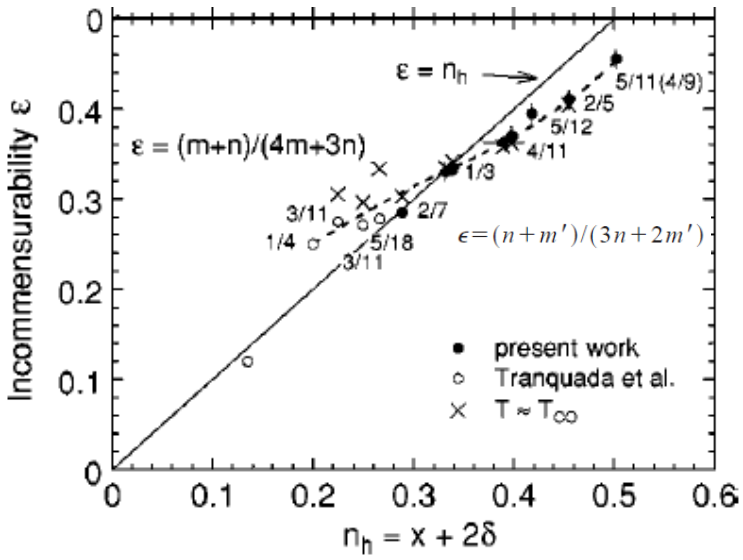

Figure 7.21: Hole concentration n_h dependence of the incommensurability ε for $n_h \leq ½$ determined at the low temperature studied. Cross symbols indicate the high temperature initial values of ε. Picture has been reproduced from Fig. 3 of ref. [26].

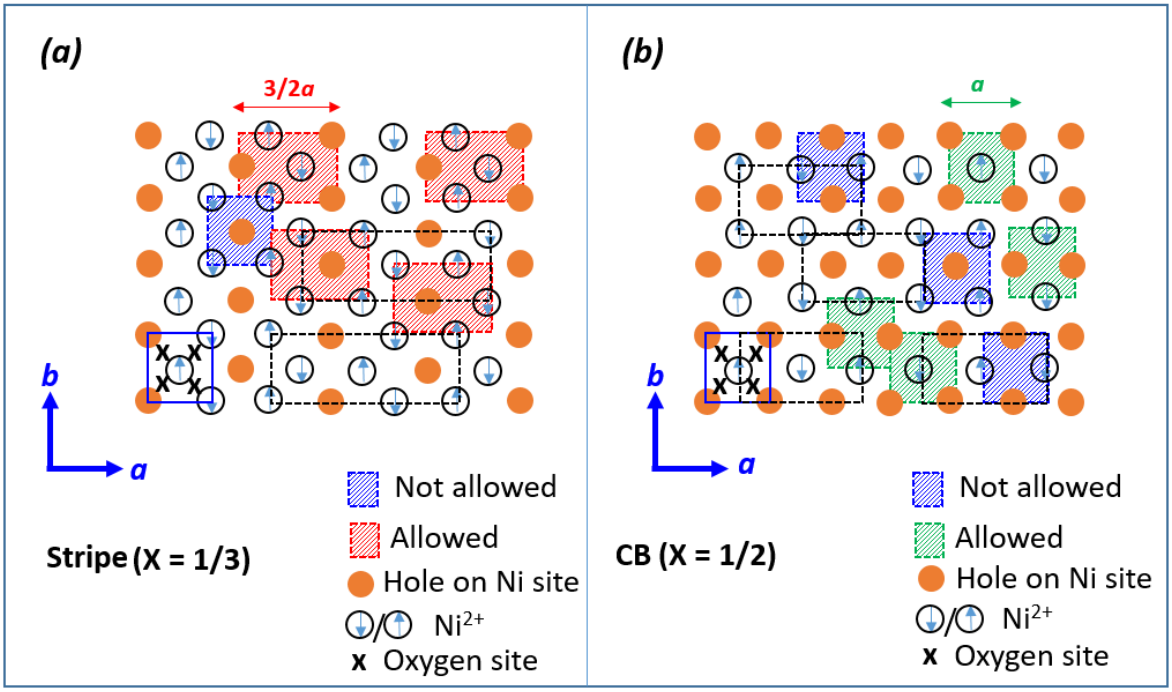

Figure 7.22: *(a-b)* cartoon of ideal stripe and checkerboard charge order pattern in orthorhombic unit cell (marked as blue empty box) of width $a = a_O = a_N\sqrt{2}$. Red shaded and green shaded box represents the allowed and possible unit cell of width $3/2a$ and a of stripe and CB charge order respectively whereas blue shaded box not allowed charge unit cell in both cases. Dashed black rectangle indicated the possible magnetic unit cell of width twice that of charge order unit cell in both order pattern. Orange filled circle, black open circle with arrow and cross represents the holes on Ni3+ site, Ni2+ with magnetic moment and oxygen site respectively.

Compound	*x*	*δ*	n_h	*X-ray (ε), [n, m']*	*Neutron (ε), [n, m']*
$Pr_2NiO_{4+\delta}$	0	0.25	0.5	0.387, [3,2]/0.5, [0,1]	0.328, [1,0]
$Pr_{1.875}Sr_{0.125}NiO_{4+\delta}$	0.125	0.125	0.375	0.354, [4,1]	0.33, [1,0]
$Pr_{1.5}5Sr_{0.5}NiO_{4+\delta}$	0.5	0	0.5	0.407, [1,1]	0.44, [1, 3]/0.5, [0, 1]

Table 2: Incommensurability and corresponding different combination of stripe and checker board commensurability observed in the present study by X-ray and neutron diffraction for the $Pr_{2-x}Sr_xNiO_{4+\delta}$ (x = 0, 0.125 and 0.5).

Models of charge order and spin configuration for all observed incommensurability (ε) has been presented in Fig. 23. As it mentioned before since there are many possibility to choose stripe or CB charge order unit cell, by taking different combinations of different possible unit cell we can develop the models for each ε following those rule for $n_h \geq 1/3$. Fig. 23 *(b)* and *(g)* shows ideal stripe and CB order with $n = 1$, $m' = 0$ and $n = 0$, $m' = 1$, respectively. Between these two stable state the incommensurate charge stripe state with the different combination of n and m' is shown in *(c-f)*. For example of ε = 0.357 stripe, $n = 4$ and $m' = 1$ means one CB unit cell of width *a* is embedded for every four stripe unit cell of width 3/2*a*. Note that in terms of magnetic structure, rational fraction imply that magnetic modulation must repeat length of $(n + m')a$ period in a unit cell of length $(3n + 2m')a$ means $(3/2a\times4 + a\times1) = 7a$ period repeats in opposite direction to complete the magnetic unit cell with length of 14*a*. It can be seen from the blue periodic curve which is just represent the (n + m') period in a magnetic unit cell of width (3n + 2m')*a*.. In this model only site centered stripe has been shown, both site and bond centered stripes exists in nickelates where oxygen or bond centered stripe appears at higher temperature just below T_{CO} and fraction of Ni or site centered stripe start to grow from the matrix of the oxygen centered stripe and become stronger at low temperature. In a similar fashion oxygen centered stripe can be evaluated following the same rule of incommensurability [14, 26]. To visualize oxygen centered stripe it is better to consider frame work of tetragonal unit cell because oxygen are located between two Ni atoms on NiO_2 layers and run along the a/b-axis of tetragonal cell whereas it run along diagonal in orthorhombic unit cell. If we switch to the tetragonal cell then we have to change the notation as well and we call the length of fundamental unit cell as a_t. So the width of CB charge order unit cell will be $2a_t$ and that of stripe charge order unit cell will be $3a_t$.

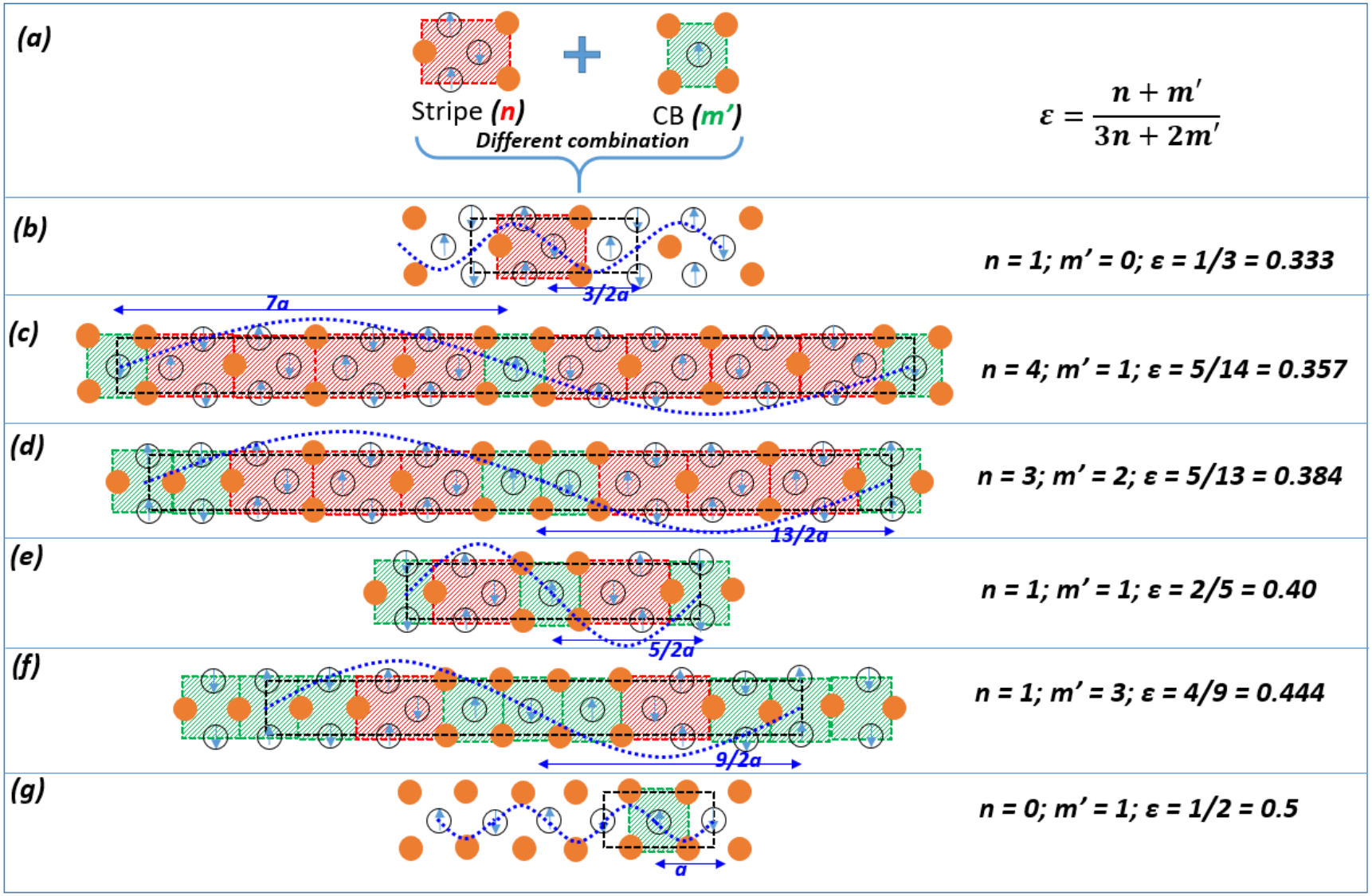

Figure 7. 23: (a) shows one of the possible charge order unit cell for stripe *(n)* and CB *(m')* and taking different combination of those *n* and *m'* we have models for each observed ε = 0.333, 0.357, 0.387, 0.4, 0.444 and 0.5 has been shown in *(b-g)*. Blue sinusoidal curve is a guideline for showing the (n + m') period in a magnetic unit cell of width (3n + 2m')*a*. Blue arrows indicates the length of charge order unit cell in that repeats in opposite direction in that magnetic unit cell. Black dashed rectangle represents the magnetic unit cell for all cases.

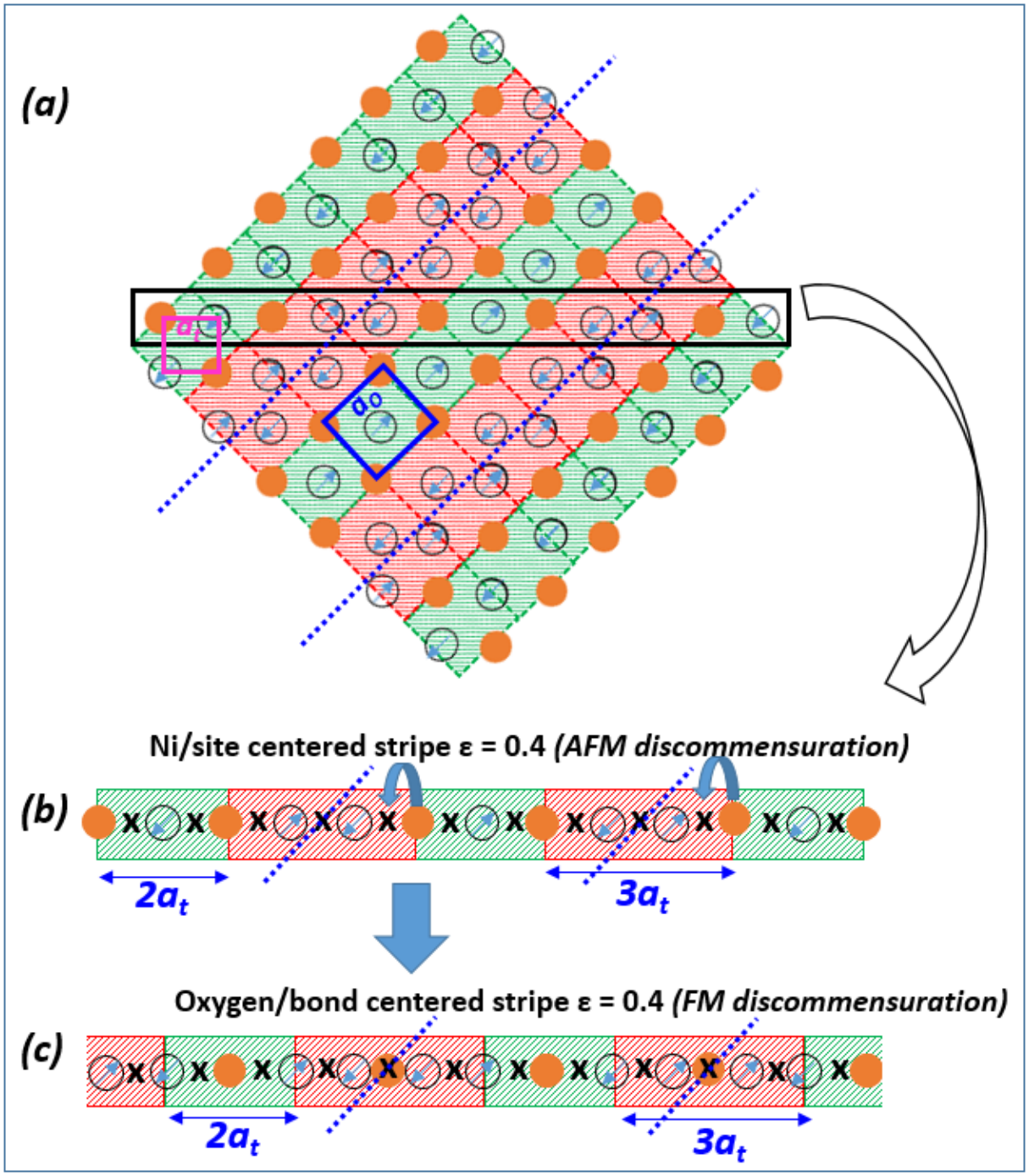

Figure 7.24: (a) Cartoon of the incommensurate *(ε = 0.4)* stripe charge order pattern shown in framework of tetragonal unit cell where pink and blue box represents the fundamental tetragonal and orthorhombic unit cell in real space. Oxygen sites are not shown. (b) Represents the one row of Ni or site centered stripe taken from that black area in (a). Here cross indicates the oxygen sites on that NiO_2 plane. (c) Represents the same row in case of oxygen or bond centered stripe, this is obtained by moving one hole for each discommensuration region from the same Ni site to nearest oxygen site (see the arrow) in *(b)* by leaving that Ni atom magnetic means Ni2+. In oxygen centered stripe discommensuration region moves to right compare to Ni centered stripe if hole moves to left. The width of the charge unit cell has been given by the length of the tetragonal unit cell *(a_t)*.

In case of incommensurability $\varepsilon = 0.4$ Fig. 23 *(e)*, if we repeat the unit cell in 2-dimension then we will have the pattern looks like in Fig. 24 *(a)* which is turned 45^0 to get tetragonal unit cell. After that taking into account any one of those horizontal section (black rectangle) separately and put the oxygen in the row between two Ni atoms we have the model like in Fig. 24 *(b)* which is Ni or site centered stipe. In order to get the oxygen centered stripe shown in Fig. 24 *(c)* we need to move one hole from Ni site to oxygen site in the discommensuration region (red shaded area) keeping the width of stripe unit cell same. Note that in oxygen centered stripe total one net magnetic spin survive inside the discommensuration region whereas in CB region it does not gibe total moment exactly opposite case compare to Ni centered stripe. Also the direction of moment in one discommensuration region is opposite to the next discommensuration region keeping the magnetic order antiferromagnetically as whole for both Ni/oxygen centered stripe. In the picture of the spin-exchange interactions for the CB charge ordered state, the exchange interaction between the nearest-neighbor sites is unique, and there is only the one between Ni^{2+} and Ni^{3+} ions. As soon as charge order becomes incommensurate, another exchange interactions works between Ni ions in the discommensuration regions and can be seen as the Ni-centered discommensuration where interaction take place between Ni^{2+} - Ni^{2+} Fig. 24 *(b)* while in oxygen centered discommensuration it is between Ni^{2+}-hole-Ni^{2+} Fig. 24 *(c)*. Because the exchange interactions for these bonds are expected to be much stronger than that between Ni^{2+} and Ni^{3+}, the energy gain due to the spin-exchange interactions is larger in the stripe state, and favors the stripe order [14]. In case of Ni centered stripe blue dotted line separate the antiparallel magnetic spin and give rise AFM discommensuration region where the hole density is lower than the average. On the other hand, for oxygen centered stripe dotted line represents the line of holes on oxygen site which increase the local hole density at that position and induce parallel spin alignment between two nearest Ni atoms via double exchange mechanism and we call it FM discommensuration. This might will help to understand the interesting feature related to spin dynamics/magnetic excitation homologous to cuprates or cobaltates.

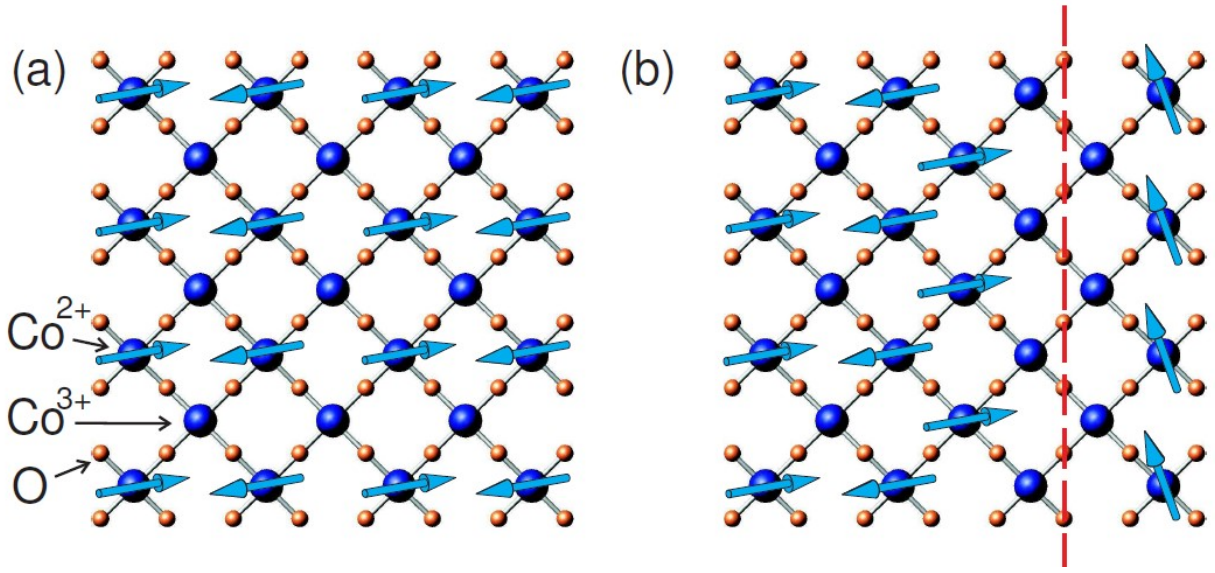

Figure 7.25: (a) Checkerboard charge and spin order at half- doping. (b) Stacking fault giving rise to short-range correlation and magnetic incommensurability in $La_{1.5}Sr_{0.5}CoO_4$ in stripe picture. Reproduced from Fig 1 of ref. [27].

Another model corresponding to stacking faults in CB ordering in half-doped $La_{1.5}Sr_{0.5}NiO_4$ has been shown in above Fig. 7.25 (taken from ref. [27]). This model highlights the possibility to have stripeless incommensurate magnetic ordering within CB charge ordering see the text in sec 7.5.1. The difference of such stacking faults with normal discommensuration is the Ni/Co spins in former case introduce the linear disclination parallel to stripe and couples between two consecutive hole sites in (b) and therefore truncate the range of wave vector of magnetic ordering. In our $Pr_{1.5}Sr_{0.5}NiO_4$ from neutron diffraction we see it becomes $\varepsilon = 0.44$ with deviation of $\Delta\varepsilon = 0.05$ from perfect magnetic ordering $\varepsilon = 0.5$ Fig. 7.14. Out of two possibilities, it is normal discommensuration either Ni or oxygen centered stripe where we should see simultaneous incommensurate stripe charge and spin order with same ε model would be like Fig. 7.23 (f), but experimentally we haven't observed corresponding incommensurate stripe charge order except CB one then it could be the other possibility that is stacking fault like Fig. 7.25 *(b)*.

7.8 Summary

Hole doping either by oxygen or Pr substitution by Sr in Pr_2NiO_4 oxide introduce hole per Ni sites on NiO_2 layer with different concentration give rise to fascinating electronic ordering associated with charge separation from checkerboard to stripe order by means of electronic phase separation as well

stripe spin correlation with charge order. X-ray and neutron single crystal diffraction are complementary tools to investigate such physical phenomena along with SQUID magnetometry which gives an idea of magnetic ordering globally and associated ordering temperature. First thing to mention is sample with half hole dope ($\delta \sim 0.25$ or $x = 0.5$) shows both charge and spin ordering at low temperature in addition oxygen ordering for oxygen dope sample, 2nd is stripe charge order emerges from matrix of CB charge region. This can be understood in the picture of phase separation and competition between two ordered ground state where at lower temperature a small part of stripe charge order is emerging from matrix of CB state exist at RT. Since the intensity of that CB charger order peaks goes down at low temperature that indicates the short range CB charge order correlation. The only difference in oxygen and sr doping is splitting of charge order peaks, when oxygen are incorporated in the sample the splitting appears where is no splitting only for Sr doping sample. This phenomena must have some connection with oxygen ordering. Similarly only for oxygen doping spins are strongly correlated in 3D which get lost along c^*-axis with introducing further hole by Sr substitution. For all cases except pure oxygen dope, charge are not long range ordered along c^*-axis they appeared as diffuse rod. Another important point is the discrepancy of incommensurability (ε) determined from X-ray and neutron diffraction measurement which has been summarized in the Fig. 7.18. There has been some discussion about the movement of holes from Ni site (site centered stripe) to oxygen site (bond centered stripe) could be responsible for. But in $La_2NiO_{4.133}$ compound Tranquada et al. [22] confirmed the movement of holes from Ni sites to oxygen sites only possible and become significant above the spin order temperature. But our low temperature study does not describe this feature as it was well below the T_{SC}. Further study is required to explain this discrepancy between X-ray and neutron measurements. The combined picture of stripe charge order can be understood as polaronic breathing type interaction in $\varepsilon = 1/3$ and $\varepsilon = ½$ static ground state.

References:

1. J.M. Tranquada, D.J. Buttrey, V. Sachan, and J.E. Lorenzo, Simultaneous Ordering of Holes and Spins in $La_2NiO_{4.125}$, Phys. Rev. Lett, 73 1003 (1994).
2. G. H. Lander, P. J. Brown, J. Spalek, and J. M. Honig, Structural and magnetization density studies of La_2NiO_4, Phys. Rev. B 40, 4463 (1989).
3. S.-H. Lee and S-W. Cheong, Melting of Quasi-Two-Dimensional Charge Stripes in $La_{5/3}Sr_{1/3}NiO_4$, Phys. Rev. Lett. 79, 2514 (1997).
4. M. Hücker, K. Chung, M. Chand, T. Vogt, J. M. Tranquada, and D. J. Buttrey, Oxygen and strontium codoping of La_2NiO_4: Room-temperature phase diagrams, Phys. Rev. B 70, 064105 (2004).
5. V. Sachan, D. J. Buttrey, J. M. Tranquada, J. E. Lorenzo, and G. Shirane, Charge and spin ordering in $La_{2-x}Sr_xNiO_{4.0}$ with x=0.135 and 0.20, Phys. Rev. B 51, 12742 (1995) .
6. S. M. Hayden, G. H. Lander, J. Zarestky, P. J. Brown, C. Stassis, P. Metcalf, and J. M. Honig, Incommensurate Magnetic Correlations in $La_{1.8}Sr_{0.2}NiO_4$, Phys. Rev. Lett. 68, 1061 (1992).
7. R. Kajimoto, K. Ishizaka, H. Yoshizawa, and Y. Tokura, Spontaneous rearrangement of the checkerboard charge order to stripe order in $La_{1.5}Sr_{0.5}NiO_4$, Phys. Rev. B 67, 014511 (2003).
8. D. J. Buttrey and J. M. Honig, Influence of Nonstoichiometry on the Magnetic Properties of Pr_2NiO_4 and Nd_2NiO_4, Journal of solid state chemistry 72, 38-41 (1988).
9. R. Saez Puche, F. Fernandez, J. Rodriguez, J. L. Martinez, Magnetic and X-ray diffraction characterization of stoichiometric Pr_2NiO_4 and Nd_2NiO_4 oxides, Solid State Communications, Vol. 72, No. 3, pp. 273-277, 1989.
10. M. T. Fernandez-Diaz, J. L. Martinez, and J. Rodriguez-Carvajal, Metamagnetism in single-crystal Pr_2NiO_4, Phys. Rev. B 47, 1993.
11. M.T. Fernfindez-Diaz, j. Rodriguez-Carvajal , J.L. Martinez 1, G. Fillion , F. Fern~ndez , and R. Saez-Puche, Structural and magnetic phase transition in Pr2NiO4, Z. Phys. B Condensed Matter 82, 275 282 (1991).
12. M. huker, Structural aspects of materials with static stripe order, Physica C 481 (2012) 3–14.
13. M. matsuda, M. Fujita, K. Yamada, R. J. Birgeneau, Y. Endoh, G. Shirane, Electronic phase separation in lightly-doped $La_{2-x}Sr_xCuO_4$, Physical Review B 65(13), 2002.
14. R. Kajimoto, K. Ishizaka, H. Yoshizawa, and Y. Tokura, Spontaneous rearrangement of the checkerboard charge order to stripe order in $La_{1.5}Sr_{0.5}NiO_4$, Phys. Rev. B 67, 014511 (2003).
15. E. Winkler, F. Rivadulla, J.-S. Zhou, and J. B. Goodenough, Evolution of polaron size in $La_{2-x}Sr_xNiO_4$, Phys. Rev. B 66, 094418 2002.
16. Web reference https://arxiv.org/pdf/cond-mat/9904357.pdf.
17. N. Ogita, S. Takanashi, M. Udagawa, K. Ohbayashi, Infrared anomaly in $(La_{1-x}Sr_x)_2NiO_{4+\delta}$, Journal of the Physical society of japan, 1992, Vol. 61, 8: pp. 3009-3010.
18. M. Ceretti, O. Wahyudi, A. Cousson, A. Villesuzanne, M. Meven, B. Pedersen, J. M. Bassat, and W. Paulus, Low temperature oxygen diffusion mechanisms in $Nd_2NiO_{4+\delta}$ and $Pr_2NiO_{4+\delta}$

via large anharmonic displacements, explored by single crystal neutron diffraction, J. Mater. Chem. A, vol. 3, no. 42, pp. 21140– 21148, 2015.

19. V. I. Anisimov and M. A. Korotin, J. Zaanen, O. K. Andersen, Spin Bags, Polarons, and Impurity Potentials in $La_{2-x}Sr_xCuO_4$ from First Principles, Phys. Rev. Lett. 68, 1992.
20. Xiang-Xin Bi and Peter C. Eklund, Polaron Contribution to the Infrared Optical Response of $La_{2-x}Sr_xCuO_{4+\delta}$ and $La_{2-x}Sr_xNiO_{4+\delta}$, Phys. Rev. Lett, 70, 1993.
21. C. H. Chen, 8-W. Cheong, and A. S. Cooper, Charge Modulations in $La_{2-x}Sr_xNiO_{4+\delta}$ Ordering of Polarons, Phys. Rev. Lett. 71 1993.
22. J.M. Tranquada, P. Wochner, A.R. Moodenbaugh, D.J. Buttrey, Field-induced staggered magnetic order in $La_2NiO_{4.133}$, Phys. Rev. B 55, R6113 (1997).
23. J.M. Tranquada, D. J. Buttrey, D. E. Rice, Phase separation, charge-density waves, and magnetism in $La_2NiO_{4+\delta}$ with $\delta = 0.105$, Phys. Rev. Lett. 70, 445, 1993.
24. J.M. Tranquada, D. J. Buttrey, V. Sachan, J. E. Lorenzo, Simultaneous ordering of holes and spins in $La_2NiO_{4.125}$, Phys. Rev. Lett. 73, 1003, 1994.
25. P. Wochner, J. M. Tranquada, D. J. Buttrey, V. Sachan, Neutron-diffraction study of stripe order in $La_2NiO_{4+\delta}$ with $\delta = 2/15$, , Phys. Rev. B 57, 1066, 1998.
26. H. Yoshizawa, T. Kakeshita, and R. Kajimoto, Stripe order at low temperatures in $La_{2-x}Sr_xNiO_4$ with 0.289.x.0.5, Phys. Rev. B, 61, 2002.
27. A. T. Savici, I. A. Zaliznyak, G. D. Gu, and R. Erwin, Stripeless incommensurate magnetism in strongly correlated oxide $La_{1.5}Sr_{0.5}CoO_4$, Phys. Rev. B 75, 184443 2007.

Chapter 8

General Conclusions and Future Perspectives

In this thesis main objective was to study the structural evolution by means of long range oxygen modulation in *(3+n)*-dimension, interesting physical ordering phenomena that takes place in discrete or mixture of two electronic ground states e.g. commensurate stripe and checkerboard-type charge order state and associated spin ordering to understand the interplay between oxygen order and electronic/magnetic order in strongly correlated hole doped Pr_2NiO_4 oxides either by substituting Pr with Sr cations or by oxygen intercalation on interstitial lattice sites. Besides, evolution of microstructure by studying complex oxygen ordering belongs to maximum eight twin individuals showing discrete phases e.g. $N = 5, 6$ *and* 9 as function of temperature at different oxygen pressure *P(O2)* have been intensively studied to understand the structural aspects in the field of low temperature phonon assisted oxygen mobility in oxygen doped $Pr_2NiO_{4+\delta}$ oxides and that enables one to investigate the polaron ordering which comes from electronic ordering coupled with phonon (lattice distortion) at very low temperature. To compare the electronic equivalency between only oxygen, Sr and O/Sr codoped Pr_2NiO_4 oxides the electronic ground state at ambient and low temperature has been investigated by measuring charge/magnetic ordering using combined X-ray and neutron diffraction technique.

To investigate strong electronic correlations such as charge, oxygen and magnetic ordering as well as lattice and spin dynamics between Sr- and oxygen doped titled compounds it is necessary to have very good quality homogeneous single crystal to perform in-situ single crystal X-ray diffraction and very big in size roughly ~ 4 cm in length is required for neutron elastic, inelastic scattering experiments. Since defects, intergrowth phase and impurities in the sample have huge effects on such above mentioned physical properties and phenomena, all the pre synthesis have been carried out with careful weighing the calculated reactants to have at least single phase and good quality

single crystal. To compensate the evaporation of nickel oxide which is another serious issue for growing single crystal of nickelates, an excess of NiO (≈ 2% mole) must have to be added to the starting stoichiometric material. This compounds are very sensitive to oxygen and in practice during crystal growth it is very difficult to control the oxygen content because of the wide range of possible oxygen uptake or release that leads to ordered superstructures of excess oxygen or vacancies and might give rise to new crystal structures forming a rich phase diagram. Several high quality single crystals of $Pr_{2-x}Sr_xNiO_{4+\delta}$ (x = 0, 0.125, 0.25 and 0.5) have been grown by travel solvent floating zone technique (TSFZ) using double mirror furnace. The oxygen uptake or release depends on reaction temperature and oxygen partial pressure in the growth chamber. Determination of the oxygen content is another big problem as it tries to equilibrate with ambient atmosphere, however using thermogravometry analysis (TGA) under different oxidizing/reducing atmosphere it is possible to measure the relative change in mass that comes only from oxygen. It has been observed that most stable phase of $Pr_2NiO_{4+\delta}$ with oxygen content of $\delta \approx 0.23$ and start to take up oxygen in the begging of increasing temperature around 50 ^{0}C while heating under O_2 flow and reaches to $\delta \approx 0.25$ at 450 ^{0}C where the average structure already transformed from orthorhombic to tetragonal. At higher temperature it loose oxygen and get stabilized at oxygen content of $\delta \approx 0.18$-0.12 and during cooling under O_2 flow the kinetics of oxygen changes is observed to be reversible see the Fig. 5.13.

To understand the average structure and mostly the complex 3D oxygen ordering and the role of related twin individuals on oxygen mobility conventional laboratory powder diffraction measurements and single crystal X-ray diffraction measurements has been performed on different diffractometers. As grown RT phases of $Pr_{2-x}Sr_xNiO_{4+\delta}$ were checked by in house STOE STADIVARI 4-circle diffractometer (μ-focused Mo source, $\lambda = 0.71073$ Å) equipped with 200K PILATUS area detector, phase of $Pr_2NiO_{4+\delta}$ was measured on MX beamline ID23 and ID29 at ESRF both diffractometer are equipped with 6M PILATUS detector. In situ high-T study and pressure dependent study of $Pr_2NiO_{4+\delta}$ were carried out on BM01 diffractometer at ESRF equipped with 2M PILATUS area detector as well on STOE. Electronic and magnetic ordering in both half doped

$Pr_2NiO_{4.25}$ and $Pr_{1.5}Sr_{0.5}NiO_4$ were studied by performing X-ray single crystal diffraction on ID28 (side station) at ESRF equipped with 1M PILATUS detector and neutron single crystal diffraction on DMC, SINQ at PSI.

Basic structure of $Pr_2NiO_{4+\delta}$ ($\delta \approx 0.25$) at ambient is orthorhombic well described in *Fmmm* space group can be seen from the both powder and single crystal X-ray diffraction but with close inspection to the well-defined splitting of *(220/-220)* reflections in powder diffraction pattern reveals the monoclinic nature indeed in *F2/m* space group having *c*-unique axis and $\gamma = 90.06^0$ see Fig. 4.2. This information is hard to obtain from single crystal X-ray diffraction as the monoclinic angle is close to 90^0 and difficult to extract the angular 2θ position of those two reflection in reciprocal space as the determination of 0.06^0 under error resolution. Similarly, the pseudomerohedral twin feature of $Pr_2NiO_{4+\delta}$ oxide and huge number of very weak oxygen or charge order peaks (most of them is under the background of XRPD pattern) are not accessible from conventional powder diffraction and even though it is possible to catch the weak superlattice reflection by synchrotron X-ray diffraction it is difficult to assign or index them individually according to their twin individuals, only way to investigate them is to perform single crystal diffraction and that is the reason why both techniques are complementary to study the local microstructure as well as average structure and phase purity in detail. However, from single crystal diffraction it is observed the structure of $Pr_2NiO_{4+\delta}$ consists of max. two times twin domains and contains oxygen order satellite that appears along with main Bragg reflections in every *(hkn/2)* plane with n = integer perpendicular to c^*-axis, where the intensity of those satellite is order of 10^{-4} less than compare to fundamental Bragg reflections. The modulation vector in reciprocal space that describe all those satellite was found to be commensurate $\boldsymbol{q^1} = \pm 0.833\boldsymbol{a^*} + 0.5\boldsymbol{b^*}$ and $\boldsymbol{q^2} = \pm 0.252\boldsymbol{a^*} + 0.249\boldsymbol{b^*} + 0.5\boldsymbol{c^*}$ and the structure can be described with help of $F2/m(\alpha_1\beta_1 0)(0s)(\alpha_2\beta_2 1/2)(00)$ superspacegroup in *(3+2)*-dimension. In addition to these 2D oxygen order peaks in *(hkn/2)*; n = integer planes there exist another type of oxygen order satellite in the diagonal *(hhl)/(h-hl)* planes with the modulation vector having α,α-component along [110/1-10] direction and γ-component along c^*-axis which explain the 3D nature of oxygen ordering. Model calculation of predicted oxygen order peak position

replicate experimental pattern except few very weak *(100)*-type superstructure reflections in *(hk0)* plane. These special reflections coming from checkerboard charge ordering of Ni^{2+}/Ni^{3+} in the half doped (hole concentration, $n_h = 2\delta = ½$) $Pr_2NiO_{4.25}$ even at room temperature and explained by the charge order modulation vector *(±2ε, 0, 1)* for each twin domain.

As grown phase of $Pr_2NiO_{4+\delta}$ at RT shows different oxygen ordering stabilized with commensurate modulation up to $N = 6$ ($\boldsymbol{q}^1 = \pm 0.833\boldsymbol{a}^* + 0.5\boldsymbol{b}^*$) measured on ID29 and N= 9 ($\boldsymbol{q}^1 = \pm 0.78\boldsymbol{a}^* + 0.56\boldsymbol{b}^*$) measured on ID23 (Fig. 4.9), reason is not clear yet to have different N phase for same compound because $N = 9$ phase (Fig. 4.12) correspond to high-T phase (T ~ 250 ^{0}C) could be different oxygen stoichiometry and depending on sample history. High-T studies of $Pr_2NiO_{4+\delta}$ indicates strong correlation of oxygen ordering in disordered phase even after phase transition ($T \geq T_{HTT}$) as the oxygen order appears as a diffuse ring and modulation of oxygen ordering changes from commensurate ($N = 6$) at RT to incommensurate ($N = 9$) already at 250 ^{0}C and gets locked in this phase. During cooling it behaves reversely means comes back to the starting orthorhombic phase with similar modulation vector. 3D oxygen ordering in *(hhl)* plane becomes 2D in nature at temperature 150 ^{0}C where splitting of oxygen order peaks with modulation vector *($\boldsymbol{q}^1 = \pm 0.317\boldsymbol{a}^* + 0.317\boldsymbol{b}^* + 0.12\boldsymbol{c}^*$)* start to melt and becomes a single reflection having zero component along c*. Besides all these different kind of oxygen ordering strong diffuse scattering surrounding the main Bragg reflections which appears as butterfly shape could be related to low and high energy phonon modes which might been coupled with oxygen and charge ordering. On the other hand complex phase diagram of oxygen ordering, average structure and thermal stability has been focused by in situ X-ray diffraction on single crystal of $Pr_2NiO_{4+\delta}$ as function of temperature at different oxygen pressure. First, transition temperature *($T_{LTO/HTT}$)* increases from 400 to 420 and 450 ^{0}C at atmospheric pressure, 50 and 75 bar of oxygen pressure respectively, second, one time twin domain in starting phase changes to two times twin domain after treating the sample under pressure, third the modulation vector of oxygen ordering remains unchanged during cooling under oxygen pressure which is completer different from the case of only temperature dependent study at atmospheric pressure. Also we were able to induce completely different and stable oxygen ordering N = 5 phase

(Fig. 6.11) with modulation vector as $\boldsymbol{q}^1 = \pm 0.6\boldsymbol{a}^* + 0.2\boldsymbol{b}^*$ after the sample was heated to high-T and cooled down to RT under vacuum (0.001 mbar) applied by standard pump. Changes in Lattice parameters, strain, oxygen order modulation which is irreversible, stabilized to several distinct N phases and twin domain evolution clearly indicates the effects of oxygen pressure on the structure in both global local scale. High pressure study is independent of oxygen content as the sample is under pressure assuming almost no change in δ but the thermal effects can change the interaction and coming both effect it can be stabilized in different phase whereas under vacuum system loose oxygen the N = 5 phase can be understood in terms of both oxygen content and vacuum effects. However in more general aspect $Pr_2NiO_{4+\delta}$ exhibits very rich and complex phase diagram in terms of higher dimensional oxygen ordering as function of temperature at different oxygen pressure which might b helpful to understand the high oxygen mobility in this compound and would be interesting to study the phase diagram when it is re-heated under pressure again.

Besides the oxygen ordering at different temperature and pressure hole doping either by oxygen and Sr or codoping in Pr_2NiO_4 induces the charge segregation on the NiO_2 plane and results very complex stripe and spin ordering depending on the hole concentration. Interplay between stripe charge and spin ordering is different in oxygen doped sample compare to only Sr-doped as in the former situation extra degree of oxygen ordering is added in addition to those charge and spin ordering while it absent for the later case. Single crystal X-ray diffraction on oxygen doped $Pr_2NiO_{4.25}$ with hole concentration $n_h = 0.5$ reveals the checkerboard-type charge ordering (ε =1/2) at RT and still exist at low temperature T = 80K along with stripe charge ordering (ε = 1/3) where the average structure and modulation vector of oxygen order remains unchanged. Similar results has been observed from single crystal neutron diffraction study on $Pr_2NiO_{4.25}$ at 2K in addition stripe spin order peaks are present but only difference is the stripe incommensurability. Neutron diffraction on Sr-doped $Pr_{1.5}Sr_{0.5}NiO_4$ sample with same hole concentration n_h =0.5 shows similar checkerboard charge ordering but incommensurate magnetic ordering (ε = 0.44) without stripe charge ordering as well no oxygen ordering at 2K. However the stripe incommensurate charge order (ε = 0.4) is evident from single crystal X-ray diffraction on $Pr_{1.5}Sr_{0.5}NiO_4$ but no CB charge order at 80K. This

is not clear yet why such ordering phenomena observed via X-ray and neutron diffraction are different, hole concentration and sample history would be possible reason for this. But if we focus on results from neutron and X-ray diffraction data separately we can draw the conclusions as follows: simultaneous CB and stripe charge order in $Pr_2NiO_{4.25}$ can emerge from nano phase separation similar to cobaltates system giving rise to hourglass shaped magnetic excitation. But system exhibits oxygen ordering that might also play the similar role to segregate the charges in nano phase regime. In this case it needs to be confirmed by measuring the magnetic excitation curve on spin order peaks and phonon excitation on oxygen order peaks using inelastic neutron scattering technique. Another features stripeless incommensurate magnetic ordering in $Pr_{1.5}Sr_{0.5}NiO_4$ could be understood in the frame of stacking fault in CB matrix similarly to half doped cobaltate again which truncate the modulation of CB charge ordering and give rise diffuse rods of CBCO evident from experiment while induce the stripe magnetic order via complex superexchange between Ni^{2+} crossing the stacking domain wall. In this case if it shows the hourglass shape magnetic excitation then it might violet the statement that stripe charge order are able to explain the origin of hourglass type magnetic spectrum mostly discussed in superconducting cuprates and other cobaltates. However, strong magnetic correlation and long range ordering along c^* has been found in oxygen doped $Pr_2NiO_{4.25}$ sample having stripe magnetic unit cell where c axis is doubled. This might be because of different spin orientation between alternation NiO_2 planes whereas the magnetic peaks appears as diffuse rod along c^* in $Pr_{1.5}Sr_{0.5}NiO_4$ indicating disorder and short range of spin order. That is why the polarized neutron in and out of plane SF/NSF scattering would be helpful to see the orientation of magnetic spin in Ni^{2+} sites. Strong and supporting features which brings the interest to carry out such SF/NSF experiments are observed magnetic hysteresis curve which appears when weak external magnetic field of 50 Oe is applied parallel to NiO_2 i.e. *a*-*b* plane and spin reorientation at very low temperature ~ 8K which is evident from inverse magnetic susceptibility curve. This hysteresis curve indicates the magnetic spin are not exact antiparallel somewhat canted on the plane and give rise to weak ferromagnetic contribution to the magnetic ordering.

Acknowledgement

I would like to express my sincere gratitude to my supervisor Dr. Antoine Villesuzanne and co-supervisor Prof. Werner Paulus for their continuous support of my Ph.D. study and related research, for their patience, motivation, and immense knowledge. Their guidance helped me in all the time of research and writing of this thesis. I could not have imagined having a better advisor and mentor for my Ph.D. thesis. Besides my supervisors, I would like to thank Dr. Monica Ceretti for enlightening me the first glance in field of single crystal growth that was very important to fulfil the aim of my thesis and for scientific and constructive discussion. My sincere thanks also goes to scientists from ESRF, Grenoble: Dr. Dmitry Chernyshov, Dr. Vadim Diadkin, Dr. Alexei Bossak, and Dr. Pieter Glatzel, who provided me an opportunity to perform *in situ* experiments in to their respective beamline and research facilities and constant support during measurements. My sincere thanks also goes to Prof. Georg Roth from RWTH from Aachen University and Dr. Martin Meven from FRM-II and Dr. Angelique Letrouit-Lebranchu from Univ. Montpellier for their active participation and insightful comments and encouragement during the experiments at ESRF. I would also like to thanks scientists from PSI, Villigen: Dr. Juerg Schefer, Dr. Matthias Frontzek and Dr. Lukas Keller for performing the neutron diffraction experiment on the diffractometer of DMC, SINQ. Without all these precious support, it would not be possible to conduct this research.

I sincerely thank also Prof. Mario Maglione for giving me the opportunity to work in the ICMCB group in Univ. Bordeaux and Prof. Philippe Papet for that in the group C2M, ICGM Univ. Montpellier. I greatly appreciate the help from technician and research engineer from Univ. Montpellier: Antonio Vieira-E-Silva for optimizing the capillary high-pressure cell, Dr. Bernard Fraisse, Dominique Granier for their technical support in X-ray powder diffraction, Corine Reibel for support in SQUID magnetic measurements, Pierre Sans for computer and IT support, Veronique Sidoux and Francois Blanc for scientific purchase and travel arrangements. I would like to thanks Dr. J.M. Bassat for the carrying out the measurements in the lab of ICMCB, Univ. Bordeaux and

Frederique Bonnet for helping me in administrative work there. I would like to thank the rest of my thesis committee: Prof. Georg Roth, Dr. Christine Martin, Prof. M. S. Ramachandra Rao, Prof. Phillippe Guionneau and Prof. Philippe Papet for their insightful comments and encouragement, but also for the hard question, which incented me to widen my research from various perspectives.

I thank my brother and fellow labmate Avishek Maity for the stimulating discussions, for the sleepless nights we were working together during experiment in home lab and in large-scale facilities. Also I thank my friends and former labmates Adrien, Bartosz, Oles, Sumit, Tran, Elizabeth and alliu for kind help, nice company and pleasant time we have had.

Last but not the least, I would like to thank my family: my parents Anup and Urmila, to my elder sisters Priyanka and Tuhina and to my brothers-in-law Subhas and Biplab for supporting me spiritually throughout writing this thesis and my life in general.

Rajesh Dutta,

University Montpellier, FR

28th September 2017

Résumé

Cette thèse porte sur l'étude des relations entre ordre structural des ions oxygène interstitiels et ordres électroniques et/ou magnétiques dans les oxydes Pr_2NiO_4 fortement corrélés et dopés en trous. Les évolutions structurales en fonction de la composition (taux de dopage) et de la température peuvent être ici décrites en termes de modulation à longue portée, en *(3+n)*-dimensions ; d'intéressants phénomènes de mise en ordre se manifestent, impliquant deux états fondamentaux électroniques, de type rubans commensurable et de type échiquier, respectivement, et associés à un ordre de spin. Le dopage en trous a été produit par substitution du strontium au praséodyme, ou par insertion d'ions oxygène interstitiels. Le structure de $Pr_2NiO_{4+\delta}$ ($\delta \approx 0.25$) à température ambiante est usuellement décrite comme orthorhombique, mais un éclatement des raies *(220/-220)* a été identifié dans le diagramme de diffraction sur poudre, conduisant à une structure monoclinique (groupe d'espace *F2/m*, $\gamma = 90.06^0$). Le diagramme de diffraction des neutrons sur monocristal comporte des raies satellites (mise en ordre des ions oxygène interstitiels) avec quatre individus, ainsi que des raies principales de Bragg pour chaque plan (*hkn*/2) perpendiculaire à l'axe c^*. Les vecteurs de modulation commensurables décrivant ces surstructures sont $\boldsymbol{q_1} = \pm 0.833\boldsymbol{a^*} + 0.5\boldsymbol{b^*}$ and $\boldsymbol{q_2} = \pm 0.252\boldsymbol{a^*} + 0.249\boldsymbol{b^*} + 0.5\boldsymbol{c^*}$, et la structure est décrite dans le groupe de super-espace $F2/m(\alpha_1\beta_10)(0s)(\alpha_2\beta_21/2)(00)$ *(3+2)*-dimensions. Le calcul théorique des positions de raies pour l'ordre des oxygènes interstitiels permet de reproduire les plans *(hk0)* déterminés expérimentalement, à l'exception de quelques raies de sur-structure *(100)* de faible intensité et provenant d'un ordre de charge Ni^{2+}/Ni^{3+} de type échiquier. Les études haute température de $Pr_2NiO_{4+\delta}$ ont mis en évidence de fortes corrélations pour la mise en ordre des ions oxygène interstitiels, même au-delà de la transition de phase où la modulation passe de commensurable (à température ambiante) à incommensurable dès 250 °C. L'ordre 3D des ions oxygène selon les plans devient 2D à 150°C, et l'éclatement des raies de mise en ordre de l'oxygène (vecteur de modulation $\boldsymbol{q_1} = \pm 0.317\boldsymbol{a^*} + 0.317\boldsymbol{b^*} + 0.12\boldsymbol{c^*}$) disparaît progressivement pour devenir une raie simple sans composante selon c^*. La température de transition $(T_{LTO/HTT})$ croît de 400 à 450 °C pour $P(O_2)$ croissant de 1 à 75 bars, et le vecteur de modulation varie irréversiblement avec $P(O_2)$. Une phase stable et ordonnée de vecteur de modulation $\boldsymbol{q_1} = \pm 0.6\boldsymbol{a^*} + 0.2\boldsymbol{b^*}$ a été mise en évidence par chauffage à haute température de l'échantillon puis refroidissement sous vide. Le dopage en trous de Pr_2NiO_4 induit une ségrégation de phase dans le plan NiO_2 et un ordre de charge et de spin complexe de type rubans, dépendant de la concentration en trous. Les relations entre ordre de charge et de spin sont de nature différente pour les phases dopées par substitution et celles dopées par insertion d'oxygène. La diffraction des neutrons sur monocristal de $Pr_2NiO_{4.25}$ a révélé un ordre de charge de type échiquier, à température ambiante et qui persiste jusqu'à 80 K, ainsi qu'un ordre de charge de type rubans où la structure moyenne et le vecteur de modulation sont inchangés. Des résultats similaires ont été obtenus par diffraction des neutrons sur $Pr_2NiO_{4.25}$ at 2 K; de plus, des raies de sur-structure pour un ordre de spin de type rubans ont été observées. La diffraction des neutrons sur $Pr_{1.5}Sr_{0.5}NiO_4$ (même concentration en trous) montre aussi un ordre de charge de type échiquier mais un ordre de spin incommensurable, sans sur-structure de charge de type rubans à 2 K. Cependant, un ordre de charge incommensurable de type rubans a été mis en évidence dans $Pr_{1.5}Sr_{0.5}NiO_4$ par diffraction des rayons X sur monocristal, à 80 K. L'émergence simultanée d'ordres de type échiquier et rubans peut se produire à partir de séparations de phase à l'échelle nanométriques dans $Pr_2NiO_{4.25}$. Un ordre magnétique incommensurable trouvé dans $Pr_{1.5}Sr_{0.5}NiO_4$ a pu être interprété comme issu de défauts d'empilement dans une matrice de type échiquier. Enfin, de fortes corrélations magnétiques, avec un ordre à longue distance de type rubans selon c*, a été observé dans $Pr_2NiO_{4.25}$.

Summary

The main objective of the thesis was to study the interplay between interstitial oxygen order and electronic/magnetic order in strongly correlated hole-doped Pr_2NiO_4 oxides. The structural evolution versus composition (i.e. doping rate) and temperature can be described by means of long-range structural modulations in *(3+n)*-dimension ; interesting physical ordering phenomena take place that involve two stable electronic ground states, i.e. commensurate stripe and checkerboard-type charge order state, associated to spin ordering. Hole doping was achieved both by substituting strontium to praseodymium and by oxygen intercalation on interstitial lattice sites. The basic structure of $Pr_2NiO_{4+\delta}$ ($\delta \approx 0.25$) at ambient is known as orthorhombic, but a close inspection to the well-defined splitting of *(220/-220)* reflections in the powder diffraction pattern reveals a monoclinic structure (*F2/m* space group, $\gamma = 90.06^0$). The single crystal diffraction pattern of $Pr_2NiO_{4+\delta}$ contains interstitial oxygen ordering satellites with four twin individuals, along with main Bragg reflections in every *(hkn/2)* plane perpendicular to the c^*-axis. The modulation vectors that describe these features was found to be commensurate $\boldsymbol{q_1} = \pm 0.833\boldsymbol{a^*} + 0.5\boldsymbol{b^*}$ and $\boldsymbol{q_2} = \pm 0.252\boldsymbol{a^*} + 0.249\boldsymbol{b^*} + 0.5\boldsymbol{c^*}$, and the structure is described in the $F2/m(\alpha_1\beta_10)(0s)(\alpha_2\beta_21/2)(00)$ superspacegroup in *(3+2)*-dimension. Model calculations of oxygen ordering peak positions replicate experimental *(hk0)* planes, except few weak *(100)*-type superstructure reflections coming from checkerboard charge ordering of Ni^{2+}/Ni^{3+}. High temperature studies of $Pr_2NiO_{4+\delta}$ indicates strong correlations of oxygen ordering in disordered phases, even after a phase transition ($T \geq T_{HTT}$) where the modulation of oxygen ordering changes from commensurate at room temperature to incommensurate already at 250 ^{0}C. 3D oxygen ordering in *(hhl)* planes becomes 2D in nature at 150 ^{0}C, where the splitting of oxygen ordering peaks with modulation vector ($\boldsymbol{q_1} = \pm 0.317\boldsymbol{a^*} + 0.317\boldsymbol{b^*} + 0.12\boldsymbol{c^*}$) start to vanish and becomes a single reflection with no component along c^*. The transition temperature $(T_{LTO/HTT})$ increases from 400 to 420 and 450 ^{0}C at atmospheric pressure, 50 and 75 bars of oxygen partial pressure, respectively, and the change in modulation vector of oxygen ordering is irreversible vs. oxygen pressure. A stable oxygen ordering phase was evidenced with modulation vector $\boldsymbol{q_1} = \pm 0.6\boldsymbol{a^*} + 0.2\boldsymbol{b^*}$ after the sample was heated to high temperature and cooled down to room temperature under vacuum. Hole doping in Pr_2NiO_4 induces a charge segregation on the NiO_2 plane and results in very complex stripe-type charge and spin ordering, depending on the hole concentration. The interplay between stripe charge and spin ordering is different in oxygen-doped samples, compared to Sr-substituted samples. Single crystal X-ray diffraction on oxygen doped $Pr_2NiO_{4.25}$ reveals a checkerboard-type charge ordering at room temperature that still exists down to T = 80 K, along with stripe-type charge ordering where the average structure and modulation vector remain unchanged. Similar results were achieved from single crystal neutron diffraction on $Pr_2NiO_{4.25}$ at 2 K; in addition, stripe-type spin order peaks are present. Neutron diffraction on $Pr_{1.5}Sr_{0.5}NiO_4$ samples (same hole concentration) shows similar checkerboard charge ordering but incommensurate magnetic ordering, without stripe-type charge ordering at 2 K. However, a stripe-type incommensurate charge order was evidenced from single crystal X-ray diffraction on $Pr_{1.5}Sr_{0.5}NiO_4$ at 80 K. Simultaneous checkerboard and stripe-type charge orders can be emerge from nano phase separation in $Pr_2NiO_{4.25}$. Another feature, i.e. stripe-less incommensurate magnetic ordering in $Pr_{1.5}Sr_{0.5}NiO_4$, could be interpreted as resulting from stacking faults in a checkerboard matrix. Also, strong magnetic correlation with stripe-type long-range ordering along c^* was found in $Pr_2NiO_{4.25}$ samples.

Etude *in situ*, par diffraction des rayons X et diffusion neutronique sur monocristaux, de la complexité structurale de l'oxyde fortement corrélé $Pr_{2-}Sr_xNiO_{4+\delta}$

Introduction.

Le développement des piles à combustible de type SOFC, de capteurs et des membranes à oxygène requiert des matériaux bon conducteurs de l'ion oxygène, et stables en température. Le challenge est actuellement de découvrir de nouveaux matériaux de ce type, pouvant en particulier permettre d'abaisser la température de fonctionnement.

Les phases de type Ruddlesden-Popper, tel $Pr_2NiO_{4+\delta}$, constituent une très prometteuse alternative aux oxydes à structure de type perovskite.

Afin de développer et optimiser de façon rationnelle des conducteurs ioniques de type Ruddlesden-Popper, il convient de comprendre les mécanismes de conduction de l'ion oxygène, ainsi que la nature des mises en ordre des ions oxygène excédentaires.

La migration de l'oxygène dans ces structures fait intervenir à la fois des mécanismes de sauts, de sauts couplés oxygène apical-oxygène interstitiel, ainsi que des modes de phonons de basse énergie.

Ce travail porte essentiellement sur l'étude de $Pr_2NiO_{4+\delta}$, avec dopage par substitution du strontium au praséodyme, pour la compréhension des instabilités structurales en fonction du taux δ d'oxygène interstitiel, de la température, de la pression et du taux de substitution Sr/Pr. Ces systèmes sont particulièrement intéressants en vue d'application, puisque la mobilité de l'ion oxygène se manifeste dès la température ambiante.

Maclage et structure de monocristaux de $Pr_{2-x}Sr_xNiO_{4+\delta}$ (x = 0, 0.125, 0.25 and 0.5), étudiés par diffraction des rayons X.

Les monocristaux de composition $Pr_{2-x}Sr_xNiO_{4+\delta}$ (x = 0, 0.125, 0.25 and 0.5) ont été synthétisés et étudiés par diffraction des rayons X, afin d'établir le diagramme de phase en fonction du taux δ d'oxygène interstitiel, à température ambiante.

Pour $Pr_2NiO_{4.25}$, la structure moyenne de groupe d'espace *Fmmm* comporte des macles et montre un ordre à longue distance de l'oxygène interstitiel (surstructures), qui a pu être indexé comme une modulation commensurable en (3+2) dimensions, avec un vecteur de modulation ($\boldsymbol{q_1}$ = ±0.831$\boldsymbol{a}$* + 0.499$\boldsymbol{b}$*). Le groupe de super-espace a pu être déterminé comme $F2/m(\alpha_1\beta_1 0)(0s)(\alpha_2\beta_2 1/2)(00)$.

Concernant la phase $Pr_{1.875}Sr_{0.125}NiO_{4+\delta}$, le changement avec le dopage revient à une transition de commensurable à incommensurable, avec un vecteur de modulation $\boldsymbol{q_1}$ = ±0.7914$\boldsymbol{a}$* + 0.5268$\boldsymbol{b}$*, et le groupe de super-espace $F2/m(\alpha_1\beta_1 0)(0s)$. Les distributions de macles ont été étudiées en détails. Pour les taux de dopage x_{Sr} = 0.25 and 0.5, aucune surstructure n'a été détectée par rayons X.

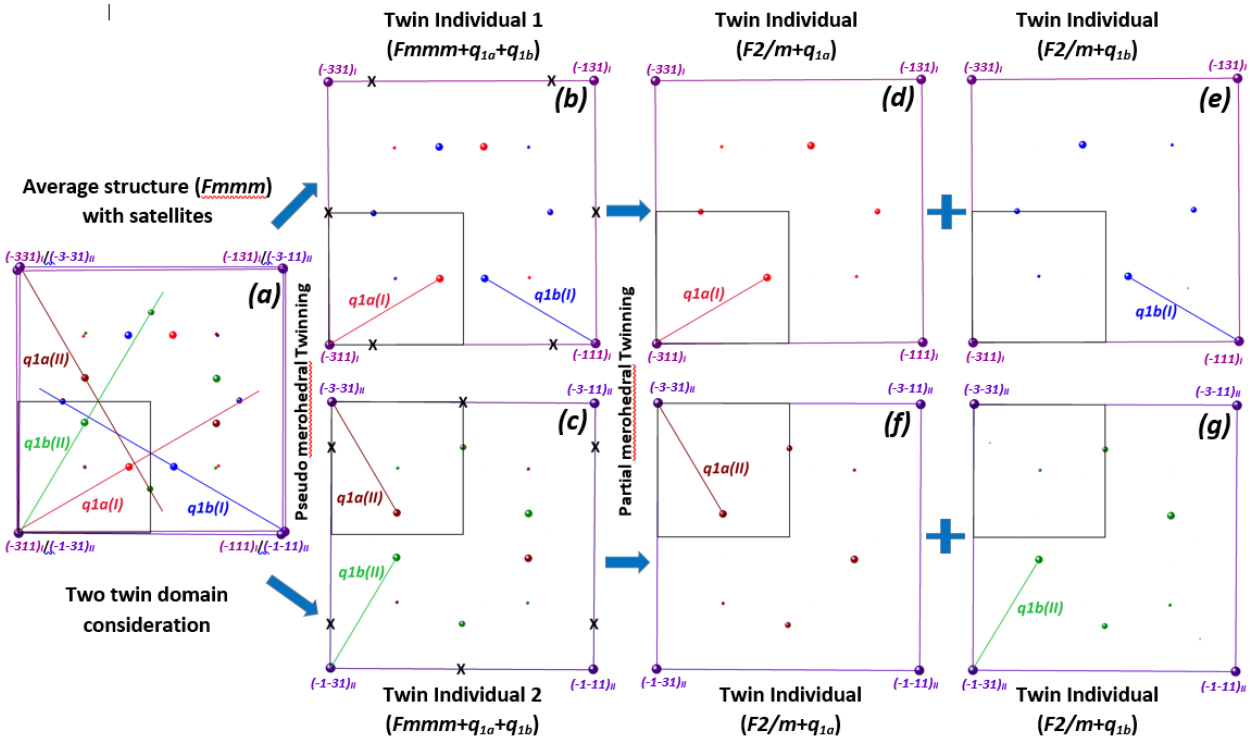

Figure 1. Prise en compte du maclage pour l'indexation des spectres de diffraction.

La figure 2 montre le diagramme de phase correspondant à cette première étude.

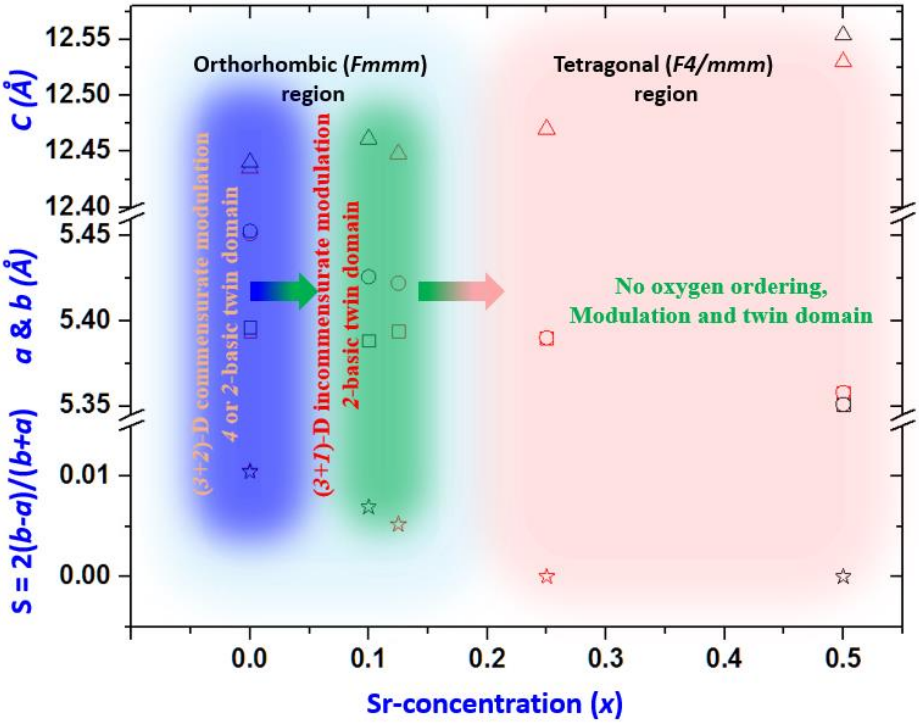

Figure 2. Diagramme de phase pour $Pr_{2-x}Sr_xNiO_{4+\delta}$ en function de x et à temperature ambiante.

Etude *in situ* des modulations structurales dans $Pr_2NiO_{4.25}$ en fonction de la température, par diffraction des rayons X (rayonnement synchrotron) sur monocristaux.

Lorsque la température augmente au-delà de la température ambiante, la modulation structurale en *(3+1)*-dimensions (quasi commensurable avec $\boldsymbol{q_1} = \pm 0.821\boldsymbol{a}^* + 0.493\boldsymbol{b}^*$) s'éloigne de la commensurabilité et l'ordre des oxygène devient 2D vers 200°C (Figure 3). La transition structurale connue à 400°C s'accompagne de la disparition de toute surstructure.

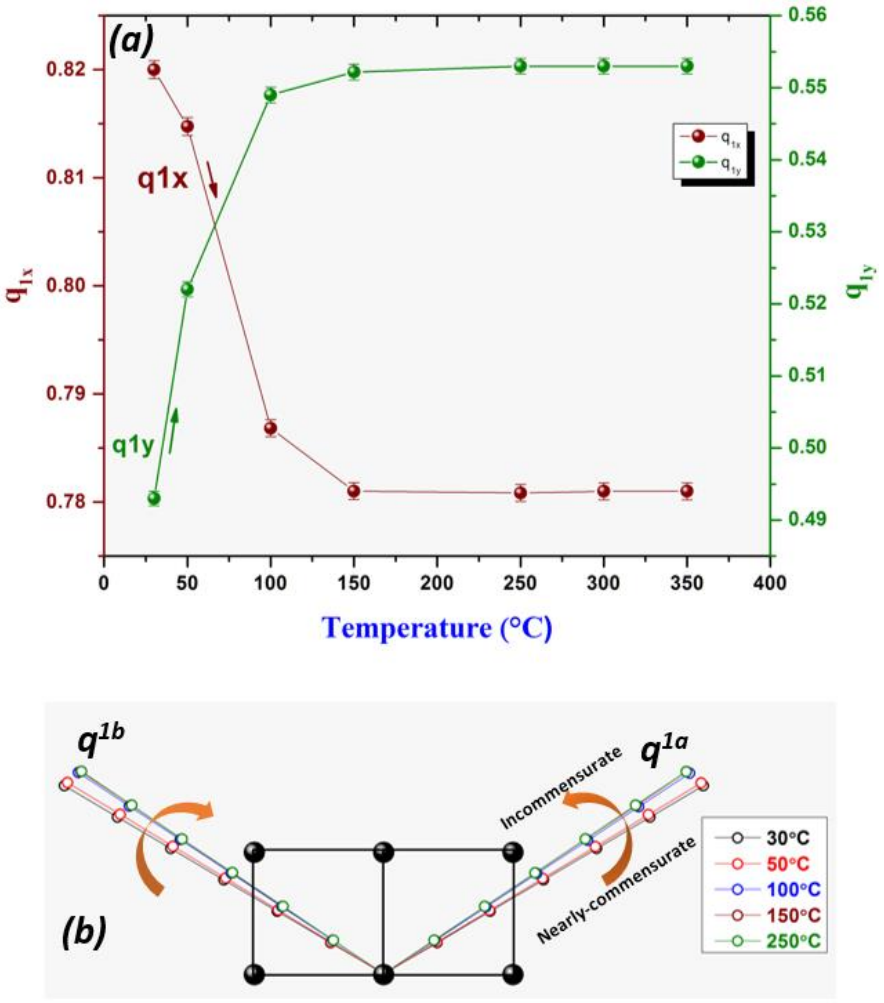

Figure 3: (a) Composantes des vecteurs de modulation en fonction de la température. (b) Illustration de la transition commensurable-incommensurable.

La figure 4 montre le diagramme de phase de $Pr_2NiO_{4.25}$ en fonction de la température. A gauche, sont montrées les phases observées en fonction du taux d'oxygène interstitiel, lors de l'oxydation électrochimique à T° ambiante. La phase de départ (*Fmmm*) comportant la modulation commensurable en *(3+2)*-dimensions persiste jusqu'à l'apparition de la phase quadratique de groupe d'espace $P4_2/ncm$; puis une phase réentrante de groupe d'espace *Bmab* est observée, de caractère orthorhombique plus marqué. Puis la température s'élève, pour le taux δ=0.25, avec toutefois un léger départ d'oxygène avec la température (échelle de droite). La modulation de l'ordre des oxygènes est très sensible à la température, passant progressivement de 3D puis 2D, pour disparaître donc à 400°C. Ces observations, ainsi que par ailleurs la

perte d'ordre lorsque $\delta<0.125$, montre que ces modulations ne sont établies que pour un taux minimum d'oxygène interstitiel.

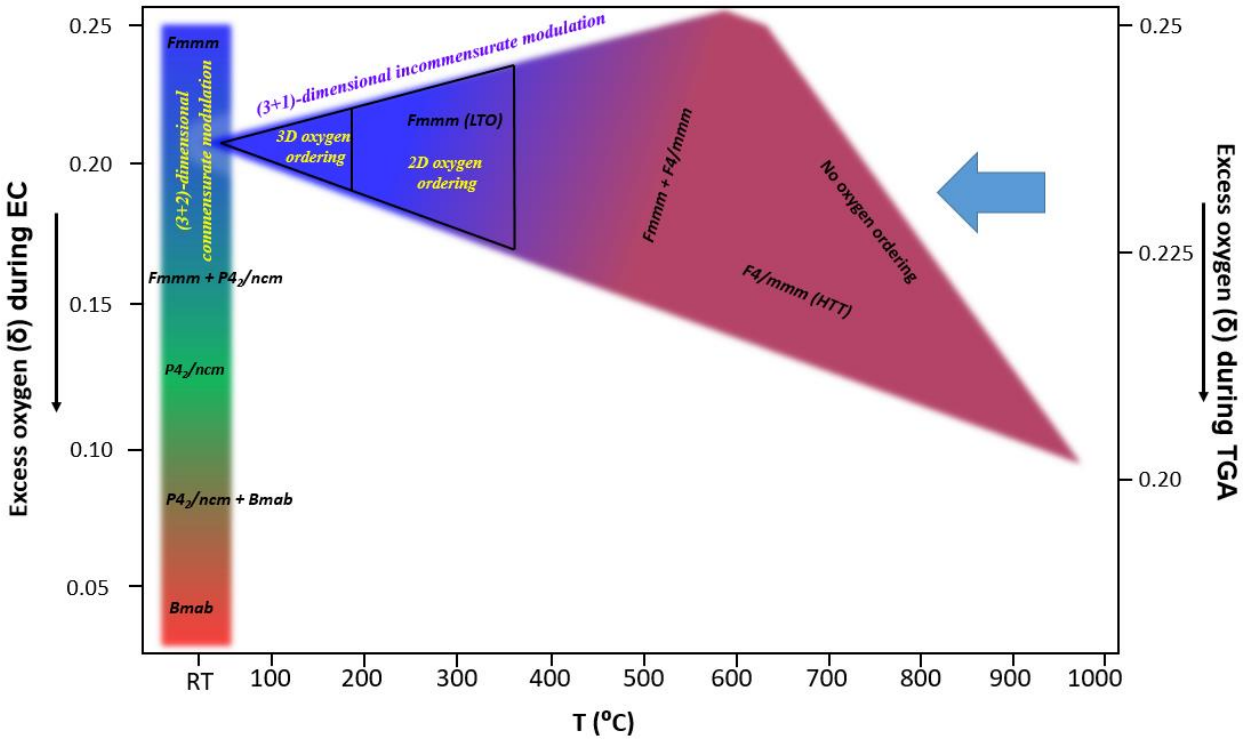

Figure 4: Diagramme de phase pour $Pr_2NiO_{4+\delta}$ selon deux processus réactionnels : (gauche) oxydation électrochimique à température ambiante ; (droite) en fonction de la température.

$Pr_{2-x}Sr_xNiO_{4+\delta}$: ordres incommensurables de charge et de spin, de type ruban, étudiés par diffraction des rayons X et des neutrons.

Le dopage par substitution Sr/Pr ou insertion d'oxygène revient à doper en trous les ions nickel ; s'ensuivent des mises en ordre de dans les plans NiO_2 de type échiquier ou rubans (ordre de charge ou orbitalaire, séparations de phases) ou à la fois de charge et de spin (rubans).

Les échantillons pour lesquels $\delta \sim 0.25$ ou $x = 0.5$ montrent à la fois un ordre de charge et de spin à basse température, en superposition à l'ordre des oxygènes interstitiels pour la phase $\delta \sim 0.25$. Les observations se comprennent comme mettant en jeu la compétition entre deux états fondamentaux, de type échiquier et ruban, respectivement.

La seule différence entre dopage Sr/Pr et insertion d'oxygène réside, ici, dans l'éclatement des pics associés à l'ordre de charge. Les corrélations de spin sont de type 3D, puis 2D lorsque le taux de trous augmente encore par dopage Sr/Pr. L'ordre de charge apparaît toujours comme à courte distance, sauf dans les cas exempts de strontium.

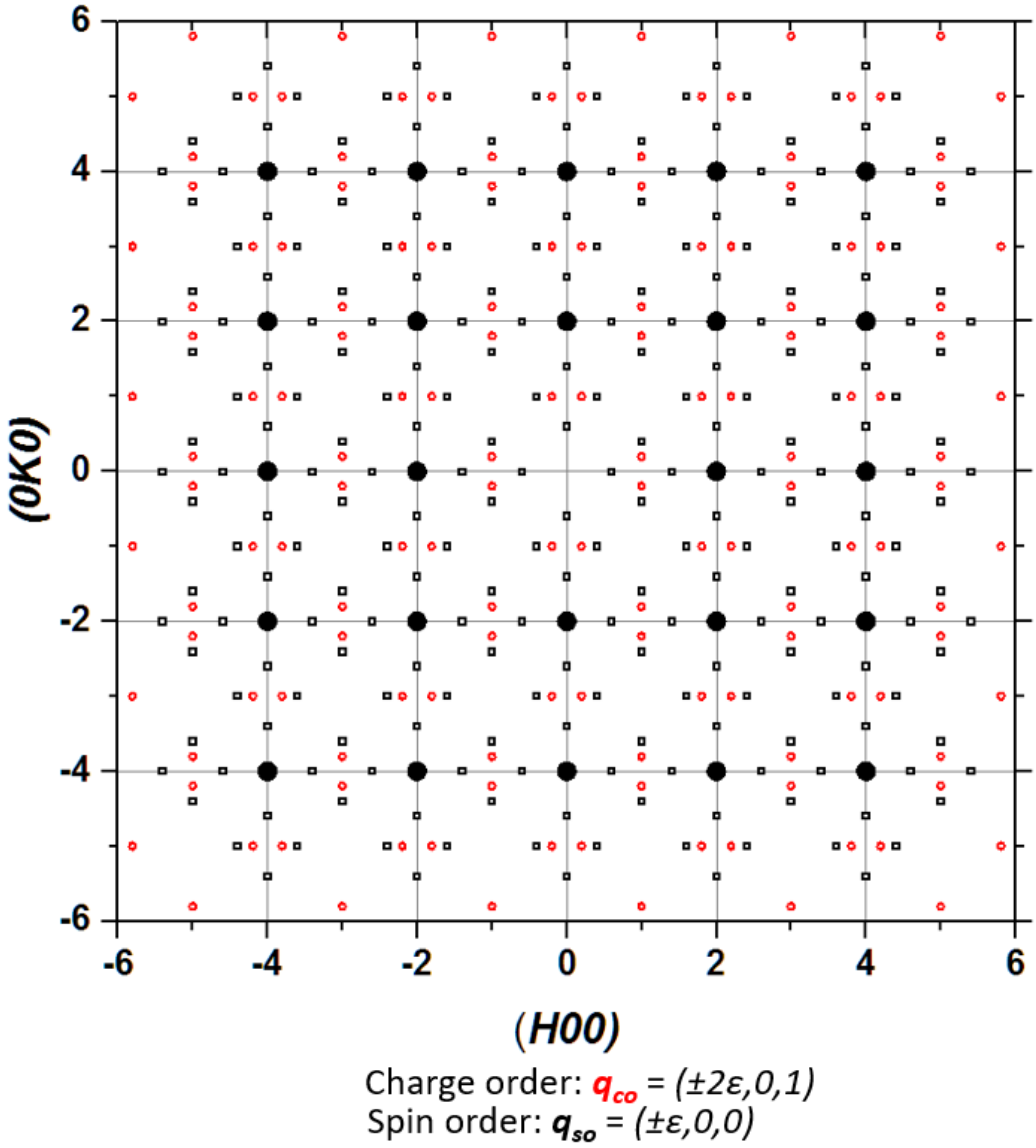

Figure 5. Représentation calculée d'une plan (hk0) montrant les pics de diffraction pour l'ordre de charge (rouge) et de spin (noir), de type ruban, pour des vecteurs de modulation de paramètre ε = 0.44.

Une inconnue demeure quant au désaccord entre degré d'incommensurabilité obtenu par rayons X, par rapport à celui obtenu par neutrons. Cependant, ces deux techniques ont permis de proposer

que l'ordre de charge de type ruban provient d'interactions de type polaroniques, de nature dynamique.

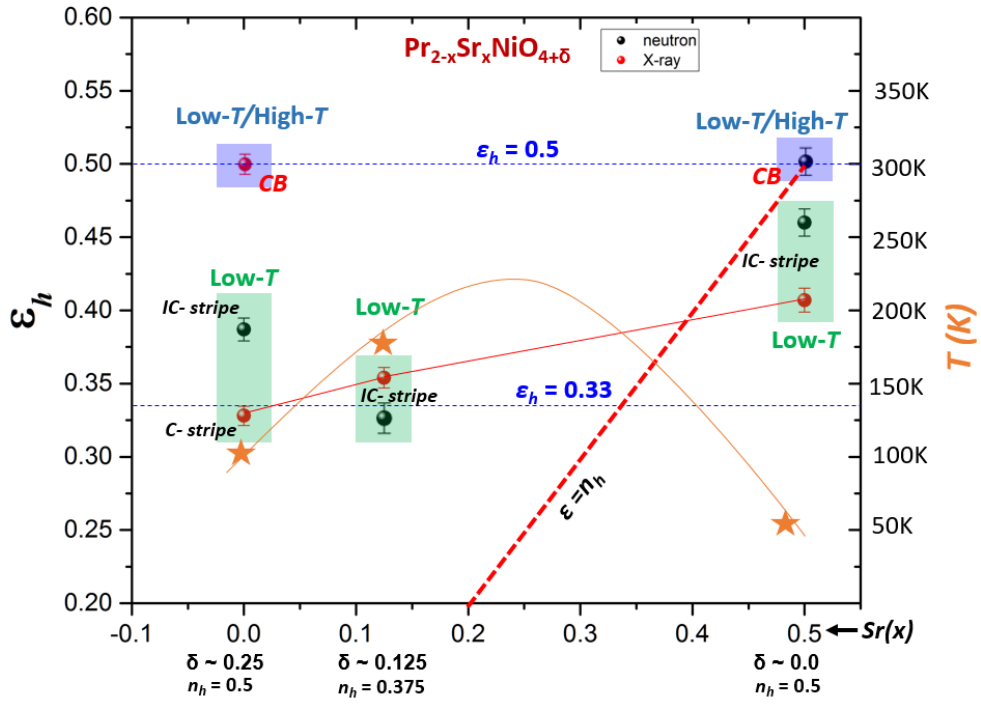

Figure 6. Diagramme de phase pour $Pr_2NiO_{4+\delta}$ établi par diffraction des rayons X et des neutrons, montrant les types d'ordre de charge en fonction du taux de trous de dopage, de la température d'ordre de spin (échelle de droite) et de l'incommensurabilité (échelle de gauche).

Etude in situ, par diffraction des rayons X et diffusion neutronique sur monocristaux, de la complexité structurale de l'oxyde fortement corrélé $Pr_{2-x}Sr_xNiO_{4+\delta}$

Les oxydes non-stœchiométriques de type Ruddlesden-Popper, tel que $Pr_2NiO_{4+\delta}$, peuvent être dopés en trous par substitution du strontium au praséodyme ou par insertion d'oxygène. Ces modes de dopage s'accompagnent de mises en ordre complexes impliquant la distribution des ions oxygène excédentaires, des ordres de charge et/ou de spin. Le diagramme de phase de $Pr_{2-x}Sr_xNiO_{4+\delta}$ a été exploré par diffraction des rayons X (en laboratoire et par rayonnement synchrotron) ainsi que neutronique. Pour la phase $Pr_2NiO_{4.25}$, nous avons mis en évidence une sur-structure incommensurable avec des réflexions satellites au 6ème ordre, produisant un spectre de diffraction très complexe avec 4 individus et 8 domaines incommensurables. Par diffractions synchrotron et neutronique, un ordre de charge de type échiquier a été identifié dès la température ambiante, suivi en dessous de 170 K par un ordre de type rubans ; un ordre de spin incommensurable s'établit au-dessous de 99 K. Ce travail a permis de révéler un ensemble complexe de phases ordonnées structuralement et électroniquement, gouvernées par des variations subtiles de stœchiométrie en strontium et oxygène.

Mots clés : Oxides fortment corrélés, Dopage par trou, Structures modules, ordre de charge-spin, Oxides non-stoechiometriques, Mobilite de l'oxygene

---

Structural Complexity in Strongly Correlated $Pr_{2-x}Sr_xNiO_{4+\delta}$, Explored by *in situ* Single Crystal X-ray and Neutron Diffraction

Non-stoichiometric oxides from the Ruddlesden-Popper series, such as $Pr_2NiO_{4+\delta}$, can be hole-doped by substituting strontium to praseodymium or by oxygen insertion. This leads to complex structural ordering involving oxygen-, charge- and spin ordering. The complex phase diagram of $Pr_{2-x}Sr_xNiO_{4+\delta}$ was explored using X-ray (laboratory and synchrotron) as well as neutron diffractions. For the doped phase of highest oxygen content ($Pr_2NiO_{4.25}$), we could evidence an incommensurate structure with satellite reflections of 6th order, yielding a very complex diffraction pattern of up to four twin-individuals and eight incommensurate domains. Checkerboard-type charge ordering was identified already at ambient temperature, while stripe charge ordering was observed below 170 K by synchrotron and neutron diffraction; incommensurate spin ordering appears below 99 K. This thesis reveals the existence of many complex oxygen and electronically ordered phases going along with small variations of the oxygen/strontium stoichiometry.

Keywords: Strongly correlated electron system, Hole doping, Modulated structure, charge-spin ordering, Non-stoichiometric oxides and Oxygen mobility

---

Institut de Chimie de la Matière Condensée de Bordeaux - UPR 9048 - ICMCB

[Oxydes et Électro-Céramiques Architecturées pour l'Énergie et l'Électronique, 87 Avenue du Dr Albert Schweitzer, 33600 Pessac, France]